UNIVERSIDADE ESTADUAL PAULISTA
"JÚLIO DE MESQUITA FILHO"
INSTITUTO DE QUIMICA DE ARARAQUARA

YULIANA PÉREZ SÁNCHEZ

Molecular Electronics and Electrochemistry: The Case of Ferrocene-tagged Interfaces and of Organic Molecular Junctions Studied by Time-dependent Methods

Thesis submitted in the Institute of Chemistry in fulfillment of the requirements for the degree of Doctor of Philosophy in chemistry

Supervisor: Prof. Dr. Paulo Roberto BUENO
Co-Supervisor: Prof. Dr. Adriano dos SANTOS

Araraquara
2023

Sánchez, Yuliana Pérez
S211m Molecular electronics and electrochemistry: the case of ferrocene-tagged interfaces and of organic molecular junctions studied by time-dependent methods / Yuliana Pérez Sánchez – Araraquara: [s.n.], 2023
164 p.: il.

Thesis (doctor) – Universidade Estadual Paulista, Instituto de Química
Advisor: Paulo Roberto Bueno
Co-advisor: Adriano dos Santos

1. Charge transfer. 2. Impedance spectroscopy. 3. Nanoeletronics. 4. Tunneling. 5. Quantum electrodynamics. I. Title.

Sistema de geração automática de fichas catalográficas da Unesp. Biblioteca do Instituto de Química, Araraquara. Dados fornecidos pelo autor(a).

Essa ficha não pode ser modificada

UNIVERSIDADE ESTADUAL PAULISTA
"JÚLIO DE MESQUITA FILHO"
INSTITUTO DE QUIMICA DE ARARAQUARA

YULIANA PÉREZ SÁNCHEZ

Eletrônica Molecular e Eletroquímica: O Caso de Interfaces Marcadas com Ferroceno e de Junções Moleculares Orgânicas Estudadas por Métodos Dependentes do Tempo

Tese apresentada ao Instituto de Química, Universidade Estadual Paulista como parte dos requisitos para obtenção do título de doutora em Química.

Orientador: Prof. Dr. Paulo Roberto BUENO
Coorientador: Prof. Dr. Adriano dos SANTOS

Araraquara
2023

CERTIFICADO DE APROVAÇÃO

TÍTULO DA TESE: "Molecular electronics and electrochemistry: the chase of ferrocene-tagged interfaces and of organic molecular junctions studied by time-dependent methods"

AUTORA: YULIANA PÉREZ SÁNCHEZ
ORIENTADOR: PAULO ROBERTO BUENO
COORIENTADOR: ADRIANO DOS SANTOS

Aprovada como parte das exigências para obtenção do Título de Doutora em Química, pela Comissão Examinadora:

Prof. Dr. NELSON RAMOS STRADIOTTO (Participaçao Virtual)
Departamento de Química Analítica, Físico-Química e Inorgânica / Instituto de Quimica - UNESP - Araraquara

Prof. Dr. PAULO ROBERTO BUENO (Participaçao Virtual)
Departamento de Engenharia, Fisica e Matematica / Instituto de Quimica - UNESP - Araraquara

Prof. Dr. FRANK MARTEN (Participaçao Virtual)
Química / University of Bath, United Kingdom

Prof. Dr. VINCENT VIVIER (Participaçao Virtual)
Laboratoire de Réactivité de Surface / Sorbonne Université

Prof. Dr. DAVID ALEJANDRO MIRANDA MERCADO (Participaçao Virtual)
Escuela de Física / Universidad Industrial de Santander, Colômbia

Araraquara, 29 de setembro de 2023

gov.br
Documento assinado digitalmente
PAULO ROBERTO BUENO
Data: 03/10/2023 10:51:38-0300
Verifique em https://validar.iti.gov.br

Impacto potencial desta pesquisa

O desenvolvimento da tese apresentada tem contribuído de maneira significativa ao desenvolvimento da teoria do quantum rate. Uma teoria que o grupo de pesquisa vem trabalhando arduamente e que, consequentemente, tem demostrado frente à comunidade cientifica, por meio das publicações dos resultados em revistas cientificas de alto impacto, a sua capacidade para interpretar processos eletroquímicos em nanoescala. Isso representa um grande avanço no entendimento de fenômenos que impactam não somente a área de sensores, mas também a área de conversão e armazenamento de energia, os quais eventualmente influem no desenvolvimento de avanços tecnológicos de dispositivos que são de suma importância para a sociedade moderna. Particularmente, a interpretação dos processos eletroquímicos em nanoescala já tem se mostrado importante na contribuição tanto no que se refere aos fundamentos quanto à aplicação no desenvolvimento de biossensores, dispositivos de interesse para a nossa sociedade moderna como lembrado na recente pandemia da COVID-19. Em conclusão, a concretização desta tese contribuiu com o caráter inovador sobre o fazer ciência e produção de conhecimento no país, permitindo a deposição de uma patente (21CI019) oriunda dos resultados aplicados da tese.

Potential impact of this research

The development of the presented thesis has significantly contributed in the building of the quantum rate theory. This theory, on which our research group has diligently worked, has been demonstrated to the scientific community through publications in high-impact scientific journals its capability to interpret electrochemical processes at the nanoscale. This represents a significant advancement in understanding phenomena that impact not only the sensor field but also energy conversion and storage, influencing eventually, the development of cutting-edge technological devices crucial to modern society. Particularly, interpreting nanoscale electrochemical processes has proven vital both in theoretical understanding and practical applications, especially in the development of biosensors, a field of great relevance as highlighted during the recent COVID-19 pandemic. Finally, the completion of this thesis contributed innovatively to the scientific landscape and knowledge production within the country, leading to the granting of a patent (21CI019) stemming from the applied results of this research.

Curriculum Vitae

Name: Yuliana PÉREZ SÁNCHEZ
Citation Name: Sánchez, Y.P.
Birth date: 11/04/1993 – Pereira (Risaralda) – Colombia
Professional address: Unesp-Instituto de Química, Departamento de Físico-Química
Rua Prof. Francisco Degni, 55, Bairro Quitandinha
CEP: 14800-060, Araraquara, São Paulo, Brazil

Education

Araraquara, Brazil
02/2019 – 09/2023
Ph.D in Chemistry (Physical Chemistry specialty)
São Paulo State University - UNESP
Thesis: *Molecular electronics and electrochemistry: The case of ferrocene-tagged interfaces and of organic molecular junctions studied by time-dependent methods.*
Supervisor: Prof. Dr. Paulo Roberto Bueno
Co-supervirsor: Prof. Dr. Adriano dos Santos

Campinas, Brazil
02/2017 – 02/2019
M.Sc. in Chemistry (Physical Chemistry specialty)
University of Campinas - UNICAMP
Dissertation: *Nitric oxide-releasing polyester coatings to improve the biocompatibility of implantable medical devices.*
Supervisor: Prof. Dr. Marcelo Ganzarolli de Oliveira

Pereira, Colombia
02/2010 – 03/2016
B.Sc. in Industrial Chemistry
and Associate degree in Chemistry
Technological University of Pereira - UTP
Final degree project: *Evaluation of a binary mixture of preservative aiming to delay the oxidative decay of the ascorbic acid from fresh juice of Citrus latifolia from crops located at Mistrato by spectrophotometry UV-VIS.*
Supervisor: Prof. Dr. Gloria Edith Guerrero Alvarez

Professional Positions

Araraquara, Brazil
22/04/2021 – 20/08/2021
Teaching Assistant
São Paulo State University - UNESP
- Undergraduate program - Chemical engineering: Kinetics and electrochemistry

Campinas, Brazil
01/08/2018 – 30/12/2018
Teaching laboratory Assistant
University of Campinas - UNICAMP
- Undergraduate program - Experimental physical chemistry

La Virginia, Colombia **09/03/2016 – 05/09/2016**	**Quality control laboratory Analyst** Rio Bajo ZF SAS ▸Elaborating programs aiming to get the registration Certificate with the Colombia National Food and Drug Surveillance Institute (INVIMA)
Pereira, Colombia **02/2013 – 03/2015**	**Teaching laboratory Assistant** Technological University of Pereira - UTP ▸Undergraduate program ▸Material warehouse laboratory
Pereira, Colombia **2012 – 2015**	**Researcher Student** Oleoquímica - OLQ (Research group) - UTP ▸Investigation and development
Neiva, Colombia **08/2011 – 01/2012**	**Internship** Schlumberger Surenco SA ▸Well services branch - fluid laboratory

Honors

- ✔ *Merit award:* Outstanding grade point average, Technological university of Pereira, Colombia (2016)
- ✔ *Merit award:* Outstanding grade point average, Technological university of Pereira, Colombia (2014)

Publications & Preprints

Published

GARROTE, B. L.; SÁNCHEZ, Y. P.; LOPES, L. C.; SANTOS, A.; BUENO, P. R. Electron transmittance through quantum capacitive states as a signal amplification mechanism for biosensing applications. Submitted in *Sensors and Actuators B: Chemical*. 134786, doi:10.1016/j.snb.2023.134786 (2024)

SÁNCHEZ, Y. P.; SANTOS, A.; BUENO, P. R. Quantum Mechanical Meaning of the Charge Transfer Resistance. *Journal of Physical Chemistry C*, 126:3151–3162, doi: 10.1021/acs.jpcc.1c07801 (2022).

SÁNCHEZ, Y. P.; SANTOS, A.; BUENO, P. R. Quantum rate efficiency of the charge transfer mediated by quantum capacitive states. *Electrochimica Acta*. 434:141194, doi:10.1016/j.electacta.2022.141194 (2022).

PINZÓN, E. F.;ALARCÓN, E. V. G.; SÁNCHEZ, Y. P.; BUENO, P. R.. Quantum Rate Dynamics and Charge Screening at the Nanoscale Level.*Physical Chemistry Chemical Physics*. 24(26):16200–16206, doi:10.1039/D2CP00199C (2022).

Patent

BUENO, P. R.; GARROTE, BEATRIZ LUCAS; LOPES, L. C.; SANTOS, A.; SANCHEZ, Y. P.; Método e Dispositivo de Amplificação de Sinal Transdutor para Ensaios Capacitivos. 2021, Brasil. Patente: Privilégio de Inovação. Número do registro: BR1020210238356, título: "Método e Dispositivo de Amplificação de Sinal Transdutor para Ensaios Capacitivos" , Instituição de registro: INPI - Instituto Nacional da Propriedade Industrial. Depósito: 26/11/2021.

Congress

- Oral presentation at 74^{th} Annual meeting of the International Society of Electrochemistry, France, 2023.
- Poster presentation at 1^{st} National congress of physics, chemistry and engineer of materials (online), 2021.
- Oral presentatio at 10^{a} Latin American congress of artificial organs and biomaterials (COLAOB), Brazil, 2018.

Scientific Events

- 16^{st} PTASchool of Electrochemistry, Institute of Chemistry, São Paulo University – USP, Brazil, 2023.
- XXXIII Congresso de Iniciação Científica, Institute of Chemistry, São Paulo State University – UNESP, Brazil, 2021.
- Festival de Química, Institute of Chemistry, University of Campinas – UNICAMP, 2017.
- Oportunidades de ahorro y de generación de energía con fuentes renovables, School of Chemistry, Technological University of Pereira - UTP, 2014.
- Química Orgánica de Productos Naturales- 1^{st} Escuela de Verano, School of Chemistry, Technological University of Pereira - UTP, 2014.
- Seminario y Taller Internacional Bioprospección Y Bioindustria, Technological University of Pereira - UTP, 2013.
- Simposio I: De la Investigación Básica al Diagnóstico y Tratamiento: Enfermedades Neurodegenerativas, Technological University of Pereira - UTP, 2013.

To the loves of my life, who gave me life
and who I am sharing it with, Anita and Andrés

Acknowledgements

This study was financed in part by the Coordenação de Aperfeiçoamento de Pessoal de Nivel Superior - Brasil (CAPES) - Finance Code 001.

I would like to thank my supervisor Prof. Paulo Roberto Bueno for the knowledge, guidance and enriching discussion.

I would like to thank my co-supervisor Prof. Adriano dos Santos for the expertise, advice, support, and helpful suggestions.

I would like to deeply thank all the members of the Nanobianics research group for all the discussions that contributed significantly to this thesis, who finished their cycle in the group, including Beatriz Garrote who started with me and helped me lay the foundations for this trip; Laís Lopes, with whom I am extremely grateful for the words of encouragement, affection, wisdom, and friendship; Thamyres Morera for her friendship and for always watching over me; Gabriela Dias for her words of support and motivation; Sarah Brandão for the words of support and kindness and those who were joining the group, Leandro Hostert and Nicolas Siqueira. And last but not least, Erika Alarcon for all the joys and sorrows shared, in addition to the batches of peptides that she kindly synthesized for this thesis, for her academic and other not-so-academic discussions that led to a beautiful friendship.

I would like to thank Prof. Eduardo Maffud Cilli for the support in the peptide synthesis; Dr. R. C. Teixeira and the Electronic Packaging Staff at CTI Renato Archer for the fabrication and characterization of the miniaturized gold electrodes; Prof. Dr. Richard L. McCreery for providing the aromatic molecular junctions; Prof. Martin Schwellberger Barbosa and Dr. Ranilson Angelo da Silva for their help in the experimental adaptation for the characterization of the molecular junctions; and Prof. Marcelo Ornaghi Orlandi who made the laboratory available for such task. Undoubtedly, their collaboration improved the scope of the research developed.

I would like to thank the group of lab technicians, the office staff (in special Rose Portasio) for the important support, and the Institute of Chemistry for the facilities.

I would like to express my deepest gratitude to my unconditional mother, who has been my driving force, without the fight she has given, without her unconditional love and support I would not be where I am now, I owe everything to her. I also thank my brothers Jorge and Victor, who despite their early age, supported me in my first academic stage, thank you for your love. I would like to thank my sisters, Mayuly and Katherine, for their words of encouragement, they have always trusted me and have been there for me despite the distance. I would like to acknowledge my sister visual artist Mayuly that inspired me to be creative in my schematic designs.

I especially thank my fiancé Andrés, for his love, friendship, and trust, for the moments of joy that he has given me, which I treasure with much warmth, for always being by my side in my darkest moments of doubt, without his help, I would not have been able to finish this chapter of my life.

I extend my gratitude to all of my friends, those I made in Brazil, Akemi, Daniela, Leonardo, Leithold, Carlos, and especially Flavia who despite the distance, took the time to listen and advise me. Also, I thank my unconditional friends that I left in Colombia, Yisell, Laura, Mauricio, Diego, Juan, Claudia and kiara.

"It is important to draw wisdom from different places. If you take it from only one place, it becomes rigid and stale."

Uncle Iroh – Avatar The Last Airbender

Abstract

The understanding of electron transmittance, including electron transfer (ET) and transport, is essential not only for comprehending biological systems but also for developing electrical components in the pursuit of fabricating electronic devices. The quantum rate theory proposes a first-principle fundamental quantum rate $\nu = e^2/hC_q$, where e is the elementary charge, h is the Planck constant and C_q is the quantum capacitance that informs on the density-of-states (DOS) as $C_q \propto e^2$DOS. This quantum rate concept is utilized to elucidate the ET rate constant k of electrochemical reaction as $k = G/C_\mu$, where G is the quantum of conductance and C_μ is the electrochemical capacitance. This thesis presents a fundamental study, within the framework of the quantum rate theory, of the ET and transport processes in two kinds of molecular junctions (MJ): electroactive self-assembled monolayer (SAM) over electrodes and aromatic monolayers sandwiched between carbon electrodes. Time-dependent methods, such as impedance spectroscopy (IS) and electrochemical impedance-derived capacitive spectroscopy (ECS), were employed for this study. The impedance data were analyzed by equivalent circuit fitting, specifically as quantum resistive capacitive (RC) point contact. Redox SAMs were formed using Ferrocene-tagged peptides and thiol molecules. These redox SAMs feature C_q, which was determined by ECS, enabling the determination of k as $k = 2(G_0/C_q)$, where G_0 represents the universally known constant for quantum conductance, approximately 77.5 μS. The reciprocal of G_0 defines the quantum resistance as $R_q = 1/G_0 \sim 12{,}9$ kΩ, establishing a quantum limit for ET. This demonstrates that the electrodynamics is governed by R_q and C_q elements. Furthermore, it was determined that R_q comprises two resistive components connected in series: the relaxation resistance (R_{qt}) and the combined resistance of solution and contact (R_s), leading to $R_q \sim 13$ kΩ. Consequently, the interpretation of R_q within the quantum rate model prompted a reassessment of the meaning assigned to the charge transfer resistance R_{ct}, revealing that R_q is equivalent to R_{ct}. Moreover, it was demonstrated that regardless of the molecular backbone, the C_q states of the redox interface mediate the ET between electroactive free species and the electrode, conforming to maximum efficiency of electron transmittance. Specifically, it was proven that an increase in the number of quantum channels N, and consequently of C_q by almost 40%, was achieved through suitable energy level alignment between the level states of the free redox species with that of the DOS of the redox SAM. This exceptional setting allowed for the amplification of the C_q signal for the detection of a biological target. As a proof-of-concept, this amplification mechanism was applied for sensing the nonstructural protein 1 (NS1) biomarker of the dengue virus, resulting in an observed increase in sensitivity of redox capacitive biosensors by at least 1,000. However, it was evidenced that the acidity of the quantum capacitive interface affects the electron transfer mediation as a result of the electrostatic repulsion between the negatively charged surface and redox charged species. Furthermore, the determination of properties G and C_μ using SI measurement of the aromatic MJs demonstrated that G and k are correlated by C_μ, implying that the associated physical concepts studied separately by the electrochemist and physics are inherently related. The results obtained in this thesis demonstrate that the quantum rate model is a suitable theory enable to address phenomena involved with electron transmittance such as electron transfer, quantum conductance, and capacitance in different MJs.

Resumo

A compreensão da transmissão de elétrons, incluindo a transferência eletrônica (TE) e o transporte, é essencial não apenas para a compreensão de sistemas biológicos, mas também para o desenvolvimento de componentes elétricos na busca pela fabricação de dispositivos eletrônicos. A teoria do *quantum rate* propõe uma velocidade quântica fundamental de primerios principios $\nu = {}^{e^2}/_{hC_q}$, onde e é a carga elementar, h é a constante de Planck e C_q é a capacitância quântica, que informa sobre a densidade de estados (DOS em inglês) como $C_q \propto e^2$DOS. O conceito de ν é utilizado para elucidar a constante de velocidade de transferência de elétrons k de reações eletroquímicas, como $k = {}^{G}/_{C_\mu}$, onde G é o quantum de condutância e C_μ é a capacitância eletroquímica. Esta tese apresenta um estudo fundamental, dentro do contexto da teoria do *quantum rate*, dos processos de TE e transporte de elétrons em dois tipos de junções moleculares (MJ em inglês): monocamadas electroativas auto-montadas (SAM em inglês) sobre eletrodos e monocamadas aromáticas ligadas entre eletrodos de carbono. Métodos dependentes do tempo como a espectroscopia de impedância (IS em inglês) e a espectroscopia capacitiva derivada de impedância (ECS em inglês), especificamente como um punto quântico resistivo capacitivo (RC). As SAMs redox foram formadas utilizando peptídeos e tióis marcados com ferroceno. Essas SAMs apresentam uma C_q, que foi obtida por ECS, permitindo a determinação de k como $k = 2({}^{G_0}/_{C_q})$, onde a constante $G_0 \sim 77{,}5$ μS é a condutância quântica. O inverso de G_0 define a resistência quântica como $R_q = {}^{1}/_{G_0} \sim 12{,}9$ kΩ, estabelecendo um limite quântico para a TE. Isso demonstra que a eletrodinâmica é governada por R_q e C_q. Além disso, foi determinado que R_q compreende dois componentes resistivos conectados em série: a resistência de relaxação (R_{qt}) e a resistência combinada da solução e do contato (R_s), resultando em $R_q \sim 13$ kΩ. Consequentemente, a interpretação de R_q levou a uma reavaliação do significado atribuído à resistência de transferência de carga R_{ct}, revelando que R_q é equivalente a R_{ct}. Além disso, foi demonstrado que, independentemente do esqueleto molecular, os estados C_q da interface redox mediam a TE entre espécies eletroativas livres e o eletrodo, dentro de uma eficiência máxima de transmissão de elétrons. Especificamente, foi comprovado que um aumento no número de canais quânticos N, e consequentemente de C_q em cerca de 40%, foi alcançado por meio de um alinhamento adequado dos níveis de energia entre os estados dos espécies redox livres e a DOS do SAM. Essa configuração excepcional permitiu a amplificação do sinal C_q para a detecção de um alvo biológico. Como prova de conceito, esse mecanismo de amplificação foi aplicado para a detecção do biomarcador da proteína não estrutural 1 (NS1 em inglês) do vírus da dengue, resultando em um aumento observado na sensibilidade dos biossensores capacitivos redox em pelo menos 1.000 vezes. No entanto, foi evidenciado que a acidez da interface capacitiva quântica afeta a mediação da transferência de elétrons como resultado da repulsão eletrostática entre a superfície carregada negativamente e as espécies redox carregadas. Além disso, a determinação das propriedades G e C_μ por meio de medições SI das MJ aromáticas demonstrou que G e k estão correlacionados por meio de C_μ, o que implica que os conceitos físicos associados estudados separadamente pelos eletroquímico e pelos físicos estão intrinsecamente relacionados. Os resultados obtidos nesta tese demostram que o modelo do *quantum rate* é uma teoria adequada que permite abordar fenômenos envolvidos com a transmissão de elétrons como a transferência eletrônica, condutância quântica e capacitância em diferentes MJs.

Resumo extendido

O estudo fundamental dos processo da TE foi construído ao longo de quase um século, utilizando abordagens clássicas e quânticas. A compreensão desse fenômeno é pertinente não apenas para a compreensão de sistemas biológicos, como a respiração e a fotossíntese, mas também para o desenvolvimento de componentes eletroquímicos, como baterias de íons de lítio e supercapacitores, elementos-chave de dispositivos eletrônicos fabricados pelo homem. Para entender a TE, interpretações macroscópicas têm oferecido teorias e modelos que, apesar de estarem estabelecidos em bases clássicas, utilizam concepções físicas quânticas e são assim referidos como abordagens semiclássicas. Sem dúvida, abordagens que envolvem elementos quânticos surgiram no início do século XX, como o uso da equação de Schrödinger e da notação de Dirac, ambos sendo ingredientes-chave para uma melhor compreensão e contextualização do processo de TE dentro de uma base mecânico quântica. No entanto, a discussão continua até os dias de hoje graças aos avanços tecnológicos que permitem à comunidade científica provar a teoria com experimentos mais precisos.

A interpretação mecânico quântica de sistemas moleculares compreende a análise tanto da dinâmica eletrônica quanto da dinâmica nuclear. Em particular, uma análise mecânico quântica do processo de TE representa um desafio monumental devido ao problema de muitos corpos envolvido em reações eletroquímicas da vida real. O significado disso é que, se a dinâmica eletrônica e nuclear de cada átomo envolvido no processo de TE for considerada, uma análise mecânico quântica se torna inviável. É sob essa suposição que aproximações são necessárias, como aquelas que permitem reduzir o sistema a elementos que representam a dinâmica chave. Por exemplo, o processo de TE pode ser formulado como uma mera transição entre dois estados quânticos únicos, referidos como estados estacionários doador D e aceptor A (ou seja, dois estados únicos) definidos ou caracterizados por um hamiltoniano que permite representar a dinâmica de maneira simplificada, com uma separação das contribuições eletrônicas e nucleares. De fato, dependendo se a análise é conduzida em termos de dinâmica eletrônica, nuclear ou ambos, o tratamento será clássico, semiclássico ou quântico-mecânico. Independentemente do tratamento usado para simular a dinâmica da TE, a conservação de energia é um requisito. Ao resolver a equação de Schrödinger, a energia associada à função de onda fornece uma imagem geral da conservação de energia, que foi concebida por Paul Dirac em 1927, que imaginou tal conservação dentro do processo de TE afirmando que "um elétron se localizará em uma espécie A somente se tiver a mesma energia que tinha na espécie D". Em outras palavras, um alinhamento do nível de energia relacionado das funções de onda (ou seja, orbital eletrônico) conduz a um forte acoplamento eletrônico entre as espécies A e D.

Não é coincidência que, em discussões clássicas, a superfície de energia potencial (SEP) seja uma ferramenta comumente usada para modelar o estado de energia das estruturas D e A, devido à abordagem da SEP poder lidar com transições eletrônicas entre estados de energia potencial E como uma função da coordenada nuclear da reação, a qual é uma variável extensiva com um único grau de liberdade que depende da posição, orientação ou momento de dipolo das estruturas D e A. Juntamente com a dinâmica nuclear, a termodinâmica é considerada dentro dessas abordagens clássicas, observando que a energia potencial é uma função termodinâmica dentro da energia livre de Gibbs G, a qual leva em conta as interações que contribuem para os estados

energéticos D e A, como flutuações de energia potencial térmica e eletrostática dentro de forças coulombianas, por exemplo. Finalmente, dentro da descrição qualitativa da reação de TE, teorias macroscópicas abordaram a TE, tendo como ponto de partida a teoria do estado de transição (TST em inglês). Consequentemente, as primeiras teorias de TE focaram na formação de um complexo ativado que controla a TE e a energia de ativação associada $\Delta G^{\ddagger}$ das reações eletroquímicas.

A teoria semi-clássica da TE amplamente aceita teve início com a teoria clássica desenvolvida por Rudolph A. Marcus nos anos 50, que ganhou o Prêmio Nobel de Química em 1992 por sua contribuição para a teoria de reações de TE em ambientes químicos homogêneos, ou seja, para TE entre espécies D/A em solução. Ao longo dos anos, outros cientistas contribuíram substancialmente no desenvolvimento da teoria de TE como por exemplo Noel Hush, Revaz Dogonadze, Heinz Gerischer and Christopher Chidsey. Inicialmente, Marcus e Hush trataram as reações de TE como uma transição adiabática, na qual há um acoplamento eletrônico forte entre os estados D e A. Nessa TE adiabática, o elétron no estado D será transferido para o estado A com a maior probabilidade, o qual é representado pelo coeficiente de transmissão κ que para este caso equivale à unidade. Como esses modelos clássicos abordaram a cinética da TE com base na TST, a constante de taxa de TE k adota o formato simples de Arrhenius como $k = \kappa \exp\left(^{-\Delta G^{\ddagger}}/_{k_B T}\right)$. Em particular, Marcus propôs que a $\Delta G^{\ddagger}$ associada a k está em função da energia de reorganização λ, que é a energia necessária para levar a configuração nuclear de D (ou seja, um íon cercado por dipolos do solvente) à de A.

Esse modelo da TE homogênea foi estendido para reações heterogêneas, ou seja, uma reação de TE entre espécies difusivas eletroativas (ou redox) e o eletrodo. Nesse caso, a interação eletrônica entre um eletrodo e as espécies difusivas requer que a cinética leve em consideração não apenas a distância entre D/A e o eletrodo, mas também a natureza das espécies D/A, devido à distribuição diferente de estados associados aos estados discretos (espécies) e contínuos (eletrodo). Destaca-se que a cinética associada à TE é controlada por um mecanismo de difusão. Geralmente, o uso de estruturas de monocamada molecularmente ordenadas surgiu como uma forma de evitar que a difusão controle a cinética da reação de TE, o que altera fundamentalmente a maneira como o modelo é usado para descrever esse evento de TE sem difusão. Assim, as SAMs redox têm sido usadas para fixar espécies redox na superfície do eletrodo, evitando os efeitos do transporte de massa.

Nessa configuração heterogênea, a reação de TE segue um processo não-adiabático ($\kappa << 1$), devido à interação eletrônica ser mais fraca já que as espécies D/A são separadas pela ponte molecular na SAM. Assim, a teoria de TE evoluiu para considerar essas complexidades, a fim de abordar os cenários de fronteira corretos. Em tais configurações, as interpretações da mecânica quântica foram feitas para abordar o acoplamento eletrônico fraco, como o uso da matriz hamiltoniana $|H_{DA}|$ para modelar o acoplamento eletrônico, que depende da distância. Além disso, análises estatísticas foram introduzidas para considerar os efeitos das flutuações térmicas na ocupação dos estados usando a função de Fermi-Dirac. Portanto, a reação de TE ocorrendo entre espécies redox imobilizadas e o eletrodo foi definida como um alinhamento de níveis de energia, em que deve haver níveis de energia disponíveis para receber um elétron (ou buraco) no filme molecular composta por estados redox ligados ao eletrodo e que a ocupação desses estados por elétrons segue uma distribuição de Fermi-Dirac. Neste ponto, essa teoria é referida como a teoria de Marcus-Hush-Chidsey.

Apesar dessa teoria ter surgido como resultado de várias contribuições distintas que a enriqueceram e permitiram avançar com a discussão, o uso da teoria com o objetivo de interpretar resultados experimentais é limitado, a cinética heterogênea sem difusão ainda não é totalmente compreendida, especialmente no que se refere ao parâmetro *ad-hoc* da λ no contexto da presença do DOS, representam um desafio para a teoria de transferência de TE. Alem disso, existem componentes quânticos que têm sido ignorados até agora, assim como a necessidade de unir a física da eletrônica em escala nanométrica e a eletroquímica.

À medida que a eletrônica evoluiu para a escala nanométrica, o estudo do transporte de elétrons por meio de moléculas é relevante, levantando uma pergunta óbvia: Qual é a diferença entre o transporte de elétrons, conforme entendido pelos físicos, e a transferência de elétrons, conforme entendido pelos químicos? Existe uma relação entre a condutância molecular e a transferência eletrônica? Uma diferença é observada na configuração experimental que está relacionada aos contatos que conformam a estrutura. Ao contrário da configuração de contato molecular único estudada em experimentos eletroquímicos, o contato de eletrodo típico usado na eletrônica molecular consiste em dois contatos, sendo as moléculas entre esses dois as que atuam como uma ponte molecular, comumente referida como junção molecular seca (MJ em inglês). A corrente elétrica flui através das moléculas ao aplicar uma diferença de potencial, ou seja, uma tensão de polarização contínua (DC bias voltage).

Em experimentos de condutância molecular que envolvem a investigação do mecanismo de transporte de elétrons através do esqueleto de moléculas orgânicas, estabelecem que a estrutura atômica das moléculas constitui a região de espalhamento onde os elétrons provenientes de um dos eletrodo atravessam a ponte molecular, com ou sem mediação da estrutura eletrônica molecular, até o outro eletrodo. A teoria mais comumente usada para interpretar a condutância de elétrons é a teoria da condutância de Landauer, que define o quantum de condutância G como $G = G_0 \sum_{n=1}^{N} T_n(\mu)$, onde $\sum_{n=1}^{N} T_n(\mu)$ leva em conta as probabilidades de transmissão $T_n(\mu)$ através de um número n de canais quânticos individuais (até um total de N) em um determinado nível de potencial químico μ, onde G_0 representa a constante universalmente conhecida para a condutância quântica, aproximadamente 77,5 μS.

A maioria dos experimentos levam à interpretação de que $\sum_{n=1}^{N} T_n(\mu)$ segue um mecanismo de tunelamento, cuja estatísticas de espalhamento pode ser considerada como proporcional a $\exp(-\beta L)$, onde β é um parâmetro relacionado à altura da barreira de potencial para os elétrons tunelarem e L é o comprimento da ponte molecular. É importante destacar as semelhanças entre o ET k e o transporte G em relação à dependência com o L; ambos os fenômenos dependem das características de transmissão de elétrons das moléculas de maneira semelhante, como observado por Abraham Nitzan, quem propôs uma relação linear entre G e k com base nessa premissa.

No entanto, devido ao fato de que as configurações experimentais da eletrônica molecular e da eletroquímica são fisicamente diferentes, as tentativas experimentais de confirmar a correlação linear de Nitzan têm sido mal sucedidas. Não apenas o ambiente do solvente foi uma fonte de diferenças entre a condutância molecular e as configurações experimentais eletroquímicas, mas também o ambiente molecular, onde medições de G, foi utilizado um contato de dois eletrodos, enquanto nas medições de k, foi utilizado um contato de um único eletrodo. Nesse contexto, técnicas experimentais que permitam seu acesso nas mesmas configurações experimentais são

necessárias não apenas para compreender a relação entre esses conceitos, mas também para compreender o papel desempenhado pelo $\kappa \propto \exp(-\beta L)$ (para mecanismos de tunelamento) em diferentes configurações e situações. Para isso, a interpretação dos dados experimentais deve ser apoiada por teorias capazes de correlacionar esses conceitos físicos de maneira consistente.

A teoria do *quantum rate* propõe uma velocidade quântica fundamental de primerios principios $\nu = {}^{e^2}/_{hC_q}$, que informa sobre o DOS como $C_q \propto e^2$DOS. Esse conceito de velocidade quântica é utilizado para elucidar a constante de velocidade de transferência de elétrons k de reações eletroquímicas, como $k = {}^{G}/_{C_\mu}$, onde C_μ é a capacitância eletroquímica. ${}^{1}/_{C_\mu}$ é definido como a combinação em série de duas contribuições capacitivas:${}^{1}/_{C_\mu} = {}^{1}/_{C_e} + {}^{1}/_{C_q}$, onde C_e corresponde à contribuição eletrostática e C_q corresponde à contribuição quântica. C_e está relacionada à separação espacial de carga, que é atribuída à carga não-Faradaica e considera as propriedades da estrutura do eletrólito, incluindo a contribuição do solvente e dos contra-íons. Por outro lado, C_q está relacionado à carga Faradaica devido à dinâmica de transferência eletrônica associada ao carregamento dos estados quânticos na reação de oxido-redução.

A relação $k = {}^{G}/_{C_\mu}$ estabelece a correlação entre k e G por meio de C_μ, implicando que os conceitos físicos associados estudados separadamente pelos eletroquímico e pelos físicos estão intrinsecamente relacionados. Sempre que se aplicam as regras de degenerescência do elêtron ($g_s = 2$) e da corrente eletroquímica ($g_r = 2$), a constante de velocidade para reaçoes eletroquímicas se simplifica a $k = g_s g_r {}^{e^2}/_{hC_q} = 4({}^{e^2}/_{hC_q})$, com a consequência direta de que C_q é a única variável experimental e todas as propriedades da interface podem ser determinadas apenas medindo C_q. A teoria *quantum rate* estabelece duas principais metodologias que nos permitem medir C_q da interface, nomeadamente, voltametria cíclica (CV em inglês) e espectroscopia capacitiva derivada de impedância (ECS em inglês).

Esta tese apresenta um estudo fundamental, dentro do contexto da teoria do *quantum rate*, dos processos de transferência e transporte de elétrons em dois tipos de MJ: monocamadas electroativas auto-montadas (SAM em inglês) sobre eletrodos e monocamadas aromáticas ligadas a dois contatos de eletrodos de carbono ("dry" MJ). Métodos dependentes do tempo, como a espectroscopia de impedância (IS em inglês), especificamente a ECS, foram empregados nesse estudo. Os dados de impedância foram analisados por meio do ajuste de circuito equivalente, já que a eletrodinâmica relativística quântica associada às moléculas que compõem as MJs pode ser modelada como um punto quântico resistivo capacitivo (RC).

As SAMs redox foram formadas utilizando peptídeos e tióis marcados com ferroceno. Essas interfaces eletroativas apresentam uma C_q, que foi determinada por ECS, permitindo a determinação de k como $k = 4({}^{e^2}/_{hC_q}) = 2({}^{G_0}/_{C_q})$. O inverso de G_0 define a resistência quântica como $R_q = {}^{1}/_{G_0} \sim 12{,}9\ \text{k}\Omega$, estabelecendo um limite quântico para a TE. Isso demonstra que a eletrodinâmica é governada pelos elementos R_q e C_q. Além disso, foi determinado que R_q compreende dois componentes resistivos conectados em série: a resistência de relaxação (R_{qt}) e a resistência combinada da solução e do contato (R_s), resultando em $R_q \sim 13\ \text{k}\Omega$. Essas resistências não podem ser separadas. Consequentemente, a interpretação de R_q dentro do modelo do *quantum rate* levou a uma reavaliação do significado atribuído à resistência de transferência de carga R_{ct}, revelando que R_q é equivalente a R_{ct}.

Além disso, foi demonstrado que, independentemente do esqueleto molecular,

os estados C_q da interface redox mediam a TE entre espécies eletroativas livres e o eletrodo, dentro de uma eficiência máxima de transmissão de elétrons. Especificamente, foi comprovado que um aumento no número de canais quânticos N e, consequentemente, de C_q em cerca de 40%, foi alcançado por meio de um alinhamento adequado dos níveis de energia entre os estados dos espécies redox livres e os estados C_q da monocamada. Essa configuração excepcional permitiu a amplificação do sinal capacitivo para a detecção de um alvo biológico. Como prova de conceito, esse mecanismo de amplificação foi aplicado para a detecção do biomarcador da proteína não estrutural 1 (NS1 em inglês) do vírus da dengue, resultando em um aumento observado na sensibilidade dos biossensores capacitivos redox em pelo menos 1.000 vezes. No entanto, foi evidenciado que a acidez da interface capacitiva quântica afeta a mediação da transferência de elétrons como resultado da repulsão eletrostática entre a superfície carregada negativamente e as espécies carregadas redox.

A determinação das propriedades G e C_μ por meio de medições SI das MJ aromáticas com diferentes espessuras em diferentes potenciais de polarização e temperaturas demonstrou que G e k estão correlacionados por meio de C_μ, como proposto pela teoria do *quantum rate*, onde as mudanças de conductância em funcão da polarização e temperatura são acompanhadas pelas mudanças de k, contrário a C_μ que se manteve invariante. Portanto, a teoria do *quantum rate* é validada por meio da análise da TE, condutância quântica e capacitância em diferentes filmes moleculares e MJs eletroativos, demonstrando assim sua abrangência para estudar differentes sistemas em nanoescala.

List of Abbreviations

A	**A**cceptor state (or specie)
AA	**A**mino **A**cid
AB	Molecular junction comprised by azobenzene molecular units
AC	**A**lternate **C**urrent
ACN	Acetonitrile
Ala	Alanine
C11-Fc	Monolayer obtained using 11-(Ferrocenyl)undecanethiol
CMOS	**C**omplementary **M**etal-**O**xide **S**emiconductor
CV	**C**yclic **V**oltammetry
Cys	Cysteine
D	**D**onor state (or specie)
DC	**D**irect **C**urrent
DIC	N,N′-Diisopropylcarbodiimide
DIPEA	N,N-Diisopropiletilamina
DMAP	4-Dimethylaminopyridine
DMF	Dimethylformamide
DOS	**D**ensity-**o**f-**S**tate
DP	**D**ifferencial **P**ulse
DPV	**D**ifferencial **P**ulse **V**oltammetry
eC	Electron-beam deposited carbon films
ECS	**E**lectrochemical Impedance-derived **C**apacitive **S**pectroscopy
EDC	1-Ethyl-3-(3-dimethylaminopropyl) carbodiimide
EDDT	2,2′-(Ethylenedioxy)diethanethil
EIS	**E**lectrochemical **I**mpedance **S**pectroscopy
ET	**E**lectron **T**transfer
EtOH	Ethyl alcohol
$\mathbf{f}_a$	Faradaic response
Fc	Ferrocene
$\mathbf{Fc}^+$	Oxidized form of ferreocene
Fc–COOH	Ferrocenecarboxylic acid
[Fc–COOH]	Fc–COOH concentration
$\mathbf{Fc}^+$**–COOH**	Oxidized protonated Ferrocenecarboxylic acid
Fc–COOH	Reduced protonated Ferrocenecarboxylic acid
$\mathbf{Fc}^+$**–COO**$^-$	Oxidized deprotonated Ferrocenecarboxylic acid
Fc–COO$^-$	Reduced deprotonated Ferrocenecarboxylic acid
FCWD	**F**ranck–**C**ondon–**w**eighted **d**ensity-of-states
FL	Molecular junction comprised by fluorene molecular units
Fmoc	9-fluo-renylmethyloxycarbonyl
FRA	**F**requency **R**esponse **A**nalysis
Glu	Glutamic acid

H^+	Proton or hydrogen ion
HBTU	N,N,N′,N′-Tetramethyl-O-(1H-benzotriazol-1-yl) uroniumhexafluorophosphate
HOBt	Hydroxybenzotriazole
HPLC	**H**igh **P**erformance **L**iquid **C**hromatography
IS	**I**mpedance **S**pectroscopy
LOD	**L**imit **o**f **D**etection
LOQ	**L**imit **o**f **Q**uantification
MJ	**M**olecular **J**unction
MW	**M**olecular **W**eight
NAB	Molecular junction comprised by nitroazobenzene molecular units
nf_a	Non-Faradaic response
NHS	N- hydroxysuccinimide
NS1	**N**onstructural **P**rotein **1**
[NS1]	NS1 concentration
PAHO	**P**an **A**merican **H**ealth **O**rganization
PB	**P**hosphate **b**uffer
PCET	**P**roton-**C**oupled **E**ctron **T**ransfer
Pep–Fc	Monolayer obtained using Fc-Glu-Ala-Ala-Cys-NH_2 peptide
Pep–rSAM	Monolayer obtained using Fc-Glu-Ala-Ala-Cys-NH_2 peptide
Pep–SAM	Monolayer obtained using Glu-Ala-Ala-Cys-NH_2 peptide
PES	**P**otential **E**nergy **S**urface
PIP	4-Methylpiperidine
PoC	**P**oint **o**f **C**are
PyBOP	Benzotriazole-1-yl-oxy-tris-pyrrolidino-phosphonium hexafluorophosphate
QPC	**Q**uantum **P**oint **C**ontact
r^2	Coefficient of regression
RC	**R**esistive **C**apacitive circuit
SAM	**S**elf-**A**ssembled **M**onolayer
SD	**S**tandard **D**eviation
SS–Pep–Fc	Monolayer obtained using Fc-Glu-Ala-Ala-Cys-Cys-NH_2 peptide
$TBAClO_4$	Tetrabutylammonium perchlorate
TFA	Trifluoroacetic acid
TIS	Triisopropylsilane
TST	**T**ransition **S**tate **T**heory

List of Symbols

a	arbitrary fitting parameter	
A	pre-exponential factor	
A_e	electroactive area	cm^{-2}
A_g	geometric area	cm^{2}
A_r	reduction peak area	cm^{2}
b	arbitrary fitting parameter	
c_*	Fermi velocity	$\mathrm{m\,s}^{-1}$
C	capacitance	$\mathrm{F\,cm}^{-2}$
$C^*(\omega)$	complex capacitive function	
C'	imaginary capacitive component	$\mathrm{F\,cm}^{-2}$
C''	real capacitive component	$\mathrm{F\,cm}^{-2}$
C_{ads}	adsorption capacitance	$\mathrm{F\,cm}^{-2}$
C_b	film bulk capacitance	$\mathrm{F\,cm}^{-2}$
C_{dl}	double layer capacitance	$\mathrm{F\,cm}^{-2}$
C_e	electrostatic capacitance	$\mathrm{F\,cm}^{-2}$
C_m	monolayer capacitance	$\mathrm{F\,cm}^{-2}$
C_q	quantum capacitance	$\mathrm{F\,cm}^{-2}$
$C_{q,a}$	anodic capacitive value	$\mathrm{F\,cm}^{-2}$
$C_{q,c}$	cathodic capacitive value	$\mathrm{F\,cm}^{-2}$
C_t	non-Faradaic capacitance	$\mathrm{F\,cm}^{-2}$
C_μ	electrochemical capacitance	$\mathrm{F\,cm}^{-2}$
dn	number of electronic particles	
$dn/d\mu$	density-of-state	
$(dn/d\mu)_l$	density-of-state of left "plates"	
$(dn/d\mu)_r$	density-of-state of right "plates"	
e	elementary charge	C
E	energy	eV
E^0	energy at equilibrium	eV

E_a	activation energy	eV
E_F	Fermi level	eV
E_F/e	formal potential	V
E_F^e/e	formal potential of Fc–COOH	V
E_F^p/e	formal potential of Pep–Fc	V
E_F^t/e	formal potential of C11–Fc	V
E_{ref}	reference energy level	eV
E_i	internal energy	eV
f	linear frequency	Hz (s^{-1})
f	Fermi–Dirac distribution function	
F	Faraday constant	C mol^{-1}
f_r	relaxation (or resonance) frequency	Hz (s^{-1})
f_c	characteristic frequency	Hz (s^{-1})
G	Gibbs free energy	J mol^{-1}
G	molecular conductance	mS
G_0	quantum conductance	mS
G_A^0	Gibbs energy of acceptor state at equilibrium	J mol^{-1}
G_D^0	Gibbs energy of donor state at equilibrium	J mol^{-1}
g_r	redox degeneracy	
g_s	electron spin degeneracy	
h	Planck constant	eV Hz^{-1}
$\hbar$	reduced Planck constant	eV s
H_{DA}	coupling matrix element or electron transfer integral	
H_{el}	electronic Hamiltonian	
i	electric current	A
i_0	exchange current	A
i_{ox}	oxidation peak current	A
i_{ox}/i_{red}	redox current peak ratio	
i_{red}	reduction peak current	A
j	density current	A cm^{-2}
j	complex number	
k	electron transfer constant rate	s^{-1}
k	wave-vector	m^{-1}
k_{app}	apparent constant rate	s^{-1}

k_B	Boltzmann constant	$\mathrm{eV\,K^{-1}}$
l	separation length	nm
L	molecular thickness or distance	nm
n	individual quantum channel	
$\mathbf{n}$	electron number involved in the redox reaction	
N	total number of quantum channels	
P_{DA}	transition probability	
pK_a	acid dissociation constant	
$\mathrm{pK}_a(Fc)$	acid dissociation constant of reduced ferrocene	
$\mathrm{pK}_a(Fc^+)$	acid dissociation constant of oxidized ferrocene	
$\mathbf{q}$	nuclear coordinate	
q	charge	C
q^0	nuclear coordinate at equilibrium	
q_A^0	nuclear coordinate of acceptor state at equilibrium	
q_D^0	nuclear coordinate of donor state at equilibrium	
R	resistance	Ω
$\mathbf{R}$	ideal gas constant	$\mathrm{J\,mol^{-1}\,K^{-1}}$
R_c	contact resistance	Ω
R_{ct}	charge transfer resistance	Ω
R_K	Von Klitzing constant	Ω
R_q	quantum resistance	Ω
R_{qt}	internal monolayer resistance	Ω
R_s	series resistance	Ω
R_t	non-Faradaic relaxation resistance	Ω
R_{td}	diffusion Faradaic resistance	Ω
s	scan rate	$\mathrm{V\,s^{-1}}$
t	time	s
T	temperature	K or °C
$T_n(\mu)$	transmission probability	
V	electric potential	V
V_{out}	potential outside electrochemical window	V
V_{ox}	oxidation peak potential	V
V_p	potential peak	V
$V_{p,a}$	anodic potential peak	V

$V_{p,c}$	cathodic potential peak	V
V_{red}	reduction potential peak	V
W	Warburg element	
$\bar{x}$	mean value	
Z^*	complex impedance	
Z'	imaginary impedance component	Ω
Z''	real impedance component	Ω
α	transfer coefficient	
α_q	coefficient deviation of electronic relaxation	
α_t	coefficient deviation of ionic relaxation	
β	tunneling decay parameter	Å^{-1}
β_G	decay parameter obtained from conductance measurement	Å^{-1}
β_k	decay parameter obtained from electrochemical measurement	Å^{-1}
Γ	electronic coupling between electrode and molecular segment	
$\Delta G^{\ddagger}$	activation energy	J mol^{-1}
ΔV_p	peak-to-peak separation	V
ν	fundamental quantum rate	s^{-1}
ν_{el}	electron hopping frequency	s^{-1}
ν_n	nuclear vibration frequency	s^{-1}
κ	transmission coefficient	
λ	reorganization energy	eV
λ_0	reorganization energy of solvational term	eV
λ_i	reorganization energy of vibrational term	eV
μ	energy level (or internal energy)	eV
μ_D	energy level of donor state	eV
μ_A	energy level of acceptor state	eV
μ_L	energy level of left electrode	eV
μ_R	energy level of right electrode	eV
η	overpotential	V
$\sigma_{\bar{x}}$	standard error of the mean	
$\sum_{n=1}^{N}$	summation of quantum channels	
τ	electron transfer time-scale	s

$\bar{\tau}$	average time between collisions	s^{-1}
τ_t	time-scale of the ionic relaxation process	s
ϕ	phase angle	$^\circ$
$\phi(\mu)$	density-of-state in function of energy	
$\phi_A(\mu_D)$	acceptor density-of-state at donor energy level	
ψ_A	wave function of acceptor state	
ψ_D	wave function of donor state	
ω	angular frequency	$\mathrm{rad\,s}^{-1}$
ω_r	relaxation angular frequency	$\mathrm{rad\,s}^{-1}$
ω_c	characteristic angular frequency	$\mathrm{rad\,s}^{-1}$

Contents

Introduction

This thesis work deals with the fundamental study of electron transfer and transport phenomena in mesoscopic systems focusing on nanoelectronic and nanoscale electrochemical devices. In these systems, neither classical nor quantum mechanics exclusively prevail. This is because they contain an ensemble of molecules that are large enough to consider that the related physics is purely governed by quantum mechanics, yet not large enough to adhere entirely to the principles of classical mechanics. Examples of such systems are redox SAMs and molecular ensembles sandwiched between electrodes. The fundamental understanding of how the electron is transferred and transported in these molecular junctions is a major challenge that requires a self-consistent theory, which allows the interpretation of experimental data. This knowledge will enable the development of novel and advanced nanoscale devices.

One part of the presented thesis focuses on the fundamental study of the phenomenon related to the ET process in heterogeneous diffusionless settings, specifically in SAM. It also investigates its role in mediating ET between the electrode and electroactive species in solution. The mechanism associated with this mediation is evaluated as a potential means of signal amplification. Additionally, the study examines the electrodynamics that influence such mechanisms. The other part centers on the demonstration of the correlation between molecular conductance and the charge transfer rate in MJ. These studies are conducted within the quantum rate theory framework and experimentally performed by impedance spectroscopy and impedance-derived capacitive spectroscopy.

The semi-classical theory developed for the ET process proposes a quantum mechanical analysis using the non-relativistic Schrödinger equation, which describes the electrodynamics properties of the electrochemical reaction. This reaction involves the exchange of electrons between the electronic states of the donors `D` and acceptor `A` species, such as ions and molecules. The rate at which this ET occurs is determined by the electron transfer rate constant k, which can be measured by established electrochemical methods that utilize electrodes to investigate redox reactions. On the other hand, the molecular conductance G, which characterizes the flow of electric current through the molecules between the electrodes under a potential difference, was theoretically found to be correlated to k. This correlation implies a connection between electron transport, as understood by physicists, and electron transfer, as understood by chemists. Within this context, the quantum rate theory demonstrates that the electrodynamics of electron transfer reactions are governed by the relativistic Dirac equation rather than the non-relativistic Schrödinger equation. Additionally, it establishes a correlation between k and G through the electrochemical capacitance C_μ, which can be experimentally verified.

0.1 Objectives

The general objective of this study is to comprehensively investigate the quantum mechanical aspects of electron transfer, capacitance, conductance and resistance within the framework of quantum rate theory. This was achieved through equivalent quantum circuit analysis of the impedance data measured for mesoscopic interfaces, focusing on the following specific objectives:

- ☑ Establish the quantum mechanical interpretation of charge transfer resistance by employing equivalent quantum circuit analysis of electrochemical interfaces.
- ☑ Demonstrate that the resistance quantum (or conductance quantum) represents the ideal scenario for electron transmittance. Investigate cases where electron transmittance deviates from the ideal adiabatic condition and incorporate the transmission coefficient, as proposed in the semi-classical theory, which relates to the specific settings of the transmission matrix probability for the tunneling mechanism of electron transfer in redox-active self-assembled monolayer interfaces.
- ☑ Prove that the alignment of formal potential levels between quantum capacitive states within the interface and non-capacitive states in solution leads to diffusionless, kinetically controlled charge transfer between the electrode and free redox species that complies with a charge transfer resistance limit, such as $R_q \sim 12.9\ \mathrm{k}\Omega$. This phenomenon is a direct result of electron transfer being mediated by the quantum capacitive states present in the interface.
- ☑ Confirm that the alignment of energy levels between free redox species and quantum capacitive states allows the enhancement of the capacitive signal, providing experimental evidence for detecting the NS1 biomarker as a proof-of-concept in the development of biosensing interfaces.
- ☑ Investigate electrostatic effects that influence the stability of energy level alignment between free redox species and quantum capacitive states, which may impact the accessibility of quantum conductive channels for the electron transfer process.
- ☑ Provide evidence for the correlation between G and k in molecular electronics settings by utilizing the electrochemical capacitance $C\mu$, demonstrating that the electrochemical and molecular electronic concepts are fundamentally connected. Specifically, demonstrate the relationship as C_μ as $k = {}^{G}/_{C_\mu}$.

By addressing these specific objectives, this thesis aims to advance our understanding of quantum mechanical phenomena in charge transfer resistance, electron transmittance, energy level alignment, and their interplay in nanoscale molecular junctions. These accomplishments allow us to design devices, such as biosensors and electronic devices.

0.2 Outline of the thesis

Chapter 1 gives the theoretical background of electron transfer/transport theories. Firstly, the development of the semi-classical theory of the ET reaction is related, describing the main concepts and principles of the homogeneous ET reaction, which was extended to the heterogeneous diffusionless setting. Additionally, the corresponding description of the electron transport phenomenon is introduced, including the theoretical approach for its correlation with the ET rate constant, as well as the description of the experimental study of this relationship. Afterward, a brief review of the quantum rate theory is presented. Finally, the main techniques to measure k of heterogeneous diffusionless setting and the limitations to interpreting the obtained results with the theory are briefly described.

Chapters 2-5 comprise the study of the quantum rate dynamics of electroactive SAMs through the equivalent quantum circuit analysis of the impedance spectroscopy data, which is detailed in chapter 2. A comparison between the ET mediation by two distinct SAMs, accordingly to the quantum rate interpretation of chapter 2, is presented in chapter 3. The corresponding results of chapter 2 and 3 have been published in the *Jornal of Physical Chemistry C* (DOI: 10.1021/acs.jpcc.1c07801) and *Electrochimica Acta* (DOI: 10.1016/j.electacta.2022.141194), respectively. Chapter 4 evaluates the application of the energy level alignment as an amplification mechanism for sensing. Specifically, it compares the quantification of nonstructural protein 1 (NS1) dengue viruses biomarker using capacitive and non-capacitive states with the typical capacitive biosensing method. The corresponding results are currently under submission to the journal *Sensor and Actuators B: Chemical*. Chapter 5 describes the evaluation of energy level stability influenced by electrostatic factors.

The final chapter reports the impedance characterization of molecular junctions measured at different potential biases and temperatures. Its interpretation is contrasted with the quantum rate theory and demonstrates that the corresponding physical concepts of conductance and ET rate are correlated.

Chapter 1

State-of-the-art

The fundamental study of the electron transfer (ET) event has been built over almost one century, using classic and quantum approaches. The understanding of such phenomenon is pertinent not only for comprehending biological systems such as respiration (GIESE; KARAMASH; FROMM, 2023) and photosynthesis (THAPA *et al.*, 2022), but also for developing of electrochemical components such as lithium-ion batteries (WANG; YANG; ZHENG, 2022) and supercapacitors (NIU *et al.*, 2022), key elements of man-made electronic devices. In order to understand the ET, macroscopic interpretations has offered theories and models that in spite of being established over classical basis they use quantum physical conceptions and are so referred as semi-classical approaches. Undoubtedly, approaches that involve quantum elements emerged at the beginning of the twenty century such as the use of Schrödinger equation and Dirac notation, both being key ingredients for a better understanding and contextualization of the ET process within quantum mechanical basis. However, the discussion continues nowadays thanks to the technology advances that allow the scientific community to defeat the theory with more precise experiments.

The quantum mechanical interpretation of molecular systems comprehends the analysis of both the electronic and nuclear dynamics. In particular, a quantum mechanical analysis of the ET process represents a monumental challenge due to the many-body problem involved in real-life electrochemical reactions. The meaning of this is that if the electronic and nuclear dynamics of each atom involved in the ET process are considered, a quantum mechanical analysis becomes unfeasible. It is under this assumption that approximations are needed such as those that allow to reduce system to elements that represent the key dynamics (GRIFFITHS; SCHROETER, 2018). For instance, the ET process can be formulated as a mere transition between two single quantum states, refereed as donor `D` and acceptor `A` stationary states (i.e., two single states), defined or characterized by a Hamiltonian that allows to represent the dynamics in a simplified way in each a separation of the electronic and nuclear contributions. Indeed, depending on whether the analysis is conducted in terms on electronic or nuclear dynamic (or both) the treatment will be classical, semi-classical or quantum mechanical in nature (MARCUS, 1956; DOGONADZE; KUZNETSOV; CHERNENKO, 1965; BUENO, 2018). Regardless of the treatment used to simulate the ET dynamics, the energy conservation is a requirement. By solving the Schrödinger equation, the energy associated to the wave function gives a general picture of the conservation energy, which was envisioned by Paul Dirac in 1927, who pictured such conservation within the ET process stating that "*an electron will localize in an `A` specie only if has the same energy as it did in the `D` specie*". In other words, an alignment of the related energy level of the wave functions (i.e., electronic orbital) that conduct to a strong electronic coupling between `A` and `D` species, as will be further discussed.

It is not coincidence that in classic discussions, the potential energy surface (PES) is commonly used tool to model the energy state of D and A structures (briefly discussed in the section 1.1), owing to PES approach can deal with electronic transitions between potential energy E states as a function of nuclear coordinate of the reaction $\mathbf{q}$[1], see additional information on nuclear configuration dynamics in Fig. 1.1*a*. Along with the nuclear dynamics the thermodynamics is considered within these classical approaches by noting that potential energy is a thermodynamic function within the Gibbs free energy **G**, accounting for interactions that contribute to the energetic D and A states, such as thermal and electrostatic potential energy fluctuations within coulombic forces, for instance. Finally, within the qualitative description of the ET reaction, macroscopic theories addressed the ET taken as a starting point the transition state theory (TST). It is worthwhile to note that the TST, developed in 1930s, contemplates the Henry Eyring's formulation to treat rates of chemical reaction and encompasses not only kinetics-theories but also thermodynamic and statistical-mechanical treatments (LAIDLER; KING, 1983). Accordingly, the first ET theories were focused in the formation of an activated complex that controls the ET and the associated activation energy $\Delta G^{\ddagger}$ of the electrochemical reactions.

1.1 The beginning of the formulation of the ET theory based on the transition state theory

At first glance, the key contributions of the quantum analysis to the development of the ET theories was by considering the ET as following tunneling mechanism for the transport of electron from D to A which takes place, *a priori*, by an electronic orbital overlap between D and A species. This is considered qualitatively (energy conservation condition is fulfilled by considering the linear combination of wave functions of D and A) or quantitatively (by considering an integral overlap in the Hamiltonian matrix elements of D and A species). However, the history of the current widely accepted ET theory started with classic developments that considered elastic distortion and charge fluctuation models(FLETCHER, 2010). The classical ET theory was developed by Rudolph A. Marcus in 50's, who won the Nobel Prize in chemistry in 1992, for his contribution to the theory of ET reactions in homogeneous chemical settings.

Before the quantum mechanics has been considered in the ET theory, the classical models such as those proposed by Marcus' and Hush's treated the ET reactions as an adiabatic process[2](MARCUS, 1956; HUSH, 1958, 1961). Adiabatic transitions describes the resultant PES for a system defined by a strong electronic coupling between the D and A states described by the individual PES in Fig. 1.1*a* (VAN V. *et al.*, 2010). Strictly, the electronic coupling is related to the matrix element in the Hamiltonian describing the outcome transition in the ET. However, for keeping it simple, this matrix electronic coupling analysis will not be discussed here, though its physical interpretation of the energy level alignment is relevant for describing the electronic coupling. Fig. 1.1*b* shows two solid surfaces, one with the lowest potential energy,

[1] $\mathbf{q}$ which, for simplicity, is an extensive variable with a single degree of freedom that depends on the position, orientation or dipole moment of D and A structures. The nuclear coordinate consider contributions from vibrational and polarization models of reactants (FLETCHER, 2010).

[2] This process involves the interaction of adiabatic electronic states that quantitatively speaking are eigenstates of the Born-Oppenheimer electronic Hamiltonian (BALZANI *et al.*, 2001)

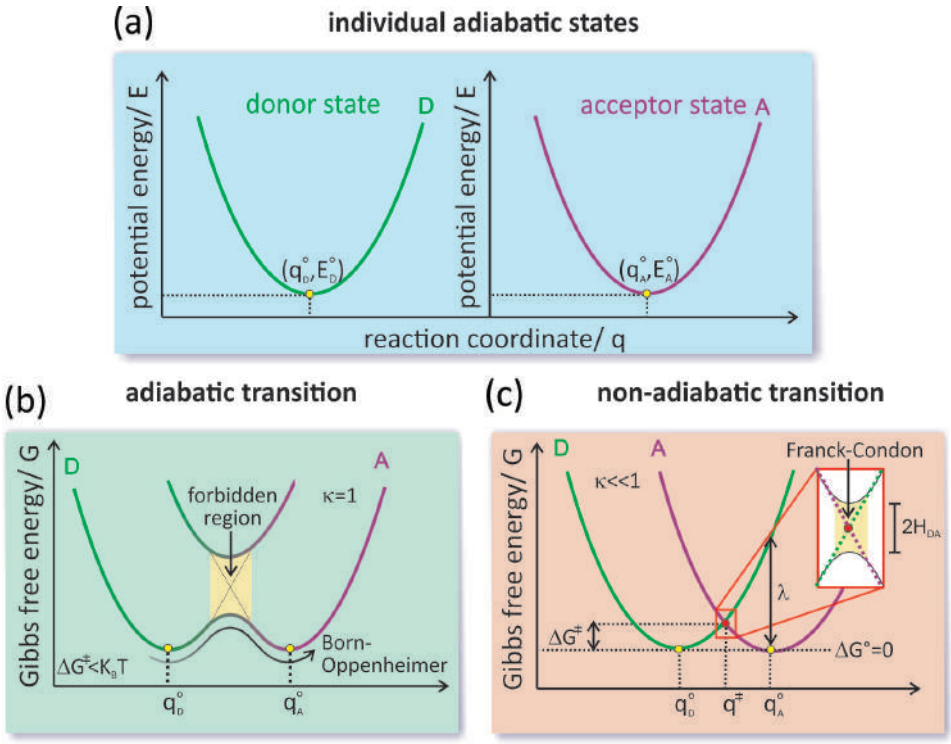

Figure 1.1: Potential energy surfaces in electron transfer process as a transition state event. (a) Adiabatic PESs for single D and A states. The minimum points indicate the equilibrium coordinates (q^0, E^0). (b) The strong electronic interaction between the D/A states results in a new adiabatic curve, the two-well surface, in which the electronic motion (not shown) adjust itself along the nuclear coordinate to success the transition thermally activated ($-\Delta G^{\ddagger} < K_B T$), with the highest probability, so $\kappa = 1$. The shade area between the upper and lower PESs is known as the forbidden region in the Landau-Zener model (GRIFFITHS; SCHROETER, 2018). (c) For a week coupling, the PESs remain almost unaltered, the transition will follow a non-adiabatic one, according to the Franck–Condon principle, from (q_D^0, G_D^0) to (q_A, G_D^0) (i.e., the system jumps between both parabolas in the interception point where $q_D^0 = q_A^0$). The electronic coupling magnitude H_{DA} is proportional to the gap between the states, and is related to energetic feature of the activated complex, as $H_{AD} = \lambda/4 - \Delta G^{\ddagger}$ when $G_D^0 = G_A^0$ ($\Delta G^0 = 0$). Note that when both parabolas does not share the same equilibrium energy $G_D^0 \neq G_A^0, \Delta G^0 \neq 0$ scenario is also possible.

Source: Author (2023).

characterized by the two wells, and the other with the highest potential energy; the gap between these potential energy curves is proportional to the electronic coupling. In this ET depiction, the electron in the D state will be transferred to the A state following the two-well PES with the highest probability. However, what is the rate of such an adiabatic transitions? As above-mentioned, the classical models addressed the ET kinetics based on the TST and adopted the Eyring's equation for the ET constant rate k, given by

$$k = A \exp\left(\frac{-\Delta G^{\ddagger}}{k_B T}\right) \tag{1.1}$$

where k_B is the Boltzmann constant and T is the temperature. The pre-exponential factor A, commonly associated to a frequency factor in the Arrhenius' kinetics, played a key role in the ET theory development, relating electronic (i.e., electronic transmission

coefficient κ[3] and electron hopping frequency ν_{el}.) and nuclear factors (i.e., nuclear vibration frequency ν_n) (BALZANI *et al.*, 2001), indicating whether the transition is adiabatic or non-adiabatic, as briefly discussed previously. The formulation of $\Delta G^{\ddagger}$ was carefully considered not only by the classical models based on TST (adiabatic), but also by the semi-classical approaches that considered perturbation methods (non-adiabatic) to formulate $\Delta G^{\ddagger}$.

In the ET adiabatic transitions, regardless the strong electronic interaction that leads to the highest ET probability $\kappa = 1$, which can be favored by short distance l ($\kappa \propto \exp(-\beta l)$, where β is the tunneling decay parameter), the determining step for the system to reach the intersection region is the nuclear vibration ($A \sim \nu_n$) sufficed by the thermal fluctuations ($-\Delta G^{\ddagger} < k_B T$) (BALZANI *et al.*, 2001). Therefore, the constant rate expression takes the simple Arrhenius format (see Eq. 1.2 and Eq. 1.3). Recalling that the transition state follows the lowest PES (see Fig. 1.1*b*), whose electronic state is constituted by the combination of both `D/A` states (i.e., strongly coupled states), in accordance to the Born-Oppenheimer approximation, conducting to the the electronic motion that suits to the changing nuclear configuration along the reaction coordinate.

Because in the non-adiabatic ET transition is the consequence of a weak electronic interaction between the `D/A` states, each single state remain almost intact and, therefore, there will be two PESs (see Fig. 1.1*c*), one related to another by an intersection point that represents the nuclear coordinates of the activated complex, which are also the nuclear coordinates at which the transition occurs, obeying two principles: the Franck–Condon, which states that the nuclear configuration is motionless while the electron is transferred ($q_D^{\ddagger} = q_A^{\ddagger}$); and the energy conservation ($G_D^{\ddagger} = G_A^{\ddagger}$) principle. However, the system passes this intersection point not only one time, but many times owing the gap be small (see Fig. 1.1*c*), as result of a weak coupling [4], that the transition probability is not unity ($\kappa << 1$). Eventually, the related constant rate not longer takes the form of Eq. 1.1, with the pre-exponential factor depending on the electronic coupling owing $A \sim \kappa$, which is contrary to an adiabatic process. Therefore, in non-adiabatic ET reactions the thermal fluctuations are not enough to pay the high energetic cost of the activation energy, they are usually considered as a photo induced process (BALZANI *et al.*, 2001).

In order to address this weak electronic interaction, the Dirac's first-order perturbation theory has been used by some authors (DOGONADZE; KUZNETSOV; CHERNENKO, 1965), building up an ET theory from a quantum mechanical insight. This perturbation method treats the electronic interaction (or coupling) by means of an additional Hamiltonian, namely the matrix element (as above-mentioned) that quantitatively relates the transition from the `D` to the `A` wave function (or state) with a perturbation[5] (NEWTON, 1991). The main implication of this approach in the ET constant, for an non-adiabatic process, is that the obtained rate constant is an exponential-like expression (see Eq. 1.6), similar to Eq. 1.1, whose pre-exponential factor takes a more complex form, in comparison with the adiabatic case, which is described in terms of the electronic Hamiltonian matrix element. And by last but not least, it brings up the discussion of ET for multiple acceptor states (i.e., probability density function treated as a Boltzmann distribution) that are represented by the exponential factor

[3] κ is also the averaged transition probability per passage of the system through the intersection region in Fig. 1.1*b* and *c*, and is exponentially dependent on the `D/A` distance (MARCUS, 1964).

[4] Mathematically described by the matrix element, briefly discussed in the section 1.3.

[5] As result of this treatment, the integral overlap is obtained as described in section 1.3.

(GERISCHER, 1990; DOGONADZE; KUZNETSOV; CHERNENKO, 1965), not only addressing homogeneous ET reaction but also envisioning the electrode reaction.

Definitely, the coupling strength is an important component beneath the fundamental construction of the ET theory. Based on the quantum mechanical treatment of the orbital overlap, it is expected that the overlap decays exponentially with the distance (FLETCHER, 2010). Bearing in mind this, the electronic interaction between species in solution shown by Fig. 1.2*a* (i.e., homogeneous reaction) and between an electrode and diffusive species shown by Fig. 1.2*b* (i.e., heterogeneous reaction), requires that the kinetics must consider not only by taking the distance between D and A distance that is hugely influenced by the molecular configuration of D and A, but also by the D and A nature owing to unlike distribution of states that govern the ET and electronic communication between these states. As the nature of D and A became more complex, from homogeneous to heterogeneous ET reaction, for instance, an immobilized molecule over an electrode can act as both D and A species, the ET model must to consider these complexities in order to address a correct boundary scenarios for the electrochemical reaction. In the following section, a brief review of how ET theories evolved will be made, summarizing the main aspects and pointing out not only the fundamental key terms of each approach, but also how they are connected.

1.2 More details about classical macroscopic ET theories, including the reorganization energy term

In electrochemical reactions, the electrolyte plays a key role in the kinetics. The understanding of solid/liquid interface structure is important for many heterogeneous applications (where the inner and the outer Helmholtz plane as well as the structure of the electric double-layer are of a key importance). Some phenomena such as the electrostatic interactions that occurs in the electrolyte phase are important. For instance, it can be mentioned the (a) ion-solvent dipole that is of fundamental importance for understanding the short range interaction that allows the solvation shell formation and (b) the ion-ion interaction that conducts to a long range interaction phenomenon that ensures the microscopic electroneutrality of the electrolyte (BARD; FAULKNER, 2000). These two examples demonstrates the complexity of the electrolyte environment that influences the ET rate. One of the key proposals of the ET theories is that the electrolyte environment must be dynamically accommodated during the ET reaction process, which requires an energy cost that has been formulated in terms of an additional energy term to that of the activation energy, which was addressed in classical and semi-classical ET theories such as those formulated in Marcus' and Hush's works.

Marcus ET theory was developed for homogeneous ET reaction (see Fig. 1.2*a*), by taking the D and A chemical species as spheres surrounded by dipoles of the solvent molecules. Therefore, in Marcus's model it was neglected the molecular electronic structure of D and A species. In particular, the non-equilibrium dielectric polarization was adopted for the calculation of the electrostatic free energy of the non-equilibrium state, wherein the dielectric polarization was treated as a vector that fluctuates accordingly to the ionic reactants' charge dynamics, which is a state comprised by an unusual polarization around the activated complex (MARCUS, 1956). Such electrostatic contribution to $\Delta G^{\ddagger}$ to the activated complex, that is $-\Delta G^{\ddagger} = {}^{(\lambda+\Delta G^0)^2}/_{4\lambda}$, is

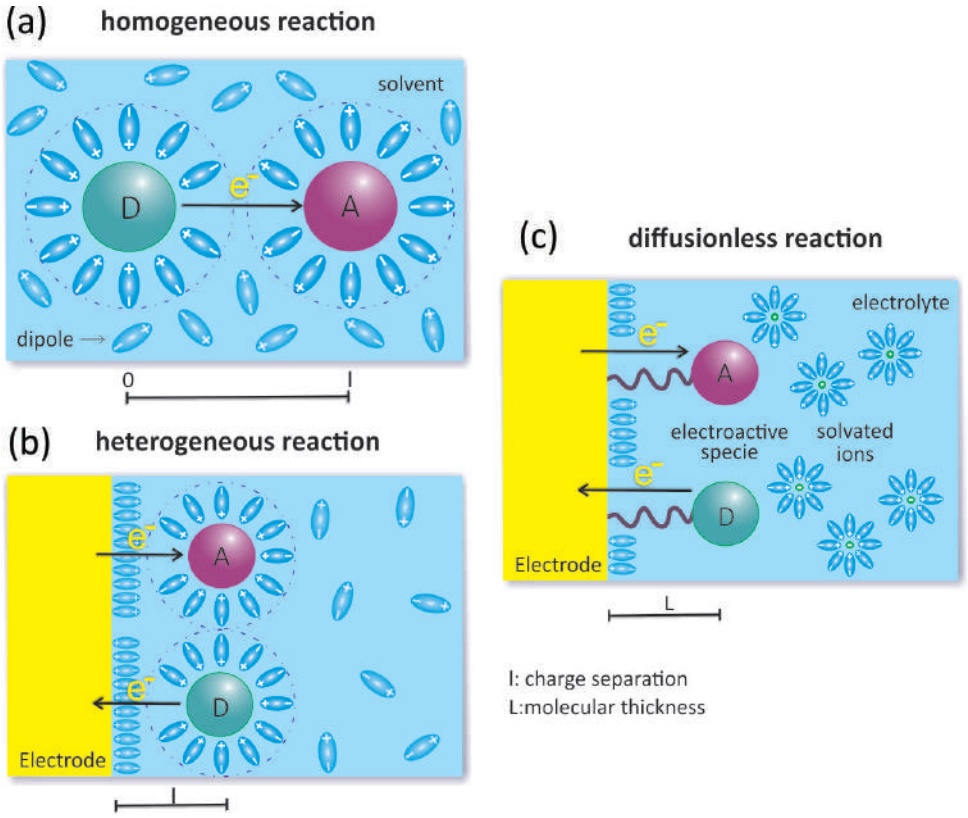

Figure 1.2: Schematic representation of diffusion controlled and diffusionless electrochemical reactions. (a) The Marcus model for ET between D and A chemical species taken as two spheres surrounded by dipoles of the solvent molecules, which are specifically oriented forming the activated complex, energetic process fulfilled by λ. Since the ET process happens in solution, the reaction is refereed as homogeneous, and depends on the mass transport. (b) The ET at the interface between an electrode and electroactive chemical species in solution is known as heterogeneous reaction, which same as (a) depends on the mass transport process. (c) A particular setting of (b) in which the electrochemical species, surrounded by the electrolytic environment, are anchored onto the electrode surface by a molecular bridge suppressing the mass transport effect, leading to a diffusionless reaction.

Source: Author (2023).

known as the reorganization energy λ[6], which is the energy required for bringing the D nuclear configuration (i.e., an ion surrounded by dipoles) to that of the A.

In Marcus theory, the pre-exponential factor was taken as an attempt frequency which, for instances, for bimolecular ET reaction is referred as the collision number. Marcus's consideration did not required the A possess a strong electronic interaction with D. On the contrary, the assumption of slight-orbital overlap between D and A was an explicit consideration in theory[7]. However, in subsequent papers Marcus proposed κ as unity (MARCUS; SUTIN, 1985), which is a limit value for adiabatic transition (BALZANI *et al.*, 2001; BARD; FAULKNER, 2000), conducting to a mixing

[6]The reorganization energy is composed by two components, the solvational λ_0 and vibrational λ_i terms, which considers the reorganization of the dipoles of the solvation shell around the A and the reorganization of D specie, respectively (MARCUS, 1993).

[7]This was formulated in accordance with the uncertainly principle in which the the lifetime of the activated complex would be enough for the success of the ET that may be achieved under a small-overlap (MARCUS, 1956) of the wave functions of D and A species.

consideration that in part is in agreement with the use of the transition state theory for the activation process of the ET. The obtained constant rate expression for homogeneous ET reaction was thus formulated as Eq. 1.2

$$k = \kappa \nu_{el} \exp\left(\frac{-(\lambda + \Delta G^0)^2}{4\lambda K_B T}\right) \tag{1.2}$$

which was extended to heterogeneous (electrode) reactions. Marcus ET model has also been used to formulate kinetic predictions associated more complex electrochemical reactions involving long-rage ET in biological systems (INIEWSKI, 2010). The key assumption of Marcus theory is the reorganization energy which is unique of his model. Other models are variants of the same proposition, whereas the reorganization is the key component that explain the whole of the solvent in the ET reactions.

The assumption of weak interaction for adiabatic ET is also presumed by Noel S. Hush for electrode reaction (see Fig. 1.2*b*) (HUSH, 1958) and later extended to homogeneous reaction (HUSH, 1961), wherein the orbital overlap was assumed to be small enough for certain limiting distances of D and A species, but large enough to allow the reaction to proceed with a $\kappa \sim 1$ (HUSH, 1958). The Hush ET theory was developed for outer-sphere reaction, specifically for coordination complex, in which ET is not considered in terms of PES, despite the assumption of a transition state, but by using electron probability density assumption. Accordingly, Hush treated the charge transfer in terms of a probability distribution and the derivation of $\Delta G^{\ddagger}$ was taken in terms of this parameter only. Not only electrostatic was considered but also thermodynamic analysis supported by classical approach such as the continuum solvating model and crystal field theory, which also considered the key role played by the solvent dielectric, likewise in Marcus model. Nonetheless, in Hush model the activation energy is defined as the energy required to bring together the D and A species, which must be suitable solvable and so, demanding an additional energy for the solvating shell formation, i.e., the associated to the energy required to change the dielectric polarization around D and A species, which ultimately is the energy required for stabilization of the transition state complex during the ET event.

Such as in the Marcus model, the formulation of $\Delta G^{\ddagger}$ by Hush did not concerned about the electronic structure of D and A species and the ET rate constant was assumed to take the typical reaction rate expression formulated by Marcus ET homogeneous settings as well as the same format is obtained for heterogeneous reaction, which is likely a limitation of both formulations that neglects the electric structure of D and A species. In summary, the ET rate constant in both Marcus and Hush models is assumed to be

$$k = \kappa \frac{k_B T}{h} \exp\left(\frac{-\Delta G^{\ddagger}}{k_B T}\right) \tag{1.3}$$

where κ equals the unity for ideal adiabatic process. Note the similarity between Eq. 1.2 and Eq. 1.3, equations coming from different formulations of ET rate constant, but is a result of the similar physical chemical premises taken by these models, such as dielectric continuum of the solvent structures as well as the adoption of macroscopic states that ignores the electronic structure of D and S states besides the weak orbital interaction. The strength of these models is that they highlighted the importance of the dielectric constant of the solvent and its influence on the activation energetic barrier. Therefore, between 50 to 60s Marcus and Hush set out a ET theoretical models that

further evolved, aiming to overcome the limitation related to classical components of these models. Therefore, quantum mechanical interpretations arises further, leading to the well-known semi-classical ET theoretical approach that will be discussed in the following section.

1.3 The quantum mechanical components of the semi-classical ET theory

ET theories as introduced previously can be interpreted from a quantum standpoint and this has been specially conducted in order to describe non-adiabatic ET transitions. This is quite straightforward if a quantum description is made by invoking changes of the wave functions of D and A during the ET that depends on the electronic coupling between D/A. This event can be described using a H_{DA} Hamiltonian, which is refereed in the quantum chemistry literature as the coupling matrix element or electron transfer integral. This electronic coupling is defined as $H_{DA} = \langle \psi_A | H_{el} | \psi_D \rangle$ (NEWTON, 1991), where H_{el} is the electronic Hamiltonian operating over the wave function of D (ψ_D) in order to obtain that of A, ψ_A. However, how is the matrix element evaluated and what is its nature? The answer to these questions will depend on the mathematical approach (NEWTON, 1991). For instance, in the Paul Dirac's first-order perturbation theory, the electronic coupling is thought as a perturbation, which must be minimal for the method to be valid. Accordingly, in order to calculate H_{DA}, wherein ψ_D and ψ_A are the frontier orbitals, the electronic coupling involves a weak orbital overlap, i.e., $\langle \psi_A | \psi_D \rangle$.

The wave mechanics treatment of the orbitals of D and A for modelling ET reactions has been a success within a constructive overlap of the wave functions having similar energy levels. The way in which the transition between two single wave functions is addressed in terms of probability P_{DA} of ET occurs between two specified energies (μ_D and μ_A), conducted fundamental discussions of ET towards a more general approach from which the rate constant was obtained using a probability function. Therefore, it was introduced the Dirac delta distribution function (NEWTON, 1991) in which statistics associated to electronic distribution of D and A were appropriately considered within the ET theory, which quite suitable to deal with both homogeneous and heterogeneous reactions. Note that this approach allows to give a more appropriate description to the electron as a indistinguishable particle in which the statistical distribution follows a different occupation compared to distinguishable particles such as ions.

For instance, using the above-mentioned approach, heterogeneous reactions (or electrode reactions) can be modelled considering the nature of D and A statistically. Owing to heterogeneous redox reactions are driven by a metallic electrode, the higher density-of-states of metal is quite important to be considered in the analysis, in such way that the electrode is modelled as a continuum and the redox species in the solution phase are modelled as discrete states, conducting to a Boltzmann distribution function of the energy states (DOGONADZE; KUZNETSOV; CHERNENKO, 1965; GERISCHER, 1990; FLETCHER, 2010). In other words, multiple A states were considered for heterogeneous reactions and were addressed separately by Revaz Dogonadze and collaborators (DOGONADZE; KUZNETSOV; CHERNENKO, 1965) and

by Heinz Gerischer (GERISCHER, 1990) in the 60´s. Particularly, Gerischer associated the ET as governed by probability function that accounts for both density-of-state $\phi(\mu)$ and the matrix element (see Eq. 1.4). In this way, for an reduction reaction occurring at certain energy levels $\mu_{\mathtt{D}}$, that is with average D state, the discrete A states $\phi_{\mathtt{A}}(\mu_{\mathtt{D}})$ participate in the ET event within a probability density for the ET as a function of time t that takes the form

$$P_{\mathtt{DA}}(t) \approx \frac{2\pi t}{h}|H_{\mathtt{DA}}|^2\phi_{\mathtt{A}}(\mu_{\mathtt{D}}) \tag{1.4}$$

where $\phi_{\mathtt{A}}(\mu_{\mathtt{D}})$ is the probability density of A states at $\mu_{\mathtt{D}}$. In other words, the probability of ET considers available density-of-states of A at $\mu_{\mathtt{D}}$, that is at the Fermi level of the electrode[8]. Note that the key energy level governing these heterogeneous reactions is that of the electrode, whereas the energy of the species are considered whenever the distribution function is provided, such as is the case of Eq. 1.5. Consequently, the ET rate constant can be obtained by differentiating Eq. 1.4, leading to the following expression, $k = {}^{2\pi}/_{\hbar}|H_{\mathtt{DA}}|^2\phi_{\mathtt{A}}(\mu_{\mathtt{D}})$(BALZANI *et al.*, 2001; SCHMICKLER, 1996), which is known as "the golden rule".

As mentioned previously, density-of-states of molecules in solution phase and of the metallic electrode follows different statistics. For the solution phase the random thermal motion of charged species and its surrounds conducts to a thermal energy distribution that follows Boltzmann occupancy in which the probability density can be expressed as a function of energy eV ($\mu = -edV$), conducting to the following expression

$$\phi_{\mathtt{A}}(eV) = \frac{1}{\sqrt{4\pi\lambda k_B T}}\exp\left(\frac{-(eV - eV_A)^2}{4\lambda k_B T}\right) \tag{1.5}$$

where the pre-exponential factor is the normalized factor of the distribution function and the exponential term is directly associated to the activation energy that is correlated to the electrostatic potential and the reorganization energy as proposed by Marcus, as described in section 1.2, see also Eq. 1.2. This probability density function is refereed in the literature as the Franck–Condon–weighted density-of-states (FCWD) (SCHMICKLER, 1996; BALZANI *et al.*, 2001). Considering FCWD probability density function, the semi-classical rate constant expression is promptly obtained, which can be easily extended to consider heterogeneous rate constant of electrochemical reactions by noting the contribution of the electronic structure of the electrode (GERISCHER, 1990), leading to Eq. 1.6 such as

$$k = \frac{2\pi}{\hbar}|H_{DA}|^2\frac{1}{\sqrt{4\pi\lambda k_B T}}\exp\left(\frac{-(\lambda + \Delta G^0 + E_F)^2}{4\lambda k_B T}\right) \tag{1.6}$$

where E_F is the Fermi level of the electrode. Eq. 1.6 is known as Marcus semi-classical ET transfer theory. The adaptation of this semi-classical theory to describe heterogeneous situations was conducted by Heinz Gerischer, who related the band positions of the electrodes to the electrode kinetics, noting that for ET reaction suitably proceeds, the electrons must be injected from the electrode (by tunnelling mechanism) via the E_F state of electrode to the A states (freely moving in the solvent environment)

[8]Note that for multiple states both D and A states, $\phi_{\mathtt{D}}(\mu_{\mathtt{D}})$ must be considered.

that are available close to the interface of the electrode (GERISCHER, 1990). The outcome of this approach for heterogeneous settings, in which the ET reaction is assumed to occur in a non-adiabatic regime such as $\kappa << 1$, is in agreement with the rate constant obtained by Dogonadze and collaborators (DOGONADZE; KUZNETSOV; CHERNENKO, 1965). In comparison with Eq. 1.2, the semi-classical rate constant model differs from the original Marcus's equation by some details that includes the pre-exponential term that accounts for the electronic coupling fact modelled via quantum mechanical approaches using the electronic coupling matrix H_{DA}, that as stated previously is able of accounting for the distance between `D` and `A`, as well as the nature of `D` and `A` (DOGONADZE; KUZNETSOV; CHERNENKO, 1965; FLETCHER, 2010).

It is important to note that for electrode reactions where `D` and `A` are free in the solution phase as shown by Fig. 1.2*b*, the ET kinetics is controlled by a diffusion mechanism. Generally, the use of organic molecularly ordered monolayer structures emerged as a way of avoiding this diffusion-controlled step during the evaluation of ET reaction, which fundamentally alters the way in which the model be used to described this diffusionless ET event. Nonetheless, in spite of this critical fundamental issue, redox organic monolayers have been used by employing self-assembly chemistry to attach redox species at the electrode surface as shown in Fig. 1.2*c*. The self-assembling chemical process is a suitable strategy to avoid the mass transport effects associated ET kinetics (CHIDSEY, 1991). Since a variety of molecules can be applied, this strategy opened an avenue of possibility for studying the electronic coupling and to evaluate the influence of the distance between the `D` or `A` from the electrode (SHAH *et al.*, 2015), constituting a key strategy for studying non-adiabatic long-range ET reactions as a particularly experimental method of scrutinised ET reactions. For instance, this approach has been useful for understanding ET in biological structures such as that operating in the photosynthesis and cellular respiration.

Eq. 1.6 was adapted by Christopher E. Chidsey (CHIDSEY, 1991), who extended this semi-classical theory for the diffusionless settings, which has been refereed as Marcus–Hush–Chidsey theory (HENSTRIDGE *et al.*, 2012; ZENG *et al.*, 2014; OLDHAM; MYLAND, 2011). Chidsey pointed out that in the ET reaction occurring between immobilized redox species and the electrode, there must be energy levels available to receive an electron (or hole) in the molecular film comprising redox states bonded to the electrode and that of the occupation of such states by electrons follows a Fermi–Dirac distribution. Therefore, the ET rate constant is proportional to the sum of each local single ET at an infinitesimal energy E, which reflects the electron occupation distribution, resulting in the following improper integral

$$k \propto \int_{-\infty}^{+\infty} \exp\left(-\frac{(E-\lambda \pm e\eta)^2}{4\lambda k_B T}\right) \frac{dE}{1+\exp\left(\frac{E}{k_B T}\right)} \tag{1.7}$$

where η is the over-potential, e is the elementary charge and the denominator in the second factor accounts for the Fermi–Dirac function. Due to the complexity for the evaluation of the improper integral, mathematical approximations were reported for certain values of λ and η, leading to more straightforward expressions (ZENG *et al.*, 2014; OLDHAM; MYLAND, 2011). Based on these expressions, quantitative predictions have been made, showing a suitable behavior at lower η, that is close to electrochemical equilibrium state, in accordance with experimental data (HENSTRIDGE *et al.*, 2012). The restriction to equilibrium condition and lower λ values suits to Eq. 1.7,

but demonstrates the limitation of Marcus–Hush–Chidsey theory as an adaptation of Marcus-Gerischer semi-classical theory for diffusionless heterogeneous settings.

The semi-classical theory endorses the interpretation of experimental results in the analyse of molecular systems that seeks for a fundamental interpretation of electron transfer and transport phenomena that requires electronic coupling analysis within an electrolyte environment and finite temperature. However, as shown briefly in the sections 1.1 – 1.3 this theory arises as an outcome of several distinct contributions that enriched it and allowed to bring the discussion further, as will be discussed in the following section, by taking quantum mechanical components that has been ignored so far, as will be discussed in section 1.5, specially in bringing together the physics of nanoscale electronics and electrochemistry. Furthermore, from the experimental point-of-view, the semi-classical ET theory is limited where the heterogeneous diffusionless kinetics is still not fully comprehended, specially in which refers to the reorganization energy *ad-hoc* parameter in the context of the presence of an electrode density-of-states, representing a challenge for the ET transfer theory, as will be discussed in the following sections.

1.4 Relationship between molecular conductance and electron transfer rate concepts

In the previous sections it was conducted a review and an overview about the theoretical fundamentals involving ET in homogeneous and heterogeneous settings. The concept of ET heterogeneous settings is of key particular importance because it is the basement for numerous technological applications of electrochemistry, ranging from sensors to solar cells, supercapacitors, batteries and so on. The heterogeneous settings of electrochemistry reactions involves the contact of the redox species with conductive electrode. Two typical examples is the contact of an electrode with redox species free in the electrolyte phase (in which there is a diffusion controlled kinetics of the reactions) or redox species chemically attached to the electrode (referred as modified electrode). The use of electroactive SAM is a special case where there is no diffusional limit for the ET.

As the electronics has evolved to nanoscale, which is referred to nanoscale electronics, it has becoming common to study the electron transport through molecules and one obvious question has been poised so far: What is the difference between electron transport as understood by physicists and the electron transfer, as understood by chemists?

In other words, is there a relationship between molecular conductance (that is studied through quantum electron transport mechanism) and the ET (as studied by from a different chemical point-of-view) phenomenon? (CUNIBERTI; FAGAS; RICHTER, 2006). One difference is noted in the experimental configuration and is related to the contacts. Contrary to the single molecular contact configuration studied in electrochemical experiments, the typical electrode contact used in molecular electronics is comprised by two contacts in which the molecules between these two contacts act as a molecular bridge as shown in Fig. 1.3, which is referred to molecular junction (MJ), which considers both electronic states. In other words, there are discrete electronic states associated with HOMO and LUMO molecular orbitals in contact with electrode levels that are treated as continuum electronic states. The electric current flows

through the molecules by applying a non-equilibrium potential difference, that is a DC bias voltage (CUNIBERTI; FAGAS; RICHTER, 2006; TAO, 2006). Measuring and interpreting the meaning of this electric current response is important in a way that it permit to understand the electron transport mechanism through molecules, something that has been referred as molecular electronics of molecular junctions, consisting of one of the most used configuration to study molecular electronics that has different applications in nanoelectronics (CUNIBERTI; FAGAS; RICHTER, 2006), such as in the design of molecular diodes, switches and transistors (KOMOTO *et al.*, 2016).

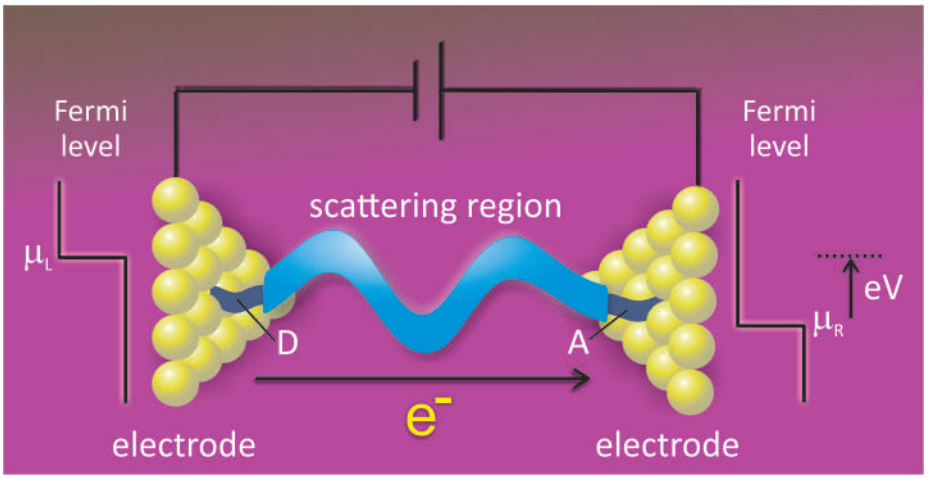

Figure 1.3: Schematic representation of a basic structure of a molecular junction comprised by a single molecule linked to two electrodes. Electron transport through the molecular bridge, the scattering region, is controlled in this case by a potential difference $edV = \mu_L - \mu_R$. `D` and `A` are the molecular fractions that are electronically coupled to the left and right electrodes, respectively (NITZAN, 2001).

Source: Author (2023).

In experiments of molecular conductance that involves the investigation of the electron transport mechanism through the backbone of organic molecules, the atomic structure of molecules constitutes the scattering region where the incoming electrons from the left electrode tunnels through the molecular bridge, with or without molecular electronic structure mediation, up to the right electrode (CUNIBERTI; FAGAS; RICHTER, 2006). The most used theory for interpreting the conductance of electrons in this molecular junction configuration is the Landauer conductance theory (LANDAUER, 1957), where the conductance quantum G_0 is associated with the transmission probability through the scatter region. The molecular bridge structure serve as a region for electrons to scatter and transmission probability describes the non-adiabatic nature of the electron transport taking as reference the ideal and adiabatic conductance quantum G_0. Therefore, the quantum of conductance G between two electron reservoirs also commonly referred as two metallic electrode contacts, is stated as

$$G = G_0 \sum_{n=1}^{N} T_n(\mu) \tag{1.8}$$

where $\sum_{n=1}^{N} T_n(\mu)$ accounts for the transmission probabilities across a number n of individual quantum channels (up to a total of N) at a given chemical potential μ level.

As previously noted, $G_0 = {}^{2e^2}/_{h}$ is the quantum conductance that is a constant value of $\sim 77.5\ \mu$S, which is expressed as a function of two other constants, that is e accounting for the elementary charge of the electron and h accounting for the Plank constant. Majority of the experiments leading to the interpretation of $\sum_{n=1}^{N} T_n(\mu)$ following a tunnelling mechanisms (see also section 1.1), in which $\sum_{n=1}^{N} T_n(\mu)$ statistics of scattering is accounted simply as $\propto \exp(-\beta L)$, where β is a parameter related to the height of the potential barrier for electrons to tunnel and L is the length of the bridge. Accordingly, it can be noted in different experiments that $G \propto \exp(-\beta L)$ (TAO, 2006; KOMOTO *et al.*, 2016; ARTES *et al.*, 2011; WIERZBINSKI *et al.*, 2013), which is interpreted as that electron quantum conductance G is dependent of the properties of the molecular structure that acts as potential barriers for electrons to tunnels through, which is in accordance with Landauer (LANDAUER, 1957), in which the molecular conductance is seen as an electron transmittance mechanism.

It is important to highlight the similarities between electron transfer k and transport G regarding the dependence with respect to the molecular length L; both phenomena are dependent on the electron transmission characteristics of the molecules in a similar manner, that is $\propto \exp(-\beta L)$. This was first theoretically noted by Abraham Nitzan (NITZAN, 2001), who proposed a relationship between G and k based on this premise. Accordingly, Nitzan addressed a relationship between $k_{D\to A}$, that refers to the electron transfer rate constant related to `D` and `A` probes and the zero bias electron conduction G_L for the same molecular bridge (see Fig. 1.3). The analysis assumes that the molecular electronic configuration is not considerably different between molecular junction and electrochemistry in such a way that the molecular conductance is assumed to be an "equilibrium potential" close to the zero bias potential perturbation such as that

$$G_L \approx \frac{8e^2}{\pi^2 \Gamma_D^L \Gamma_A^R} k_{D\to A} \tag{1.9}$$

where Γ is the electronic coupling of between left (`D`,`L`) and right (`A`,`R`) electrodes within the nearest segment of the molecular bridge, see Fig. 1.3. This work of Nitzan's significantly contributed to the study of molecular junctions and definitively pioneered in establishing a relationship between two scientific inter-disciplines (physics and chemistry) areas that were developed as complete separated fields for two related phenomena, that is those of electron transfer and transport. Furthermore, it was stressed out that the electronic transmission characteristics of these nanoscale settings rely mainly on the electronic interaction between the molecule and the electrode (or electrodes), as well as between the localized molecular orbitals. This was the fundamental basis for the computational calculations at the time (NITZAN; RATNER, 2003), and still is nowadays (MCCREERY, 2022).

Nevertheless, owing to that the molecular electronics and electrochemical experimental setting are physically different, experimental attempt to evaluate Nitzan's model for both quantities k and G for identical molecular bridge settings and to confirm the Nitzan's linear correlation between k and G as predicted by Eq. 1.9 has been unsuccessful. For instance, David Beratan and co-workers explored the molecular conductance and ET kinetics of different chemical structure as function of bridge length (WIERZBINSKI *et al.*, 2013) and a quantitative correlation was noted between indirect calculation of k (see Fig. 1.4*a*) and direct conductance measurements (see Fig. 1.4*b*), but instead of a linear correlation, a power-law relationship $G = ak^b$ was

experimentally obtained, where a and b are arbitrary fitting parameters such as that $b = \beta_G/\beta_k$ within β_G and β_k stated as exponential decay constant obtained from conductance and electrochemical measurements, respectively. The corresponding values of β were determined from the slope of the attenuation plots shown in Fig. 1.4. Instead of the expected linear correlation between k and G, in which $\beta_G = \beta_k$, according to the expected relationship stated by Nitzan's model, experimentally what was observed was that $\beta_G/\beta_k < 1$.

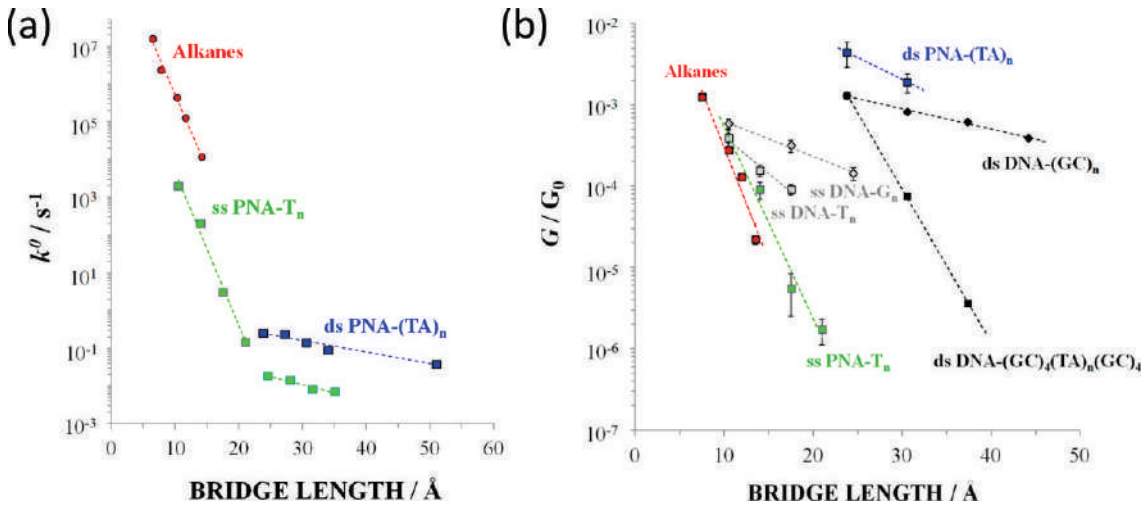

Figure 1.4: Attenuation plots on semi-logarithmic scale for alkanes and peptide nuclei acid strains. (a) k as function of bridge length, where the constant rates were obtained by plotting the peak separation *versus* s and fitting the data using the Marcus theory. (b) G as function of bridge length, where the single-molecule conductances were measured using Scanning Tunneling Microscope controlled Break Junction.

Source: Reprinted with permission from (WIERZBINSKI et al.*, 2013). Copyright 2013 American Chemical Society.*

Thus, the results were interpreted as being owing to energy barrier differences between ET rate and conductance measurements *per se* (WIERZBINSKI *et al.*, 2013). In other words, the applied potential difference between the electrodes for measurements of the molecular conductance and the applied electrochemical potential between the electrode and the redox group in the electrochemical ET experimental settings were considered different and not equivalent. An additional difference is that molecular measurements were carried out in "dry" (in the absence of electrolyte) condition, whereas electrochemical measurements were conducted under "wet" (in the presence of an electrolyte) conditions (WIERZBINSKI *et al.*, 2013). Not only the solvent environment was a source of differences between the two experimental settings, but also the molecular environment in which for measurements of G it was used a two electrode contact, whereas for measurements of k it was a single electrode contact (WIERZBINSKI *et al.*, 2013).

Despite the emerging theoretical approaches to study charge transfer and transport phenomena of MJs are reported (SOWA; MOL, *et al.*, 2018; SOWA; LAMBERT, *et al.*, 2020; SOWA; MARCUS, 2021), they have been not contrasted with experimental data, which does not allow their validation. In this context, experimental techniques that allow to access to both G and k quantities in the same experiment settings are necessary not only to understand the relationship between both G and k concepts, but also to understand role played by the transmission coefficient $\propto \exp(-\beta L)$ (for

tunnelling mechanism) in different configurations and situations. To do so, the interpretation of the experimental data must be supported by theories able to correlate these physical concepts in a sustained way.

1.5 The quantum rate theory and its application for the study of mesoscopic junctions

In seeking for a fundamental understanding of electron transfer and transport phenomena operating at nanoscale level, our research group has proposed a theory that has been able of assisting in the interpretation of experimental results addressed in the both fields. Almost one decade ago, this first-principle theory started to be developed through the study of the electrochemical capacitance C_μ phenomenon and has contributed to the understanding of the electronic transmission, such as the ET process of electrochemical reactions. Before describing the theoretical approximation that enables the study of electrochemical interfaces and molecular junctions, the so-called quantum rate theory is following described (BUENO, 2023c).

This novel theory defines the Eq. 1.10 as the fundamental quantum rate ν, which is the ratio between the reciprocal of the Von Klitzing constant $^1/_{R_K}$ = 38.7 μS (VON KLITZING, 2019) and the quantum (or chemical) capacitance C_q (BUENO, 2023a,b).

$$\nu = \frac{e^2}{hC_q} \tag{1.10}$$

If one considers the energy $E = {}^{e^2}/_{C_q}$ associated with the electronic structure and rewritten Eq. 1.10, leads to $E = h\nu = \hbar c_* \cdot \mathbf{k}$, where c_* is the Fermi velocity and $\mathbf{k}$ is the wave-vector. Meaning that the quantum rate principle ν contemplates the Planck-Einstein relationship and predicts that the dynamics of electrons during electrochemical reaction follows a relativistic dynamics that complies with Dirac equation (BUENO, 2023a,b), contrary to above-described quantum approaches based on the Schrödinger (non-relativistic) equation.

The relativistic dynamics allows to consider the electron spin degeneracy g_s in the quantum rate theory through of G_0, as noted by Landauer (LANDAUER, 1992), leading to $G_0 = g_s({}^{e^2}/_h) \sim 77$ μS, a universal constant (IMRY; LANDAUER, 1999). The inverse of G_0 is the resistance quantum R_q with a value of $\sim$ 12.9 kΩ. Note that G_0 describes the ideal adiabatic conductance when $\sum_{n=1}^{N} T_n(\mu)$ equals the unity (i.e, $G = G_0$), implying an perfect transmittance of a single electron in a single perfect quantum channel ($N = 1$). A more realistic consideration is accounted for by the non-adiabatic conductance modelled using the scattering statistics, as described in the previously section (see Eq. 1.8).

Considering the typical capacitance definition $^1/_C = {}^{dV}/_{dq}$, where q is the charge $dq = -edn$, the electrochemical potential difference $d\mu$ associated with dV as $d\mu = -edV$ is the driven force for transferring the electrons between `D` and `A` states, leading to ${}^{e^2}/_{C_q} = {}^{d\mu}/_{dn}$. In order to obtain the expression for C_q, one can rewrite the latter equation as $C_q = e^2({}^{dn}/_{d\mu})$. In this way, it is easily demonstrated that the quantum capacitance informs on the density-of-state (DOS) as $C_q \propto {}^{dn}/_{d\mu}$ (BUENO, 2018).

The ratio between G and C_q permits the definition of the constant rate k (see Eq. 1.11), which is a frequency directly proportional to ν. Also, note that C_q allows

to establish the correlation between G and k (BUENO, 2020), as Nitzan's model had attempted, as discussed previously. Although the relationship between G and k correlated concepts has been noted and attempted to be established, it was not fully clear in spite they were separately formulated for more than 60 years. Thus, as a consequence of understanding the quantum capacitive phenomenon, the quantum rate theory successfully correlated these two phenomena in a single and first-principle (BUENO, 2018), which will be demonstrated experimentally in this thesis.

$$k = \frac{G}{C_q} = \frac{G_0}{C_q}\sum_{n=1}^{N} T_n(\mu) = g_s \nu \sum_{n=1}^{N} T_n(\mu) \tag{1.11}$$

Eq. 1.11 deals with electron transmission process at the zero-temperature limit. However, the ET reaction of real electrochemical systems requires to consider the temperature influence. Therefore, a thermodynamics analysis is conducted using the statistical mechanics for accounting the thermal broadening level of $E = {}^{e^2}/_{C_q}$, where the degeneracy of the electron is important within an energy occupancy of levels that follows the Fermi–Dirac distribution function $f = [1 + \exp({}^{E^\ddagger}/_{k_B T})]^{-1}$ (BUENO, 2018; MIRANDA; BUENO, 2019). Consequently, Eq. 1.12 defines the number of available C_q states dn to be occupied per interval of energy $d\mu$, wherein the occupancy of those states by the electrons follows the function f, where the potential energy of electrons in the electrode is modelled as $-eV = \mu - E_F = E$, with E_F stating for the Fermi level of the redox moieties chemically attached to the electrode (see Fig. 1.5) (BUENO, 2018; BUENO; CRUZEIRO, *et al.*, 2021).

$$C_q = \frac{e^2 N}{k_B T} f(1-f), \tag{1.12}$$

Fig. 1.5 shows schematically the DOS shape of an electroactive interface which describes the C_q states associated with the A ($\mathrm{DOS_A}$) and D ($\mathrm{DOS_D}$) redox moieties. The access to those states is controlled by eV and the energy level of the electrode is the reference level (E_{ref}). Thus, when $\mu = E_F$, there is an energy level alignment between the states of electrode and that of the A/D redox moieties, leading to a maximum occupancy of C_q due to $f = {}^1/_2$, as predicted by Eq. 1.12.

All of these treatments lead us to a suitable quantum rate expression for real non-adiabatic electrochemical reactions. Furthermore, it is important to highlight that the transmission scattering matrix $\sum_{n=1}^{N} T_n(\mu)$ has its electrochemical counterpart $|H_{DA}|$ (see section 1.3), implying that the electron coupling between D and A is considered in the quantum rate theory, which can be employed to study the electron coupling not only in electrochemical systems as alternative of cumbersome methods (ZHU *et al.*, 2021), but also in molecular electronics wherein this novel theory has began to be applied (SANTOS *et al.*, 2020). Note that $\sum_{n=1}^{N} T_n(\mu)$ and $\kappa = \exp(-\beta L)$ imply a quantum mechanical tunneling mechanism, so G is stated as function of κ and N, such as $G = \kappa G_0 N$ (BUENO, 2020), resulting in the following expression

$$k = \kappa \frac{k_B T}{h} \left(f\,(1-f)\right)^{-1} = \kappa \frac{k_B T}{h} f^{-2} \exp\left(-\frac{E^\ddagger}{k_B T}\right) \tag{1.13}$$

Marcus constant rate can now be derived as special setting of Eq. 1.11, by considering a Boltzmann approximation to Eq. 1.13 (BUENO, 2020), that is, under conditions where $1 << \exp({}^{E^\ddagger}/_{k_B T})$ and $f \sim \exp({}^{-E^\ddagger}/_{k_B T})$, resulting in Eq. 1.3. This allows

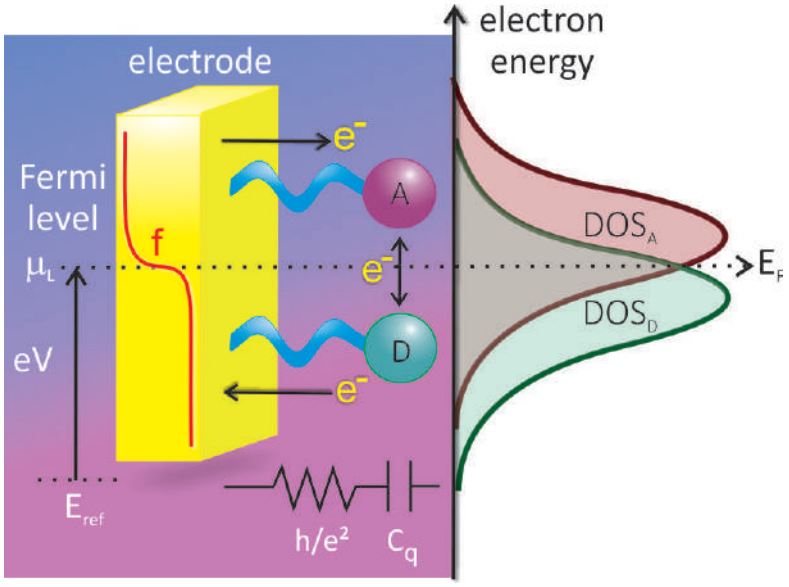

Figure 1.5: Exemplification of electroactive molecules self-assembled onto a metallic electrode surface. The electron transfer between A/D redox moieties and the electrode results in a Faradaic current. Whenever the Fermi level of the monolayer equals the formal potential energy of the electrode it can noted that is $\mu_L = E_F$. At E_F/e, half of the molecular (or capacitive) states are oxidized and the other half are reduced, and the corresponding DOS is described by Gaussian-like shape in the intersection area between DOS_A and DOS_D shapes. The parallel ET dynamics between between A/D redox moieties is also possible (FELICIANO; BUENO, 2020). Since each individual molecule acts as a quantum capacitive dot, the ensemble can be modelled as a quantum RC circuit, where the average value of $R_q = h/e^2$ and C_q can be experimentally measured at E_F.

Source: Author (2023).

to confirm that Marcus's homogeneous ET theory is a particular subset of the more general quantum rate principle, as described by Eq. 1.11.

As above mentioned, $E^{\ddagger}$ comprehends the semi-classical ET nomenclature shown in 1.2, which is referred from now on as E, since $E = E_i + \lambda$, where E_i is ΔG^0. In the quantum rate theory framework, changes in E_i reflects changes in the internal energy (e.g., μ), such as $\mu = E_i/n = -eV$ can be rewritten as $E_i = -neV$, which is the driving force of the ET transfer reaction. Therefore, in agreement with the original proposal of Marcus for λ, the energy term can be simply modelled as a constant external potential associated with the dielectric constant of the solvent over D and A species and independent of μ variations.

Nevertheless, electrochemical interfaces involve two charging processes with different physical nature. These capacitive phenomena give rise to the concept of C_μ, which is more suitable to describe the non-Faradaic and Faradaic charging processes of electrochemical interfaces comprised by redox moieties attached to electrodes as shown in Fig. 1.5 (BUENO; DAVIS, 2014b). Hence, $1/C_\mu$ is defined as the series combination of two capacitive contribution in series as $1/C_\mu = 1/C_e + 1/C_q$ corresponds to (BUENO; DAVIS, 2014b), where C_e is the electrostatic and C_q is the quantum contribution. C_e is related to the spacial separation of charge, for which is attributed the non-Faradaic charge, accounts for the properties of the electrolyte structure, and in turns the solvent and counter-ions contribution. Whereas C_q is related to the Faradaic charge due to the ET dynamics associated with the charging of the quantum states in

the redox reaction. A general definition of C_q implies to considered the whole electronic structure of a quantum capacitor, as ${}^{e^2}/_{C_q} = {}^{1}/_{(dn/d\mu)_l} + {}^{1}/_{(dn/d\mu)_r}$, where $\left({}^{dn}/_{d\mu}\right)_l$ and $\left({}^{dn}/_{d\mu}\right)_r$ are the DOS of the left and right "plates". In the difussionless heterogeneous case, one of these "plates" is a metallic electrode (the left, $\left({}^{dn}/_{d\mu}\right)_l$, for instance), whose DOS is quite large in comparison with that of the redox moieties attached over the electrode as shown by Fig. 1.5, leading to $C_q \propto {}^{dn}/_{d\mu_r}$ (BUENO, 2018). Therefore general form of the quantum rate expression for electrochemical interfaces takes the following form

$$k = \frac{G}{C_\mu} = G_0 \sum_{n=1}^{N} T_n(\mu) \left(\frac{1}{C_e} + \frac{1}{C_q} \right) \tag{1.14}$$

The ET dynamics associated with the ET reaction between `A/D` redox moieties occurring within the SAM impacts on the capacitive contributions of C_μ (Fig. 1.5). A recently quantum computational study confirmed the existence of such dynamics (FELICIANO; BUENO, 2020), which treated the `A/D` redox moieties as 2D-like structure for which was associated a DOS that is compensated by counter ions in the electrolyte, leading to an equivalence between these capacitive contributions due to the "C_e" and C_q states are superimposed, so $C_e \sim C_q$. Then, one can establish that ${}^{1}/_{C_\mu} = {}^{2}/_{C_q}$. This supports the requirement of the additional degeneracy to k, which was referred as the degeneracy associated with two possible oxidation and reduction states that result in the anodic and cathodic electrochemical currents (ALARCÓN; SANTOS; BUENO, 2021), in which g_r takes a value of 2. Therefore, Eq. 1.14, for these particular situations is obtained as

$$k = g_s g_r \frac{e^2}{hC_q} = g_r \frac{G_0}{C_q} = g_s g_r \frac{E}{h} \tag{1.15}$$

corresponding to $k = 4({}^{e^2}/_{hC_q})$ with a direct consequence that C_q is the only experimental variable and all the properties of the interface can be determined (MIRANDA; BUENO, 2016) solely by measuring C_q. The quantum rate theory establishes two main methodologies that allow us to measure C_q of the interface, namely, cyclic voltammetry (CV) and impedance-derived capacitive spectroscopy (ECS) (ALARCÓN; SANTOS; BUENO, 2021). The advantage of using ECS is that it allows us to determine separately the non-Faradaic and Faradaic electric currents, permitting to obtain a detail picture of the interface through the circuit elements associated with each of the non-Faradaic and Faradaic processes (GOES *et al.*, 2012; LEHR *et al.*, 2017). Moreover, C_q can be experimentally measured as a function of V (MIRANDA; BUENO, 2016), leading to a DOS shape that is experimentally accessible and varies (in a reversible form) with the solvent environment, observing that as the electrolyte environment is more polar fewer states are available for occupancy at a particular electrode potential and faster is ET kinetics (BUENO; DAVIS, 2014a). Accordingly, the application of Eq. 1.12 is a powerful theoretical tool not only able to evaluate the DOS distribution of capacitive states, but also to study the effects that influence the electron transfer/transport process, contributing to a better understanding of such phenomenon as demonstrated in this thesis.

1.6 Experimental evaluation of the ET constant rate

Given the complexity of ET theory, particularly for a heterogeneous settings, in which generally immobilized redox molecular species onto the electrode surface also present a quantum transport communication with the electrode besides the ET rate constant, the experimental study of the ET kinetics has not been an easy task. There are different electrochemical techniques based on potential sweep and impedance measurements that have been used to study ET phenomenon. Parameters such as λ, η, T, A/D electronic coupling (A/D distance) and electrolyte environment conditions (FINKLEA; RAVENSCROFT; SNIDER, 1993; RAVENSCROFT; FINKLEA, 1994; FORSTER; FAULKNER, 1994a,b; SMALLEY *et al.*, 2003; ARIKUMA *et al.*, 2010) have been studied in correlation with the semi-classical ET theory in other to interpret the trends (SMALLEY *et al.*, 2003; ARIKUMA *et al.*, 2010). However, due to a quite different experimental configuration in which the semi-classical ET theory was established (homogeneous settings), measurements of k for a diffusionless interfacial conditions has been limited in providing theoretical insights, such as to understanding the meaning of λ in heterogeneous settings of measurements.

Over the years of investigations some experimental methodologies became more (likely because of the facility of the methodology) than others in order to measure k in heterogeneous settings of ET reactions. Most common methodologies are primary based on controlled potential such as chronoamperometry (CHIDSEY, 1991) and voltammetry methods (LAVIRON, 1979). These methods have been frequently used, but the determination of k is conducted an indirect way outside of the equilibrium electrochemical condition in which an approximation solution of Eq. 1.7 can be considered for the heterogeneous setting. These potential-step experiments require to take the system out of the electrochemical equilibrium by means of a potential perturbation V in order to access k of the ET reaction. Nonetheless, conceptually, k is a kinetic parameter that must be considered at a dynamical equilibrium condition of the reaction, which in the case of a redox monolayer reacting with an electrode is associated to a resonant Faradaic current and the redox reaction occurs in the diffusionless regime, as discussed previously. In particular, chronoamperometry techniques as illustrated in Fig. 1.6*a*, allows us to depict the logarithm of the apparent constant rate k_{app} as a function of the η, that is $\eta = V - {}^{E_F}/_{e}$, where ${}^{E_F}/_{e}$ is the formal potential, for which k is obtained when the potential of the electrode of $V = {}^{E_F}/_{e}$ (CHIDSEY, 1991). On the other hand, the Laviron´s methodology of calculating k is an intricate experimental way that also requires potential measurements in the non-equilibrium regime, where k is determined from the slope of anodic and cathodic branches of a plot of the electrode potential peak V_p *versus* the logarithm of the scan rate $s = {}^{dV}/_{dt}$, obtained from different cyclic voltammetric (CV) scans as shown in Fig. 1.6*b* (LAVIRON, 1979).

Note that both above-mentioned studies indirectly obtain k by means of studying cathodic and anodic processes associated to the potential step methodologies, thus there are strongly dependent on the symmetry factor namely as the transfer coefficient α (BARD; FAULKNER, 2000). In other words, k_{app} measured at over-potentials correspond to a redox kinetics that is out of the equilibrium in which one direction of the ET is favoured over the other. This strategy is likely unsuitable to access the nature of k at a proper equilibrium regime. Notwithstanding the indirect way for determining k, the above mentioned methods have allowed us to study factors (HORSLEY *et al.*, 2014a; UNNI; BURGESS, 2021; HORSLEY *et al.*, 2014b; SHAH *et al.*, 2015) that

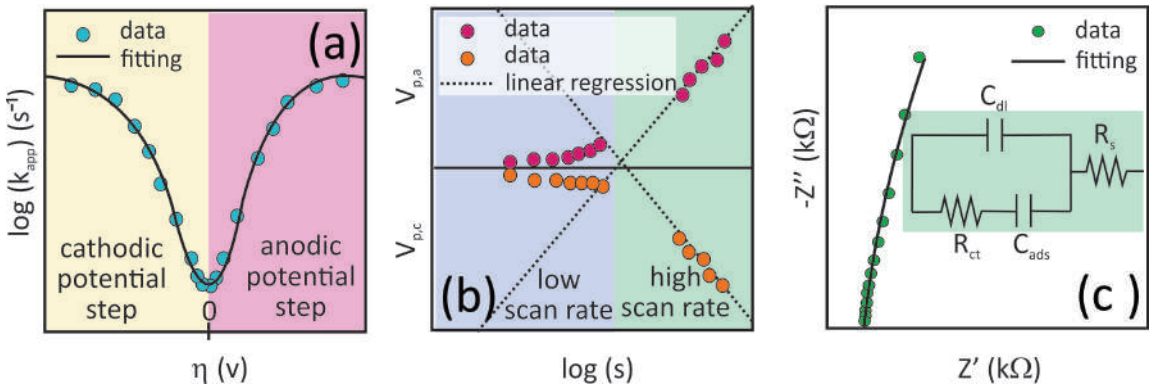

Figure 1.6: Experimental data treatment for k determination at equilibrium using controlled potential and impedance methodologies. (a) Tafel plot of $\log(k_{app})$ *versus* η, where each local constant rate corresponds to linear regression of the linear region of transient of electric current. k is obtained by extrapolation at $\eta = 0$, i.e., $V = {}^{E_F}/_{e}$ (CHIDSEY, 1991). (b) Plot of potential peaks *versus* $\log(s)$, where the anodic potential peak $V_{p,a}$ and cathodic potential peak $V_{p,c}$ are obtained from cyclic voltammograms measurements at different scan rates s. At high s, a linear behavior is obtained with the slope reporting the value of the transfer coefficient used for the calculation of k (LAVIRON, 1979). (c) Nyquist impedance plot fitted according to the Randles equivalent circuit as shown in the inset, which was modified to modelling the electrochemical response of a redox monolayer. R_{ct} and C_{ads} are the only variables used for the calculation of k according to the methodology introduced by Creager (CREAGER; WOOSTER, 1998), where the resistance of the interface was interpreted as the charge transfer resistance R_{ct} and the capacitance C_{ads} as an adsorption capacitance.

Source: Author (2023).

influence the diffusionless interfacial ET kinetics in redox electrode reactions (CHATTOPADHYAY; BANDYOPADHYAY; DEY, 2021; CHATTOPADHYAY; MUKHERJEE, *et al.*, 2021; LACHMANOVÁ *et al.*, 2021).

Contrary to transient perturbation methods, AC methodologies have been used in order to access to k at equilibrium by means of small amplitude perturbations around the equilibrium potential of the electrode. Therefore, the perturbation occurs at the formal potential ${}^{E_F}/_{e}$ of the electrode, in which the variable-frequency AC voltammetry data is analyzed by means of fitting the raw data using the Randles equivalent circuit model (CREAGER; WOOSTER, 1998). The circuit model used in such type of approach is shown in Fig. 1.6*c*, which describes resistive and capacitive elements (BARD; FAULKNER, 2000). The solution resistance R_s is obtained as the high-frequency intercept on the real axis of the Nyquist impedance plot, usually interpreted as a series resistance that does not interfere with the calculation of k. The charge transfer resistance R_{ct} is related to the difficult of exchange Faradaic current. The double layer capacitance is noted as C_{dl}. The adsorption pseudocapacitance is denoted as C_{ads} and is associated with the molecular coverage of electroactive species per unit area of the electrode. From these fitted elements the ET rate constant is obtained using the expression $k = {}^{1}/_{(2R_{ct}C_{ads})}$ (CREAGER; WOOSTER, 1998). In spite of these circuit elements were not related within the semi-classical theory in this type of study, it is shown that this methodology is an straightforward way for experimentally obtaining the k of redox-active monolayers (LI *et al.*, 2021; ZHANG *et al.*, 2021; BOITEL-AULLEN *et al.*, 2021).

Hence, experimental approaches that overcome the problem of evaluating k at

non-equilibrium conditions are welcome for studying the ET kinetics of this particular setting of electrochemical reaction that, as noted, has served as a prototype for studying the physical-chemistry fundamentals of ET reactions. In addition, a more self-consistent theory that emerges from first-principle methods are desired for a better understanding of the electrochemical reactions, as is the case of the quantum rate model that explains the origin of the charge transfer resistance and of the pseudo-capacitive absorption of the redox species over the electrode, as denoted in the Creager's studies of redox-active monolayers (CREAGER; WOOSTER, 1998).

These methods permit to study k in a more straightforward way than that proposed by Chidsey (CHIDSEY, 1991). Nonetheless, to advance beyond the adaptation of the semi-classical theory to the heterogeneous situations it is important to understand the physical meaning of R_{ct} and C_{ads} as it is the case of the quantum rate theory that incorporates the meaning of the conductance quantum (LANDAUER, 1957) within the concept of ET, which was briefly introduced in section 1.4. The C_{ads} capacitance has its meaning contained in the concept of quantum capacitance, largely referred as pseudo-capacitive (CREAGER; WOOSTER, 1998) phenomenon.

Note that quantum rate theory not only provides a suitable physical way interpreting k but it also that permits to studying it experimentally in a suitable way since the conductance quantum and the quantum capacitance that defines k are directly obtained experimentally via impedance methodologies. Note that also that the quantum rate theory, therefore, not only theoretically encompasses Marcus homogeneous ET theory as a particular setting of the theory, but also permits to study the quantum mechanics behind ET phenomenon. The direct measurement of k is achieved by measuring the quantum capacitance C_q of the interface, as was discussed in section 1.5 (BUENO; BENITES; DAVIS, 2016; BUENO, 2018). Therefore, this theory has been successfully tested to describe the ET and its correlation with the conductance quantum and the quantum capacitance of an electrochemical interface not only for redox-monolayers (BUENO; DAVIS, 2014b) but also for semiconductive films (PINZON; SANTOS; BUENO, 2021) and solid-state molecular junctions (SANTOS *et al.*, 2020) as well as it was successfully applied to understand the electrodynamics within a single-layer graphene (MIRANDA; BUENO, 2016) when embedded in an electrolyte environment.

1.7 Conclusion

The study of charge transmission process has been a matter of study for the scientific community, processes such as electron transfer and transport have been addressed separately by the electrochemists and physicist, respectively. The fundamental study of the constant rate of ET reactions has been a journey spanning more than a century, resulting in a complex theory that has allowed electrochemists to understand long-range ET reactions associated with biological processes such as respiration. However, this widely-known theory ignores some quantum mechanical components such as the quantum capacitance. On the other hand, the electron transport phenomenon associated to the molecular conductance was theoretically correlated to the constant rate. Nonetheless, differences in the experimental setup between electrochemical and molecular electronics configuration have represented a main limitation to prove this

conductance-rate relationship. Within this context, the quantum rate theory is proposed not only to understand the charge transmission processes but also to access experimentally to the quantum properties such quantum capacitance and conductance using time-dependent methods for a specific configuration, whether it is an electrochemical system or an molecular electronic setup.

References

ALARCÓN, E. V. G.; SANTOS, A.; BUENO, P. R. Perspective on Quantum Electrochemistry. A Simple Method for Measuring the Electron Transfer Rate Constant. **Electrochimica Acta**, v. 398, p. 139219, 2021. DOI: 10.1016/j.electacta.2021.139219.

ARIKUMA, Y. *et al.* Electron hopping over 100 Åalong an α helix. **Angewandte Chemie International Edition**, Wiley Online Library, v. 49, n. 10, p. 1800–1804, 2010.

ARTES, J. M. *et al.* Direct measurement of electron transfer distance decay constants of single redox proteins by electrochemical tunneling spectroscopy. **Acs Nano**, ACS Publications, v. 5, n. 3, p. 2060–2066, 2011.

BALZANI, V. *et al.* **Electron transfer in chemistry**. Wiley-VCH Weinheim, 2001. v. 1.

BARD, A. J.; FAULKNER, L. R. **Electrochemical Methods Fundamentals and applications**. 2nd: John Wiley and Sons, 2000.

BOITEL-AULLEN, G. *et al.* Electron transfer inside a decaferrocenylated rotaxane analyzed by fast scan cyclic voltammetry and impedance spectroscopy. **ChemElectroChem**, Wiley Online Library, v. 8, n. 18, p. 3506–3511, 2021.

BUENO, P. R. **On the electromagnetic nature of Planck constant**. 2023a. arXiv: 2302.10797 [physics.gen-ph].

BUENO, P. R. **Quantum electromagnetic rate theory of the electron and the meaning of the fine-structure constant**. 2023b. arXiv: 2302.12886 [physics.gen-ph].

BUENO, P. R.; DAVIS, J. J. Elucidating redox-level dispersion and local dielectric effects within electroactive molecular films. **Analytical chemistry**, ACS Publications, v. 86, n. 4, p. 1997–2004, 2014a.

BUENO, P. R. Electron transfer and conductance quantum. **Physical Chemistry Chemical Physics**, Royal Society of Chemistry, v. 22, n. 45, p. 26109–26112, 2020.

BUENO, P. R. Quantum Rate Theory and Electron-Transfer Dynamics: A Theoretical and Experimental Approach for Quantum Electrochemistry. **arXiv preprint arXiv:2305.18359**, 2023c.

BUENO, P. R. **The Nanoscale Electrochemistry of Molecular Contacts**. Springer, 2018. (SpringerBriefs in Applied Sciences and Technology). ISBN 978-3-319-90486-3. DOI: 10.1007/978-3-319-90487-0.

BUENO, P. R.; BENITES, T. A.; DAVIS, J. J. The Mesoscopic Electrochemistry of Molecular Junctions. **Scientific Reports**, v. 6, p. 18400, 2016. DOI: 10.1038/srep18400.

BUENO, P. R.; CRUZEIRO, V. W., *et al.* The density-of-States and equilibrium charge dynamics of redox-active switches. **Electrochimica Acta**, v. 387, p. 138410, 2021. ISSN 0013-4686. DOI: 10.1016/j.electacta.2021.138410.

BUENO, P. R.; DAVIS, J. J. Measuring Quantum Capacitance in Energetically Addressable Molecular Layers. **Analytical Chemistry**, v. 86, n. 3, p. 1337–1341, 2014b. ISSN 0003-2700. DOI: 10.1021/ac403135b.

CHATTOPADHYAY, S.; BANDYOPADHYAY, S.; DEY, A. Kinetic isotope effects on electron transfer across self-assembled monolayers on gold. **Inorganic Chemistry**, ACS Publications, v. 60, n. 2, p. 597–605, 2021.

CHATTOPADHYAY, S.; MUKHERJEE, M., *et al.* Contributions to cytochrome c inner- and outer-sphere reorganization energy. **Chemical science**, Royal Society of Chemistry, v. 12, n. 35, p. 11894–11913, 2021.

CHIDSEY, C. E. D. Free-energy and temperature-dependence of electron-transfer at the metal-electrolyte interface. **Science**, v. 251, n. 4996, p. 919–922, 1991. ISSN 0036-8075. DOI: 10.1126/science.251.4996.919.

CREAGER, S. E.; WOOSTER, T. T. A new way of using ac voltammetry to study redox kinetics in electroactive monolayers. **Analytical chemistry**, ACS Publications, v. 70, n. 20, p. 4257–4263, 1998.

CUNIBERTI, G.; FAGAS, G.; RICHTER, K. **Introducing molecular electronics: A brief overview**. 1. ed.: Springer, 2006.

DOGONADZE, R. R.; KUZNETSOV, A. M.; CHERNENKO, A. A. Theory of homogeneous and heterogeneous electronic processes in liquids. **Russian Chemical Reviews**, IOP Publishing, v. 34, n. 10, p. 759, 1965.

FELICIANO, G. T.; BUENO, P. R. Two-Dimensional Nature and the Meaning of the Density of States in Redox Monolayers. **The Journal of Physical Chemistry C**, ACS Publications, v. 124, n. 27, p. 14918–14927, 2020.

FINKLEA, H. O.; RAVENSCROFT, M. S.; SNIDER, D. A. Electrolyte and temperature effects on long range electron transfer across self-assembled monolayers. **Langmuir**, ACS Publications, v. 9, n. 1, p. 223–227, 1993.

FLETCHER, S. The theory of electron transfer. **Journal of Solid State Electrochemistry**, Springer, v. 14, n. 5, p. 705–739, 2010.

FORSTER, R. J.; FAULKNER, L. R. Electrochemistry of spontaneously adsorbed monolayers. Effects of solvent, potential, and temperature on electron transfer dynamics. **Journal of the American Chemical Society**, ACS Publications, v. 116, n. 12, p. 5453–5461, 1994a.

FORSTER, R. J.; FAULKNER, L. R. Electrochemistry of spontaneously adsorbed monolayers. Equilibrium properties and fundamental electron transfer characteristics. **Journal of the American Chemical Society**, ACS Publications, v. 116, n. 12, p. 5444–5452, 1994b.

GERISCHER, H. The impact of semiconductors on the concepts of electrochemistry. **Electrochimica Acta**, v. 35, n. 11-12, p. 1677–1699, 1990. ISSN 0013-4686. DOI: 10.1016/0013-4686(90)87067-c.

GIESE, B.; KARAMASH, M.; FROMM, K. M. Chances and challenges of long-distance electron transfer for cellular redox reactions. **FEBS letters**, Wiley Online Library, v. 597, n. 1, p. 166–173, 2023.

GOES, M. S. *et al.* A Dielectric Model of Self-Assembled Monolayer Interfaces by Capacitive Spectroscopy. **Langmuir**, v. 28, n. 25, p. 9689–9699, 2012. ISSN 0743-7463. DOI: 10.1021/la301281y.

GRIFFITHS, D. J.; SCHROETER, D. F. **Introduction to Quantum Mechanics**. 3. ed.: Cambridge University Press, 2018. DOI: 10.1017/9781316995433.

HENSTRIDGE, M. C. *et al.* Marcus–Hush–Chidsey theory of electron transfer applied to voltammetry: A review. **Electrochimica Acta**, Elsevier, v. 84, p. 12–20, 2012.

HORSLEY, J. R. *et al.* Unraveling the interplay of backbone rigidity and electron rich side-chains on electron transfer in peptides: the realization of tunable molecular wires. **Journal of the American Chemical Society**, ACS Publications, v. 136, n. 35, p. 12479–12488, 2014a.

HORSLEY, J. R. *et al.* Unraveling the interplay of backbone rigidity and electron rich side-chains on electron transfer in peptides: the realization of tunable molecular wires. **Journal of the American Chemical Society**, ACS Publications, v. 136, n. 35, p. 12479–12488, 2014b.

HUSH, N. S. Adiabatic rate processes at electrodes. I. Energy-charge relationships. **Journal of Chemical Physics**, American Institute of Physics, v. 28, n. 5, p. 962–972, 1958.

HUSH, N. S. Adiabatic theory of outer sphere electron-transfer reactions in solution. **Journal of the Chemical Society, Faraday Transactions**, Royal Society of Chemistry, v. 57, p. 557–580, 1961.

IMRY, Y.; LANDAUER, R. Conductance viewed as transmission. **Reviews of Modern Physics**, v. 71, n. 2, s306–s312, 1999. ISSN 0034-6861. DOI: 10.1103/RevModPhys.71.S306.

INIEWSKI, K. **Nanoelectronics: nanowires, molecular electronics, and nanodevices**. McGraw Hill Professional, 2010.

KOMOTO, Y. *et al.* Single-molecule junctions for molecular electronics. **Journal of Materials Chemistry C**, Royal Society of Chemistry, v. 4, n. 38, p. 8842–8858, 2016.

LACHMANOVÁ, Š. *et al.* Charge transfer in self-assembled monolayers of molecular conductors containing tripodal anchor and terpyridine-metal redox switching element. **Electrochimica Acta**, Elsevier, v. 384, p. 138302, 2021.

LAIDLER, K. J.; KING, M. C. The development of transition-state theory. **Journal of Physical Chemistry**, v. 87, n. 15, p. 2657–2664, 1983.

LANDAUER, R. Conductance from transmission: common sense points. **Physica Scripta**, IOP Publishing, v. 1992, T42, p. 110, 1992.

LANDAUER, R. Spatial variation of currents and fields due to localized scatterers in metallic conduction. **Ibm Journal of Research and Development**, v. 1, n. 3, p. 223–231, 1957. ISSN 0018-8646. DOI: 10.1147/rd.13.0223.

LAVIRON, E. General expression of the linear potential sweep voltammogram in the case of diffusionless electrochemical systems. **Journal of Electroanalytical Chemistry**, v. 101, n. 1, p. 19–28, 1979. ISSN 1572-6657. DOI: 10.1016/s0022-0728(79)80075-3.

LEHR, J. *et al.* Mapping the ionic fingerprints of molecular monolayers. **Physical Chemistry Chemical Physics**, v. 19, n. 23, p. 15098–15109, 2017. ISSN 1463-9076. DOI: 10.1039/c7cp01500c.

LI, T. *et al.* Nanoscale Silicon Oxide Reduces Electron Transfer Kinetics of Surface-Bound Ferrocene Monolayers on Silicon. **The Journal of Physical Chemistry C**, ACS Publications, v. 125, n. 50, p. 27763–27770, 2021.

MARCUS, R. A. Chemical and electrochemical electron-transfer theory. **Annual Review of Physical Chemistry**, Annual Reviews, Inc., v. 15, n. 1, p. 155–196, 1964.

MARCUS, R. A. Electron-transfer reactions in chemistry - theory and experiment. **Reviews of Modern Physics**, v. 65, n. 3, p. 599–610, 1993. ISSN 0034-6861. DOI: 10.1103/RevModPhys.65.599.

MARCUS, R. A. On the theory of oxidation-reduction reactions involving electron transfer. I. **Journal of Chemical Physics**, American Institute of Physics, v. 24, n. 5, p. 966–978, 1956.

MARCUS, R. A.; SUTIN, N. Electron transfers in chemistry and biology. **Biochimica et Biophysica Acta-Bionergetics**, Elsevier, v. 811, n. 3, p. 265–322, 1985.

MCCREERY, R. L. Carbon-based molecular junctions for practical molecular electronics. **Accounts of Chemical Research**, ACS Publications, v. 55, n. 19, p. 2766–2779, 2022.

MIRANDA, D. A.; BUENO, P. R. Chemical Hardness of Mesoscopic Electrochemical Systems Directly Analyzed from Experimental Data. **Journal of Physical Chemistry C**, v. 123, n. 34, p. 21213–21223, 2019. ISSN 1932-7447. DOI: 10.1021/acs.jpcc.9b04020.

MIRANDA, D. A.; BUENO, P. R. Density functional theory and an experimentally-designed energy functional of electron density. **Physical Chemistry Chemical Physics**, v. 18, n. 37, p. 25984–25992, 2016. ISSN 1463-9076. DOI: 10.1039/c6cp01659f.

NEWTON, M. D. Quantum chemical probes of electron-transfer kinetics: the nature of donor-acceptor interactions. **Chemical Reviews**, ACS Publications, v. 91, n. 5, p. 767–792, 1991.

NITZAN, A. A relationship between electron-transfer rates and molecular conduction. **The Journal of Physical Chemistry A**, ACS Publications, v. 105, n. 12, p. 2677–2679, 2001.

NITZAN, A.; RATNER, M. A. Electron transport in molecular wire junctions. **Science**, American Association for the Advancement of Science, v. 300, n. 5624, p. 1384–1389, 2003.

NIU, L. *et al.* Conductive metal–organic frameworks for supercapacitors. **Advanced Materials**, Wiley Online Library, p. 2200999, 2022.

OLDHAM, K. B.; MYLAND, J. C. On the evaluation and analysis of the Marcus–Hush–Chidsey integral. **Journal of electroanalytical chemistry**, Elsevier, v. 655, n. 1, p. 65–72, 2011.

PINZON, E. F.; SANTOS, A.; BUENO, P. R. Density of States of a Nanoscale Semiconductor Interface as a Transduction Signal for Sensing Molecules. **ACS Applied Electronic Materials**, ACS Publications, v. 3, n. 8, p. 3411–3417, 2021.

RAVENSCROFT, M. S.; FINKLEA, H. O. Kinetics of electron transfer to attached redox centers on gold electrodes in nonaqueous electrolytes. **The Journal of Physical Chemistry**, ACS Publications, v. 98, n. 14, p. 3843–3850, 1994.

SANTOS, A. *et al.* Introducing mesoscopic charge transfer rates into molecular electronics. **Physical Chemistry Chemical Physics**, v. 22, n. 19, p. 10828–10832, 2020. ISSN 1463-9076. DOI: 10.1039/d0cp01621g.

SCHMICKLER, W. **Interfacial electrochemistry**. Oxford University Press, Inc., 1996.

SHAH, A. *et al.* Electron transfer in peptides. **Chemical Society Reviews**, Royal Society of Chemistry, v. 44, n. 4, p. 1015–1027, 2015.

SMALLEY, J. F. *et al.* Heterogeneous electron-transfer kinetics for ruthenium and ferrocene redox moieties through alkanethiol monolayers on gold. **Journal of the American Chemical Society**, ACS Publications, v. 125, n. 7, p. 2004–2013, 2003.

SOWA, J. K.; LAMBERT, N., *et al.* Beyond Marcus theory and the Landauer–Büttiker approach in molecular junctions. II. A self-consistent Born approach. **The Journal of Chemical Physics**, AIP Publishing LLC, v. 152, n. 6, p. 064103, 2020.

SOWA, J. K.; MARCUS, R. A. On the theory of charge transport and entropic effects in solvated molecular junctions. **The Journal of Chemical Physics**, AIP Publishing LLC, v. 154, n. 3, p. 034110, 2021.

SOWA, J. K.; MOL, J. A., *et al.* Beyond Marcus theory and the Landauer-Büttiker approach in molecular junctions: A unified framework. **The Journal of chemical physics**, AIP Publishing LLC, v. 149, n. 15, p. 154112, 2018.

TAO, N. J. Electron transport in molecular junctions. **Nature nanotechnology**, Nature Publishing Group, v. 1, n. 3, p. 173–181, 2006.

THAPA, B. S. *et al.* Overview of electroactive microorganisms and electron transfer mechanisms in microbial electrochemistry. **Bioresource Technology**, Elsevier, v. 347, p. 126579, 2022.

UNNI, B.; BURGESS, I. J. Electrochemical and surface enhanced infrared absorption spectroscopy studies of TEMPO self-assembled monolayers. **Electrochimica Acta**, Elsevier, v. 381, p. 138263, 2021.

VAN V., T. *et al.* The diabatic picture of electron transfer, reaction barriers and molecular dynamics. **Annual Review of Physical Chemistry**, Annual Reviews, v. 61, p. 149–70, 2010.

VON KLITZING, K. Essay: Quantum Hall Effect and the New International System of Units. **Physical Review Letters**, v. 122, n. 20, 2019. ISSN 0031-9007. DOI: 10.1103/PhysRevLett.122.200001.

WANG, C.; YANG, C.; ZHENG, Z. Toward practical high-energy and high-power lithium battery anodes: present and future. **Advanced Science**, Wiley Online Library, v. 9, n. 9, p. 2105213, 2022.

WIERZBINSKI, E. *et al.* The single-molecule conductance and electrochemical electron-transfer rate are related by a power law. **Acs Nano**, ACS Publications, v. 7, n. 6, p. 5391–5401, 2013.

ZENG, Y. *et al.* Simple formula for marcus–hush–chidsey kinetics. **Journal of Electroanalytical Chemistry**, Elsevier, v. 735, p. 77–83, 2014.

ZHANG, S. *et al.* Absence of a Relationship between Surface Conductivity and Electrochemical Rates: Redox-Active Monolayers on Si (211), Si (111), and Si (110). **The Journal of Physical Chemistry C**, ACS Publications, v. 125, n. 33, p. 18197–18203, 2021.

ZHU, G. Y. *et al.* Crossover between the adiabatic and nonadiabatic electron transfer limits in the Landau-Zener model. **Nature communications**, Nature Publishing Group, v. 12, n. 1, p. 1–10, 2021.

Chapter 2

Quantum Resistance Study of the Electron Transfer Process

The quantum rate theory emerged as an outcome of a detailed study of the quantum capacitance phenomena of nanoscale conducted in electrochemical interfaces, defining the ET rate constant by noting its relationship with the quantum of conductance. This has been not previously studied in the field of electrochemistry nor previously addressed in existing ET theories as noted in chapter 1. However, the electrochemists do recognize the influence of the conductance/resistance property of the solution on the electrochemical experiments as a variable that must be controlled (or taken into account) during electrochemical measurements conducted in electrode's ET reactions. Nevertheless, the series resistance has been disregarding as simply a resistive term containing some contact contribution, unrelated to the charge transfer resistance itself. The charge transfer resistance is considered during studies of the ET rate that in terms of equivalent circuit analysis is a term within an equivalent circuit analysis wherein Randles's circuit is a particular example. Frequently, there are different versions of the Randles's circuit as shown below in Fig. 1.6. The equivalent circuit analysis of an interface is useful for studying ET rate constant using time-dependent methods such as impedance spectroscopy, in which the charge transfer resistance is particular term within the methodology. In other words, the measuring of the ET rate constant can be interpreted within different theories as shown in chapter 1, but the connection between the ET rate constant and the charge transfer resistance is not established from a microscopic point-of-view and the meaning of the charge transfer resistance has not been received the attention it requires from an atomistic and mesoscopic point-of-view. Accordingly, this chapter aims to interpret the charge transfer resistance within a mesoscopic view and within a quantum mechanical description that is in agreement with the quantum rate theory. In summary, the meaning of the charge transfer resistance within the quantum rate theory is studied using redox-active self-assembled monolayer interfaces with two main purposes:

- ☑ To establish the quantum mechanical meaning of the charge transfer resistance within the quantum rate theory, which is conducted by using equivalent quantum circuit analysis of the interfaces;

- ☑ To demonstrate that the resistance quantum (or conductance quantum) is the ideal situation of electron transmittance. Whenever the transmittance of an electron is lower than the ideal adiabatic condition, the transmission coefficient taken into account as it was stated in the semi-classical theory. The transmission coefficient is a result of a specific setting of the transmission matrix probability

for the tunneling mechanism of ET that is the mechanism that operates, particularly, in the ET occurring in redox-active self-assembled monolayer interfaces.

2.1 Introduction

In solid-state physics, the resistance R to the current passage under a potential driven force is treated as the inverse of electric conductance G between large DOS (e.g., metals), which is explained according to the Sommerfeld model (KITTEL, 2004). This free electron gas model describes the electron flow (di) within the electronic structure - a sea of electrons within positive nuclei- under a potential difference (dV), which is quantified by $G = {}^{di}/_{dV}$ (or $R = {}^{1}/_{G} = {}^{dV}/_{di}$), known as the Ohm's law. Since the electrons are flowing freely, the losing of kinetic energy due to the collision with the nuclei can be thought as a resistance. Therefore, the distance L defined by the mean free path that the electron travels before collide ($L = \nu\bar{\tau}$ where ν is the velocity component and $\bar{\tau}$ is the average time between collisions), is only but the length dependence of the resistance. However, this model is unable to predicts which is the resistance when potential tends to zero.

Note that whether the configuration is that of molecular electronics (see Fig. 1.3) or electrochemistry (see Fig. 2.1*b*), there is a scattering region in which the transferring electron travels, which is inherently to such configurations due to that region is the molecular bridge. Therefore, the role-play of the electronic structure of the molecular bridge must be considered in this discussion, which can be achieved if one analyses the electric current changes di due chemical potential variations $d\mu$ stated by the quantum mechanics (Eqs. 2.1) (DATTA, 1997), which is in function of the parameters ν and L, and the DOS of the molecular bridge defined as ${}^{dn}/_{d\mu} = {}^{2L}/_{h\nu}$, where L is the molecular length. Thus, recalling that the induced chemical potential difference is correlated with changes in potential as $d\mu = -edV$ (better explained at the end of this introduction), Eq. 2.1 can be rewritten as follows (BUENO; DAVIS, 2020),

$$\begin{aligned} di =& -d\mu \left(\frac{e\nu}{L}\right)\left(\frac{dn}{d\mu}\right) \\ =& edV \left(\frac{e\nu}{L}\right)\left(\frac{2L}{h\nu}\right) \\ =& \left(\frac{2e^2}{h}\right) dV \end{aligned} \tag{2.1}$$

Note that if the obtained expression is reorganized as ${}^{di}/_{dV} = {}^{2e^2}/_{h}$, one can obtain the conductance quantum G_0 from the Landauer formalism (i.e., $G_0 = g_s({}^{e^2}/_{h})$, where $g_s = 2$). In other words, the Landauer equation establishes a maximum conductance G when a single channel ($N = 1$) is considered and the transmittance is perfect ($T_n = 1$), resulting in $G = G_0 \sim 77.5\mu S$, a constant that can be thought as a quantized number of G, whose reciprocal $R = {}^{1}/_{G} \sim 12.9\ k\Omega$, is the minimal resistance (constant and consequently independent of the potential) with which the electron is transferred.

It is worthwhile to highlight that, in quantum mechanics, the linear relationship between current and potential is valid, contrary to that established in electrochemistry by the Butler-Volmer equation, which describes an exponential relationship as follows,

$$i = i_0 \left[exp\left(\alpha \frac{e}{k_B T}\eta\right) - exp\left((1-\alpha)\frac{e}{k_B T}\eta\right)\right] \tag{2.2}$$

where i_0 is the exchange current, and α and η are the usual parameters introduced in chapter 1. In particular, for a diffusionless configuration shown in Fig. 2.1, and for small $\eta \approx 0$ ($\eta = V - {}^{E_F}/_{e}$)[1], close to equilibrium, the Eq. 2.3 for the conductance of a single electron can be obtained as the derivative ${}^{di}/_{dV}$.

$$G = \frac{1}{R_{ct}} = \frac{e i_0}{k_B T} \tag{2.3}$$

Therefore, the conductance in electrochemistry is in function of i_0 and the thermal voltage ${}^{k_B T}/_{e}$. On the other hand, the charge transfer resistance is obtained from the inverse of the same expression as $R_{ct} = {}^{k_B T}/_{e i_0}$ (BARD; FAULKNER, 2000). Note that i_0 is the Faradaic current, the resonant current obtained when the electrochemical reaction is in equilibrium condition, which involves an equilibrium charge dynamics mention by section 1.5. For that reason, the flow of electrons (conductance) in an equilibrium regime given in a electrochemical reaction is essentially quantum mechanical in nature, and is closely related with the ET constant rate through the C_μ as discussed in section 1.5.

In the brief introduction of the quantum rate theory, the general rate constant expression $k = {}^{G}/_{C_\mu}$ was introduced, which gives information about the time-scale of the ET process by noting that $k^{-1} = \tau$. For the quantum rate theory, each redox molecule that constitutes the redox-active monolayer is modelled as a RC quantum point (or electrochemical microstate) as depicted by Fig. 2.1. Thus, at ${}^{E_F}/_{e}$ the electron flux from/to the electrode to/from reduced/oxidized microstates is characterized by a time-scale $\tau = R_q C_\mu$, in which $R_q = {}^{h}/_{2e^2}$ and $C_\mu = {}^{1}/_{c_q} + {}^{1}/_{c_e}$: The first term accounts for the elements that demand extra effort in order to the ET event occurs, such as the molecular bridge (or quantum channel) acting as the scattering region; and the second term, the series combination of two capacitive contribution c_q and C_e, as explained previously. Note that, the total quantum capacitance accounts all the individual quantum channels n, $C_q = c_q N$. Therefore, C_q depends on the number of available n to be occupy and C_e depends on the charge separation length l (i.e., $C_e \propto {}^{1}/_{l}$), which is estimated to be between 0.1 and 0.3 nm. Note that the molecular thickness L, around 1 to 2 nm, defines a length of charge separation related to the non-Faradaic capacitive process, referred here as C_t (see Fig. 2.3*a*). Now, when the length scales are compared, $l << L$, leads to $C_e >> C_q$, and hence $C_q \sim C_\mu$.

As discussed in the derivation of Eq. 1.15, since $C_e >> C_q$ and the degeneracy conditions are established, the spin degeneracy of electron $g_s = 2$ and the degeneracy of a quantum electrochemical channel that provides two possible redox states g_r=2, C_q is the only variable required to determine k owing to $k = 4({}^{e^2}/_{C_q}) = {}^{2G_0}/_{C_q}$ (ALARCÓN; SANTOS; BUENO, 2021), recalling that $2G_0$= 155 μS.

[1] At small η a linear behavior can be observed as Fig. 1.6*a* shows.

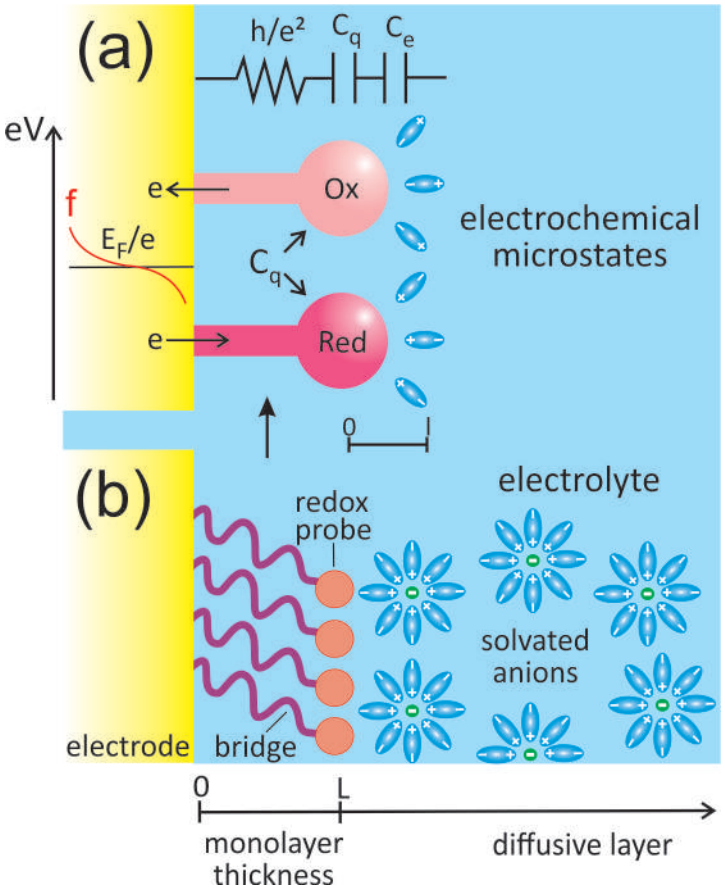

Figure 2.1: (a) Schematic representation of electrochemical microstates, which can be modelled as a RC quantum point, represent the individual redox molecules in the oxidized (Fc^+) and reduced (Fc) states at E_F/e, which constitute the SAM in (b). The occupation (or unoccupation) of capacitive states (c_q), generate two direction electric currents (g_r degeneracy), follows a charge compensation by the electrolyte (c_e), known as the charge screening (PINZÓN *et al.*, 2022). (b) Schematic representation of the redox monolayer tethered upon electrode surface in an electrolyte environment. The redox probe Fc is represented by an orange circles connected to the electrode through a "bridge" (the backbone of the peptide). The applied energy modulated the direction of the electric current. For instance the energy level of the electrode E_F/e is represented in equilibrium with the redox film and the occupation of states is accordingly to the probability function f.

Source: (SÁNCHEZ; SANTOS; BUENO, 2022).

To better understand the correlation between Marcus's and quantum rate theories it must be recalled that in the introduction section (section 1.4) the molecular conductance and ET transfer processes were dependent of the, e.g. of molecular length or of the bridge between `D` and `A` and somehow related. In both electron transport and ET there is a tunneling mechanism operating, which in the case of ET is represented within the κ term, see section 1.2), whereas in molecular electron transport the term that is relevant for account for tunnelling is $T_n(\mu)$ (see section 1.5). The transmission matrix is a general probabilistic matrix that can account for κ and tunnelling process as particular case and, therefore, $T_n(\mu)$ can be stated as $T_n(\mu, L)$ for the particular case of a redox-active monolayer settings, in which $\sum_{n=1}^{N} T_n(\mu) \propto N \exp(-\beta L) = N\kappa$, where $N\kappa$ is the transmission coefficient for the tunneling regime modulated by the number of channels N characterized by a homogeneous length L, which describes the

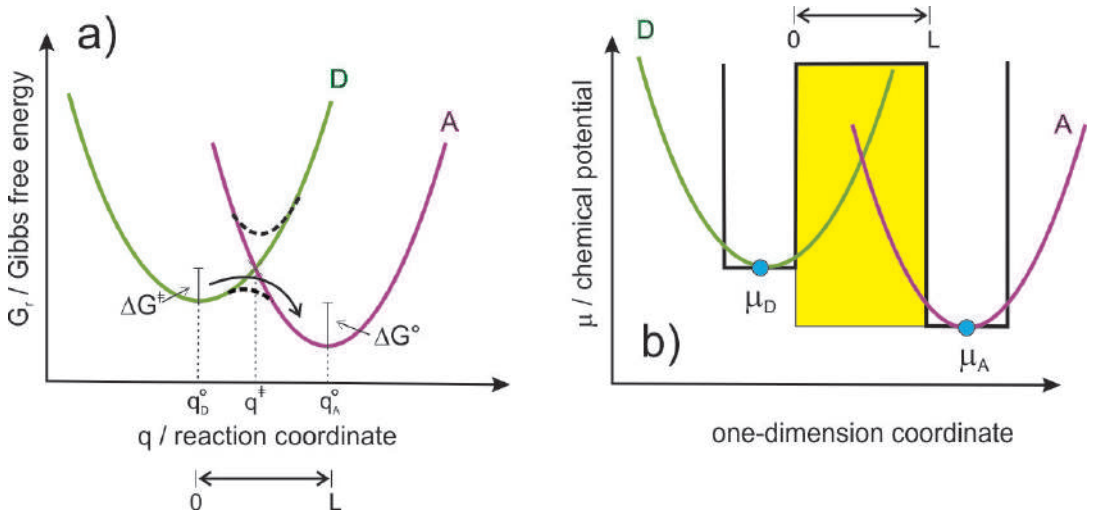

Figure 2.2: (a) PES for adiabatic transition of a homogeneous ET reaction in Marcus theory, explained in section 1.1. (b) Potential wells of the energy levels μ of D and A in overlap with the PES in order to reinterpreted the Marcus theory base on the quantum rate approach. Note that the minimum chemical potential position in both well is different, hence the variation in $d\mu$ leads to electrons flow (the Faradaic current di) through the density of quantum channel states ($^{dn}/_{d\mu}$) between D and A states, traveling along the quantum channel length L, with a velocity ν, which gives rise to the conductance quantum $G = {}^{1}/_{R_{ct}}$. In this way, the meaning of G for the Marcus homogeneous ET approach is given within this theory.

Source: (SÁNCHEZ; SANTOS; BUENO, 2022).

electronic coupling between D and A states in the quantum rate theory (BUENO, 2020).

This above-demonstrated equivalence, between transmission matrix and κ as a particular settings of the transmission matrix for electron tunnelling, establishes a connection between Marcus ET and quantum rate theories, providing a means of introducing the quantum conductance G in the Marcus theory for homogeneous ET reaction, as a remarkable outcome of the quantum rate theory. This is pictured in Fig. 2.2, which shows the PES (previously introduced in section 1.1) and the potential wells, as the analogous element in terms of the quantum rate description of the ET (SÁNCHEZ; SANTOS; BUENO, 2022). Whereas for q in Fig. 2.2*a*, is the length L of the distance separation between D and A, for Fig. 2.2*b* the pathway along with one-dimensional ET occurs is the length of the quantum channel, in which electrons travel from D to A or vice versa. Regarding to the ordinate axis in a quantum rate description, chemical potential is more appropriate for depicting the energy levels of the electrons in the internal structures of D and A. As mentioned in section 1.5, this μ is related to the total internal energy E_i, as $\mu = (^{dE_i}/_{dn})$, where dn is the number of electronic particles exchanged during the ET event, averaged over an ensemble of D and A species, which is equivalent to the number of quantum channels involved in the electrochemical reaction.

Finally, the variations in $\mu = \mu_{\mathrm{D}} - \mu_{\mathrm{A}}$, are due to the exchange of electrons between D and A and are induced by fluctuations of the internal potential of D and A species, such that this difference, for a single ET occurring between D and A, is quantifiable and equivalent to dV. Accordingly, the correlation $d\mu = -edV$ is established, which is used in the derivation of $^{di}/_{dV}$ from Eq. 2.1.

Once the concepts of quantum resistance (or quantum conductance) where introduced and connected with Marcus ET theory in side-by-side with the quantum rate

theory, and since the quantum rate theory incorporates Marcus ET as a particular settings, the meaning of the charge transfer resistance in quantum mechanical terms can be experimentally studied using time-resolved methods, such as impedance spectroscopy. In this chapter it will be studied impedance data of a diffusionless ET reaction and it will be proved that the charge transfer resistance has a quantum mechanical meaning that enhances our comprehension of ET phenomenon.

2.2 Materials and methods

The experimental methodology followed for aiming the main objective of this chapter was the fundamental procedure in the development of the majority of chapters of this Ph.D thesis. Therefore, this section 2.2 will be referenced in the chapters 3-5, in order to avoid repetition and center in describing the methodology of the related chapter.

2.2.1 Chemical reagents

Table 2.1 compiles the reagents and materials used, the enterprise where they were purchased from and their purpose in the development of this thesis. Aqueous solutions were prepared using Milli-Q water (Simplicity®water purification system, Millipore, 18.2 MΩ cm at 25°C).

2.2.2 Peptide synthesis and characterization

Ferrocene-tagged peptide Fc-Glu-Ala-Ala-Cys-Cys-NH_2 was synthetized by solid-phase peptide synthesis using the Fmoc-strategy on Rink amide resin (0.52 mmol g^{-1}), as reported elsewhere (ALARCÓN; SANTOS; BUENO, 2021).

Briefly, the synthesis was performed at 2-fold excess relative to the amino component in the resin, using DIC/HOBt coupling reagents in DMF during 2h. The success of the coupling was monitored by the ninhydrin reaction. Before adding the subsequent AA, Fmoc group was deprotected by 20% PIP/DMF. Afterwards, the Fc redox probe was introduced at the N-terminus (Glu) by reaction with the aid of DMAP and PyBOP in DMF, over 24 h. The peptide cleavage was carried out using TFA/TIS/EDDT/H_2O (94:1:2.5:2.5, v/v) during one and a half hour. After that, the peptide was precipitated with cold ethyl ether anhydrous and separated from soluble non-peptide material by centrifugation. The peptide was extracted in a 1:1 mixture of solvent A (TFA/H_2O, 0.045% v/v) and solvent B (TFA/ACN, 0.036% v/v) and lyophilized.

The obtained product was purified, using high performance liquid chromatography (HPLC) with a semi-preparative reverse phase Phenomenex C18 column (250 × 10 mm, 5 μm particle size, 300 Å). A linear gradient elution employed was from 25 to 55% of solvent B for almost 90 min. The purity of peptide was qualitatively analyzed using an analytical Shimadzu system with a reverse phase column (ZORBAX 300SB-C18, 4.6 × 150 mm, 5 μm particle size, detection at 220 nm), a linear gradient of 5 to 95% of solvent B for 30 min, flow rate of 1 mL min^{-1}. The identity of the peptide was confirmed by ion-trap Mass Spectrometry using a Brucker system in positive ion mode (see Appendix A).

Table 2.1: List of chemical reagents used in chapter 2.

Reagent	Company	Purpose
Alumina suspensions (1 μm, 0.3 μm, and 0.05 μm)	Buehler	Mechanical polishing of gold electrodes
Polishing cloths (MASTERTEX®)	Buehler	
Sodium hydroxide (NaOH)	Sigma-Aldrich	Electrochemical cleaning of gold electrodes
Ethyl alcohol (EtOH)	Sigma-Aldrich	
Sulfuric acid (H_2SO_4)	Qhemis	
N-α-Fmoc-S-trityl-L-cysteine (Fmoc-Cys(Trt)-OH)[a]	AAPPTEC	Amino acids (AA) for peptide synthesis
N-Fmoc-L-alanine (Fmoc-Ala-OH)[a]	AAPPTEC	
N-α-Fmoc-L-glutamic acid β-*tert*-butyl ester (Fmoc-Glu(OtBu)-OH)[a]	AAPPTEC	
Rink amide resin (0.52 mmol g^{-1})	Sigma-Aldrich	Solid phase peptide synthesis
N,N′-Diisopropylcarbodiimide (DIC)	Sigma-Aldrich	AA coupling reagents for the peptide synthesis
Hydroxybenzotriazole (HOBt)	Sigma-Aldrich	
4-Methylpiperidine (PIP)	Sigma-Aldrich	Reagents for Fmoc removal
Dimethylformamide (DMF)	Sigma-Aldrich	
3-Ferrocenylpropionic anhydride	Sigma-Aldrich	Coupling of the ferrocene (Fc) redox probe in the synthesized peptide
4-Dimethylaminopyridine (DMAP)	Fluka Chemika	
Benzotriazole-1-yl-oxy-tris-pyrrolidino-phosphonium hexafluorophosphate (PyBOP)	Fluka Chemika	
Triisopropylsilane (TIS)	Fluka Chemika	Peptide-resin cleavage and resin precipitation
Trifluoroacetic acid (TFA)	Sigma-Aldrich	
2,2′-(ethylenedioxy)diethanethil (EDDT)	Sigma-Aldrich	
Ethyl ether anhydrous	Sigma-Aldrich	
HPLC-grade acetonitrile (ACN)	Sigma-Aldrich	Peptide syntheisis, SAM fabrication and solvent for electrochemical characterization
Tetrabutylammonium perchlorate ($TBAClO_4$)	Sigma-Aldrich	Electrolyte for electrochemical characterization

[a]Fmoc (9-fluo-renylmethyloxycarbonyl)

2.2.3 Equipment and electrodes

Electrochemical measurements were performed using an AUTOLAB potentiostat from METROHM, controlled by NOVA software, equipped with a frequency response analysis (FRA) module. A three-electrode setting was used as electrochemical cell, comprising a platinum mesh as the counter electrode, Ag | AgCl (3M KCl) as the reference electrode, and gold electrode as working electrode from METROHM (diameter of 2 mm, geometric area A_g of 0.03142 cm^2). The supporting electrolyte employed was 20 mM $TBAClO_4$ in ACN/H_2O (1:4, $^v/_v$) .

Working electrode pre-treatment: Gold electrode surfaces were mechanically polished using a MASTERTEX®polishing cloth and aluminium suspensions with decreasing particle sizes (1, 0.3, and 0.05 μm). Sonication in water for 5 min was performed before changing the aluminium suspension particle size to remove adhered particles. Subsequently, the electrodes were electrochemically cleaned performed a CV in 0.5 M NaOH (200 cycles from $-$ 1.5 to $-$ 0.5 V at 100 mV s^{-1}), followed by water rinsing and immersion in ethanol with magnetic stirring for 20 min. After that, the electrodes were electrochemically polished performed a CV in 0.5 M H_2SO_4 (25 cycles from $-$ 0.2 to 1.5 V at 100 mV s^{-1}). From the last cycle of the sulphuric acid cleaning step, the electroactive surface area (A_e = 0.044 $\pm$0.001 cm^2)[2] was calculated by integrating the cathodic peak using the value of 410 $\mu C\ cm^{-2}$ (see Appendix B) (TRASATTI; PETRIL, 1992). In order to achieve well-organized SAM with a reproducible electrochemical response, the quality of the gold surfaces was ensuring by monitoring the surface roughness, which was determined by dividing the A_e by the electrode geometry area, whose value was kept lower than 1.7.

Self-assembled monolayer fabrication: Right after the sulphuric acid cleaning step described above, the electrodes were rinsed with water and dried in a nitrogen environment before immersing in fresh solution of 2 mM of peptide in ACN/H_2O (1:1, $^v/_v$) during 16 h at room temperature (25°C) in order to obtain the redox SAM (SS–Pep–Fc). Afterwards, the modified surfaces were rinsed with 1:1 ACN/H_2O and H_2O according to reference (GARROTE; SANTOS; BUENO, 2020).

2.2.4 Electrochemical measurements

CV was performed aiming to evaluate the monolayer quality and to determine the E_F/e of the redox monolayer, which was measured from 0.0 to 0.7 V (three cycles) at 100 mV s^{-1}. The formal potential of the SAMs was resolved as $E_F/e \sim (V_{ox}+V_{red})/2$, where V_{ox} and V_{red} are the oxidation and reduction potential peaks, respectively, as illustratively shown by Fig. 2.4.

EIS was conducted at two different potentials outside ($V_{out} = 0.1$ V) and inside the electrochemical window ($E_F/e = 0.35$ V) in frequency range of 100 kHz to 0.1 Hz with a peak-to-peak amplitude of 10 mV, for a total of 60 logarithmically arranged frequencies.

[2] A_e was used to normalize electrochemical signals for calculating current densities and capacitances per unit of area

2.2.5 Impedance spectroscopy and capacitive spectra

Capacitive spectra were constructed using a complex capacitive function $C^*(\omega) = {}^1/_{j\omega Z^*(\omega)}$ obtained from the EIS raw data $Z^*(\omega)$, where j is the complex number $\mathbf{j} = \sqrt{-1}$ and ω is the angular frequency $\omega = 2\pi f$; and f is the linear frequency (BUENO, 2018; BUENO; BENITES; DAVIS, 2016; BUENO; MIZZON; DAVIS, 2012). The capacitive complex function allows us to obtain capacitive spectra using the following relationship $C^*(\omega) = C' + jC''$, where C' and C' are the real and the imaginary capacitive components, respectively; which are calculated using the mathematical equations $C' = \phi Z''$ and $C'' = \phi Z'$, where Z' and Z'' are the real and imaginary impedance components, respectively; and $\phi = {}^1/_{(\omega|Z|^2)}$, where $|Z|$ is the modulus of the impedance.

2.2.6 Equivalent circuit analysis

Equivalent circuit analysis was performed in order to access to the values of the circuital elements, which was achieved by fitting EIS or capacitive spectra to appropriate equivalent circuit model of the interface (see Fig. 2.3*a*), which is comprised by two branches, namely, the non-Faradaic and Faradaic (GOES *et al.*, 2012; LEHR *et al.*, 2017). Table 2.2 compiles the description of the circuit elements, their graphical determination, how they are related and involved in relaxation process. The values of equivalent circuit elements obtained from the fitting were reported as a mean value $\bar{x}$ with the standard error of the mean ($\bar{x} \pm \sigma_{\bar{x}}$) calculated for at least three independently fabricated interfaces.

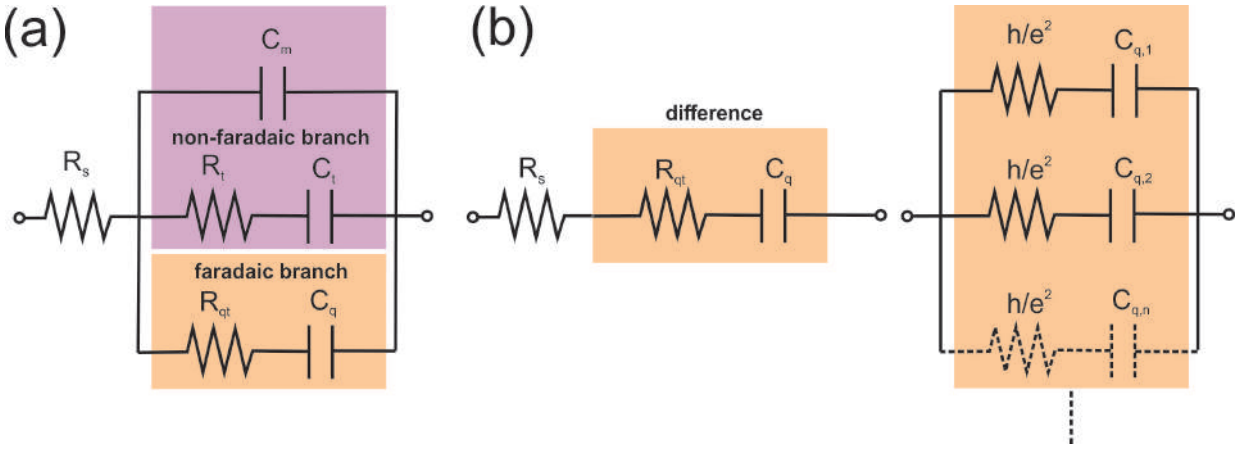

Figure 2.3: (a) Entire equivalent circuit for a diffusionless interfacial electrochemical process in which there are two types of phenomena: the non- Faradaic and the Faradaic. The elements of the circuit involved with colored boxes are defined in table 2.2. The value R_s refers to the series resistance that encompasses the resistance of both the contact and the electrolyte. (b) At the Fermi level, the dominant process is the Faradaic response in which the equivalent circuit is composed of the series of resistances R_s and R_{qt} and of the capacitance C_q. (c) The experimental electrochemical response of the interface is an average value, as indicated in the equivalent circuits shown in (a) and (b). The quantum RC model of the interface predicts that this average value constitutes a parallel series of the individual quantum resistor ${}^h/_{2e^2}$ and capacitor c_q, in which their combination constitutes the quantum thermodynamics microstate of the interface.

Source: (SÁNCHEZ; SANTOS; BUENO, 2022).

Table 2.2: Description of the elements obtaining by equivalent circuit fitting depicted in Fig. 2.3*a*.

	Element	Description	Graphical determination	Associated time-scale τ
non-Faradaic	C_m monolayer capacitance	Capacitance of the monolayer constituted from a combination of the double layer C_{dl} and that of the film bulk C_b.	Real capacitive value at high frequency in the Nyquist capacitive plot.	
	C_t capacitance	Charge separation due to the ions inside the bulk of the film.	Semi-circle diameter of the Nyquist capacitive plot.	$\tau_t = R_t C_t$
	R_t resistance	Resistance associated to the ion relaxation process inside the bulk of the film.	Not possible	
Faradaic	C_q quantum capacitance	Charge storage due to the electron occupancy.	Semi-circle diameter of the Nyquist capacitive plot.	$\tau = R_{qt} C_q$
	R_{qt} quantum resistance	Resistance of each quantum channel that comprises the monolayer.	Not possible.	

Source: (GOES et al.*, 2012; LEHR* et al.*, 2017).*

2.3 Results and discussion

The study of the capacitive phenomena of redox molecular interfaces has been a main interest issue in our research group (BUENO; FABREGAT-SANTIAGO; DAVIS, 2013; BUENO; DAVIS, 2014; PICCOLI, J. P. *et al.*, 2016), which has not been limited for organic molecules but also for semi-conductor films (PINZON; SANTOS; BUENO, 2021) and graphene (LOPES; SANTOS; BUENO, 2021). Through capacitive spectra analysis, the distinction between the Faradaic from non-Faradaic response has allowed to demonstrate that the dominant contribution in the capacitive activity is quantum in nature (GOES *et al.*, 2012; LEHR *et al.*, 2017). Recently, a previous work was concerned in access to the ET rate constant between immobilized redox probe and electrode by means of the quantum rate expression aforementioned (ALARCÓN; SANTOS; BUENO, 2021), demonstrating that this approach is valid to calculate the constant, which was in agreement with the typical procedures, such as Laviron's. In this context, the first chapter of this Ph.D thesis, will demonstrate that the quantum mechanical rate principle is also suitable for the understanding of other properties such as the resistance and conductance, focusing the spotlight on the charge transfer resistance interpretation of diffusionless electrochemical reaction, which was published in (SÁNCHEZ; SANTOS; BUENO, 2022).

Monolayers fabricated by redox peptide self-assembled on gold electrodes form stable redox interfaces characterized by reversible electrochemical process, whose current-voltage curve, shown by Fig. 2.4*a*, depicts two well defined peaks related to oxidation/reduction process of the Fc from the the SS–Pep–Fc, with $\Delta V_p = V_{ox} -$

$V_{red} \approx 20$ mV, $i_{ox}/i_{red} \approx 1$ and $E_F/e \approx 0.35$ V. The current peak reports on the Faradaic current, which is defined by the derivative of the charge q with respect to time t as $dq/dt = C_q(dV/dt) = C_q s = i$ (ALARCÓN; SANTOS; BUENO, 2021), which allows us to calculate C_q directly from this relationship and to obtain it from analogous capacitive-voltage curve as shown by Fig. 2.4*b*. Accordingly, cathodic $C_{q,c}$ and anodic $C_{q,a}$ values at ~ 0.35 V can be used in the calculation of k by using the Eq. 1.15 (i.e., $k = 4e^2/hC_q$, where $4e^2/h \sim 155$ μS). Hence, for a average value of the anodic and cathodic capacitive contributions is ~ 8 μF, the estimated k is ~ 19 s^{-1}, which within experimental error, is equivalent to that obtained by impedance methodology as will be demonstrated further (see Table 2.4).

Notwithstanding the simple way in obtaining C_q from $C_q = i/s$, EIS is required not only to reveal circuit element contributions separately in the interface, but also to support in the interpretation of the quantum rate. Therefore, once the E_F/e was estimated, ECS was performed with two different potentials: V_{out}= 0.1 V and $E_F/e \sim$ 0.35 V. For simplicity, these potentials will be referred to as non-Faradaic and Faradaic responses of the redox molecular film, respectively.

The impedance data recorded at those potentials are characterized mainly for the elements described by table 2.2, which are frequency (or time) dependent and defines relaxation process, such as ion relaxation (τ_t) inside the bulk of the monolayer and electronic relaxation (τ) due to redox process. This phenomenon can be better

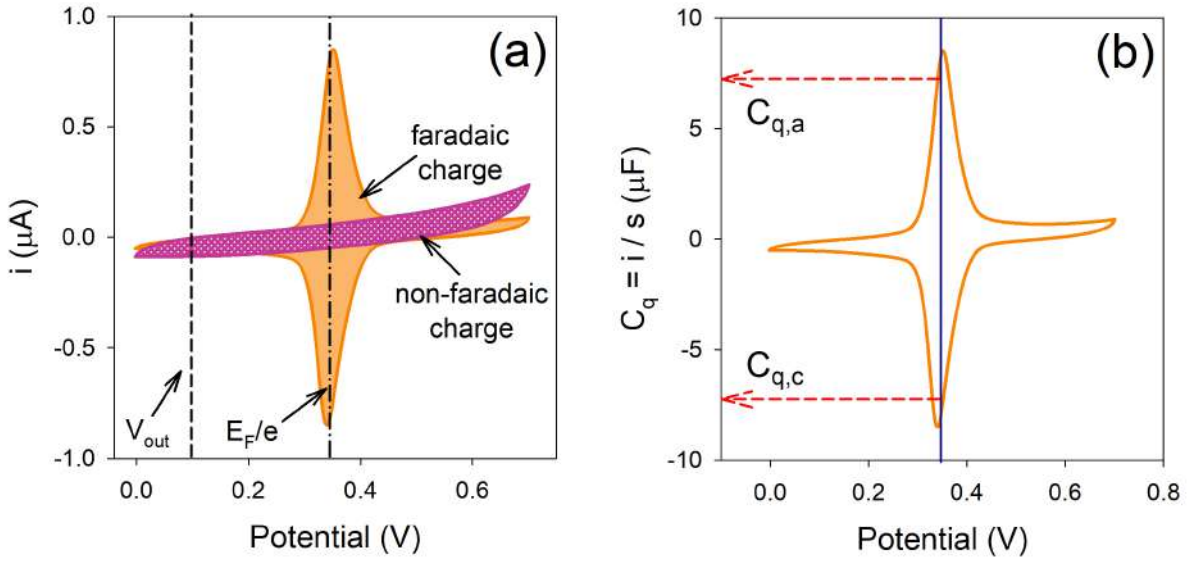

Figure 2.4: (a) Cyclic voltammogram of SS–Pep–Fc performed in 20 mM $TBAClO_4$ in ACN/H_2O (1:4, v/v) using Ag | AgCl (3 M KCl) as the reference electrode. Relevant information for analyzing the electrochemical response is indicated, such as the E_F/e and V_{out} values. The orange peaks correspond to the amount of Faradaic charge attributed to the redox process, which is dominant over the non-Faradaic charge depicted by the hatched area (i.e., interfacial charge separation characterized by C_m and C_t, see table 2.2). (b) Capacitive plot obtained by the normalization of the electric current i by the scan rate s, providing two possible values of $C_{q,a}$ and $C_{q,c}$, which are utilized to calculate the value of k as predicted by using the quantum rate methodology (ALARCÓN; SANTOS; BUENO, 2021).

Source: (SÁNCHEZ; SANTOS; BUENO, 2022).

understood by analysing the complex capacitive function that describes it. For instance, for non-Faradaic (nf_a) relaxation can be described by the Cole-Cole equation[3] (see Eq. 2.4), which relates the non-Faradaic capacitive processes in function of angular frequency ω that results in the capacitive complex diagram shown by the inset in Fig. 2.5*b*.

$$C^*_{nf_a}(\omega) = C_m + \frac{C_t}{1 + (j\omega\tau_t)^{(1-\alpha_t)}} \tag{2.4}$$

where α_t accounts for a deviation of an idealized Debye dielectric type of relaxation ($0 \leq \alpha_t < 1$). This phenomena is the responsible for the non-Faradaic capacitive response of non-electroactive monolayers embedded in electrolytes, as discussed in more detail elsewhere (GOES *et al.*, 2012; LEHR *et al.*, 2017).

On the other hand, the electronic relaxation quantified by $\tau = R_q C_q$, which determines the ET constant rate $k = \tau^{-1}$, is associated with the Faradaic response (f_a) as described by the complex capacitive function analogous to $C^*_{nf_a}(\omega)$,

$$C^*_{f_a}(\omega) = C_t + \frac{C_q}{1 + (j\omega\tau)^{(1-\alpha_q)}} \tag{2.5}$$

where α_q accounts for a deviation of an idealized relaxation and is sensible to the dispersion of the redox DOS function attributed to the solvent environments (BUENO; FABREGAT-SANTIAGO; DAVIS, 2013; BUENO; DAVIS, 2014). Currently, the correlation of the electrolyte environment effect on the DOS distribution is matter of study in our research group. Hence, the analysis of this parameter does not compromise the aim of this chapter due to the analysis is intended to approach other phenomenon.

In this way, the Eqs. 2.4 and 2.5 describe the capacitive response in function of frequency (i.e., $\omega = 2\pi f$), which are depicted by the semi-circles in Fig. 2.5*b* that provides relevant information when compared to the traditional EIS Nyquist spectra shown by Fig. 2.5*a*. For instance, the experimental value of C_t can be graphically estimated by noting the value of the inset Nyquist semicircle capacitive plot diameter obtained at V_{out} (black dots), which corresponds to an estimated value of $\sim 6\ \mu\text{F cm}^{-2}$. This value of C_t corresponds to only 3% of the value of C_q of $\sim 200\ \mu\text{F cm}^{-2}$, which is also estimated from the diameter of the semicircle obtained at E_f/e (blue triangles).

As was demonstrated, C_q does dominate the capacitive response over C_t, which along with C_m posses dielectric capacitive character, hence these are a type of electrostatic capacitances referred to as C_e in Eq. 1.14 (i.e., $C_m < C_t$ and $C_t << C_q$). This demonstration is the basis of the theoretical origin for the empirical pseudocapacitance terminology (BUENO, 2019), a capacitance which is known to be related to the Faradaic response and Faradaic currents occurring in electrochemical interfaces but that had not had, up to recent years (BUENO, 2019), a theoretical explanation for the phenomenon.

The dominance of the quantum capacitive at E_F/e allows us to make approximations, such as the spectral subtraction of the non-Faradaic relaxation from the Faradaic, which results in the plot shown by the green square dots in Fig. 2.5*b*, which clearly demonstrates that the non-Faradaic relaxation is negligible compared to the Faradaic for EIS spectra obtained at the E_F/e. This result was in agreement with the

[3]This equation is typically used to describe dielectric relaxation processes (JONSCHER, 1999).

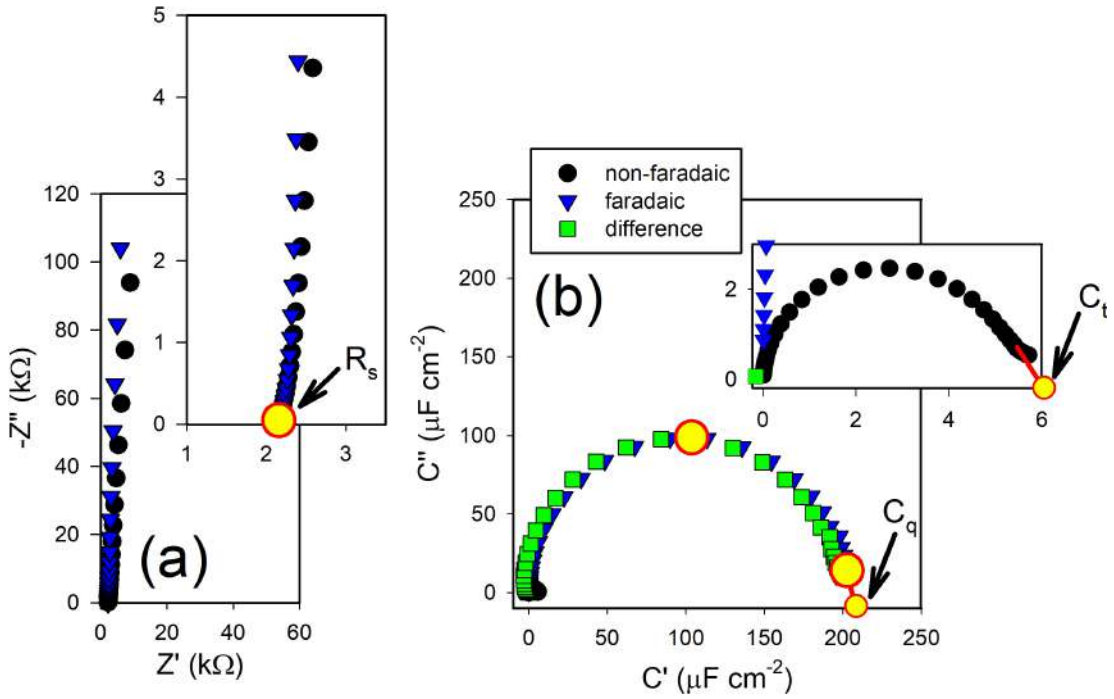

Figure 2.5: (a) Complex impedance diagram obtained for the SS–Pep–Fc at V_{out} and E_f/e potentials that are referred to as non-Faradaic and Faradaic responses, respectively. (b) Complex capacitance diagram of (a). The square green dot curve corresponds to the spectral subtraction of the non-Faradaic from the Faradaic response, demonstrating that the Faradaic response is dominant over the non-Faradaic.

Source: (SÁNCHEZ; SANTOS; BUENO, 2022).

differences between Faradaic and non-Faradaic charges observed in Fig. 2.4*a*. Consequently, Eqs. 2.4 and 2.5 can be approximated to the following expression (BUENO, 2018)

$$C^*(\omega) = \frac{C_q}{1 + (j\omega\tau)^{(1-\alpha_q)}} \sim C_q[1 - (j\omega\tau)^{(1-\alpha_q)}] + O(\omega^2) \tag{2.6}$$

where the second term is a mathematical expansion of the frequency dependent response of a quantum point contact modeling the interface, in where $O(\omega^2)$ accounts for a second-order term (BUENO, 2018), confirming that the simplification of the interface response from Eq. 2.5 to Eq. 2.6, is equivalent to considering each molecule at the interface as a quantum capacitive point contact. Eq. 2.6 can be used to model the response of the interface and has previously been used to develop highly sensitive biosensing devices (BUENO; FERNANDES; DAVIS, 2017) additionally, it also explains the conductive and capacitive behavior of single layer graphene (LOPES; SANTOS; BUENO, 2021).

As a result, following Eq. 2.6, the equivalent circuit of Fig. 2.3*a* simplifies to that shown in Fig. 2.3*b*, which is a quantum RC equivalent circuit composed solely of a series of two resistive components; R_s and R_{qt} settled in series with the quantum capacitance C_q. The meaning of R_s and R_{qt} in the context of quantum resistance $R_q = {}^1/_G$ will demonstrate to us that R_{ct}, as interpreted in the traditional equivalent circuit analysis of electrochemical interfaces, must be revisited. This will be done after the

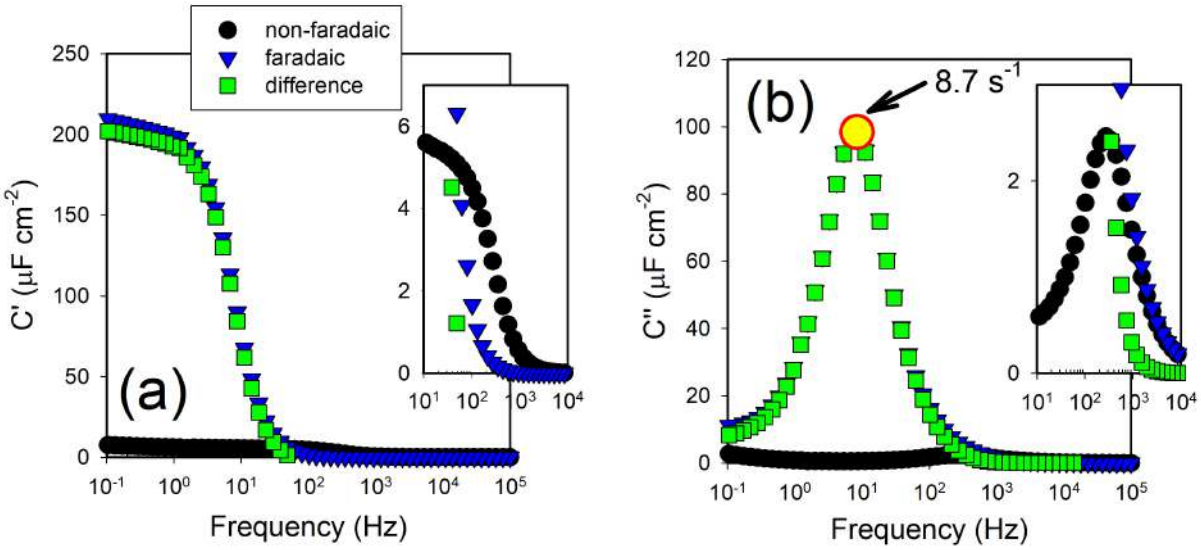

Figure 2.6: Bode capacitive diagrams from ECS data. (a) The real component (C') of the complex capacitance as a function of frequency. (b) The imaginary component (C'') of the complex capacitance as a function of frequency. It is evident that the non-Faradaic response is negligible compared to the Faradaic response.

Source: (SÁNCHEZ; SANTOS; BUENO, 2022).

corroboration of the quantum interpretation of k by ECS analysis.

As discussed at the beginning of section 2.1, k can be calculated if the value of C_q is known. Hence, by simple division of 155 μS by 8.6 μF (graphically determined) for an A_e of ~ 0.044 cm^2, gives an estimated k value of ~ 18 s^{-1} (for three different electrodes, this value is, on average, 18 ± 2 s^{-1} as indicated in Table 2.3), which is in good agreement with the CV analysis (see Fig. 2.4*b*) where the value of k was estimated as ~ 19 s^{-1} and is compiled in Table 2.3.

A different approach for k determination can be realized recalling the electronic relaxation phenomenon, in particular, by means of the relaxation frequency f_r of the ET transfer process. Since $k = \tau^{-1} = {}^{2G_0}/_{C_q}$, half of this value leads to $f_r = {}^{G_0}/_{C_q}$. The value of f_r can be obtained directly from the imaginary capacitive Bode diagram, corresponding to the plot of C'' *versus* frequency as shown in Fig. 2.6*b*, in where the peak maximum corresponds to f_r, which has a value of 8.7 s^{-1}. Twice this value provides an estimated k of ~ 17.2 s^{-1}, which is in good agreement with that estimated from the CV and from ECS (see Table 2.3).

Table 2.3: Values of k obtained by CV and ECS methods.

Method	k/s^{-1}
CV	19 ± 2
ECS graphic	18 ± 2
ECS fitting	16 ± 3

Source: (SÁNCHEZ; SANTOS; BUENO, 2022).

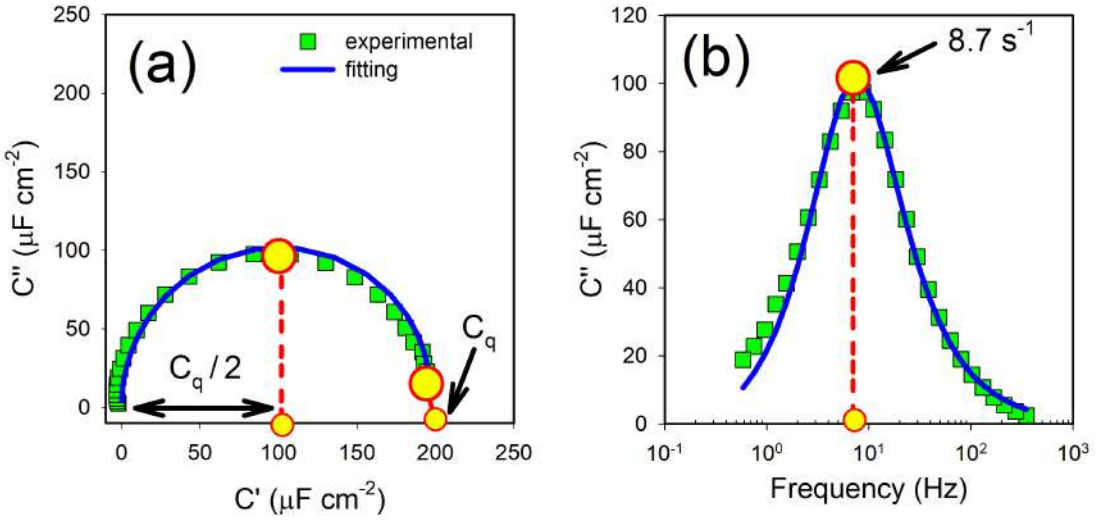

Figure 2.7: (a) Nyquist capacitive diagram and the fitting (blue curve) to the equivalent circuit of Fig. 2.3. (b) Bode diagram of (a). The value of 8.7 s^{-1} corresponds to a characteristic frequency $f_c = k/2$ that disregards g_r in the interpretation of k.
Source: (SÁNCHEZ; SANTOS; BUENO, 2022).

This alternative method is accurate thanks to the interpretation of g_r in the quantum rate expression, which is related to the number of electrochemical states, i.e., oxidized and reduced states, or the two directions of the electric current in this electrochemical interface (see Fig.2.1*a*). This is also reinforced by another reasoning concerning with the angular frequency mode with which the EIS is performed, which can be converted from the mathematical definition $hf = \hbar\omega$, where $\hbar = h/2\pi$. Hence, working with the angular form of the f_r of the ET process, ω_r can be rewritten as $\omega_r = 2G_0/C_q = 2e^2/\hbar C_q$, where g_r is, *a priori*, disregarded. Similarly with f_r, ω_r is obtained at the maximum of the Nyquist capacitive diagram as shown (with a yellow dot) in Fig. 2.7*a*. At this maximum, there is a maximum of C'' that corresponds to a conductance of $G_0 = \omega_r C'' = 2e^2/h$. Moreover, this maximum C'' is the equivalent to the half of the C_q, leading to $G_0 = \omega_r = C_q/2 = 2e^2/\hbar$; and rewritten the expression and recalling that $G_0 = 2e^2/\hbar$, one obtains $\omega_r = 4e^2/\hbar C_q$, meaning that $2G_0$ corresponds to $\omega_r = 2\omega_c$. The angular resonance frequency ω_r should be equal to the characteristic frequency ω_c, and twice the difference between each of these frequencies is the required presumption related to assuming a value of 2 for the electrochemical number g_r, in which the conductance of G_0, at resonance, must be $g_r G_0$ with a $g_r = 2$ instead of only G_0. A different analysis of the ET process led us to the same conclusion regarding g_r, which confirmed the correctness of the interpretation of the quantum rate in this type of electrochemical setting, where a g_r degeneracy of 2 is evidenced.

So far, we have described the experimental application of the quantum rate theory for obtaining k, whether by means of CV or ECS (graphically or circuit analysis), as well as the circuit parameters summarized in Table 2.4. Now, we are going to close this chapter with the interpretation of the meaning of R_{ct} within this theory by considering as a starting point the definition of G as result of the correlation of tunneling

Table 2.4: Circuit parameters and k values of SAM-Fc.

Parameter	$\bar{x} \pm \sigma_{\bar{x}}$
$R_t(k\Omega)$	0.7 ± 0.3
C_m (μF cm^{-2})	2.6 ± 0.3
C_t (μF cm^{-2})	5 ± 1
$R_s(\Omega)$	$2{,}040 \pm 50$
C_q (μF cm^{-2})	230 ± 10
R_{qt} (Ω)	59 ± 1
$r_q(\Omega)$	$13{,}100 \pm 400$
k (s^{-1})	16 ± 3

Source: (SÁNCHEZ; SANTOS; BUENO, 2022).

mechanism in electron transfer and transport processes as described in the introduction 2.1, i.e, $G = \kappa G_0 N$. In particular for N, can be experimentally estimated from the C_q thermalized function (Eq. 1.12) at E_F/e where $f = 1/2$; hence, $N = (4k_BTC_q)/e^2$. For a C_q of 230 μF cm^{-2} as the mean value obtained from the fitting of data from three different and independent electrodes to the equivalent circuit model depicted in Fig. 2.3*a*, one can calculate N as 6.3×10^{12}. Note that, similar to $C_q = Nc_q$, in where the value 230 μF cm^{-2} is a total contribution of each c_q of the microstates that conform the molecular ensemble N, thus, $G = \kappa G_0 N$ is the total conductance, which can be associated to R_{qt}, i.e., $G = 1/R_{qt}$, the quantum resistance of the whole ensemble equal to 59 Ω (Table 2.4), which corresponds to $\sim$ 16.9 mS. Hence, knowing the values of G and N, β can be estimated from $G = G_0 \exp(-\beta L)N$, where L is required to be known. Therefore, a value of $L \sim 1.8$ nm, estimated from ellipsometry for a redox monolayer fabricated with a similar peptide structure (PICCOLI, J. *et al.*, 2018), Fc-Glu-Ala-Ala-Ala-Cys-NH_2, was used in this calculation. Thus, for SS–Pep–Fc, $\beta \sim 1.34$ Å^{-1}, which is in agreement with those obtained from the literature for non-adiabatic ET reactions ($\sim$1.3 Å^{-1})(FINKLEA; HANSHEW, 1992).

It is important to highlight that the demonstration of the tunneling regime as an electron transfer and transport mechanism in this system by means of the calculation of β using a thickness value of a monolayer different of that studied here, is still valid by observing the following. If one does the backwards calculation, starting form β values reported in the literature for peptide structures, which varies from 1 to 1.4 Å^{-1}, one estimates values of L between 2.41 and 1.72 nm, respectively. Meaning that, in spite of the difference of one unit of AA, for the L used the obtained β is within the expected range for peptide structures. One can conclude that this method can be used to evaluate the electron tunneling in different structures and conditions, for instance.

Having demonstrated the reciprocity between R_{qt} with G, in where the tunneling mechanism operates, we can move towards the final discussion to the interpretation of R_{ct} within the quantum rate model. From the frequency analysis in terms of the angular form above discussed, one can express k in radians as $k = 2\omega_c = g_r\omega_c$, which allows us to interpret the term $\omega\tau$ in Eq. 2.6, for which there is a certain external

perturbation ω that will be in resonance with ω_c, which we identifies as ω_r. At the resonance condition, $C^*(\omega_r) = C_q$, therefore the term $\omega_r\tau$ must be equal to the unity, thus one can express $f_r = {}^1/_{(2\pi\tau)}$, which leads to the following expression,

$$\frac{k}{2} = \frac{1}{2\pi\tau} = \frac{1}{2\pi(R_qC_q)} = f_c \tag{2.7}$$

and from Fig. 2.7*b*, it is known that f_c = 8.7 s^{-1}. So, the question is, which are the values of R_q and C_q that leads to $\sim$ 8.7 s^{-1}? From the equivalent circuit analysis, we get a value corresponding to C_q, R_{qt} and R_s[4]; and it is $R_s + R_{qt} = R_q$, along with C_q, that leads to $f_c \sim 8$ s^{-1}. Therefore, one can conclude that R_q establishes a quantized limit of the minimal resistance (or of the maximum of conductance G_0), whose value is $\sim$ 12.9 kΩ (or $R_q = {}^1/_{2G_0}$), meaning that g_r is associated with the redox states of the electrochemical reaction and not to the pure physical meaning of $G_0 = {}^{2e^2}/_h \sim 77.5$ μS. Furthermore, a possible separation of those resistance in Fig. 2.3*b* is only fictitious due to the minimum physical value possible for the resistance of a single electron, within a quantum mechanical interpretation, is established as the sum of both contribution, which is equivalent, as we demonstrated theoretically, to what has been referred to in electrochemical textbooks as charge transfer resistance, R_{ct} (BARD; FAULKNER, 2000).

It is worthwhile to note that in f_c, $G = {}^1/_{(R_s+R_{qt})}$ and ${}^G/_{C_q} = {}^{(G/N)}/_{c_q}$; in accordance with the quantum rate model, the experimentally measured k value incorporates $\kappa \sim \exp(-\beta L)$ and, as expected, decays exponentially as a function of distance. This observation of the minimal/maximum resistance/conductance in the ET rate processes is interpreted within the physical meaning of the quantum resistance/conductance that establishes that there is a minimal/maximum limit of resistance/conductance for the transfer of a single electron between two states. Undoubtedly, the obtained experimental quantum resistance value of $\sim$13 kΩ (see Table 2.4), within experimental error (3.1%), matched the theoretical value of $\sim$12.9 kΩ.

In this way, it is demonstrated that in the Faradaic response governing the ET process at ${}^{E_F}/_e$, ET kinetics depends on R_s, encompassing resistances not only that of solution but also the resistance of the cable, ohmic contact and that related to the chemical attachment of the molecule to the electrode. This R_s must be maintained as an important series term to the capacitance during the ECS analysis of the interface, if a quantum mechanical interpretation of the ET is meant. Therefore, R_s, generally interpreted as the resistance of solution or electrolyte, is a main part of the resistance/ conductance of the system and cannot be disregarded in the analysis of the Faradaic component of the ET process, nor in the equivalent circuit analysis, as usually done (Fig 1.6*c*) (BARD; FAULKNER, 2000). In addition to revisit the meaning of R_s, the role of R_{qt} was revisited as well, which has been considered as part of a parasitic response or disregarded only as a solution resistance (CREAGER; WOOSTER, 1998; BUENO; FABREGAT-SANTIAGO; DAVIS, 2013), showing its importance in the interpretation of the ET, in spite of be only about 3% of R_s.

[4]Also graphically obtained in the high frequency region of the impedance diagram, as depicted in Fig. 2.5*a*

2.4 Conclusion

The quantum rate model allows an accurate interpretation of ET process occurring at mesoscopic interfaces, such as redox monolayer onto electrode surface, whose ET kinetics is defined as G/C_q ratio, in which the states of degeneracy must be established. It was possible not only to demonstrate that, as a ET theory, it encompasses the Marcus ET model, but also to clearly prove that the associate resistance to G, R_q is quantized. Furthermore, it was elucidated that the R_q modulates the ET kinetics and involves two resistive terms, in series, the relaxation resistance R_{qt} and the solution and contact R_s series resistance, which cannot be separated. Hence, the meaning conferred to R_q within the quantum rate model lead us to revisit the interpretation of R_{ct}, which turned on pointing out that R_q is equivalent to R_{ct}, despite this conflicts with its traditional interpretation in the equivalent circuit analyses. Finally but not least, it was described an straightforward method to calculate k of an heterogeneous electrochemical reaction, in which the determination of C_q, as the only variable, can be obtained from CV plot, or by ECS data, whether graphically from the Nyquist or bode capacitive plots or by fitting to the equivalent circuit.

Such findings confirm that the Landauer formalism in molecular electronics is a common property that, within a suitable quantum mechanical interpretation of the electron dynamics, have a common foundation in quantum mechanics. This work indicates that controlling the properties of electrochemical interfaces at the nanometer molecular scale will enable the development of novel and advanced electrochemical quantum devices.

References

ALARCÓN, E. V. G.; SANTOS, A.; BUENO, P. R. Perspective on Quantum Electrochemistry. A Simple Method for Measuring the Electron Transfer Rate Constant. **Electrochimica Acta**, v. 398, p. 139219, 2021. DOI: 10.1016/j.electacta.2021.139219.

BARD, A. J.; FAULKNER, L. R. **Electrochemical Methods Fundamentals and applications**. 2nd: John Wiley and Sons, 2000.

BUENO, P. R. Nanoscale origins of super-capacitance phenomena. **Journal of Power Sources**, Elsevier, v. 414, p. 420–434, 2019.

BUENO, P. R.; DAVIS, J. J. Charge transport and energy storage at the molecular scale: from nanoelectronics to electrochemical sensing. **Chemical Society Reviews**, Royal Society of Chemistry, v. 49, n. 21, p. 7505–7515, 2020.

BUENO, P. R.; FERNANDES, F. C.; DAVIS, J. J. Quantum capacitance as a reagentless molecular sensing element. **Nanoscale**, Royal Society of Chemistry, v. 9, n. 40, p. 15362–15370, 2017.

BUENO, P. R.; MIZZON, G.; DAVIS, J. J. Capacitance spectroscopy: A versatile approach to resolving the redox density of states and kinetics in redox-active self-assembled monolayers. **The Journal of Physical Chemistry B**, ACS Publications, v. 116, n. 30, p. 8822–8829, 2012.

BUENO, P. R. Electron transfer and conductance quantum. **Physical Chemistry Chemical Physics**, Royal Society of Chemistry, v. 22, n. 45, p. 26109–26112, 2020.

BUENO, P. R. **The Nanoscale Electrochemistry of Molecular Contacts**. Springer, 2018. (SpringerBriefs in Applied Sciences and Technology). ISBN 978-3-319-90486-3. DOI: 10.1007/978-3-319-90487-0.

BUENO, P. R.; BENITES, T. A.; DAVIS, J. J. The Mesoscopic Electrochemistry of Molecular Junctions. **Scientific Reports**, v. 6, p. 18400, 2016. DOI: 10.1038/srep18400.

BUENO, P. R.; DAVIS, J. J. Measuring Quantum Capacitance in Energetically Addressable Molecular Layers. **Analytical Chemistry**, v. 86, n. 3, p. 1337–1341, 2014. ISSN 0003-2700. DOI: 10.1021/ac403135b.

BUENO, P. R.; FABREGAT-SANTIAGO, F.; DAVIS, J. J. Elucidating capacitance and resistance terms in confined electroactive molecular layers. **Analytical chemistry**, ACS Publications, v. 85, n. 1, p. 411–417, 2013.

CREAGER, S. E.; WOOSTER, T. T. A new way of using ac voltammetry to study redox kinetics in electroactive monolayers. **Analytical chemistry**, ACS Publications, v. 70, n. 20, p. 4257–4263, 1998.

DATTA, S. **Electronic transport in mesoscopic systems**. Cambridge university press, 1997.

FINKLEA, H. O.; HANSHEW, D. D. Electron-transfer kinetics in organized thiol monolayers with attached pentaammine (pyridine) ruthenium redox centers. **Journal of the American Chemical Society**, ACS Publications, v. 114, n. 9, p. 3173–3181, 1992.

GARROTE, B. L.; SANTOS, A.; BUENO, P. R. Label-free capacitive assaying of biomarkers for molecular diagnostics. **Nature Protocols**, 2020. ISSN 1754-2189. DOI: 10.1038/s41596-020-0390-9.

GOES, M. S. *et al.* A Dielectric Model of Self-Assembled Monolayer Interfaces by Capacitive Spectroscopy. **Langmuir**, v. 28, n. 25, p. 9689–9699, 2012. ISSN 0743-7463. DOI: 10.1021/la301281y.

JONSCHER, A. K. Dielectric relaxation in solids. **Journal of Physics D: Applied Physics**, IOP Publishing, v. 32, n. 14, r57, 1999.

KITTEL, C. **Introduction to solid state physics**. John Wiley & Sons, 2004.

LEHR, J. *et al.* Mapping the ionic fingerprints of molecular monolayers. **Physical Chemistry Chemical Physics**, v. 19, n. 23, p. 15098–15109, 2017. ISSN 1463-9076. DOI: 10.1039/c7cp01500c.

LOPES, L. C.; SANTOS, A.; BUENO, P. R. Measuring quantum conductance and capacitance of graphene using impedance-derived capacitance spectroscopy. **Carbon**, Elsevier, v. 184, p. 821–827, 2021.

PICCOLI, J. *et al.* Redox Capacitive Assaying of C-Reactive Protein at a Peptide Supported Aptamer Interface. **Analytical Chemistry**, v. 90, n. 5, p. 3005–3008, 2018. ISSN 0003-2700. DOI: 10.1021/acs.analchem.7b05374.

PICCOLI, J. P. *et al.* The self-assembly of redox active peptides: Synthesis and electrochemical capacitive behavior. **Peptide Science**, Wiley Online Library, v. 106, n. 3, p. 357–367, 2016.

PINZON, E. F.; SANTOS, A.; BUENO, P. R. Density of States of a Nanoscale Semiconductor Interface as a Transduction Signal for Sensing Molecules. **ACS Applied Electronic Materials**, ACS Publications, v. 3, n. 8, p. 3411–3417, 2021.

PINZÓN, E. F. *et al.* Quantum Rate Dynamics and Charge Screening at the Nanoscale Level. **Physical Chemistry Chemical Physics**, Royal Society of Chemistry, v. 24, n. 26, p. 16200–16206, 2022.

SÁNCHEZ, Y. P.; SANTOS, A.; BUENO, P. R. Quantum Mechanical Meaning of the Charge Transfer Resistance. **Journal of Physical Chemistry C**, v. 126, p. 3151–3162, 6 2022. DOI: 10.1021/acs.jpcc.1c07801.

TRASATTI, S.; PETRIL, O. A. Real surface-area measurements in electrochemistry. **Electrochimica Acta**, v. 328, n. 1-2, p. 353–376, 1992. ISSN 0013-4686. DOI: 10.1016/0022-0728(92)80162-W.

Chapter 3

Quantum Capacitive Mediation of the Electron Transfer Process

For heterogeneous ET transfer occurring between free redox species and a metallic electrode the kinetics is controlled by mass transport phenomenon. On the other hand, if redox species are covalently attached to a metallic electrode, the ET reaction follows a diffusionless kinetics. These different charge-transfer kinetic mechanisms can be studied through the relationship between j and s obtained in cyclic voltammetry experiments. For instance, if j is linear with the square root of the scan rate s, i.e. $j \propto s^{1/2}$, according with Randles-Sevcik's equation, there is a diffusional kinetic control (BARD; FAULKNER, 2000), whereas if a linear behavior between j and s is obtained, i.e. $j \propto s$, the kinetics is not longer controlled by diffusion and is said to follow diffusionless mechanism, which can be studied by following the formalism developed by Laviron (LAVIRON, 1979).

It was demonstrated that the ET kinetics in a diffusionless setting can be modelled by the quantum rate theory. This is particularly studied for redox-active species assembled over metallic electrodes and the quantum rate theory complies with Laviron's approach. In the case of the presence of a redox species in solution in contact with a redox monolayer, the electron transport from the redox species in solution to the electrode occurs via the quantum capacitive redox states of the interface within a quantum efficiency that obeys quantum transport and without diffusional control. This chapter aims to discuss how the quantum electron transport occurs through the quantum capacitive states of the interface. The ET kinetics is studied in the presence of a redox self-assembled monolayers intermediating the redox kinetics with the free redox species in solution. This is a fundamental study that was strategically selected for investigating how quantum phenomenon operates and can be useful for specific applications. Therefore, the objectives of this chapter are:

- ☑ To demonstrate that whenever an alignment of the formal potential levels of capacitive (within the interface) and non-capacitive (free in solution) states is attained, the charge transfer between electrode and free redox species in solution occurs in a diffusionless kinetically controlled setting, which is a consequence of ET be mediated by the quantum capacitive states of the interface;

- ☑ To prove that this ET mediation of the capacitive states of the interface complies with a charge transfer resistance limit such as $R_q \sim 12.9$ kΩ, meaning that the mediation occurs with a quantum rate efficiency.

3.1 Introduction

During the introduction of classical ET theories discussed in chapter 1, the electrolyte medium was addressed as a key component of the kinetics. In particular, Marcus' theory establishes an important and determinant parameter that considers the environmental effect on the ET reaction that is referred as the reorganization energy λ of the solvent. This required energetic cost that implies a rearrangment of the outer (solvational) and/or inner sphere (vibrational) structures of the solvent molecules is central in Marcus ET theory. Since the Marcus' theory was based on the TST and the activation energy is written in terms of λ, it can be noted that λ is the kinetic limiting term of electrochemistry reactions. For that reason, the transport of electrons through `D` and `A` states that govern electrochemical reactions is slower than the transport of electrons between solid-state nanoscale electronic states.

The transfer of electrons between `D/A` states with electrode is well-known to be kinetically limited by diffusion, as schematically illustrated by the inset in Fig. 3.1*a*. For instance, the Ferrocenecarboxylic acid (Fc–COOH) in solution acts as a `D` and `A` states accordingly to the applied potential. The current-voltage and the impedance response performed at E_F^e/e confirms the Faradaic activity and difussive process, respectively (see Fig. 3.1*a*). The Faradaic branch of the Randles' circuit of the interface depicted in the inset is comprised by R_{ct} in series with W, the well-known Warburg element that models diffusive process characterized by the region where the impedance response has an angle of 45° at low frequencies (< 10 Hz), which means that the value of the real impedance equals the absolute value of the imaginary part (BARSOUKOV; MACDONALD, 2005), as illustrated by the impedance Nyquist in the inset of Fig. 3.1*a*.

On the other hand, whenever `D/A` states are chemically (or physically) anchored to the metallic electrode, the ET reaction is no longer limited by diffusion, and the current-voltage and the impedance response is different in comparison with the latter case, as shown by Fig. 3.1*b*. Note that the different profiles of the voltammetry and EIS (and ECS) response at the low-frequency limit for diffusion-controlled and diffusionless reactions are modelled by a different equivalent circuit. Instead of W for modeling low-frequency response in diffusion-dependent ET kinetics C_q is used. Therefore, for diffusionless case the kinetics is governed by C_q instead of W element (see Eq. 2.6). The differences between these two processes can also be identified using CV recorded at different s, as above-mentioned. Differences in the exponential dependence of i_p to s for diffusion and diffusionless ET mechanisms as a half and unit, respectively, are a proof of the dissimilar charge-transfer mechanisms operating in each of these electrochemical heterogeneous settings.

Owing to these facts, careful theoretical analysis is required in order to investigate the electrochemical response of such unlike ET kinetics, which have been ignored during the theoretical analysis of the kinetic mechanisms proposed by Marcus–Hush–Chidsey theory, as discussed in chapter 1. In this way, the suitable incorporation of low-frequency limiting circuit for modelling electrode kinetics into an ET theory, should sustain the EIS analysis. For instance, although Creager has identified the existence of a pseudo-capacitive contribution to this diffusionless-controlled ET kinetics, it has not been identified (or discussed) how this capacitive element fits the theoretical model proposed by Marcus-Hush-Chidsey theory (CREAGER; WOOSTER, 1998). However, in one of his works, wherein he focused on interpreting the entire molecular bridge in connecting to the redox-active states chemically attached to the electrode,

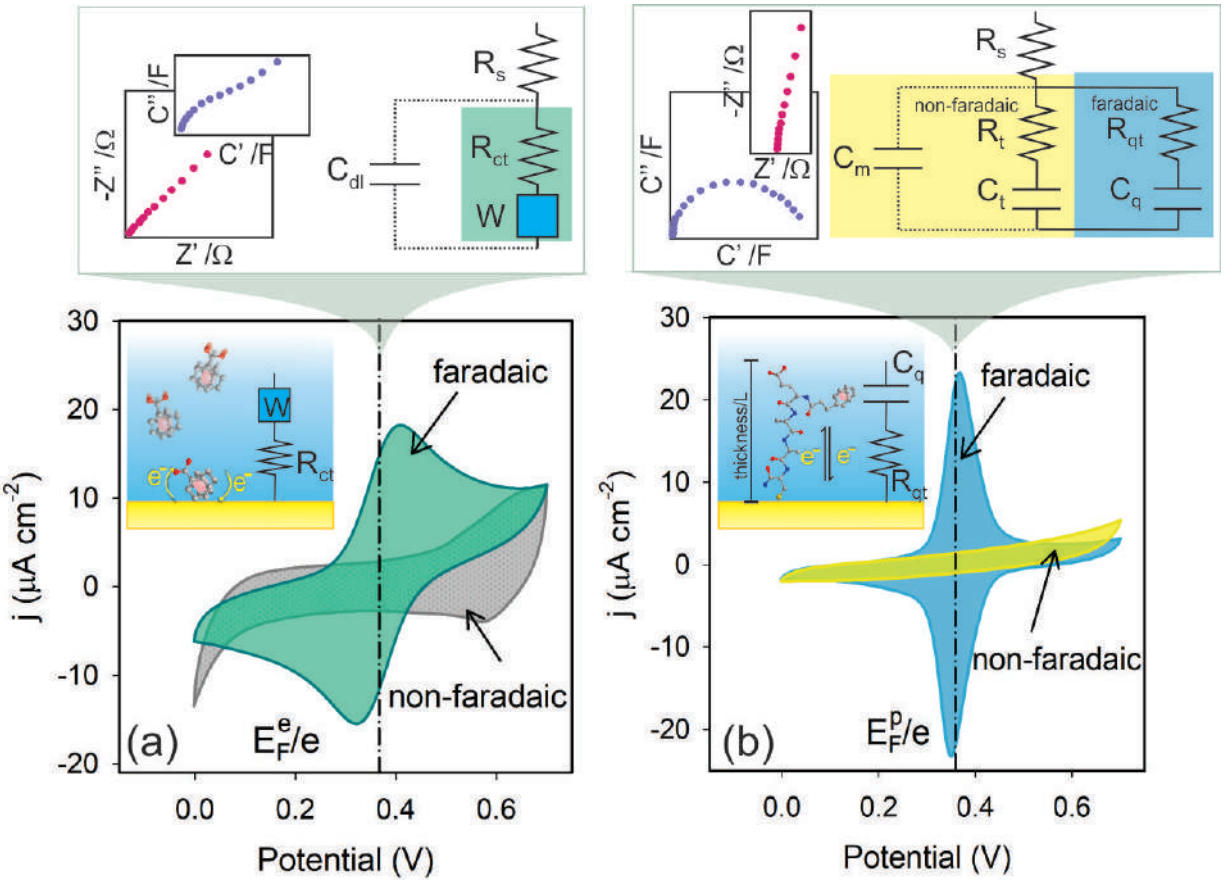

Figure 3.1: Heterogeneous ET reaction controlled by diffusion or diffussionless process occurring in different junctions. (a) Typical CV response of a diffusion controlled ET reaction between electrode and Fc–COOH in the electrolyte environment, schematically represented by the inset, with a formal potential of $E_F^e/e \sim 0.36$ V. Top right, the Randles circuit that models impedance response shown as Nyquist diagrams (left) in his impedimetric and capacitive forms. (b) Typical CV response of a diffusionless ET process occurring in electrochemical interfaces comprising redox probe chemically attached to the electrode as shown by the inset. Same as (a), the vertical hatched strait line indicates the value of the formal potential $E_F^p/e \sim$ 0.36 V (Pep–Fc). The equivalent circuit that models the impedance response shown as Nyquist diagrams as discussed in detail in chapter 2. Owing to the attachment of `D` and `A` species to the electrode, the ET transfer kinetics are no longer controlled by diffusion, and the W element is replaced by C_q, whereas R_{ct} is now denoted as R_q to emphasise its quantum mechanical nature (SÁNCHEZ; SANTOS; BUENO, 2022a).

Source: Adapted from (SÁNCHEZ; SANTOS; BUENO, 2022b).

allowed to confirm that the communication of electrons through the molecular bridge with the electrode occurs through a quantum mechanical tunnelling mechanism (WEBER; CREAGER, 1994).

C_q reveals the shape of the DOS of a molecular junction as $C_q \approx e^2$DOS, which can be experimentally obtained as described elsewhere (BUENO; CRUZEIRO, *et al.*, 2021; PINZÓN *et al.*, 2022), and is characterized by a Gaussian-like shape that is essentially controlled by the dispersion of the $f(1-f)$ term of the thermal-broadened capacitive function (see Eq. 1.12). Therefore, the energy $E = e^2/C_q$ associated with this electronic structure provides a unique characteristic to be exploited through a suitable energy level alignment with the energy levels of the redox-free species in solution.

Accordingly, this chapter will demonstrate experimentally that when the energy level alignment is attained, the capacitive DOS could serve as accessible conductive quantum channels for `D` and `A` states present in a bulk solution to communicate with the electrode (see Fig. 3.2). Moreover, it will be proved that this electronic "harvest" from `D` and `A` states embedded in an electrolyte environment follows a maximum quantum rate efficiency and consequently with diffusionless kinetics.

3.2 Materials and methods

The experimental methodology followed that procedure described in section 2.2 and is complemented by the reported in this section 3.2.

3.2.1 Chemical reagents

Table 3.1 enlists the additional reagents and materials used, which complement Table 2.1 in chapter 2. Also, related information about the enterprise where the reagents were purchased from and their purpose in the development of this chapter are written. Aqueous solutions were prepared using Milli-Q water (Simplicity®water purification system, Millipore, 18.2 MΩ cm at 25°C).

Table 3.1: List of chemical reagents used in chapter 3.

Reagent	Company	Purpose
Rink amide resin (0.5 mmol g^{-1})	AAPPTEC	Solid phase peptide synthesis
Dimethylaminopyridine (DMAP)	Sigma-Aldrich	Coupling of the ferrocene (Fc) in the synthesized peptide
N,N,N′,N′-Tetramethyl-O-(1H-benzotriazol-1-yl) uroniumhexafluorophosphate (HBTU)	Sigma-Aldrich	
N,N-Diisopropiletilamina (DIPEA)	Sigma-Aldrich	
Triisopropylsilane (TIS)	Sigma-Aldrich	Peptide-resin cleavage
11-(Ferrocenyl)undecanethiol	Sigma-Aldrich	Redox SAM fabrication
Ferrocenecarboxylic acid (Fc–COOH)	Sigma-Aldrich	Redox molecule as probe in solution

3.2.2 Peptide synthesis and characterization

Ferrocene-tagged peptide Fc-Glu-Ala-Ala-Cys-NH_2 was synthetized by solid-phase peptide synthesis using the Fmoc-strategy on Rink amide resin (0.5 mmol g^{-1}), as reported elsewhere (PICCOLI *et al.*, 2018).

Briefly, the synthesis was performed at 2-fold excess relative to the amino component in the resin, using DIC/HOBt coupling reagents. The success of the coupling was monitored by the ninhydrin reaction. Before adding the subsequent AA, Fmoc group was deprotected by 20% PIP/DMF for 20 min. Afterwards, the Fc redox

probe was introduced at the N-terminus (Glu) by reaction with one molar equivalent 1:0.1 3-ferrocenylpropionic anhydride/DMAP in DMF during 2 h. Subsequently, 1:2 HBTU/DIPEA (related to Fc content) was added to the reaction vessel and let overnight over shaking (90 rpm). The peptide cleavage from resin and removal of the side chain protecting groups was performed with 95% TFA, 2.5% TIS and 2.5% water (H_2O) for 2 h. After that, the peptides were precipitated with cold ethyl ether anhydrous and separated from soluble non-peptide material by centrifugation. The peptide was extracted in a 1:1 mixture of solvent A (TFA/H_2O, 0.045% $^{v}/_{v}$) and solvent B (TFA/ACN, 0.036% $^{v}/_{v}$) and lyophilized.

The obtained product was diluted in 1:4 A/B (injection volume 5 mL) to be purified, using a HPLC system on a Beckman System Gold using a semi-preparative reverse phase Phenomenex Jupiter C18 column (250 $\times$ 10 mm, 5 μm particle size, 300 Å). A linear gradient elution employed was from 30 to 50% of solvent B for almost 40 min. The flow rate was 5 mL min^{-1} at room temperature and the UV detection was monitored at 220 nm.

The purity of peptide was qualitatively analyzed using an analytical Shimadzu system with a reverse phase Phenomenex Jupiter C18 column (150 $\times$ 4.6 mm, 5 μm particle size, 300 Åpore size) linear gradient of 5 to 95% of solvent B for 30 min, flow rate of 1 mL min^{-1} and UV detection at 220 nm (see Appendix C).

3.2.3 Equipment and electrodes

Electrochemical measurements were performed using the equipment (AUTOLAB potentiostat), electrochemical cell (three-electrode) and supporting electrolyte (20 mM $TBAClO_4$ in ACN/H_2O 1:4, $^{v}/_{v}$) as reported by chapter 2. Gold working electrodes were pre-treated as described in the previous chapter. Mean average A_e of 0.038 and 0.045 cm^2 were obtained (see Appendix B) for the deposition of thiol and peptide, respectively; and were used to normalize electrochemical signals for calculating current densities and capacitances per unit of area for both SAMs.

Self-assembled monolayer fabrication: Right after the sulphuric acid cleaning step, the electrodes were rinsed with water and dried with nitrogen. Posteriorly, they were immersed for 16 h at room temperature (25 °C) in either 6 mM of thiol in EtOH or 2 mM of peptide in ACN/H_2O (1:1, $^{v}/_{v}$) in order to obtain the redox SAMs C11–Fc and Pep–Fc, respectively, according to (GARROTE; SANTOS; BUENO, 2020).

3.2.4 Electrochemical measurements

The quality of the redox SAMs was evaluated by CV as described by chapter 2, from which the E_F/e of the redox monolayers was calculated as $E_F/e \sim (V_{ox}+V_{red})/2$. Afterwards, EIS was conducted at two different potentials outside ($V_{out} = 0.1$ V) and inside the electrochemical window as detail in chapter 2. V_{out} was the same for C11–Fc and Pep–Fc SAMs. However, there was a distinct E_F/e for each SAM, identified as E_F^t/e for C11–Fc and E_F^p/e for Pep–Fc SAMs. Eventually, capacitive spectra were constructed using a complex capacitive function obtained from the EIS raw data as already explained previously.

Density-of-states distribution

The capacitive DOS shapes of Figure 3.7 were measured at scanning potentials from 0.2 to 0.7 V for the C11–Fc and from 0.2 V to 0.6 V for Pep–Fc SAMs with a potential perturbation amplitude of 10 mV at room temperature (25 °C) using 20 mM $TBAClO_4$ as the supporting electrolyte in ACN/H_2O (1:4, v/v) . These measurementes were performed at the equilibrium frequency, previous refereed as f_c in chapter 2, corresponding to a specific low-frequency limit where the imaginary component C'' of $C^*(\omega) = C' + jC''$ is a minimum. Meanwhile, C'' is the minimum, and C' is the maximum with a value corresponding to approximately the diameter of the semicircle of the Nyquist capacitive plot (as reported in Fig. 3.4*b* and 3.5*b*). This low-frequency limit theoretically corresponds to the frequency tending to null ($\omega \to 0$) of Eq. 2.6.

3.2.5 Equivalent circuit analysis

The values of the circuital elements were obtained by fitting EIS or capacitive spectra to appropriate equivalent circuit models of the interface shown by Fig. 3.2. The values of equivalent circuit elements obtained from the fitting were reported as a mean value $\bar{x}$ with the standard error of the mean ($\bar{x} \pm \sigma_{\bar{x}}$) calculated for three and four independently fabricated interfaces, for C11–Fc and Pep–Fc, respectively.

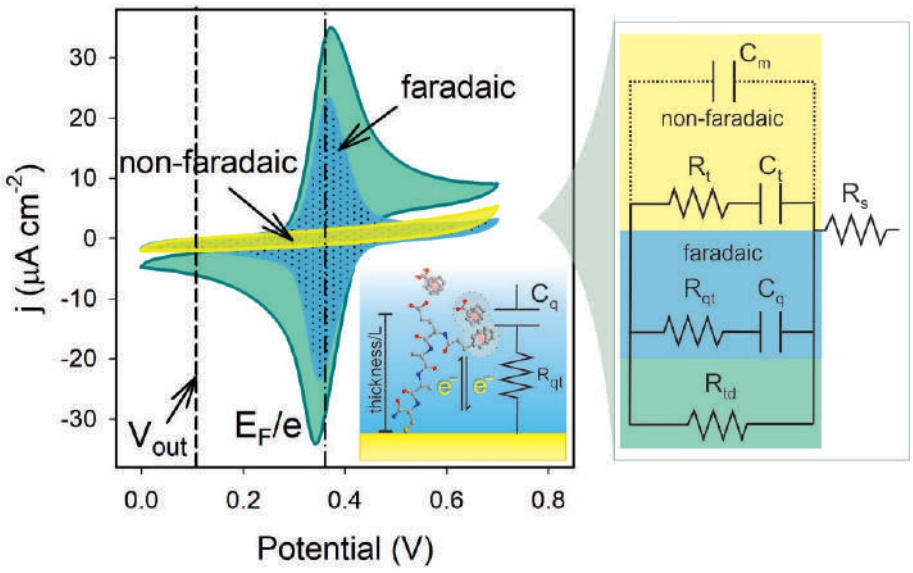

Figure 3.2: Faradaic (in blue) and non-Faradaic (in yellow) electrochemical activities of a diffusionless electrochemical reaction as it is measured almost ideally for redox-active monolayers. In green, the Faradaic current changes due to the presence of the redox probe in solution (i.e., Fc–COOH), as shown schematically by the inset. Right, the equivalent circuit that models the electrochemical activity measured at E_F/e. Accordingly, an EIS spectrum measured in V_{out} will be fitted to an equivalent circuit comprising the circuit elements highlighted in yellow, whereas a spectrum measured at E_F/e is fitted with all the circuit elements of the interface, but largely governed by R_q and C_q series elements. Note the presence of R_{td} as parallel resistive term representing an extra current contribution due to the presence of Fc–COOH and its direct non-capacitively coupled communication with the electrode.

Source: Adapted from (SÁNCHEZ; SANTOS; BUENO, 2022b).

3.3 Results and discussion

In chapter 2 the meaning of R_q was interpreted for a diffusionless setting. This chapter the correlation between G and C_q is analysed in the presence of a redox probe (Fc–COOH) in the solution environment, as illustratively shown in the inset of Fig. 3.2. The analysis of $i = C_q s$ dynamics was conducted using two different electroactive SAMs, which were named Pep–Fc and C11–Fc. The equivalent circuit analysis conducted focuses in the interpretation of quantum circuit elements in which, as will be demonstrated, external circuit elements, such as the series resistance R_s that comprises contact and solution resistance are part of the quantum resistance $R_q \sim 12.9$ kΩ of the interface.

Firstly, the CVs for Pep–Fc and C11–Fc highlights the reversible electrochemical process shown in blue and green, respectively (see Fig. 3.3*a*). The E_F^t/e is located at 0.45 V, whereas E_F^p/e is located at a lower potential $\sim$ 0.36 V, providing a significant difference of $\sim$ 100 mV between the energy levels of both quantum capacitive states. Parameters such as $i_{ox}/i_{red} \approx 1$ and $\Delta V_p \approx 20$ mV, confirm this reversible electrochemical behavior. In particular, the ratio i/s reports on a diffusionless kinetics that controls these heterogeneous ET reactions, which eventually was confirmed by the equivalent circuit analysis further discussed (see Table 3.2).

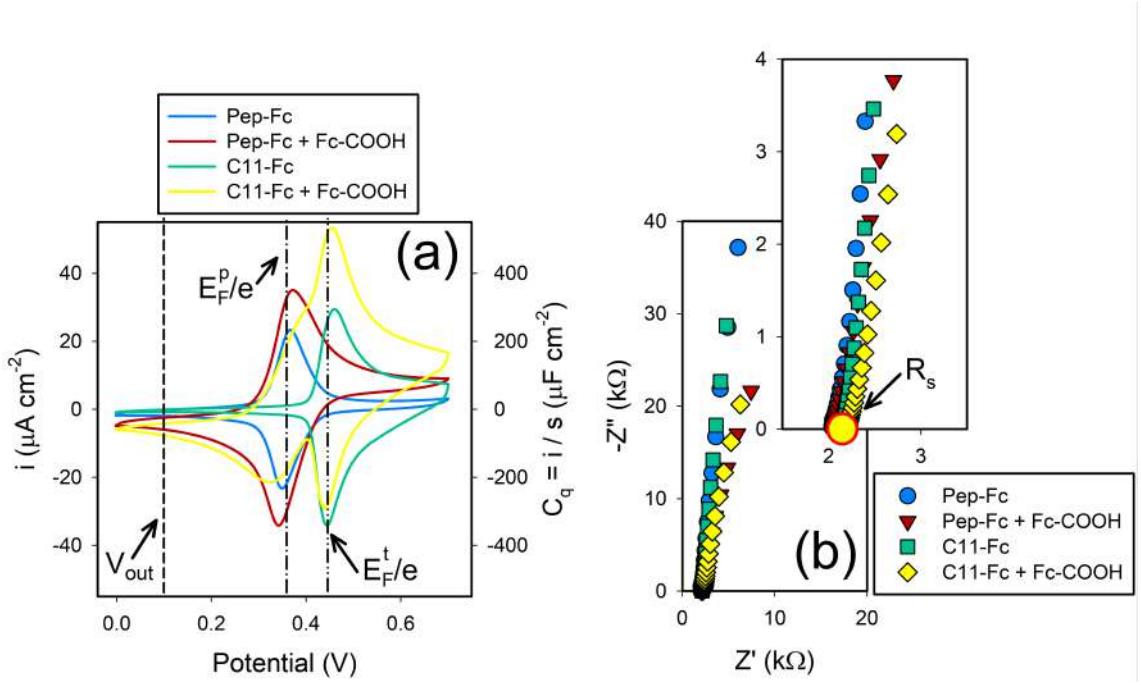

Figure 3.3: (a) Electric current and quantum capacitive ($C_q = i/s$, with a s value of 0.1 V s^{-1}) plots for C11–Fc and Pep–Fc interfaces in the absence (green and blued curves) and presence (yellow and wine curves) of Fc–COOH in a supporting electrode of 20 mM $TBAClO_4$. Note that the values of the potentials $E_F^t/e \sim 0.45$ V, $E_F^p/e \sim 0.36$ V, and $V_{out} \sim 0.1$ V correspond to the formal potential of C11–Fc, Pep–Fc, and the potential out of the Faradaic window, respectively. The peak-to-peak separation ΔV_p is around $\sim$15 and $\sim$18 mV for C11-Fe and Pep–Fc, respectively. (b) EIS spectra obtained for monolayers in the presence and and absence of Fc–COOH. R_s states for the series resistance comprising the resistance of contact and solution.

Source: (SÁNCHEZ; SANTOS; BUENO, 2022b).

The equivalent circuit shown in Fig. 3.2 allows to separate the intrinsic non-Faradaic effects from the Faradaic dynamics of the total electrochemical response, more specifically of the impedance data of the quantum capacitive interfaces. As result of the addition of Fc–COOH molecules in the electrolyte, this circuit was slightly modified by considering a resistive element, identified as R_{td}. The presence of R_{td}, operating in parallel with the Faradaic branch, is interpreted as an electron transport resistance associated with the "diffusive" transmittance of the electrons directly from `D` or `A` moieties in a solution phase environment to the electrode.

The EIS data highlighted a constancy of the R_s observed in Nyquist plot, which is indicated by the yellow dot of Fig. 3.3*b*. This is expected considering that R_s must be constant whether the electrode material and the electrolyte composition are unaltered, as was the case for both analyzed molecular system. Hence, the average values of R_s obtained for Pep–Fc and C11–Fc were 2,030 and 2,120 Ω, respectively, which are statistically similar within the statistical deviations (see Table 3.2).

In particular, in the capacitive form of the EIS data, the capacitive Nyquist plots obtained at E_F^p/e and E_F^t/e confirm the governance of the $i = C_q s$ over the electrochemical activity, as shown in Fig. 3.4*b* and Fig. 3.5*b*, respectively. Consequently, the related ET kinetics for both capacitive interfaces are governed by C_q. Note that the C_q obtained by equivalent circuit-fitting analysis is in agreement with those obtained by CV (see Fig. 3.4*a* and Fig. 3.5*a*) and were ~ 190 μF cm^{-2} and ~ 380 μF cm^{-2} for Pep–Fc and C11–Fc, respectively (see Table 3.2). Whereas the non-Faradaic C_t capacitive contribution is negligibly less than 3% of the Faradaic C_q contribution (see Appendix D).

As described in chapter 2, at $^{E_F e}/_e$ the impedance of the capacitive interface is governed by the $R_q = R_s + R_{qt}$ resistive elements in series with C_q, which defines $\tau = R_q C_q$ of the ET process. Hence, the time-scale $\tau = k^{-1}$ of both capacitive interfaces in the absence and presence of Fc–COOH was experimentally verified applying Eq. 2.7, wherein the values of the circuital elements or the value of f_c were used. For instance, the values of k calculated through the values reported in Table 3.2, of ~ 18 s^{-1} and ~ 11 s^{-1} for Pep–Fc and for C11–Fc, respectively, are in agreement with that obtained graphically by the Bode capacitive diagrams of Fig. 3.4*c* and 3.5*c*, respectively.

In addition, the analysis of the ET mechanism operating in such experimental settings was realized by means of the potential barrier calculation, as explained in chapter 2. Thus, β values were obtained applying the expression $\beta = {}^{-ln(G/G_{0N})}/_L$ once the values of G, N[1] and L[2] are previously known. Consequently, β values around ~ 1.3 Å^{-1} and ~ 1.2 Å^{-1} were obtained for Pep–Fc and C11–Fc, respectively (see Table 3.2). These values agree with those obtained by others considering the tunnelling mechanism for the transport of electrons in non-adiabatic regime (SHAH *et al.*, 2015; ALEMÁN; BIANCO; VENANZI, 2013; FINKLEA; HANSHEW, 1992) of different types of monolayers.

As result of that the ET process of both capacitive interfaces, in the absence and presence of Fc–COOH, follows a tunneling mechanism and that proceeds within a

[1]The obtained quantum channel values were $5.5 \pm 0.3 \times 10^{12}$ and $9 \pm 1 \times 10^{12}$ for the Pep–Fc and the C11–Fc junctions, respectively, in the absence of Fc–COOH.

[2]The estimated lengths of L reported by literature were ~ 1.8 nm and ~ 2 nm for Pep–Fc (PICCOLI *et al.*, 2018) and C11–Fc (BUENO; FERNANDES; DAVIS, 2017), respectively.

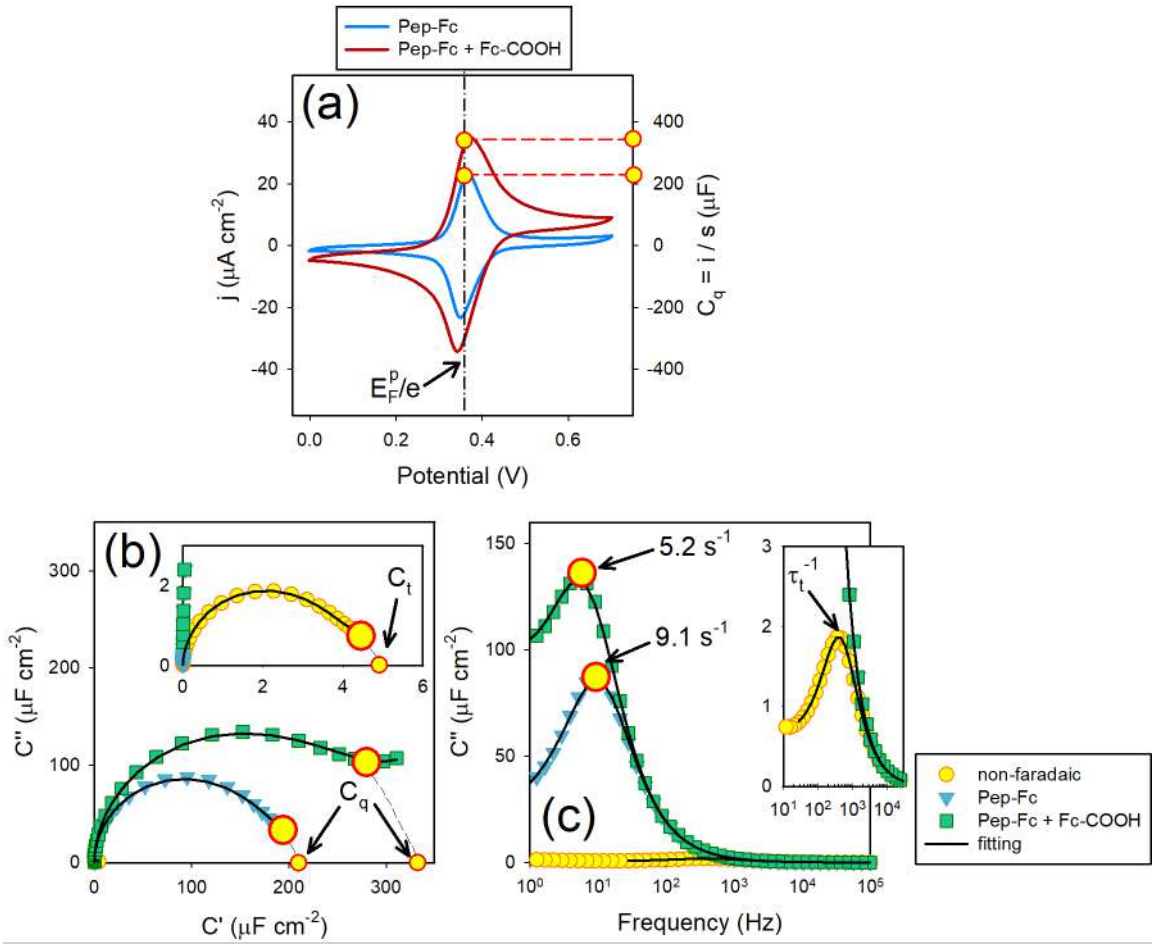

Figure 3.4: (a) Cyclic voltammetry obtained for Pep–Fc in the absence (blue) and presence (wine) of Fc–COOH in 20 mM $TBAClO_4$ supporting electrolyte. (b) Complex capacitive plot for Pep–Fc in the absence (blue triangle) and presence (green square) of Fc–COOH in 20 mM $TBAClO_4$ supporting electrolyte as measured at 0.36 V (corresponding to E_F^p/e). Accordingly to Eq. 2.6, at the low-frequency limit ($\omega \rightarrow 0$), the diameter of the Nyquist spectra provides C_q. The inset of (b) corresponds to the complex capacitive plot of the non-Faradaic response of the interface as measured in the V_{out} potential (0.1 V). (c) Bode capacitive diagram obtained in the same conditions of (b) with the inset corresponding to non-Faradaic response of the interface. The f_c values of 9.1 and 5.2 s^{-1} reports on the rate k of 18.2 and 10.6 s^{-1} in absence and presence of Fc–COOH, respectively. The inset in (c) shows $\tau_t^{-1} = 1/R_tC_t$ of the non-Faradaic contribution.

Source: (SÁNCHEZ; SANTOS; BUENO, 2022b).

quantum resistance limit $R_q \sim 12.9$ kΩ (see Table 3.2), one can propose that the transmittance of the electrons is conducted with the intermediation of C_q states. That is, in the presence of Fc–COOH moieties in the electrolyte environment, the `D` (Fc–COOH) or `A` (Fc^+-COOH) states in the solution phase can communicate with the electrode through Fc/Fc^+ redox capacitive C_q states (contained in both C11–Fc and Pep–Fc SAMs) with a resistance of R_q or R_{td}. By using the Fc/Fc^+ pair of redox capacitive C_q states, a path for the quantum mechanical hopping of electrons is established, which is characterized by a quantum efficiently $R_q \sim 12.9$ kΩ. Whereas parallel paths for the communication of the Fc/Fc^+ redox states of Fc–COOH in the solution phase with the electrode without capactive intermediation exists as well. However, by using

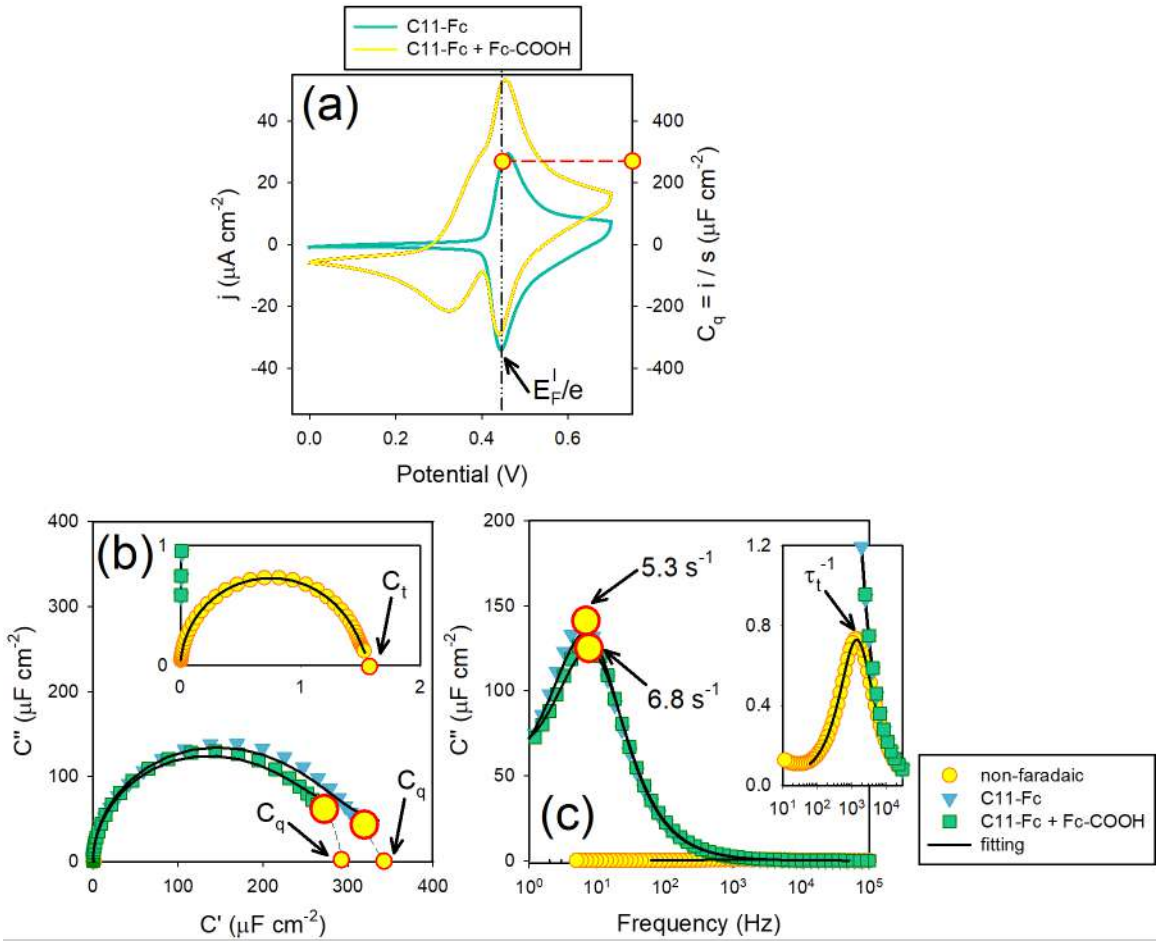

Figure 3.5: (a) Cyclic voltammetry obtained for C11–Fc in the absence (green) and presence (yellow) of Fc–COOH in 20 mM $TBAClO_4$ supporting electrolyte. (b) Complex capacitive plot for C11–Fc in the absence (blue triangle) and presence (red square) of Fc–COOH in 20 mM $TBAClO_4$ supporting electrolyte as measured at 0.45 V (corresponding to E_F^t/e) with the diameter of the semicircles corresponding to C_q. Accordingly to Eq. 2.6, at the low-frequency limit ($\omega \rightarrow 0$), the diameter of the Nyquist spectra provides C_q. The inset of (b) corresponds to the complex capacitive plot of the non-Faradaic response of the interface as measured in the V_{out} potential (0.1 V). (c) Bode capacitive diagram obtained in the same conditions of (b) with the inset corresponding to the non-Faradaic response of the interface. The f_c values of 5.3 and 6.8 s^{-1} reports on the rate k of 10.6 and 13.6 s^{-1} in absence and presence of Fc–COOH, respectively. The inset in (c) shows $\tau_t^{-1} = 1/R_tC_t$ of the non-Faradaic contribution.

Source: (SÁNCHEZ; SANTOS; BUENO, 2022b).

the parallel paths, there is an energetically unfavorable situation, leading to a much higher R_{td} resistance than for the transit of the electrons through R_q. Accordingly, by conducting electrons through the R_{td} alternative path, the efficiency of the electronic communication with the electrode is drastically reduced by at least three orders of magnitude (see Table 3.2).

In this way, the role played by the redox (Fc/Fc^+) capacitive states has been demonstrated, whenever they are mediating the electron transfer and transport to the electrode coming/going from `D` and `A` species in solution. However, this electronic communication is dependent on the magnitude of the coupling of the energy levels of `D` and `A` in the solution bulk with that of `D` and `A` states chemically anchored to the

Table 3.2: Circuit parameters and calculated values for R_q, G, β and k, for both redox interfaces embedded in an electrolyte solution containing or not 100 μM Fc–COOH. Values are reported as $\overline{x} \pm \sigma_{\overline{x}}$, where $\overline{x}$ refers to the mean average value and $\sigma_{\overline{x}}$ refers to the standard error of the mean of at least three independent modified electrodes measured.

	Pep–Fc		C11–Fc	
	0 μM	100 μM	0 μM	100 μM
C_q (μF cm^{-2})	190 ± 10	310 ± 10	380 ± 40	340 ± 40
R_s (Ω)	$2{,}030 \pm 50$	$2{,}100 \pm 100$	$2{,}120 \pm 40$	$2{,}170 \pm 70$
R_{qt} (Ω)	33 ± 5	40 ± 10	70 ± 10	60 ± 10
R_{td} (kΩ)		250 ± 10		400 ± 100
R_q (Ω)	$12{,}400 \pm 400$	$13{,}700 \pm 600$	$13{,}900 \pm 200$	$14{,}000 \pm 400$
G (mS)	32 ± 4	33 ± 7	14 ± 2	19 ± 6
β (Å^{-1})	1.297 ± 0.009	1.33 ± 0.01	1.230 ± 0.004	1.213 ± 0.009
k (s^{-1})	18.2 ± 0.5	10.6 ± 0.1	11 ± 1	12 ± 1

Source: (SÁNCHEZ; SANTOS; BUENO, 2022b).

electrode. Meaning that it is required to achieve an energy alignment between formal energy levels of non-capacitive Fc–COOH/Fc$^+$–COOH states added to the electrolyte and that of the Fc/Fc$^+$ redox capacitive states immobilized in the electrode surface. Herein, there are two situations, the first one, wherein the energy levels are alignment, i.e., $E_F^p \approx E_F^e$ (see Fig. 3.4*a*), which is achieved when Pep–Fc is in presence of Fc–COOH; and the other situation, a weaker energy alignment, i.e., $E_F^t \neq E_F^e$ (see Fig. 3.5*a*), when C11-Fc is the SAM that is with the Fc–COOH molecules added to the electrolyte. Therefore, an appropriate electronic coupling maximizes the number of quantum channels available for ET as following discussed.

As shown in Fig. 3.4*a*, the formal potential of the Fc–COOH is numerically equivalent to the formal potential of the Pep–Fc, i.e., $E_F^p/e \approx E_F^e/e \sim 0.36$ V (see Fig. 3.1*a* and Fig. 3.4*a*). These equivalent formal potential values offer a unique experimental condition to evaluate the quantum ET efficiency between Fc–COOH and the electrode intermediated by the capacitive states of the Pep–Fc junction by means of the study of the quantum rate dynamics. Contrary to a direct electrode reaction described by semi-classical theory where there is an alignment of Fc–COOH states with that of the electrode (section 1.3), the ET mediation by Fc/Fc$^+$ capacitive states is explained by the quantum rate theory, which proposes that each peptide–Fc molecule anchored to the electrode acts as a quantum point contact (QPC), which can be modelled by a quantum resistive-capacitive contact (inset of Fig. 3.2) that defines the ET rate constant $k = 1/\tau$. As above-discussed analysis, it was demonstrated that R_q and C_q does govern the diffusionless kinetics, thus, in their absence, the ET reaction between Fc-COOH and the electrode will be controlled by diffusion (see Appendix E).

In spite of the capacitive feature of Fc–COOH cannot be proved by EIS (see Appendix F) (or any other) method whether a three-dimensional degree of freedom exists (i.e., mass transport process), avoiding the confinement of charges in a restricted region of space, there is an energy levels distribution associated to Fc-COOH, namely, HOMO-LUMO, which is defined by $E = e^2/C_q \sim \Delta\mu$ (BUENO, 2018), corresponding

to E_F^e that can be aligned with those of the interface of the peptide E_F^p as it is attached to the electrode (see Fig. 3.6). For that reason, when Fc–COOH is added to the electrolyte the resultant CV of the Pep–Fc (red curve), as compared with the response of solely Pep-Fc (blue curve), that is in the absence of Fc-COOH, depicts an only one redox process at an equivalent formal potential $E_F^e/e = E_F^p/e$, with an increment of Faradaic current (or capacitance $C_q = i/s$) of 30% (from $\sim$ 20 μA cm^{-2} to $\sim$ 30 μA cm^{-2}). This increase in C_q affects k (see Table 3.2), as predicted by the quantum rate model (see Eq. 1.15), whose value is in agreement with that obtained using the values of f_c obtained from Fig. 3.4*c* in $k = g_r f_c$, obtaining constant rate values from $\sim$ 18 (Pep–Fc) to $\sim$ 10 s^{-1} (Pep–Fc + Fc–COOH).

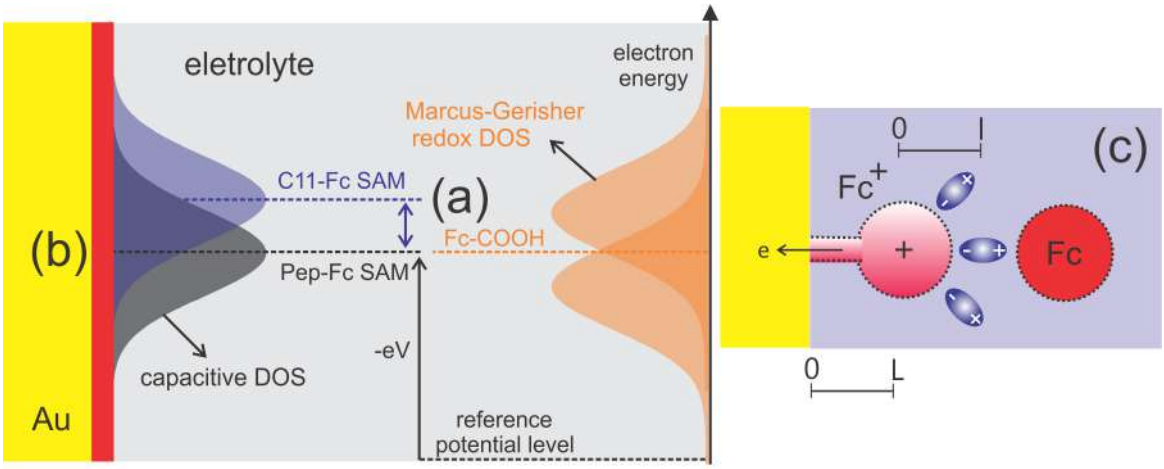

Figure 3.6: Schematic representation of ET mediated by the quantum capacitive states. (a) Strong alignment of the capacitive energy levels of the interface Pep–Fc with Fc–COOH states in the bulk solution. (b) Weak alignment of the capacitive energy levels of the interface C11–Fc with Fc–COOH states. Note that the energy levels of the Fc-COOH states are described by Marcus-Gerischer redox DOS as discussed in section 1.3. Hashed lines indicate the formal potential of the solution and electrode states' energy levels. (c) QPC interacting with an Fc centre (red circle) of Fc–COOH in the solution phase. The mediating capacitive states leads to a two-step ET event owing to the fact that the electron resides in the Fc/Fc$^+$ state in the interface before resides in the Fc-COOH or electrode state.

Source: (SÁNCHEZ; SANTOS; BUENO, 2022b).

The equivalent circuit analysis of both capacitive interfaces in the presence of Fc-COOH agrees with the EIS graphical analysis, providing accurate values of R_q and C_q. It is worth to note that R_{td} is three orders of magnitude higher than R_q (see Table 3.2), meaning that it does not influence (with a minimum loss of energy) the efficiency of the electron transport through the R_qC_q channels, owing to $R_q = R_s + R_{qt} \sim 13$ kΩ remains within a quantum limiting value. On the other hand, the increment of C_q in the presence of Fc–COOH is interpreted as an increment in the number of quantum channels as $N = {}^{k_BTC_q}/_{e^2 f(1-f)}$ available for the ET. This suggests a superposition of the HOMO–LUMO of Pep–Fc with the HOMO–LUMO states of Fc–COOH that lead to additional paths for the transport of electrons through available quantum capacitive states. Following the quantum rate reasoning that predicts $k = {}^{G}/_{C_q}$ and recalling that $G = \kappa G_0 N = {}^{\kappa G_0 k_B TC_q}/_{e^2 f(1-f)}$, it is highlighted that both k and G depend on a single state of the $C_q = e^2({}^{dn}/_{d\mu})$ function and on the entire distribution of the redox density-of-states $({}^{dn}/_{d\mu})$.

Fig. 3.7 shows the DOS as a function of the energy state (eV) of the electrode for the different junctions investigated in this chapter. In particular, Fig. 3.7*a* exhibits a similar profile between the DOS distribution of Pep–Fc in the absence and presence of Fc–COOH states. Both DOS shapes have a maximum at $E_F^p/e \sim 0.36$ V, as expected. Note that Fc–COOH does not influence the energy distribution of states, but does increase the population of states, owing to an increase in the number of N (peak height at the maximum). This clearly indicates an increment in the population of the DOS (consequently of N) in the presence of Fc–COOH.

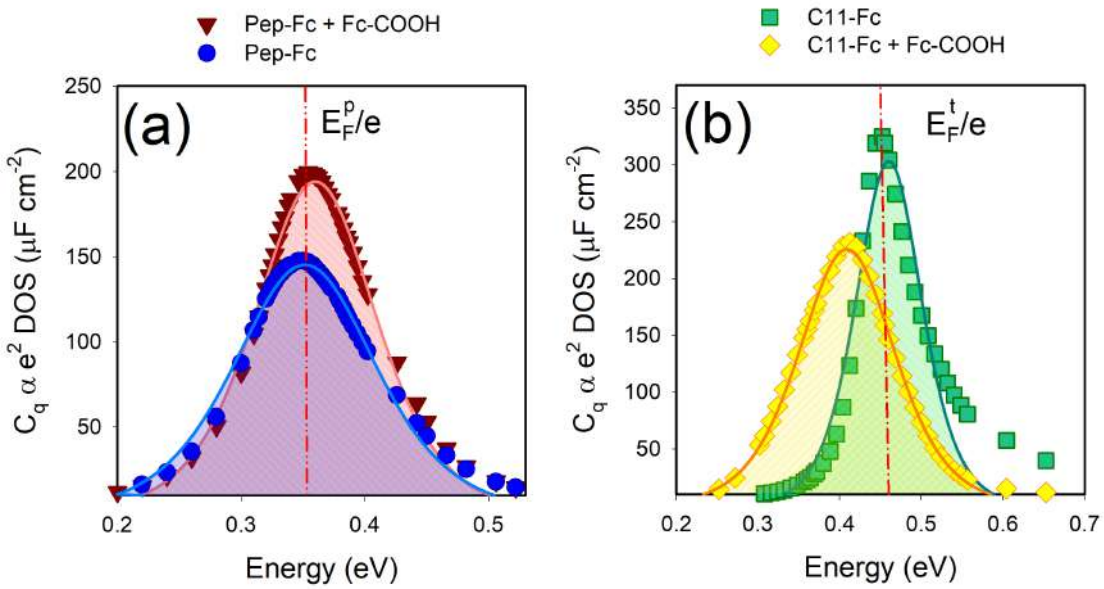

Figure 3.7: Distribution of the redox density-of-states for (a) Pep–Fc and (b) C11–Fc interfaces in the presence and absence of an Fc–COOH redox probe in the solution phase. These DOS shapes correspond to the electronic distribution of states of the interface as measured by computing C_q as a function of the electrode potential (owing to $C_q \propto$ DOS). Both Gaussian shapes in (a) have an equivalent standard deviation ~ 0.4 mV and position of the maximum, whereas the Gaussian shapes in (b) the position of the maximum is different, though they have similar standard deviations ~ 0.35 mV.

Source: (SÁNCHEZ; SANTOS; BUENO, 2022b).

Finally but not least, important information is proved by the analysis of the ET mediation of C11–Fc, which depicts a shift in the energy levels for Fc-COOH of ~ 100 mV (see Fig. 3.1*a* and Fig. 3.5*a*). In this case, the energy level of the intermediated capacitive states corresponds to the formal potential of $E_F^t/e \sim 0.45$ V, which is a few millivolts different from E_F^t/e (Fc-COOH) ~ 0.36 V. As result, there are two separated ET processes, which are superposed (see Appendix G). Additionally, an increment of the anodic peak current at 0.45 V is observed (yellow curve in Fig. 3.5*a*).

The separation of these Faradaic processes is better evaluated in Fig. 3.7*b*, which exhibits an unusual positions of the maximum of the DOS distribution. Note that in this case, the increment of the electric current cannot be solely associated with (or is not fully originating from) the quantum capacitive states of the interface, owing there is no appreciable difference between the capacitance of the interface in the absence and presence of Fc–COOH (see Fig. 3.5*b*). In consequence, the rate constant k, calculated whether from equivalent circuit or from graphical (bode diagram, see

Figure 3.5*c*) analysis, remains unaltered. Additionally, the obtained values of R_q, indicates a slightly increase, but within statistics error, the these values obtained are within the theoretical limit of $\sim$ 12.9 kΩ (see Table 3.2). This leads us to conclude that, despite a great difference observed in the CV and DOS shapes that conducted to different current contributions owing to differences in the alignment of the energy levels between the capacitive and non-capacitive coupling of C11–Fc and Fc–COOH states, the efficiency with which electrons are transported to the interface by quantum RC channels is still fully governed by the quantum rate resistive limit.

3.4 Conclusion

The DOS of redox molecules suitable assembled over conductive electrodes acts as an accessible conductive quantum channels in an ET reaction between electrode and redox states in solution. Independent of the backbone structure of the redox monolayer, the related phenomenon operating in the ET process follows the quantum mechanical efficiency, such as the minimum quantum resistance, in agreement with the quantum rate theory. Moreover, regardless that such ET process occurs whether in a single or two-step mechanism (i.e., quantum capacitive mediation), the efficiency of the charge transport is not affected. Furthermore, the appropriate alignment of energy levels of the capacitive states (coupled to the electrode) with that of the bulk solution leads to a increase of the number of quantum channels N that are available for the ET reaction, which is a favorable setting that could have potential application in the development of novel and advanced electrochemical nanoscale devices.

References

ALEMÁN, C.; BIANCO, A.; VENANZI, M. **Peptide materials: From nanostuctures to applications**. 1st: John Wiley and Sons, 2013.

BARD, A. J.; FAULKNER, L. R. **Electrochemical Methods Fundamentals and applications**. 2nd: John Wiley and Sons, 2000.

BARSOUKOV, E.; MACDONALD, J. R. **Impedance spectroscopy theory, experiment, and applications**. 2nd: John Wiley and Sons, 2005.

BUENO, P. R.; FERNANDES, F. C.; DAVIS, J. J. Quantum capacitance as a reagentless molecular sensing element. **Nanoscale**, Royal Society of Chemistry, v. 9, n. 40, p. 15362–15370, 2017.

BUENO, P. R. **The Nanoscale Electrochemistry of Molecular Contacts**. Springer, 2018. (SpringerBriefs in Applied Sciences and Technology). ISBN 978-3-319-90486-3. DOI: 10.1007/978-3-319-90487-0.

BUENO, P. R.; CRUZEIRO, V. W., *et al.* The density-of-States and equilibrium charge dynamics of redox-active switches. **Electrochimica Acta**, v. 387, p. 138410, 2021. ISSN 0013-4686. DOI: 10.1016/j.electacta.2021.138410.

CREAGER, S. E.; WOOSTER, T. T. A new way of using ac voltammetry to study redox kinetics in electroactive monolayers. **Analytical chemistry**, ACS Publications, v. 70, n. 20, p. 4257–4263, 1998.

FINKLEA, H. O.; HANSHEW, D. D. Electron-transfer kinetics in organized thiol monolayers with attached pentaammine (pyridine) ruthenium redox centers. **Journal of the American Chemical Society**, ACS Publications, v. 114, n. 9, p. 3173–3181, 1992.

GARROTE, B. L.; SANTOS, A.; BUENO, P. R. Label-free capacitive assaying of biomarkers for molecular diagnostics. **Nature Protocols**, 2020. ISSN 1754-2189. DOI: 10.1038/s41596-020-0390-9.

LAVIRON, E. General expression of the linear potential sweep voltammogram in the case of diffusionless electrochemical systems. **Journal of Electroanalytical Chemistry**, v. 101, n. 1, p. 19–28, 1979. ISSN 1572-6657. DOI: 10.1016/s0022-0728(79)80075-3.

PICCOLI, J. *et al.* Redox Capacitive Assaying of C-Reactive Protein at a Peptide Supported Aptamer Interface. **Analytical Chemistry**, v. 90, n. 5, p. 3005–3008, 2018. ISSN 0003-2700. DOI: 10.1021/acs.analchem.7b05374.

PINZÓN, E. F. *et al.* Quantum Rate Dynamics and Charge Screening at the Nanoscale Level. **Physical Chemistry Chemical Physics**, Royal Society of Chemistry, v. 24, n. 26, p. 16200–16206, 2022.

SÁNCHEZ, Y. P.; SANTOS, A.; BUENO, P. R. Quantum Mechanical Meaning of the Charge Transfer Resistance. **Journal of Physical Chemistry C**, v. 126, p. 3151–3162, 6 2022a. DOI: 10.1021/acs.jpcc.1c07801.

SÁNCHEZ, Y. P.; SANTOS, A.; BUENO, P. R. Quantum rate efficiency of the charge transfer mediated by quantum capacitive states. **Electrochimica Acta**, Elsevier, p. 141194, 2022b.

SHAH, A. *et al.* Electron transfer in peptides. **Chemical Society Reviews**, Royal Society of Chemistry, v. 44, n. 4, p. 1015–1027, 2015.

WEBER, K.; CREAGER, S. E. Voltammetry of redox-active groups irreversibly adsorbed onto electrodes - treatment using the marcus relation between rate and overpotential. **Analytical Chemistry**, v. 66, n. 19, p. 3164–3172, 1994. ISSN 0003-2700. DOI: 10.1021/ac00091a027.

Chapter 4

Enhancement of Quantum Capacitive Signal and Amplification Mechanism for Sensing

Electroactive interfaces featuring quantum capacitive states have been successfully used as label-free based sensors (FERNANDES; GÓES, *et al.*, 2013; CECCHETTO; FERNANDES, *et al.*, 2017; SANTOS; BUENO; DAVIS, 2018; CECCHETTO; SANTOS, *et al.*, 2020; PINZON; SANTOS; BUENO, 2021; GARROTE; LOPES, *et al.*, 2022). In the previously chapter, it was demonstrated that the energy alignment between energy levels of capacitive (redox moieties within interface) and non-capacitive (redox molecule free in solution) states leads to an increment of quantum channels available for mediating the ET reaction, resulting in an increase of Faradaic current (or capacitance $C_q = {}^{i}/_{s}$). The enhancement of such electrochemical activity represents a potential strategy to increase the signal sensitivity of electrochemical interfaces aimed to detect a specific analyte. Consequently, this chapter aims to apply this energy level alignment strategy as amplification mechanism for sensing. In summary, the amplification mechanism is studied using capacitive and non-capacitive states for quantification of nonstructural protein 1 (NS1) dengue viruses biomarker, with a main specific objective:

- ☑ To demonstrate that the capacitive signal of a biosensing interface using a redox self-assembled monolayer can be enhanced by means of the alignment of the energy levels between redox states that are free in solution phase and quantum capacitive states attached to the interface of the electrode, allowing the enhanced detecting of NS1 dengue biomarker. The amplification signal for detecting NS1 as shown here as a proof-of-concept of this signal amplification methodology.

4.1 Introduction

The ET dynamics of electroactive interfaces is governed by R_q and C_q as depicted in Fig. 4.1*a*, and the C_q reports on the corresponding DOS as demonstrated in chapter 3. Whenever this electroactive interface is modified with suitable biological receptors chemically attached close to the redox moieties (see Fig. 4.1*b*) that selectively bind with the biological target, as depicted by Fig. 4.1*c* (MARQUES *et al.*, 2015; PICCOLI *et al.*, 2018), the resultant $i \propto C_q$ is used as a transducer signal for detection of biological analytes in a label-free format (SANTOS; DAVID; BUENO, 2014; LOPES; SANTOS; BUENO, 2022). Specifically, the bond target-receptor produces a discharged of the

C_q states, implying a decrease in the electron occupancy that eventually affects the electrochemical activity of the reaction, that is a decrease of $i \propto C_q$ signal (MARQUES *et al.*, 2015; PICCOLI *et al.*, 2018). Thus, the C_q signal has demonstrated to be a novel, highly sensitive, and specific transducer signal for biological target detection (FERNANDES; GÓES, *et al.*, 2013; CECCHETTO; FERNANDES, *et al.*, 2017; SANTOS; BUENO; DAVIS, 2018) in complex biological samples such as blood (GARROTE; LOPES, *et al.*, 2022).

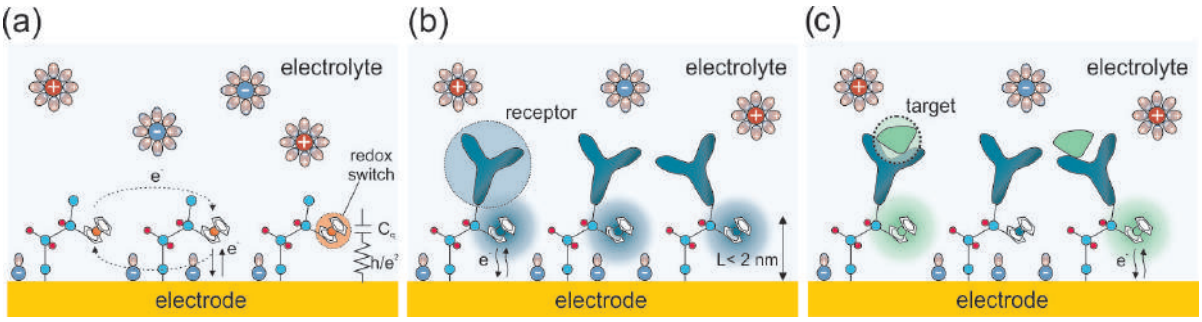

Figure 4.1: Schematic representation of a capacitive biosensing interface. (a) Redox self-assembled monolayer in which individual quantum capacitive moieties acts as a resistive-capacitive channel modeled as quantum R_qC_q states. (b) The C_q associated to the redox moiety is sensitive to variations in its surrounding environment in a way that if a modification of this moieties is attained with specific receptors, the interface can be used as an electrochemical recognition signal of a target of analytical interest. (c) Receptor-target binding that produces variation of C_q, which responds sensitively to changes in the target concentration, permitting different ways of capacitively sensing biomarkers.

Source: (GARROTE; SÁNCHEZ, et al.*, 2024).*

Therefore, measuring variations in the Faradaic capacitance C_q as a function of a biomarker concentration, analytical curves can be constructed to further quantify the biomarker in real samples (FERNANDES; SANTOS, *et al.*, 2014). Note that the transducer signal of the capacitive sensing devices feature a diffusionless ET rate dynamics, contrary to the traditional impedimetric signal transducers, which compute the variations in the R_{ct} associated with a diffusion-controlled electrochemical reaction occurring between redox-free probe and an electrode (BAHADIR; SEZGINTURK, 2016). Furthermore, this novel and highly sensitive method for sensing biological analytes operates in a label-free format, meaning that this platform does not require additional steps and labeled reagents such as label-based methodologies (SANTOS; DAVID; BUENO, 2014; LOPES; SANTOS; BUENO, 2022). Hence, it has become an alternative electroanalytical approach to the most common impedimetric and non-Faradaic capacitive methods for sensing biological molecules in a label-free format (AISSA *et al.*, 2019; GARROTE; LOPES, *et al.*, 2022; LOPES; SANTOS; BUENO, 2022).

Consequently, capacitive transducers enable the development of reagentless point-of-care (PoC) molecular diagnostic devices as portable and low-cost alternatives to traditional laboratory methods based on polymerase chain reaction or enzyme-linked immunosorbent assays (LAND *et al.*, 2019). The importance of PoC devices lies on real-time diagnosis of infectious diseases, which allows the implementation of suitable surveillance methodologies against viruses, and effectively prevents outbreaks (DEROCO; WACHHOLZ J.; KUBOTA, 2021). The sensitivity of the PoC assay is important for ensuring the detection of trace levels of the analyte and permitting the

dilution of small amounts of biological samples without compromising the specificity of the analytical results.

Although the electrochemical capacitive method has an inherently high sensitivity, enhancements in signal sensitivity can bring additional advantages. For instance, the quantum signal amplifier electrochemical mechanism (see Fig. 4.2), discussed in the previous chapter, is a potential strategy for signal enhancement of the electrochemical current, in which an energy alignment between C_q capacitive states at the interface and the electronic states of redox-free probes within the solution environment, allows the amplification of the signal sensitivity to detect a biomarker, as demonstrated in this chapter. From the practical point of view, in comparison with current signal amplifier strategies coupled with electrochemical transducers, such as nanoparticles, enzyme catalytic strategies, and isothermal DNA/RNA amplification methods (LIU *et al.*, 2018), the strategy proposed stands out due to comply with the real-time PoC concepts, unlike those strategies that require additional steps and labeling.

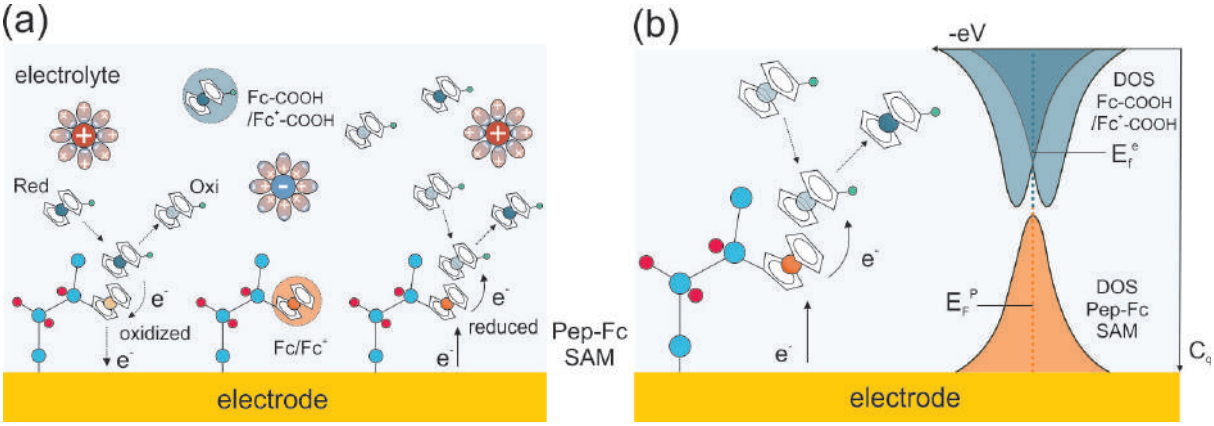

Figure 4.2: Schematic representation of the quantum signal amplifier electrochemical mechanism. (a) The electrodynamics operating in a redox capacitive monolayer (Pep–Fc) at a formal potential of $^{E_F}/_{e}$ in the presence of redox free Fc–COOH moieties within the electrolyte. (b) Strong energy alignment between the quantum capacitive Fc/Fc^+ energy states of the Pep-Fc and those $Fc–COOH/Fc^+$-COOH energy state free in the electrolyte, showing the alignment of the DOS of the capacitive states (orange Gaussian) to the DOS of redox Fc–COOH free (blue Gaussian) in the electrolyte, which are different in nature as discussed in chapter. 3.
Source: (GARROTE; SÁNCHEZ, et al.*, 2024).*

As a proof-of-concept, the quantum signal amplifier methodology was used for the quantification of low levels of NS1 in undiluted commercial human serum, a biomarker for Dengue infection (MULLER; YOUNG, 2013). Dengue is an RNA virus member of the *Flaviviridae* family which is causative of dengue fever and severe dengue fever (GUZMAN *et al.*, 2016). In humans, Dengue virus is transmitted by the bite of an infected female *Aedes aegypti* mosquito and it constitutes a health-threat throughout countries in Africa, Asia and the Americas (SILVA *et al.*, 2018). In the later context, Brazil is one of the countries with more dengue fever cases. According to the Pan American Health Organization (PAHO), the country registered approximately 2.4 millions cases in 2022 (P.A.H.O, 2023). The early detection of dengue fever could prevent from decease by keeping the patients under observation for possible haemorrhage consequences of severe dengue fever, in addition to enabling the control of the *Aedes aegypti* population. Accordingly, this chapter demonstrates the potential use of

an amplifier signal methodology to enhance the sensitivity of the assay to detecting low NS1 concentrations.

4.2 Materials and methods

The experimental methodology aims to fulfill the main objective of this chapter. Note that the Ferrocene-tagged peptide Fc-Glu-Ala-Ala-Cys-NH_2 used in this chapter is the same used in chapter 3.

4.2.1 Chemical reagents

Table 4.1 compiles additional reagents used in this chapter indicating their provider and purpose. Complementary information can be found in Table 2.1 in chapter 2. Aqueous solutions were prepared using Milli-Q water (Simplicity®water purification system, Millipore, 18.2 MΩ cm at 25°C).

Table 4.1: List of chemical reagents used in chapter 4.

Reagent	Company	Purpose
Acetone	Qhemis	Cleaning of miniaturezed gold electrode
Isopropyl alcohol	Synth	
1-Ethyl-3-(3-dimethylaminopropyl) carbodiimide (EDC)	Sigma-Aldrich	Capacitive sensing interface fabrication for viral protein NS1 detection
N- hydroxysuccinimide (NHS)	Sigma-Aldrich	
SuperBlock™	ThermoFisher	
Monoclonal antibody anti-NS1 (cat. no. ab41616)	Abcam	
Sodium phosphate dibasic dodecahydrate ($Na_2HPO_4 \cdot 12H_2O$)	Sigma-Aldrich	Phosphate buffer (PB) solution (pH 12 mM, pH 7.4) preparation
Potassium dihydrogen phosphate (KH_2PO_4)	Sigma-Aldrich	
Recombinant NS1 (cat. no. ab181950)	Abcam	NS1 aliquots preparation
Human serum	Sigma-Aldrich	

4.2.2 Equipment and electrodes

Electrochemical measurements were performed using AUTOLAB potentiostat, three-electrode electrochemical cell and 20 mM $TBAClO_4$ in ACN/H_2O 1:4, v/v as supporting electrolyte, as reported in chapter 2. Miniaturized gold electrodes were designed and microfabricated by Dr. R. C. Teixeira and the Electronic Packaging Staff at CTI Renato Archer, Brazil. Briefly, the Si/SiO_2 wafers were patterned using laser-writer photolithography. Afterwards, a Ti adhesion layer was deposited (10 nm thickness), followed by Au layer (100 nm thickness) using lift-off procedure (see Appendix H).

A_e of the miniaturized working electrode (SiO_2/Au) was 0.0314 cm^2.

Working electrode pre-treatment: The gold microchips were cleaned by immersing the miniaturized electrodes in different solvents during 12 min with sonication, starting with isopropyl alcohol, and followed by acetone, isopropyl alcohol, and Milli-Q water. Afterwards, the Au microchips were dried with nitrogen and exposed to UV/ozone during 30 min in the UV/Ozone ProClearner^{TM} equipment from Bioforce Nanosciences.

Capacitive sensing interface fabrication: Right after the cleaning procedure, the miniaturized electrodes were immersed for 16 h at room temperature (25 °C) in 30 μL of 2 mM of peptide in ACN/H_2O (1:1, v/v) inside closed tubes, in order to obtained the redox-tagged interface Pep–Fc, according to (GARROTE; SANTOS; BUENO, 2020). Afterwards, the electrodes were rinsed with ACN/H_2O (1:1, v/v). Subsequently, the carboxylic acids groups from the glutamic acid at the C-terminal group of the peptide chain were activated by the EDC/NHS carbodiimide reaction ((HERMANSON, 2008)). The microchips were incubated in 20 μL of EDC/NHS solution (1:1, v/v), using 0.2 M EDC and 0.05 M NHS aqueous solutions for 30 min at 25°C. Afterwards, the microchips were washed with ultrapure water and PB and incubated in the anti-NS1 antibody solution (1 μL from the stock antibody solution was diluted in 99 μL of PB) for 1 h. Then, the electrodes were rinsed with PB. The remaining NHS esters were blocked by incubating the microchips in SuperBlock^{TM} blocking buffer for 30 min at 25°C to prevent non-specific adsorption, and then rinsed with PB solution prior to the electrochemical characterization.

4.2.3 Electrochemical measurements

The modification of the electrode interfaces was evaluated by CV and EIS as described by chapter 2, using a portable Palmsens potentiostat equipped with FRA module. From these CV measurements the E_F/e of the SAMs were obtained as described previously. Afterwards, EIS was conducted at two different potentials outside ($V_{out} = 0.1$ V) and inside ($E_F/e \sim 0.36$ V) the electrochemical window. For assays with amplifier signal (in presence of Fc–COOH) operating, the E_F/e corresponded to the potential at which an energy alignment (see Fig. 4.2*b*) is achieved between electrode and redox free species states, i.e., that of the interface, i.e., $E_F/e \sim 0.36$ V as shown by Fig. 4.3*a*. All experiments were carried out for at least three different microchip electrodes and standard errors were obtained from these replicates.

4.2.4 Equivalent circuit analysis

The values of the circuital elements were obtained by fitting EIS or capacitive spectra of the redox SAM interface, using the equivalent circuit studied in chapter 3 (see Fig. 3.2). The values of equivalent circuit elements obtained from the fitting were reported as a mean value $\bar{x}$ with the standard error of the mean ($\bar{x} \pm \sigma_{\bar{x}}$) calculated for four independently fabricated interfaces.

4.2.5 NS1 analytical curve with or without signal amplification

After the fabrication of capacitive sensing interfaces, the analytical curves for quantification of NS1 dengue virus biomarker with or without amplifier signal were obtained, corresponding to measuring the signal of the interface in presence or absence of 100 μM Fc–COOH redox couple in the electrolyte, respectively. Prior to the incubation with the NS1 samples, at least one blank measurement was recorded to quantify the matrix effect of the commercial serum. For this purpose, the biosensing interfaces were incubated for 30 min at 25°C in undiluted commercial serum and then, washed with PB and ultrapure water and subsequently characterised by EIS for measuring the signal parameters of the interface and the subsequent construction of the analytical curves. This step was repeated until the stability of the interface was completely achieved, i.e. when the variations of the analytical signal $1/C_q$ were lower than 5%. $1/C_q$ were calculated from C_q values graphically obtained from ECS spectra as the diameter of the semicircle of the complex capacitance Nyquist plot as depicted in Figure 4.3*b*.

The analytical curves were constructed by incubating these biosensing interfaces with undiluted commercial serum samples containing increasing concentrations of NS1 biomarker ranging from 10^{-2} to 10^{6} pg mL^{-1}. Each sample was incubated for 30 min at 25°C following by rinsing the electrodes with PB and ultrapure water and measurements of EIS spectrum of the interface. The analytical curves were obtained by plotting the relative response percentages (RR%) of each NS1 sample *versus* the logarithmic concentration range of the target, with RR% obtained as

$$RR\% = \left[\left(\frac{1}{C_{q_n}} - \frac{1}{C_{q_0}}\right) \Big/ \frac{1}{C_{q_0}}\right] \times 100 \tag{4.1}$$

where $1/C_{q_0}$ corresponds to the inverse of the C_q value of the blank and $1/C_{q_n}$ as the inverse of the C_q value of each sampling interface.

The linear regression statistics of the analytical curves provided the limit of detection (LOD) and limit of quantification (LOQ), analytical parameters that were calculated according to the IUPAC definition as LOD = 3 $\times$ SD/b and LOQ = 10 $\times$ SD/b, where SD corresponds to standard deviation of the linear regression fitting with b as the slope (SHRIVASTAVA; GUPTA, 2011).

Accuracy of NS1 assay

Complementary assay was performing using a spike methodology to evaluate the accuracy of the signal amplification methodology in quantifying the NS1 biomarker in the serum samples. Three undiluted serum samples containing 2.5, 17 and 35 pg mL^{-1} of NS1 were prepared and were used for incubation of the biosensing interfaces during 30 min at 25°C on the biosensing interface. Afterwards, these electrodes were rinsed with PB and ultrapure water and characterised by EIS method. The RR% values were calculated by Eq. 4.1 and by interpolating the results to the analytical curve, from which the NS1 concentration in each spiked sample were estimated. The accuracy of NS1 concentration is mathematically defined as recovery percentage R(%) as following

$$R(\%) = \frac{[NS1]_m}{[NS1]} \times 100 \tag{4.2}$$

where [NS1] is the NS1 prepared concentration and $[NS1]_m$ is the concentration measured through the analytical curve. Values of $R(\%)$ that are close to 100% represent high accurate results.

4.3 Results and discussion

Similar for the SAM formation onto the typical electrode surfaces studied in chapter 3, an increment of Faradaic current is obtained for Pep–Fc SAM in the presence of 100 μM Fc–COOH, resulting in one-and-a-half-fold increased of j, as shown by the CVs curves obtained in the absence (orange) and presence (blue) of Fc–COOH in the electrolyte (see Figure 4.3*a*). The CV plots depict two well-formed oxidation and reduction peaks that lead to $^{E_f}/_e \sim 0.36$ V (within experimental error) and peak-to-peak separation of $\Delta E \sim 20$ mV. Therefore, this Faradaic process is considered electrochemically reversible owing to $\Delta E < 90$ mV at 0.1 V s^{-1}. Furthermore, this electrochemical reversibility is confirmed by noting that $^{i_{ox}}/_{i_{red}} \sim 1$ (BARD; FAULKNER, 2000).

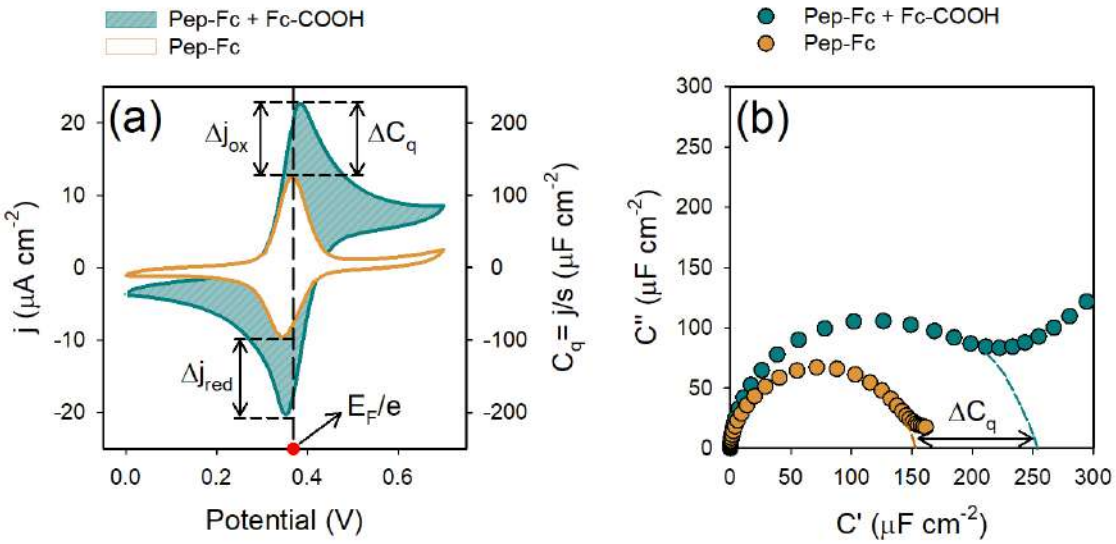

Figure 4.3: Increment of the electrochemical response due to increase in the number of available quantum channels within the interface favored by energy alignment at $E_F \sim 0.36$ eV. (a) CV response of a Pep-Fc SAM interface in the absence (orange curve) and presence (blue curve) of 100 μM Fc–COOH. The increase in the C_q at the interface is computed using the formula $C_q = i/s$, where s is the scan rate. (b) Nyquist capacitive diagrams for Pep-Fc SAM in the presence (blue circles) and absence (orange circles) of a redox Fc–COOH signal amplifier.
Source: (GARROTE; SÁNCHEZ, et al.*, 2024).*

This increase in the Faradaic j is the result of the electronic coupling between Fc states contained in the Pep-Fc interface with those of Fc–COOH free moieties, resulting in an increment of available N for electron transport from the solution phase (containing an Fc/Fc^+ redox pair associated with the Fc–COOH structure) to the electrode, as concluded in chapter 3. Recalling that this intermediate electron transport occurs without diffusive-controlled kinetics and the transport of electrons through mediating C_q moieties follows a quantum rate mechanical rule within a resistance quantum $R_q \sim 12.9$ kΩ.

Since $i = C_q s$, the capacitive increase observed in Figure 4.3*a* is in agreement with that obtained in Figure 4.3*b* by using ECS method. For instance, by comparing the semicircle diameters of the Nyquist capacitive plot (see Figure 4.3*b*) in the absence and presence of Fc–COOH; there is an increase in the capacitance from $\sim$ 150 μF cm^{-2} to $\sim$ 250 μF cm^{-2}, which is confirmed by the values reported in Table 4.2 that were obtained by fitting the data to the equivalent circuit model studied in chapter 3 (see Appendix I.1). Recalling that this C_q increment is related to an increase in the total number of N available for transporting electrons through the quantum capacitive states such as $N = {}^{k_B T C_q}/_{e^2 f(1-f)}$, as explained in chapter 3.

Table 4.2: Circuit parameters and calculated values for R_q, G, β and k, for Pep-Fc SAM containing or not 100 μM Fc–COOH. Values are reported as $\overline{x} \pm \sigma_{\overline{x}}$, where $\overline{x}$ refers to the mean average value and $\sigma_{\overline{x}}$ refers to the standard error of the mean of four independent modified miniaturized electrodes measured.

	0 μM	100 μM
C_q (μF cm^{-2})	160 $\pm$ 20	280 $\pm$ 30
R_s (Ω)	2,000 $\pm$ 100	2,200 $\pm$ 300
R_{qt} (Ω)	130 $\pm$ 20	240 $\pm$ 20
R_{td} (kΩ)		3000 $\pm$ 3000
R_q (Ω)	13,100 $\pm$ 700	19,000 $\pm$ 2000
G (mS)	8 $\pm$ 1	3.5 $\pm$ 0.8
β (Å^{-1})	1.345 $\pm$ 0.003	1.46 $\pm$ 0.02
k (s^{-1})	31 $\pm$ 4	12.3 $\pm$ 0.8

Source: (GARROTE; SÁNCHEZ, et al.*, 2024).*

It is important to highlight that the electrochemical performance of the modified miniaturized gold electrodes is similar to the redox SAM assembled onto the commercial disk electrodes used in chapter 3. As demonstrated in (DUTTA *et al.*, 2021), the control of the roughness factor is the key factor that influences the formation of the monolayer. Accordingly, miniaturized gold electrodes were fabricated with controlled roughness, which is evidenced in the previous electrochemical characterization.

Afterwards, the sensing interface was fabricated to evaluate the application of electrochemical signal amplification. Thus, in order to detect the NS1 biomarker, an anti-NS1 protein was attached to the Pep–Fc interface, each fabrication step was monitored by ECS performed at $\sim$ 0.36 V in 20 mM TBA in ACN/H_2O (1:4, v/v) in the absence and presence of the redox amplifier as Fig. 4.4*a* and *b* show, respectively. Note the steady response of the redox interface modified with the NS1 receptor (with and without signal amplifier) after to be embedded in commercial serum, meaning that the biological matrix has minimum effects on the capacitive response.

The capacitive response as a function of NS1 concentrations ([NS1]), measured in absence and presence of Fc–COOH in solution after the incubation step with the target, is shown in Fig. 4.5*a* and *b*, respectively. Afterwards, the obtained values of C_q were used to construct the analytical curves of NS1 with and without signal amplification aiming to analyse the sensitivity for both configuration. The RR% of each

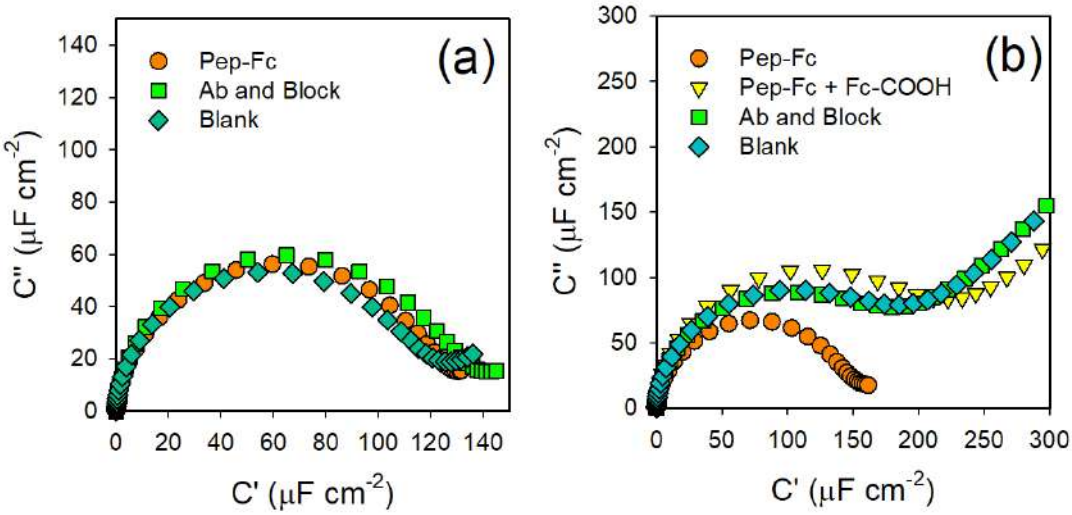

Figure 4.4: Capacitive Nyquist plot of the receptive interface fabrication process measured in 20 mM $TBAClO_4$ in ACN/H_2O (1:4, v/v) as supporting electrolyte in the (a) absence and (b) presence of 100 μM Fc-COOH. Note that the plot in orange circles related to Pep–Fc in (b) was measured without the redox probe in solution.

Source: Adapted from (GARROTE; SÁNCHEZ, et al.*, 2024).*

sample was calculated using Eq. 4.1 and plotted against the [NS1] to obtain the intended analytical curve (see Figure 4.6).

The assay without the signal amplifier shows a linear response in [NS1] ranging from 10^3 to 10^6 pg mL^{-1} within an r^2 linearity statistics of 0.98 (orange circles in Figure 4.6), whereas the assay response in the presence of Fc–COOH shows two linear responses: i) one within a lower [NS1] ranging from 10^{-2} to 10^3 pg mL^{-1} (r^2 of 0.99),

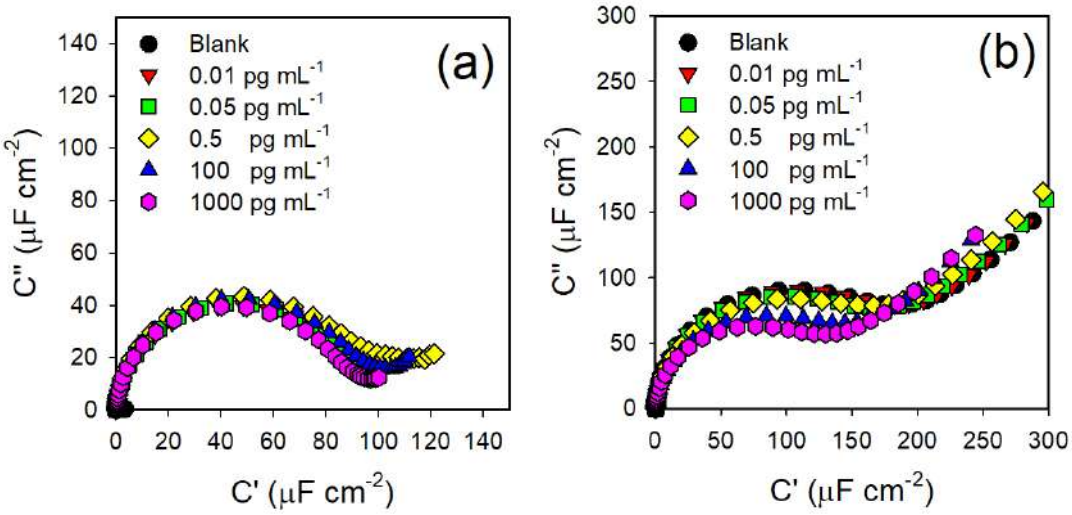

Figure 4.5: Capacitive Nyquist plot of some representative NS1 concentration performed in 20 mM $TBAClO_4$ in ACN/H_2O (1:4, v/v) as supporting electrolyte in the (a) absence and (b) presence of 100 μM Fc-COOH.

Source: Adapted from (GARROTE; SÁNCHEZ, et al.*, 2024).*

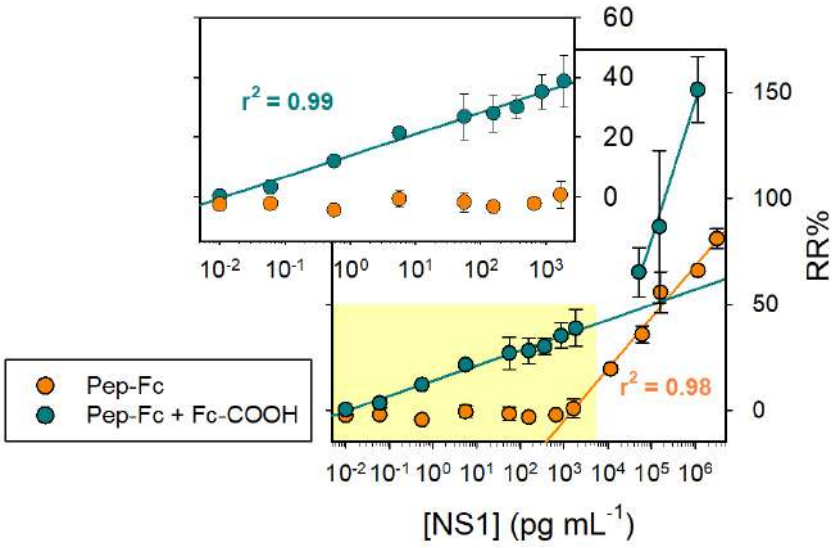

Figure 4.6: Relative response, RR%, of the biosensing assay comprising redox-peptide SAM (Pep–Fc) in the absence (orange) and presence (blue) of Fc-COOH as redox amplified (Pep–Fc + Fc-COOH) measured for different concentrations (ranging from 10^{-2} to 10^{6} pg mL^{-1}) of the analyte NS1. The yellow shadowed area corresponds to the inset figure that compares the performance of non-amplified and amplified analytical curves and linear regressions at lower NS1 concentrations, that is, from 10^{-2} to 10^{3} pg mL^{-1}.

Source: Adapted from (GARROTE; SÁNCHEZ, et al.*, 2024).*

as depicted in the inset, and ii) another within a higher [NS1] ranging from 5×10^4 to 10^6 pg mL^{-1}. Note that i) corresponds to the [NS1] range in which the assay without Fc–COOH was unable to respond. The LOD of this analytical curve was 0.7 pg mL^{-1} with a limit of quantification LOQ of 2.2 pg mL^{-1}. LOD and LOQ values for the non-amplified analytical curves were 0.5 ng mL^{-1} and 1.8 ng mL^{-1}, respectively. To summarize, it has been observed that the lower [NS1] detected with the signal amplifier was almost 1,000 times lower than the lowest [NS1] detected without the Fc-COOH, demonstrating that the energy alignment of the redox-free DOS states in the electrolyte with the DOS of the quantum capacitive interface does increase the sensitivity of redox capacitive biosensors by at least 1,000 times.

Finally, the recovery of RR% of $1/C_q$ signal of the interface with the amplifier signal was evaluated by means of the spike-like assaying methodology. Three commercial human serum samples containing 2.5, 17, and 35 pg mL^{-1} NS1 were prepared and incubated at the biosensing interface. After the measurement of the C_q signal of each sample, the RR% was calculated, which was replaced in the analytical curve in blue dots shown by the inset of Figure 4.6. In this way, the NS1 concentration were computed with a R(%) that can be calculated by comparing the concentration of the sample [NS1] with that effectively measured [NS1]$_m$ using Eq. 4.2. This R(%) analysis for the different samples is compiled in Table 4.3.

It can be observed that the obtained R(%) ascribed to the quantification of the samples containing 17 and 35 pg mL^{-1} of NS1 showed a very good R(%) that is close to 100%. The case of the 2.5 pg mL^{-1} that constitutes the lower [NS1] sample evaluated by this methodology demonstrated certain inaccuracy (R(%) = 140 $\pm$ 20%), which

Table 4.3: NS1 spike assays (duplicates) performed by computing the $1/C_q$ analytical signal using the amplifier signal methodology, as illustrated in Fig. 4.6

[NS1] (pg mL^{-1})	[NS1]$_m$ (pg mL^{-1})	R(%)
2.5	3.5 ± 0.4	140 ± 20
17.0	16 ± 5	100 ± 30
35	36 ± 3	103 ± 8

Source: (GARROTE; SÁNCHEZ, et al.*, 2024).*

is explained by the proximity of the 2.5 pg mL^{-1} concentration to LOQ of the assay. This represents a source inaccuracy owing to the fact that whenever looking for quantifying lower concentration close to the LOQ, there are errors owing to the fitting procedure to the analytical curve that, as expected, increases at this region of the analytical curve.

4.4 Conclusion

It was possible to demonstrate that the energy level alignment of capacitive and non-capacitive states permits the amplification of the electrochemical capacitive current signal of the interface for the quantification of the NS1 DENV biomarker in undiluted serum samples. Moreover, the use of miniaturized gold electrodes in the analytical assays demonstrated the potential use of this platform in PoC devices, which shows satisfactory results whenever the amplification of the signal is possible.

In spite of the detection of NS1 using capacitive interfaces has been already reported (CECCHETTO; FERNANDES, *et al.*, 2017; SANTOS; BUENO; DAVIS, 2018; CECCHETTO; SANTOS, *et al.*, 2020), this is the first time that NS1 has been quantified in undiluted serum samples with a capacitive transducer in picograms levels. Furthermore, the improving of the sensitivity obtained by applying this novel strategy can be important for the detection of small biological molecules, as well as the possibility of enhancing the specificity of the methodology by allowing the dilution of complex biological samples. Hence, false positive errors associated with matrix effects can be avoided, enabling a better analysis of small amounts of biological samples.

As a proof-of concept, it was shown that the sensitivity is possible to be increased by more than 1,000 times in the amplified quantum capacitive detection of NS1 DENV biomarker. For instance, the method enables the diagnosis of DENV infection at a very early stage that can be used in a PoC format.

References

AISSA, S. B. *et al.* Design of a redox-active surface for ultrasensitive redox capacitive aptasensing of aflatoxin M1 in milk. **Talanta**, v. 195, p. 525–532, 2019.

BAHADIR, E. B.; SEZGINTURK, M. K. A review on impedimetric biosensors. **Artificial Cells, Nanomedicine, and Biotechnology**, v. 44, p. 248–262, 1 2016.

BARD, A. J.; FAULKNER, L. R. **Electrochemical Methods Fundamentals and applications**. 2nd: John Wiley and Sons, 2000.

CECCHETTO, J.; FERNANDES, F. C., *et al.* The capacitive sensing of NS1 Flavivirus biomarker. **Biosensors and Bioelectronics**, v. 87, p. 949–956, 2017.

CECCHETTO, J.; SANTOS, A., *et al.* Serological point-of-care and label-free capacitive diagnosis of dengue virus infection. **Biosensors and Bioelectronics**, v. 151, p. 111972, 2020.

DEROCO, P.; WACHHOLZ J., D.; KUBOTA, L. Recent advances in point-of-care biosensors for the diagnosis of neglected tropical diseases. **Sensors & Actuators B: Chemical**, v. 349, p. 130821, 2021.

DUTTA, G. *et al.* Impact of surface roughness on the self-assembling of molecular films onto gold electrodes for label-free biosensing applications. **Electrochimica Acta**, v. 35, p. 138137, 2021. ISSN 0013-4686.

FERNANDES, F. C.; GÓES, M. S., *et al.* Label free redox capacitive biosensing. **Biosensors and Bioelectronics**, v. 50, p. 437–440, 2013.

FERNANDES, F. C.; SANTOS, A., *et al.* Comparing label free electrochemical impedimetric and capacitive biosensing architectures. **Biosensors and Bioelectronics**, v. 57, p. 96–102, 2014.

GARROTE, B. L.; LOPES, L. C., *et al.* Reagentless Quantum-Rate-Based Electrochemical Signal of Graphene for Detecting SARS-CoV-2 Infection Using Nasal Swab Specimens. **ACS sensors**, ACS Publications, v. 7, n. 9, p. 2645–2653, 2022.

GARROTE, B. L.; SÁNCHEZ, Y. P., *et al.* Electron transmittance by means of quantum capacitive states as a signal amplification mechanism for biosensing applications. **Sensors and Actuators B: Chemical**, v. 66, p. 134786, 2024. DOI: 10.1016/j.snb.2023.134786.

GARROTE, B. L.; SANTOS, A.; BUENO, P. R. Label-free capacitive assaying of biomarkers for molecular diagnostics. **Nature Protocols**, 2020. ISSN 1754-2189. DOI: 10.1038/s41596-020-0390-9.

GUZMAN, M. G. *et al.* Dengue infection. **Nature Reviews Disease Primers**, v. 2, p. 16055, 1 2016.

HERMANSON, G. **Bioconjugate Techniques**. 2nd: Academic Press Maryland Heights, 2008. p. 214–233.

LAND, K. *et al.* REASSURED diagnostics to inform disease control strategies, strengthen health systems and improve patient outcomes. **Nature Microbiology**, v. 4, p. 46–54, 2019.

LIU, Y. *et al.* Advances in signal amplification strategies for electrochemical biosensing. **Current Opinion in Electrochemistry**, v. 12, p. 5–12, 2018.

LOPES, L. C.; SANTOS, A.; BUENO, P. R. An outlook on electrochemical approaches for molecular diagnostics assays and discussions on the limitations of miniaturized technologies for point-of-care devices. **Sensors and Actuators A: Physical**, v. 4, p. 100087, 2022.

MARQUES, S. M. *et al.* Sensitive label-free electron chemical capacitive signal transduction for D-dimer electroanalysis. **Electrochimica Acta**, v. 182, p. 946–952, 2015.

MULLER, D. A.; YOUNG, P. R. The flavivirus NS1 protein: Molecular and structural biology, immunology, role in pathogenesis and application as a diagnostic biomarker. **Antiviral Research**, v. 98, p. 192–208, 2 2013.

P.A.H.O. **Reported cases of Dengue fever in the Americas. PLISA health information platform for the Americas**. 2023. Available from: `https://www3.paho.org/data/index.php/es/temas/indicadores-dengue/dengue-nacional/9-dengue-pais-ano.html`. Visited on: 26 Apr. 2023.

PICCOLI, J. *et al.* Redox Capacitive Assaying of C-Reactive Protein at a Peptide Supported Aptamer Interface. **Analytical Chemistry**, v. 90, n. 5, p. 3005–3008, 2018. ISSN 0003-2700. DOI: `10.1021/acs.analchem.7b05374`.

PINZON, E. F.; SANTOS, A.; BUENO, P. R. Density of States of a Nanoscale Semiconductor Interface as a Transduction Signal for Sensing Molecules. **ACS Applied Electronic Materials**, ACS Publications, v. 3, n. 8, p. 3411–3417, 2021.

SANTOS, A.; BUENO, P. R.; DAVIS, J. J. A dual marker label free electrochemical assay for Flavivirus dengue diagnosis. **Biosensors and Bioelectronics**, v. 100, p. 519–525, 2018.

SANTOS, A.; DAVID, J. J.; BUENO, P. R. Fundamentals and Applications of Impedimetric and Redox Capacitive Biosensors. **Journal of Analytical and Bioanalytical Techniques**, v. 7, p. 1–15, 016 2014.

SHRIVASTAVA, A.; GUPTA, V. B. Methods for LOD and LOQ determination. **Chronicles of Young Scientists**, v. 2, p. 21–25, 1 2011.

SILVA, J. V. *et al.* Current status, challenges and perspectives in the development of vaccines against yellow fever, dengue, Zika and chikungunya viruses. **Acta Tropica**, v. 182, p. 257–263, 2018.

Chapter 5

Influence of the Acidity of the Quantum Capacitive Interface on the Mediation of the Diffusionless Electron Transfer Process

This chapter deals with the examination of the influence of the acidity featuring the redox interface on the diffusionless kinetics. The acidity of the carboxylic acid groups located in the vicinity of redox sites from the SAM may influence not only on the charge process of quantum capacitive states but also the energy level alignment. In the previously chapter, it was shown that the accessibility of additional available quantum channels was successfully accomplished thanks to the energy level alignment, a particular setting for the ET that is favored when the energetic states of the redox capacitive molecules are at the same energy of non-capacitive redox states that are free in the solution phase environment. It has been shown that the occupancy of quantum states is susceptible to environmental changes(GARROTE; SANTOS; BUENO, 2019). Also, the diffusionless interfacial ET kinetics of electrode reactions is sensible to several factors such as λ, η, T, and `A/D` electronic coupling as introduced in chapter 1. Particularly, the pH of the environment has an effect on both diffusion and diffusionless redox reactions whenever the involved molecular structure has groups that undergo protonation/deprotonation reaction, such as carboxylic acid groups (DE SANTIS *et al.*, 1994; DEL CAÑO *et al.*, 2018; MÁRQUEZ *et al.*, 2020; TAN *et al.*, 2023), leading to the formation of positively/negatively charged interfaces or species accordingly the pH of the environment.

Accordingly, this chapter aims to study the effects of the electrostatic interactions between charged interfaces and redox species in solution due to deprotonation of their carboxylic groups, which impact the dynamics of ET in the interfaces as well as the energy level alignment. To do so, the acid dissociation constant pK_a of the Fc–COOH, non-electroactive and electroactive SAMs, were determined. Also, the electrochemical characterization of the Faradaic activity of Fc–COOH at different concentrations mediated by the quantum capacitive states of the redox monolayer were evaluated. The main specific objective of this chapter can be stated as:

- ☑ To study the effects of the electrostatic interaction between charged quantum capacitive interface and redox species free in solution, which undergo deprotonation of the carboxylic acid groups, on the diffusionless kinetics and the quantum properties such as C_q and R_q, by considering the effect of the different concentration of redox states free in solution environment in the electrodynamics

performed in the interface.

5.1 Introduction

Reactions involving only electron transfer have been discussed theoretically (chapter 1) and experimentally (chapter 2-4). However, atom transfer reaction can take place in addition to the ET, which is the case of the proton-coupled electron transfer (PCET) reactions. Such reactions involve a concerned (not necessary syncronous) transfer of electrons and protons (H^+) (MAYER, 2004) and they are reactions that depend on the the solvent properties. For instance, PCET reactions given in protic solvents are under different effect compared to those undergoing in aprotic solvents (MCCARTHY; DEMPSEY, 2017), where the capacity for forming hydrogen bonds is fundamental to stabilize the H^+ (BARRETTE; JOHNSON; SAWYER, 1984). Protic solvents contain hydrogens that form hydrogen bonds, such as those bonded to oxygen, nitrogen, or sulfur, which can exchange H^+ rapidly, whereas aprotic solvents have all their hydrogen is bound to carbon, lacking this feature (CAREY; SUNDBERG, 2007).

An example of PCET reaction is the one undergone by ferrocenylcarboxylic acid-based molecules ($Fc(CH_2)_nCOOH$), which is strongly dependent on pH (DE SANTIS *et al.*, 1994). For those molecules, it has been demonstrated that the pH influences the formal potential value, wherein the position of the acid group, which can be modulated by the number of bridging methylene units ($(CH_2)_n$), defines the strength of the carboxylic acid, in such way that the closer the carboxylic acid group to the Fc/Fc^+, the stronger the carboxylic acid group (DE SANTIS *et al.*, 1994). This feature is quantified by the acid dissociation constant pK_a, low values of pK_a indicate the facility to give H^+ (PETRUCCI; HARWOOD; HERRING, 2002). For instance, the ferrocenecarboxylic acid (Fc–COOH) undergoes deprotonation easily owing to intramolecular charge stabilization by electrostatic effect, in comparison with its counterparts when n equals 1 or 2 methylene units (DE SANTIS *et al.*, 1994). In addition, when the metal centre of Fc–COOH is in the oxidized form, the value corresponding to $pK_a(Fc^+) \sim 4.5$ is lower than that for the reduced form $pK_a(Fc) \sim 7.8$. The PCET reaction for Fc–COOH is described by the scheme in Fig 5.1*a*.

The pH dependency of the E_F/e is a typical characteristic of PCET systems (see Fig. 5.1*b*), which can be exploited for the pK_a determination using electrochemical methods such as the potential sweep techniques (COSTENTIN; ROBERT; SAVÉANT, 2010) for redox molecules in solution (DE SANTIS *et al.*, 1994; VĚŽNÍK *et al.*, 2019). This phenomenon is pictured in Fig 5.1, which shows the potential-pH plot (see Fig 5.1*b*), known as Pourbaix diagram, for one electron-one proton (e^-/H^+) process for the Fc–COOH (see Fig 5.1*a*). This diagram indicates the regions of existence of the oxidized/reduced protonated (i.e, Fc^+–COOH/Fc–COOH) and deprotonated (i.e, Fc^+–COO^-/Fc–COO^-) species. Note that at the extreme of the pH-axis the redox process is pH-independent (horizontal solid lines), whereas between $pK_a(Fc^+) - pK_a(Fc)$, the redox process is pH-dependent (slope), that is, wherein the PCET reaction takes place (COSTENTIN; ROBERT; SAVÉANT, 2010).

The relationship between pH and E_F/e is given by Eq. 5.1 (COSTENTIN; ROBERT; SAVÉANT, 2010), where $E_F/e(app)$ is the measured formal potential, E_F°/e is the standard formal potential, R is the ideal gas constant, $K_a(Fc)$ and $K_a(Fc^+)$ are the acid

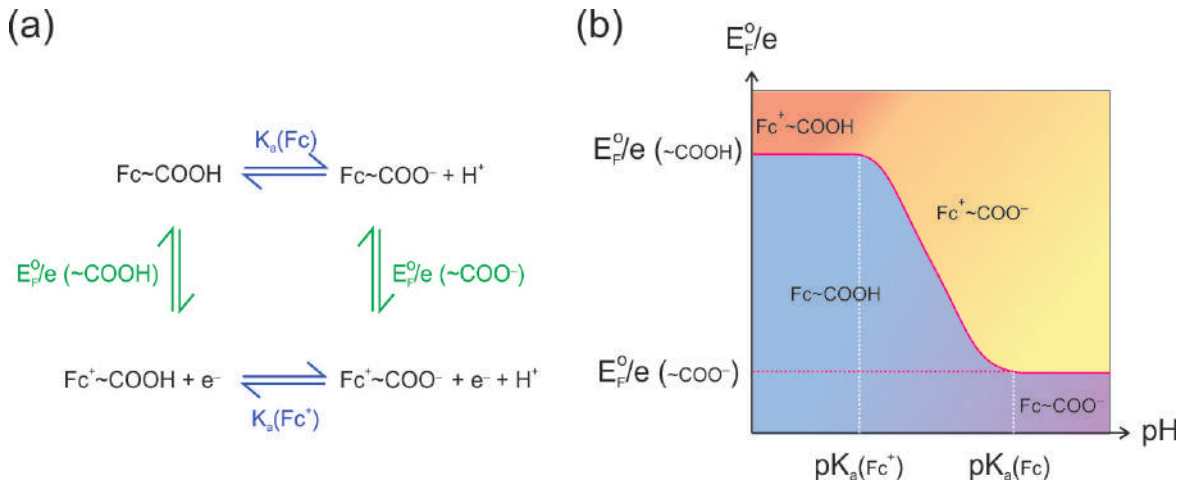

Figure 5.1: (a) Proton-coupled electron transfer reaction for Fc–COOH in aqueous solvent. (b) Pourbaix diagram showing E_F/e as function of pH for e^-/H^+ system in (b). Solid line separates the oxidized and reduced species and its slope is expected to be around 60 mV/pH unit, whereas dotted lines delimit the separation of regions of existence of protonated and deprotonated species. The intersection of the solid and doted line indicates the pK_a values.
Source: Adapted from (DE SANTIS et al.*, 1994; COSTENTIN; ROBERT; SAVÉANT, 2010).*

dissociation constants of reduced and oxidized forms, respectively. Eq. 5.1 can be characterized by electrochemical measurements as aforementioned.

$$E_F/e(app) = E_F^\circ/e + \frac{RT}{F} ln \left[\left(\frac{K_a(Fc)}{K_a(Fc^+)} \right)^{(1/2)} \left(\frac{[H^+] + K_a(Fc^+)}{[H^+] + K_a(Fc)} \right) \right] \tag{5.1}$$

Also, some electroactive interfaces can undergo PCET reactions such as redox protein-nanoparticles conjugates (DEL CAÑO *et al.*, 2018), iron porphyrind-based monoalyers (MÁRQUEZ *et al.*, 2020) and metallopolymers (TAN *et al.*, 2023), which are characterized by containing electronegative atoms in their chemical structure that participate in the H^+ exchange. Hence, the solution pH influences the ET kinetics of such electroactive monolayers (COSTENTIN; ROBERT; SAVÉANT, 2010). For that reason, the evaluation of the dissociation constant of redox interfaces of this nature is an important task to be performed to study not only the ET kinetics but also the associated mechanism.

In chapter 3, it was shown that an increment of quantum channels available for ET reaction was achieved due to an energy alignment between energy levels of capacitive (redox molecule within interface the) and non-capacitive (redox molecule free in solution) states, whose ET kinetics obeys the quantum mechanical principle. In this context, the influence of the acidity of the quantum capacitive interface on the diffusionless kinetics is evaluated in this chapter. The ET reaction of Fc–COOH, at different concentrations, was studied with the intermediation of ferrocene-tagged SAM using the quantum rate theory. Furthermore, the results of the ET mediation were compared with the effect of a molecular dielectric by using a non-electroactive monolayer with an equivalent chemical structured to the ferrocene-tagged SAM, which supports the assumption of the ET mechanism mediated by capacitive states.

5.2 Materials and methods

The general experimental methodology followed the procedure described in section 2.2. Two peptides were used in order to obtain the SAMs; the ferrocene-tagged peptide Fc-Glu-Ala-Ala-Cys-NH_2 (used in section 3) and the non-redox peptide Glu-Ala-Ala-Cys-NH_2. Note that the chemical structure of both peptides only differs by the ferrocene molecule.

5.2.1 Chemical reagents

Table 5.1 compiles additional reagents used in the development of this chapter, the enterprise where they were purchased from and their purpose. Information of additional reagents used are found in Tables 2.1 and 3.1. Aqueous solutions were prepared using Milli-Q water (Simplicity®water purification system, Millipore, 18.2 MΩ cm at 25°C).

Table 5.1: List of chemical reagents used in chapter 5.

Reagent	Company	Purpose
Acetic acid (CH_3COOH)	synth	Britton–Robinson buffer solution preparation for pK_a determination
Boric acid (H_3BO_3)	Sigma-Aldrich	
Phosphoric acid (H_3PO_4)	Sigma-Aldrich	
Potassium ferricyanide ($K_3[Fe(CN)_6]$)	Sigma-Aldrich	Electroactive species for pK_a determination of SAM
Potassium ferrocyanide ($K_4[Fe(CN)_6]$)	Synth	

5.2.2 Peptide synthesis and characterization

Non-electroactive peptide Glu-Ala-Ala-Cys-NH_2 was synthetized by solid-phase peptide synthesis using the Fmoc-strategy on Rink amide resin (0.5 mmol g^{-1}), where the peptide cleavage from the resin was performed after the removal of Fmoc of the N terminus (Glu), as described in section 3.2. Also, the purification and subsequent characterization was carried out as described in section 3.2 (see Appendix J).

5.2.3 Equipment and electrodes

Electrochemical measurements were performed using the AUTOLAB potentiostat, the three-electrode electrochemical cell and supporting electrolyte (20 mM $TBAClO_4$ in ACN/H_2O 1:4, v/v) as reported by chapter 2 for the typical characterization, whereas for the measurements in pH-controlled medium, the modification of the supporting electrolyte are described latter. Gold working electrodes were pre-treated as described in chapter 2. Mean average EAA of 0.045 and 0.042 cm^{-2} were obtained for the deposition of non-redox (Pep–SAM) and redox peptide (Pep–rSAM) monolayers, respectively; and were used to normalize electrochemical signals for calculating current densities and capacitances per unit of area for both SAMs.

Self-assembled monolayer fabrication: Right after the sulphuric acid cleaning step, the electrodes were rinsed with water and dried with nitrogen. Posteriorly, they were immersed for 16 h at room temperature (25 °C) in 2 mM of either non-electroactive or electroactive peptide in ACN/H_2O (1:1, v/v) to obtain the Pep–SAM and Pep–rSAM, respectively, according to (GARROTE; SANTOS; BUENO, 2020). In chapter 3 and chapter 4, the redox monolayer was named Pep–Fc, in this chapter we referred to this same monolayer as Pep–rSAM for simplicity.

5.2.4 Electrochemical measurements

The electrochemical response of Fc–COOH at different concentrations [Fc–COOH] was measured using bare and modified electrodes with peptide monolayers with either electroactive or non-electroactive characteristic, that is Pep–rSAM and Pep–SAM, respectively. CVs were recorded as described by chapter 2, from which the E_F/e of the Fc–COOH in the different settings was obtained. Afterwards, EIS was conducted at the related E_F/e as well as at V_{out}, as detailed in chapter 2. Capacitive spectra were constructed using a complex capacitive function obtained from the EIS raw data as already explained previously.

Preparation of Fc–COOH aliquots: A stock solution of 1500 μM Fc–COOH was prepared in 20 mM $TBAClO_4$ in ACN/H_2O (1:4, v/v). Subsequently, serial dilutions were performed using 20 mM $TBAClO_4$ in ACN/H_2O (1:4, v/v) as the diluent to prepare Fc–COOH aliquots with concentrations ranging from 1 to 1500 μM Fc–COOH.

Determination of pKa

The pK_a of the Fc–COOH, Pep–SAM and Pep–rSAM were determined by differential pulse voltammetry (DPV) using the same three-electrode cell. The measurements were performed on buffered solutions prepared using the Britton–Robinson system. The potential sweep in anodic and cathodic directions (potential range for Fc–COOH of 0 – 0.7 V and for both SAMs of -0.2 – 0.7 V) were carried out at pulsed potential (70 mV) during and short pulses (70 ms). Also, ECS was used for the pK_a calculation of the particular case of Pep–rSAM, wherein the EIS were measured on the same buffer solutions at E_F/e calculated from the related DPV profiles.

Preparation of Britton-Robinson buffer solutions: The electrolyte medium constituted by 20 mM $TBAClO_4$ in ACN/H_2O (1:4, v/v) was modified using the Britton–Robinson system to obtain buffer solutions in the pH range of 3 – 8.3. Buffered electrolyte solutions were prepared from an equal mixture of 0.04 M CH_3COOH, 0.04 M H_3BO_3, and 0.04 M H_3PO_4 (MONGAY; CERDA, 1974). The pH value was adjusted using 0.2 M NaOH. The pH of the buffer solutions was measured using a glass electrode (Sensoglass). For the pK_a determination of Fc–COOH, the buffer solutions were prepared with 100 μM Fc–COOH. Whereas for the pK_a determination of Pep–SAM, 2 mM $[Fe(CN)_6]^{3-/4-}$ was used as electroactive species in the buffer preparation. In particular, for the pK_a determination of Pep–rSAM, non-redox probe was added in the buffered electrolyte solution.

5.2.5 Equivalent circuit analysis

The values of the circuital elements were obtained by fitting EIS or capacitive spectra, using an equivalent circuit based on the previously studied in chapter 3 (see Fig. 3.2), otherwise will be indicated. The values of equivalent circuit elements obtained from the fitting were reported as a mean value $\bar{x}$ with the standard error of the mean ($\bar{x} \pm \sigma_{\bar{x}}$) calculated for two (Pep–SAM) and for three (Pep–rSAM) independently fabricated interfaces.

5.3 Results and discussion

5.3.1 PCET reaction of the Fc–COOH free in solution

The electrodynamics between the Fc–COOH free in solution and the gold electrode is controlled by diffusion process (see Appendix K), as expected for heterogeneous reaction between the redox probe in solution and metallic electrode. Once the Fc–COOH species reach the metallic surface, the ET reaction proceeds under electrochemical reversibility, as shown in the CV in Fig.5.2, wherein well-defined peaks are depicted for

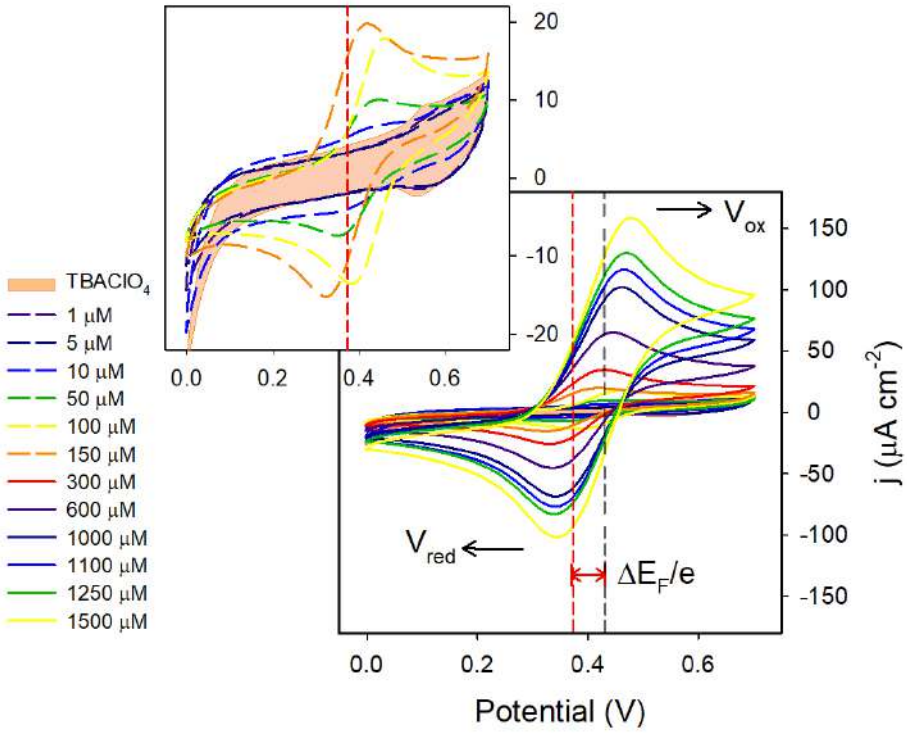

Figure 5.2: Cyclic voltammetry of Fc–COOH at different concentrations in ACN/H_2O (1:4, v/v) performed using bare gold electrode. The inset shows that the electrochemical response at low [Fc–COOH] is indistinguishable from the non-faradaic capacitive of the electrolyte medium ($TBAClO_4$). The red dashed vertical line indicates the $E_F/e \sim 0.36$ V, which shifts to higher potential as the [Fc–COOH] increases ($\Delta E_F/e$). The peak potential shifting V_{red} and V_{ox} to lower and higher potentials, respectively, leads to the electrochemical response out of equilibrium, with $\Delta E > 90$ mV.

Source: Author (2023).

concentration higher than 50 μM. They correspond to redox reaction of ferrocenecarboxylic/ferroceniumcarboxylic acid on the electrode surface. For concentrations between 50 - 600 μM, the obtained parameters that feature electrochemical reversibility, that is $\Delta E < 90$ mV and $i_{ox}/i_{red} \sim 1$, are in agreement with the expected values (BARD; FAULKNER, 2000). Note that the ET process of concentrations lower than 50 μM goes unnoticed, as shown by the inset in Fig.5.2, owing to the resultant Faradaic current not surpassing the non-Faradaic current that constitutes the double layer capacitance of $\sim$ 20 μF cm^{-2} (see Fig.5.3*b*), which is close to what is reported in the literature (10 – 40 μF cm^{-2} (BARD; FAULKNER, 2000)). Whereas as [Fc–COOH] increases, the resultant Faradaic current surpasses the non-Faradaic current.

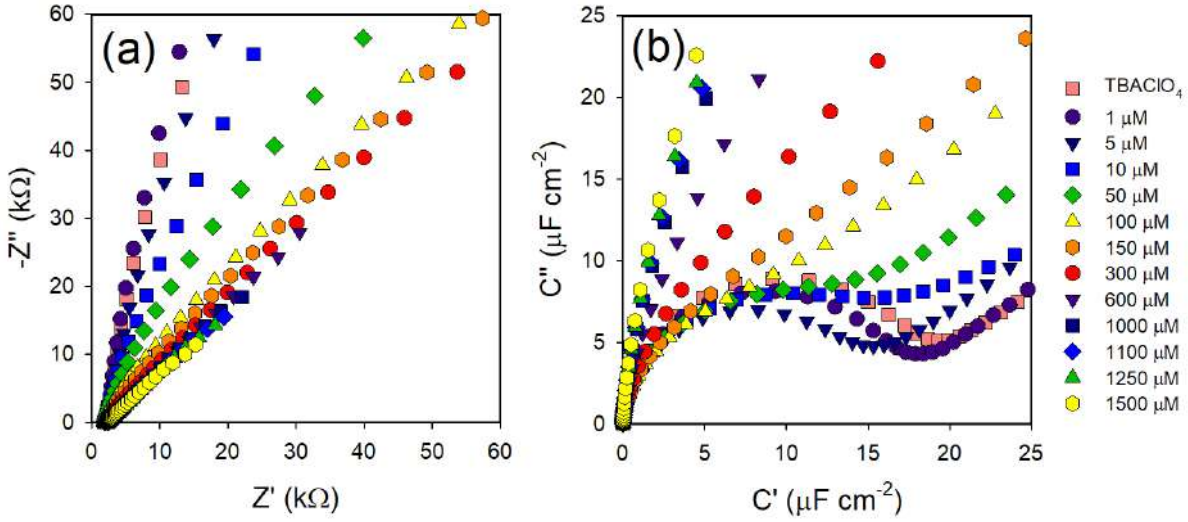

Figure 5.3: Complex impedance (a) and capacitive (b) diagrams of Fc–COOH at different concentration in ACN/H_2O (1:4, v/v), measured using unmodified electrode.
Source: Author (2023).

The influence of the acidity of the carboxylic group of the ferrocene on the ET process is observed in Fig.5.4*a*, which is in agreement with that noted in the literature (DE SANTIS *et al.*, 1994). E_F/e close to low potentials (i.e., $\sim$ 0.36 V) is characteristic of the redox process of the deprotonated form of the ferrocene Fc–COO^- (DE SANTIS *et al.*, 1994), which is confirmed by the electrochemical determination of the pK_a shown in Fig.5.4*b*. The plot depicts E_F/e *versus* pH, where the values of V_{ox} and V_{red} for the determination of E_F/e at certain pH were obtained from the corresponding DPV anodic and cathodic curves, respectively (see Fig.5.4*a*). Note that the pH-independent acid region is absent in Fig.5.4*b*, this is due to the $TBAClO_4$ precipitating at buffered solutions with pH < 3.

Fig.5.4*b* depicts the pH-dependent region (inclined curve) and the pH-independent basic region. The intercept of the linear trend of both characteristic regions indicate the pK_a value (i.e., 5.47 $\pm$ 0.03). Therefore, the ferrocenecarboxylic acid in 20 mM $TBAClO_4$ in ACN/H_2O (1:4, v/v) with a pH = 6.67, undergoes redox reaction with the gold electrode (m) in its deprotonated form in agreement with the literature (DE SANTIS *et al.*, 1994), as follows

$$Fc - COO^- \rightleftharpoons Fc^+ - COO^- + e^-(m) \tag{5.2}$$

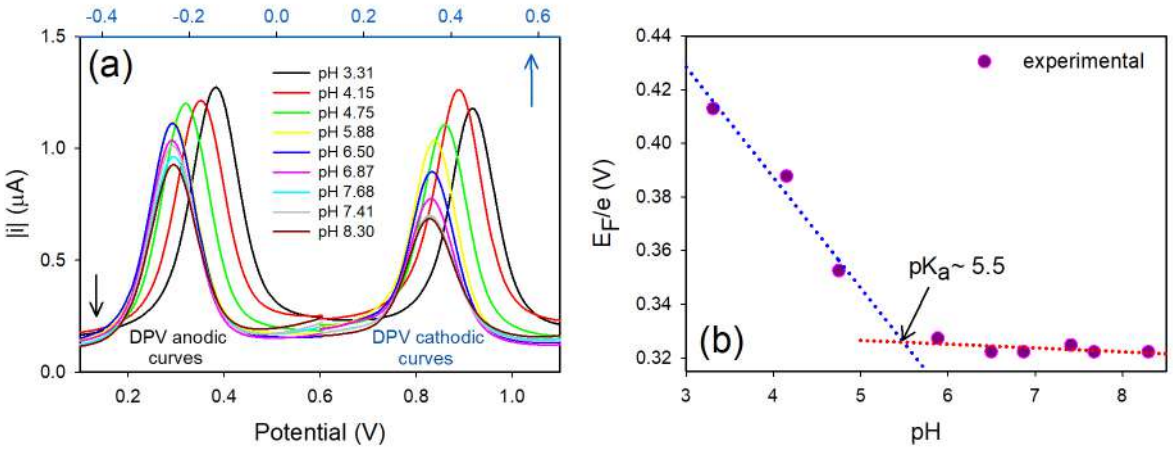

Figure 5.4: Acid dissociation constant determination of Fc–COOH. (a) DP anodic and cathodic voltammograms for buffered solutions of Fc–COOH varying the pH. The corresponding values of V_{ox} and V_{red} were used to determine $^{E_F}/_{e}$ in (b). (b) Pourbaix diagram of the PCET of Fc–COOH in organic/aqueous solvent. The intercept of the inclined curve (with a slope ~ 40 mV/pH) and the constant line informs on the value of $pK_a \sim 5.5$.

Source: Author (2023).

5.3.2 Influence of the acidity of the non-electroactive interface on the ET reaction of the Fc–COOH in solution

Whenever the electrode is modified with a non-redox monolayer, the electrochemical reversibility described by Eq. 5.2 is disrupted, as is the case of the Pep–SAM obtained by using a non-redox peptide. The CVs shown in Fig.5.5 depict profiles that do not follow the Nernstian behavior, that is, the electrochemical response upon change of potential cannot be predicted by the Nernst Equation (BARD; FAULKNER, 2000). For instance, at $^{E_F}/_{e}$ the concentrations of oxidized and reduced species at the electrode surface are not equal leading to nonequivalent anodic and cathodic currents. For that reason, the obtained peaks are not properly defined, and the values of the parameters $\Delta E > 180$ mV and $^{i_{ox}}/_{i_{red}} \neq 1$ corroborate that the electrochemical activity is far from the reversibility, contrary to what is obtained for the bare electrode (see Fig.5.2). The change in electrochemical response of Fc–COO^-/Fc^+–COO^- caused by the peptidic monolayer implies that although Pep–SAM does not act as a total molecular blockage, it represents a potential barrier to be overcome for the ET to succeed, as described in chapter 1. Therefore, the obtained Faradaic current is lower than that measured for the bare electrode (see Fig.5.8*a*).

The molecular dielectric of the Pep–SAM contributes to the non-Faradaic capacitive response (GOES *et al.*, 2012; LEHR *et al.*, 2017) shown by the blue shadowed in the inset of Fig.5.5, which is not distinguished from that current-voltage curves of low [Fc–COOH], possibly due to the very low Faradaic current. Note that for concentrations higher than 50 μM, the $^{i_{ox}}/_{i_{red}} < 1$ suggests that the reduction tends to be more favored over the oxidative reaction, regardless of the ET process is limited by the diffusion (see Appendix L). This is attributed to the negatively charged surface of the Pep–SAM owing to the deprotonation of the carboxylic groups of Glu at one extremity of the non-redox peptide, which was deduced by analyzing the pK_a of Pep–SAM. The electrochemical determination of this pK_a was based on the Faradaic current suppression due to changes of pH (ZHAO *et al.*, 1999), using electroactive

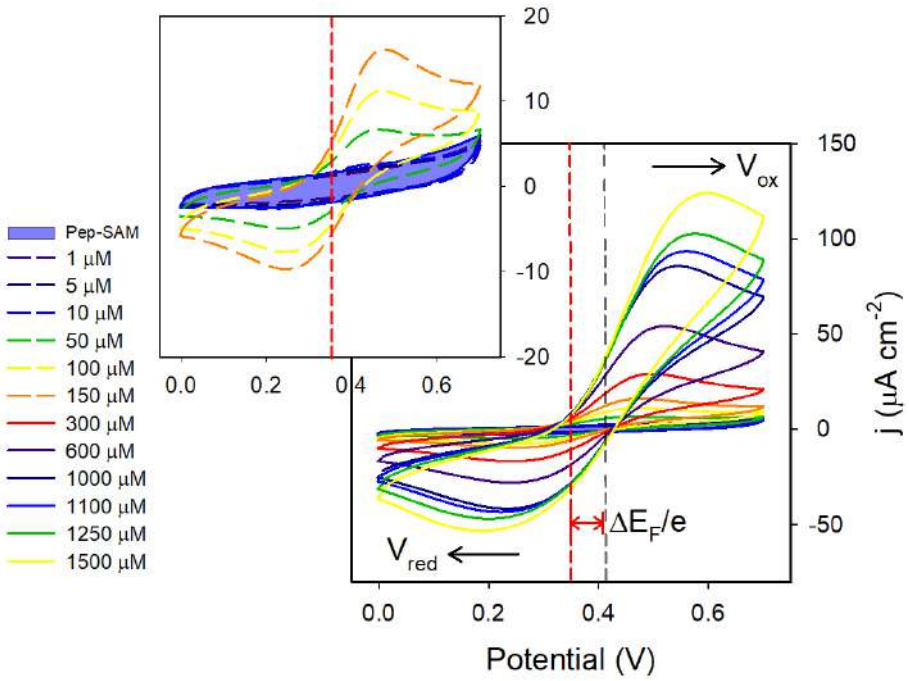

Figure 5.5: Cyclic voltammetry of the non-redox monolayer SAM measured at different concentrations of Fc–COOH in ACN/H_2O (1:4, $^{v}/_{v}$). The inset shows that the electrochemical response at low [Fc–COOH] is coverd up by the non-faradaic capacitive of molecular dielectric of SAM. The red dashed vertical line indicates the $^{E_F}/_{e}$, which shifts to higher potential as the [Fc–COOH] increases ($\Delta^{E_F}/_{e}$). The peak potential shifting V_{red} and V_{ox} to lower and higher potentials, respectively, implies an non-equilibirum electrochemical, with $\Delta E > 90$ mV.
Source: Author (2023).

species, such as $[Fe(CN)_6]^{3-/4-}$ (SWEBOCKI *et al.*, 2020; FARIAS *et al.*, 2021). In this way, the changes of Faradaic current observed in the DP anodic and cathodic voltammograms measured at different pH (see Fig. 5.6*a*), allowed us to determine the pK_a of Pep–SAM whether by using the anodic ($pK_a = 5.1 \pm 0.1$) or cathodic ($pK_a = 5.2 \pm 0.1$) peak currents (see Fig. 5.6*b* and *c*). The obtained pK_a indicates that in the studied electrolyte medium, the Pep–SAM surface is charged negatively, which does not affect the approach of the Fc^{+}–COO^{-} species to be reduced.

The impedance data depicted in Fig. 5.7 revels detailed information about the influence of this molecular dielectric on the ET of the redox probe. In particular, the capacitive Nyquist plot shown in Fig. 5.7*b* confirms the non-Faradaic capacitance observed in Fig. 5.5, which is barely modified as the [Fc–COOH] increases. This non-Faradaic capacitance is known as C_t, which was introduced in chapter 2 (see Table 2.2), its value can be obtained by equivalent circuit fitting (see Appendix M), which is found between ~ 7 and ~ 9 μF cm^{-2} (see Table 5.2).

Note that impedimetric Nyquist plot reveals an interesting activity (see Fig.5.7*a*), well defined semi-circles appear at concentration higher than 150 μM Fc–COOH, whose diameter report on the charge transfer resistance R_{ct}. The values obtained by equivalent circuit fitting vary between 30 - 290 kΩ (see Table 5.2). This resistance decreases exponentially with the increment of [Fc–COOH] as depicted in Fig.5.8*b*, which is in accordance with the rise of the peak currents shown in Fig.5.8*a*. It is worth highlighting that the R_{ct} values in the presence of the monolayer are 1000-fold higher

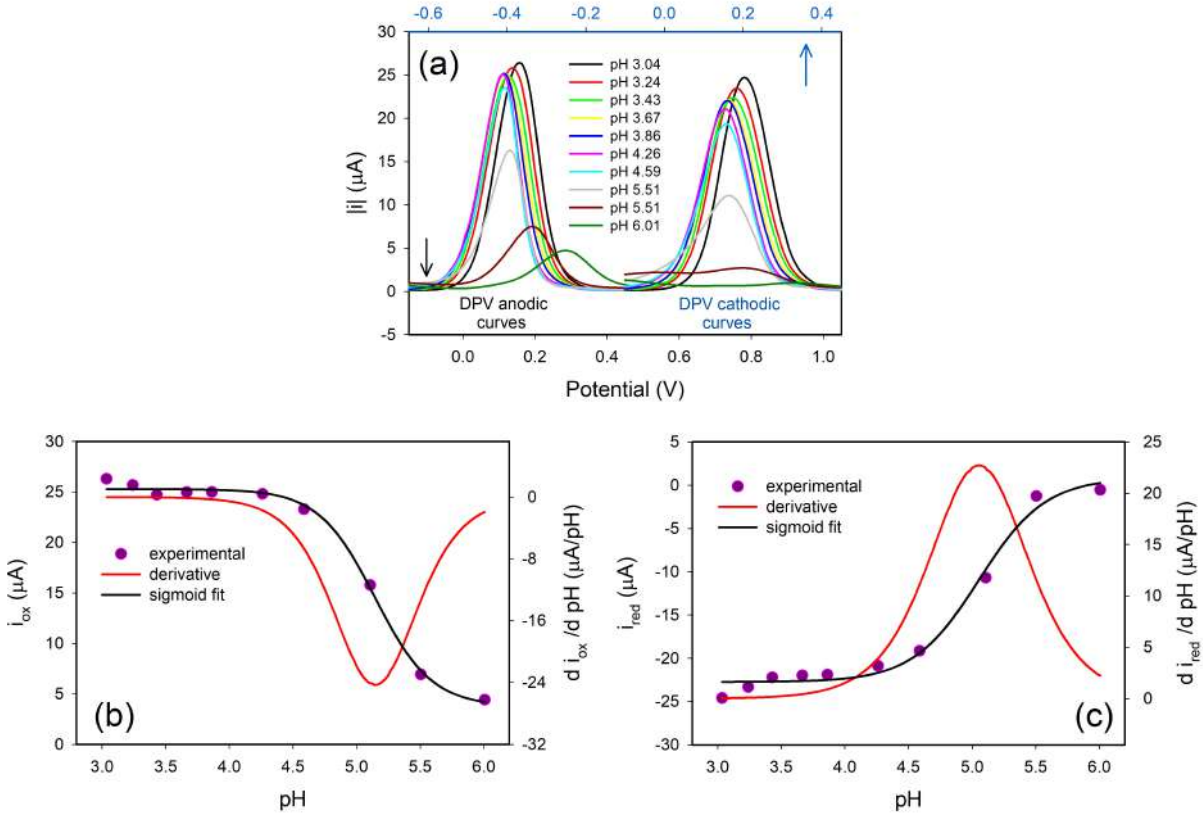

Figure 5.6: Acid dissociation constant determination of Pep–SAM. (a) DP anodic and cathodic voltammograms for buffered solutions varying the pH. Obtained values of anodic (b) and cathodic (c) peak currents from (a) *versus* pH. Both plots depict a sigmoid tendency in function of pH and the related peak values of the derivative plot of the sigmoid fit informs on the value of $pK_a \sim 5.2$.

Source: Author (2023).

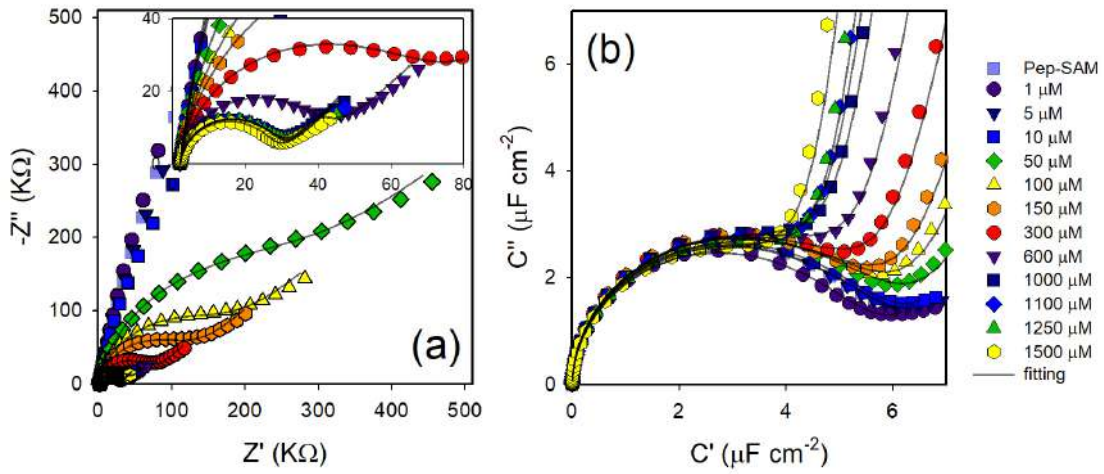

Figure 5.7: Complex impedance (a) and capacitive (b) diagrams of the non-redox monolayer SAM measured at different concentrations of Fc–COOH in ACN/H_2O (1:4, v/v).

Source: Author (2023).

than those for Fc–COOH in solution in the bare gold electrode (see Fig.5.8*b*), which demonstrates the insulating feature of the non-redox peptide monolayer.

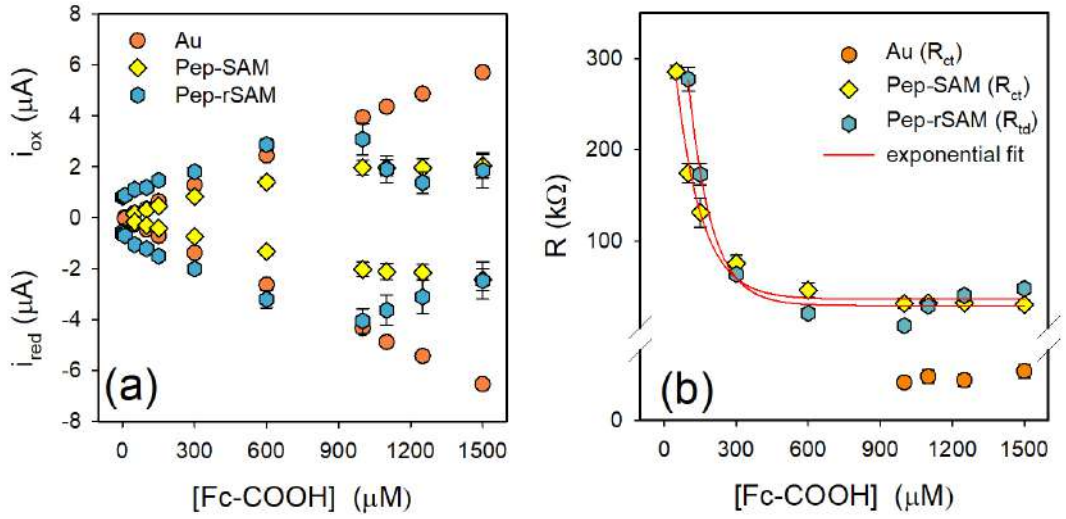

Figure 5.8: Comparison of the peak current (a) and resistance values (b) in function of [Fc-COOH] for the three different systems; unmodified electrode (Au), Pep–SAM and Pep–rSAM. Note that in (b) the resistance for Au and Pep–SAM is referred as R_{ct} whereas for PEp–rSAM is R_{td} as introduced in the chapter 3. Exponential decay regression for Pep–SAM (r^2 = 0.9897) and Pep-rSAM (r^2 = 0.9826) indicate that the corresponding resistance decreases exponentially with [Fc-COOH]. There are only R_{ct} values for the most concentrated Fc–COOH solutions measured using bare electrode due to the related values of the diluted solutions were not possible to be obtained within an acceptable fitting error.

Source: Author (2023).

For Pep-SAM (non-electroactive) the quantized properties (e.g., C_q) cannot be experimentally accessed owing to there are not confined quantum redox states in its molecular structure. However, the Faradaic activity observed in the current-voltage plot when redox species are in solution, such as Fc–COOH (or even $[Fe(CN)_6]^{3-/4-}$), is the result of that the ET follows the tunneling mechanism, which operates at nanoscale molecular thickness as is the case of this SAM, which only differs from that studied in chapter 3 by the ferrocene molecule bonded in the terminal of the peptidic structure.

5.3.3 Influence of the acidity of the electroactive interface on the ET reaction of the Fc–COOH in solution

In contrast to the scenario where a considerable increment of R_{ct} was observed for the redox reaction between the Fc–COOH and the electrode, caused by the "blocking effect" of the non-redox peptide insulating layer, the quantum capacitive states represent a excellent strategy for suppressing such blockade due to the associated electronic structure acts as the available channels for electrons to be transferred with a minimum resistance (i.e., $R_q \sim 12.9$ kΩ). The mediation of the ET between redox states in solution and that of the electrode by the redox capacitive states was described by chapter 3, wherein the particular concentration of 100μM Fc–COOH was studied.

Since the ET mediation is based on the energy level alignment, the capability of this feature in terms of the robustness of energy coupling was tested herein, considering that the more Fc–COOH species are in solution, the more E_F/e (or Fermi level) shifting is observed, as shown in Fig. 5.9.

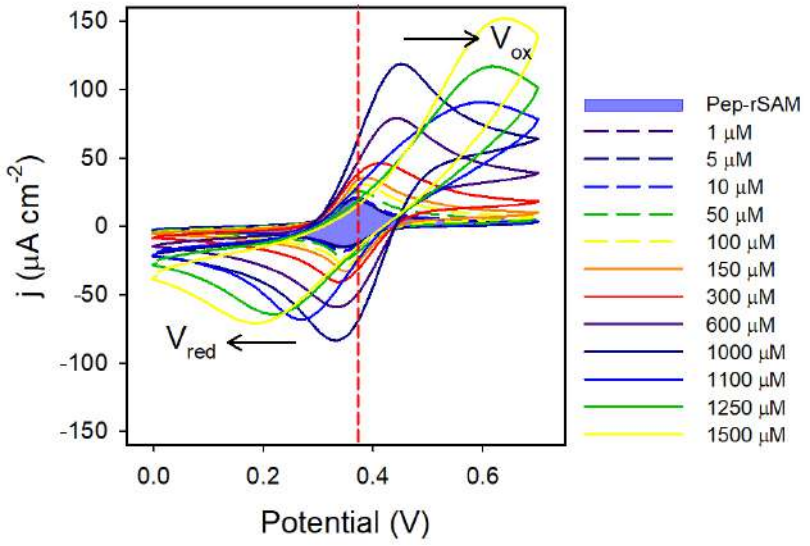

Figure 5.9: Cyclic voltammetry of the redox monolayer Pep–rSAM measured at different concentrations of Fc–COOH in ACN/H_2O (1:4, v/v). The red dashed line indicates the E_F/e, which shifts to higher potential as the [Fc–COOH] increases ($\Delta E_F/e$). The peak potential shifting V_{red} and V_{ox} to lower and higher potentials, respectively, lead to the electrochemical response out of equilibrium, $\Delta E > 90$ mV.

Source: Author (2023).

Although the redox process of tethered Fc and free Fc–COOH are coupled, as shown in the CV (see Fig. 5.9), wherein single peaks for reduction and for oxidation are depicted, it is evident that the electrochemical behavior of the whole system changes in function of [Fc–COOH]. Firstly, it's worth noting that the electrochemical reversibility, $\Delta E < 90$ mV and $i_{ox}/i_{red} \sim 1$, is maintained at [Fc–COOH] < 600 μM. Within that concentration range, there is an increment of Faradaic current compared to the direct redox reaction with the electrode (Fig. 5.8*a*). This is expected because of the availability of conductive quantum channels of Pep–rSAM ($C_q \propto$ DOS) resulting from the sustained energy level alignment (see Table 5.2), that is, the obtained value of E_F/e is found around of 0.36 – 0.37 V.

While Faradaic current varies linearly with [Fc–COOH] in concentration between 1 - 600 μM, a significant deviation from this behavior is observed when [Fc–COOH] ≥ 1000 μM, where the Faradaic current drastically decreases, as shown in Fig. 5.8*a*. This decrease in Faradaic current is attributed to the surface charge of the Pep–rSAM, resulting from deprotonation of the carboxylic groups of Glu. Although it was not possible to determine the pK_a using the Pourbaix diagram due to the studied pH range, which did not yield the pH-independent acid region (see Fig. 5.10*b*), the change of C_q in function of pH allowed for this determination (see Fig. 5.10*d*). The obtained value of $pK_a \sim 4.5$ was close to that of Pep–SAM, that is, $pK_a \sim 5$.

Thus, the negatively charged surface of Pep–rSAM does not affect the ET mediation by the C_q states at [Fc–COOH] ≤ 600 μM, allowing Fc–COO^-/Fc^+–COO^- to

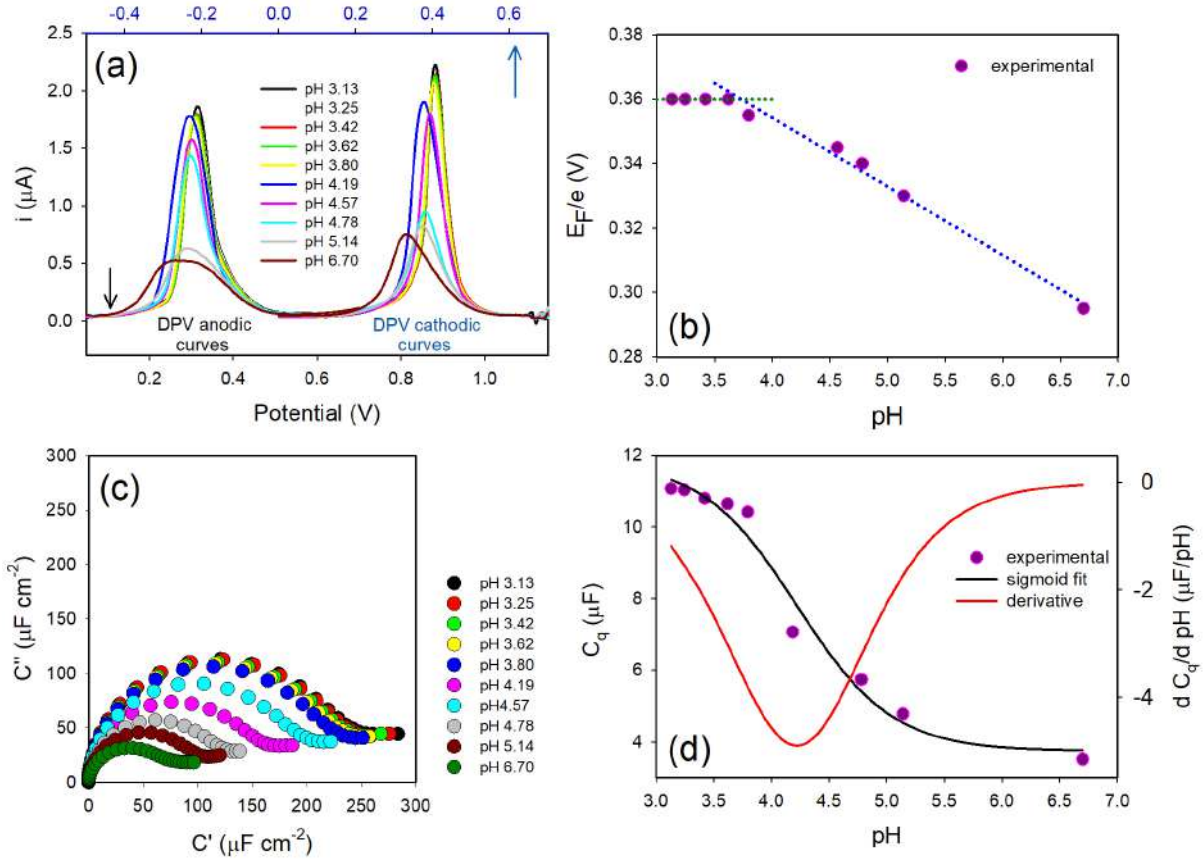

Figure 5.10: Acid dissociation constant determination of Pep–rSAM. (a) DP anodic and cathodic voltammograms for buffered solutions varying the pH. (b) Pourbaix diagram of the PCET of Pep–rSAM in organic/aqueous solvent. Only two regions were obtained, the pH-independent basic and the pH-dependent one (inclined curve with a slope ~ 20 mV/pH). (c) Nyquist capacitive plot for buffered solutions varying the pH. (b) The obtained values of C_q *versus* pH shows a sigmoid tendency in function of pH, wherein the related peak value of the derivative plot of the sigmoid fit informs on the value of $pK_a \sim 4.5$.

Source: Author (2023).

approach at the interface in order to undergo redox reaction. However, at [Fc–COOH] ≥ 1000 μM, the electrochemical response is not longer in equilibrium, with $\Delta E > 120$ mV and $i_{ox}/i_{red} < 0.8$. The electrostatic stability of Fc^{+}–COO^{-} allows its approach to the negatively charged surface undergoing reduction, favoring the backward reaction of Eq. 5.2. Also, as a result of the loss of the electrochemical equilibrium is that the C_q states do not mediate the ET reaction anymore, as following explained.

Nyquist diagrams shown in Fig. 5.11 confirm the increase of C_q and, eventually, the loss of the ET mediation by the related C_q states as [Fc-COOH] increases. In general, three regions are distinguished: (I) region at low [Fc-COOH] where the capacitive behavior dominates and C_q is increasing (see Fig. 5.11*b*); followed by an intermediate region (II) as [Fc-COOH] increases, where the capacitive dominance in the electrochemical activity is unnoticed; and finally, a high impedance region (III) at large [Fc-COOH] (see Fig. 5.11*a*). Note that there is still a capacitive contribution in the electrochemical response, but is not the dominant (see Table 5.2).

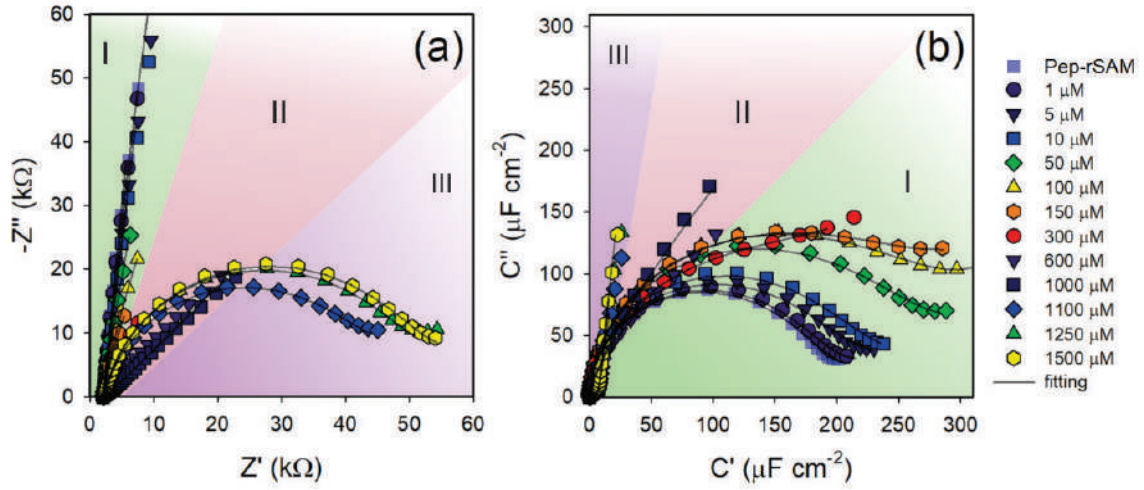

Figure 5.11: Complex impedance (a) and capacitive (b) diagrams of the redox monolayer Pep–rSAM measured at different concentrations of Fc–COOH in ACN/H_2O (1:4, v/v). Both Nyquist plots show three regions that indicate the characteristic dominance of the electrochemical response: (I) quantum capacitive dominance; (II) intermediate or transition region; and (III) resistive dominance.

Source: Author (2023).

In particular, the C_q values obtained from equivalent circuit fitting (see Table 5.2) are in agreement with the above-discussed. Fig. 5.12*a* plots C_q as a function of [Fc–COOH], reveling the quantum capacitance increment from $\sim$ 210 to $\sim$ 470 μF cm^{-2} within the concentration range that corresponds to the region (I) in Fig. 5.11, increasing to N available for the ET mediation.

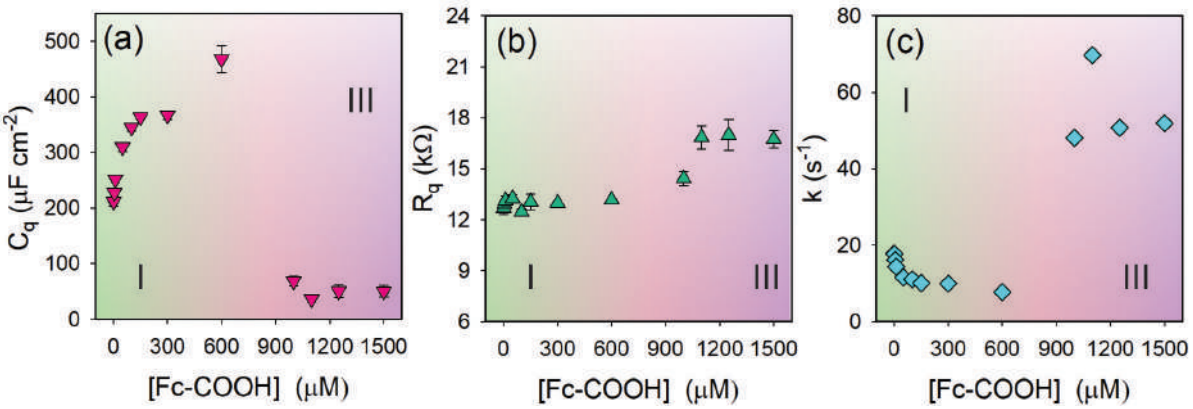

Figure 5.12: Behavior of the quantum elements (a) C_q and (b) R_q that dominate the (c) ET kinetics k of the Pep–rSAM in function of [Fc–COOH]. Note that when the C_q increases exponentially, the ET process obeys the quantized resistance limit, where R_q remains constant $\sim$ 12.9 kΩ, within the experimental error. Same as Fig. 5.11, (I) and (III) indicates the region where C_qR_q governs or not the electrochemical response, respectively.

Source: Author (2023).

Table 5.2: Equivalent circuit elements obtained by the raw impedance data fitting using the equivalent circuit shown in Fig. M.1 for Pep–SAM and in Fig. 3.2 and for Pep–rSAM. Note that the equivalent circuit shown in Appendix N was used to models the electrochemical response of [Fc–COOH] > 1000 for Pep–rSAM. R_q was calculated as contribution of both R_s and R_{qt} accordingly chapter 2. k was calculated considering the g_r degeneracy equals to 2.

	Pep–SAM		Pep–rSAM			
μM	C_t (μF cm^{-2})	R_{ct} (kΩ)	R_{td} (kΩ)	C_q (μF cm^{-2})	R_q (kΩ)	k (s^{-1})
0	8 ± 2			212 ± 8	12.7 ± 0.4	17.7 ± 0.1
1	7.6 ± 0.9			212 ± 4	12.7 ± 0.3	17.69 ± 0.05
5	8.2 ± 0.8			228 ± 1	12.9 ± 0.2	16.16 ± 0.02
10	8.3 ± 0.9			252 ± 6	13.1 ± 0.3	14.39 ± 0.06
50	9 ± 1	285 ± 7		310 ± 8	13.3 ± 0.2	11.60 ± 0.05
100	9 ± 1	170 ± 10	280 ± 10	345 ± 7	12.5 ± 0.2	11.06 ± 0.05
150	9 ± 1	130 ± 160	170 ± 10	364 ± 4	13.1 ± 0.4	10.03 ± 0.06
300	8.4 ± 0.9	75 ± 9	63 ± 4	367 ± 8	12.99 ± 0.06	9.98 ± 0.04
600	8.1 ± 0.8	46 ± 8	20.7 ± 0.3	470 ± 20	13.2 ± 0.1	7.73 ± 0.09
1000	7.8 ± 0.6	32 ± 5	7 ± 2	69 ± 9	14.4 ± 0.4	48.1 ± 0.3
1100	7.6 ± 0.6	32 ± 5	29 ± 10	36 ± 5	16.8 ± 0.7	69.7 ± 0.3
1250	7.4 ± 0.5	32 ± 5	40 ± 3	50 ± 10	17.0 ± 0.9	50.8 ± 0.5
1500	7.1 ± 0.4	30 ± 5	48 ± 2	50 ± 10	16.7 ± 0.5	51.9 ± 0.4

Source: Author (2023).

After the intermediate region (II), at [Fc–COOH] ≥ 1000 μM corresponding to the region (III), the interface becomes more saturated with Fc–COO$^-$/Fc$^+$–COO$^-$ species. This saturation results in an electrostatic repulsion between the negatively charged monolayer and Fc–COO$^-$/Fc$^+$–COO$^-$ at the interface, leading to a modification of the C_q states occupation and a 7-fold decreases in C_q, as shown in Fig. 5.12*a*. As a consequence, the conductive channels N are no longer available for mediating the ET. Note that even the accessibility to the C_q states of the Pep–rSAM itself (without Fc–COOH states in solution) is hindered at such high concentrations, which implies that the energy of this electronic structure changed, leading to the loss of the energy alignment previously observed in the non-equilibrium electrochemical response of the CVs.

Furthermore, the calculated values of R_q using R_s and R_{qt} obtained from the equivalent circuit fitting (see Table 5.2) indicate that whenever the quantum redox states mediate the redox reaction between states in solution and the electrode, the electron is transferred with a quantum resistance limit (see Fig. 5.12*b*). In other words, the ET process in region the (I) is governed by R_q and C_q. On the other hand, the redox reaction that takes place in the region (III) experiences efficiency loss due to the related R_q

values being far from the quantized limit, approximately $R_q > 17$ kΩ (see Table 5.2). It is important to highlight that the efficiency loss is mainly attributed to the changes in R_{qt} as [Fc–COOH] increases. The value of R_{qt} rose from 23 ± 5 Ω to 400 ± 200 Ω, whereas the values of R_s remained constant at 2000 ± 100 for the entire concentration range. The coefficient of variation of R_{qt} is 0.05, indicating its constancy.

The parallel paths to ET mediation mentioned in chapter 3 are evidenced in Fig. 5.8*b*, which depicts the obtained values of the resistance associated to Pep–rSAM (R_{td}) that are in agreement with those of Pep–SAM (R_{ct}), which does not feature C_q states to mediate the ET. As a result of the high resistances, the parallel paths demand high energetic costs for the ET to succeed. Note that R_{td} is higher than the resistance of the path mediated by the C_q states within the quantized limit (i.e., R_q).

Finally, the obtained ET kinetics employing the quantum rate expression (Eq.1.15) considering $g_r = 2$, describes two differentiated kinetics as shown in Fig. 5.8*c*. Following the behavior of C_q where there is an ET mediation with quantum efficiency, the obtained profile of $k \propto C_q^{-1}$. Furthermore, for this particular situation the corresponding f_c can be observed in the capacitive bode plot (see Appendix N), and the obtained values are in agreement with that of k. However, f_c is not spotted when the energy of the capacitive interface changes, as explained previously. Therefore, the kinetics related to the region (III) depicts a slow ET process as the quantum elements R_q and C_q do not govern. The sluggish constant rate could reflect the high energetic barrier that the ET process must overcome for the electron to be transferred by tunneling, where the quantum states can not longer mediate such process.

5.4 Conclusion

The stability of the energy level alignment of energy levels is strongly dependent on the occupancy of states of the capacitive interface, which can be compromised by electrostatic effects caused by the surface charge of the monolayer and the concentration of redox probe, specially when such electroactive species undergo proton-coupled electron transfer reactions. When the related phenomenon operating in the ET process follows quantum mechanical efficiency, such as the minimum quantum resistance in agreement with the quantum rate theory, the stability of the energy level alignment will lead to major accessibility of conductive N increasing C_q, in response to an increment of non-capactive states in solution. These results could support in designing of electronic devices such as in the sensing application explored in the former chapter.

References

BARD, A. J.; FAULKNER, L. R. **Electrochemical Methods Fundamentals and applications**. 2nd: John Wiley and Sons, 2000.

BARRETTE, W. C.; JOHNSON, H.-W.; SAWYER, D. T. Voltammetric evaluation of the effective acidities (pKa) for Broensted acids in aprotic solvents. **Analytical chemistry**, v. 56, n. 11, p. 1890–1898, 1984.

CAREY, F. A.; SUNDBERG, R. J. **Advanced organic chemistry: part A: structure and mechanisms**. Springer Science & Business Media, 2007.

COSTENTIN, C.; ROBERT, M.; SAVÉANT, J.-M. Update 1 of: Electrochemical approach to the mechanistic study of proton-coupled electron transfer. **Chemical Reviews**, v. 110, n. 12, pr1–pr40, 2010.

DE SANTIS, G. *et al.* Controlling the acidity of the carboxylic group by a ferrocene based redox switch. **Inorganica chimica acta**, Elsevier, v. 225, n. 1-2, p. 239–244, 1994.

DEL CAÑO, R. *et al.* Hemoglobin becomes electroactive upon interaction with surface-protected Au nanoparticles. **Talanta**, v. 176, p. 667–673, 2018.

FARIAS, E. D. *et al.* Uncovering the relationship between the structure and acid-base properties for hyperbranched polyester-polyols self-assembled on carbon surfaces. **Journal of Electroanalytical Chemistry**, Elsevier, v. 880, p. 114819, 2021.

GARROTE, B. L.; SANTOS, A.; BUENO, P. R. Label-free capacitive assaying of biomarkers for molecular diagnostics. **Nature Protocols**, 2020. ISSN 1754-2189. DOI: 10.1038/s41596-020-0390-9.

GARROTE, B. L.; SANTOS, A.; BUENO, P. R. Perspectives on and precautions for the uses of electric spectroscopic methods in label-free biosensing applications. **ACS sensors**, ACS Publications, v. 4, n. 9, p. 2216–2227, 2019.

GOES, M. S. *et al.* A Dielectric Model of Self-Assembled Monolayer Interfaces by Capacitive Spectroscopy. **Langmuir**, v. 28, n. 25, p. 9689–9699, 2012. ISSN 0743-7463. DOI: 10.1021/la301281y.

LEHR, J. *et al.* Mapping the ionic fingerprints of molecular monolayers. **Physical Chemistry Chemical Physics**, v. 19, n. 23, p. 15098–15109, 2017. ISSN 1463-9076. DOI: 10.1039/c7cp01500c.

MÁRQUEZ, I. *et al.* Active Role of the Buffer in the Proton-Coupled Electron Transfer of Immobilized Iron Porphyrins. **Inorganic Chemistry**, v. 60, n. 1, p. 42–54, 2020.

MAYER, J. M. Proton coupled electron transfer: a reaction chemist's view. **Annual Review of Physical Chemistry**, v. 55, p. 363–390, 2004.

MCCARTHY, B. D.; DEMPSEY, J. L. Decoding proton coupled electron transfer with potential pKa diagrams. **Inorganic Chemistry**, v. 56, n. 3, p. 1225–1231, 2017.

MONGAY, C.; CERDA, V. A Britton-Robinson buffer of known ionic strength. **Annali di Chimca**, v. 64, n. 5, 1974.

PETRUCCI, R. H.; HARWOOD, W. S.; HERRING, F. G. **General chemistry: principles and modern applications**. Prentice Hall, 2002. v. 1.

SWEBOCKI, T. *et al.* In pursuit of key features for constructing electrochemical biosensors–electrochemical and acid-base characteristic of self-assembled monolayers on gold. **Supramolecular Chemistry**, v. 32, n. 4, p. 256–266, 2020.

TAN, K.-J. *et al.* Redox Polyelectrolytes with pH-Sensitive Electroactive Functionality in Aqueous Media. **Langmuir**, v. 39, n. 8, p. 2943–2956, 2023.

VĚŽNÍK, J. *et al.* Elusive pKa of aminoferrocene determined with voltammetric methods in buffered and unbuffered systems and practical aspects of such experiments. **Electrochimica Acta**, Elsevier, v. 318, p. 534–541, 2019.

ZHAO, J. *et al.* Determination of surface pKa of SAM using an electrochemical titration method. **Electroanalysis: An International Journal Devoted to Fundamental and Practical Aspects of Electroanalysis**, v. 11, n. 15, p. 1108–1113, 1999.

Chapter 6

Quantum Rate Model for the Study of Molecular Junctions

The correlation between molecular conductance and charge transfer rate has been proposed as a nonlinear rate–conductance relationship (ARTES *et al.*, 2011; WIERZBINSKI *et al.*, 2013; VENKATRAMANI *et al.*, 2014), as briefly described in the introductory chapter. Recently, our research group has demonstrated that the ET constant rate operates in dry experimental setting, using azobenzene molecular junctions (MJs) with different thicknesses (SANTOS *et al.*, 2020). The interpretation of the IS data through the mesoscopic elements such as C_μ and R_q led to expand the physical insights in the molecular electronics field, opening up new avenues of possibilities to be explored, aiming to understand the electric properties of the MJs within the quantum rate theory framework. This chapter deals with the detailed study of the rate-conductance relationship described by the quantum rate expression. In summary, the electric properties of a set of aromatic MJs were measured by impedance spectroscopy (IS) at different bias potentials and temperature ranges. The obtained response was studied within the quantum rate theory framework, with a main objective:

- ☑ To demonstrate that for molecular electronics settings the conductance G and the electron transfer rate k are correlated by the electrochemical capacitance C_μ as $k = G/C_\mu$, showing that the electrochemical and molecular electronic concepts are not physically different.

6.1 Introduction

The capability of the MJs in transporting electric current received special attention by the molecular electronics field in order to understand and design molecular devices (MCCREERY, 2022; GUPTA *et al.*, 2023). The variety of molecular composition that can be modulated by synthesis provides versatility in terms of electronic structure that confers special properties to these devices. In particular, the application of molecules in the development of miniaturized devices can be attained due to their nanometer scale, which represents an advantage over the limiting size of the complementary metal-oxide semiconductors (CMOS) (MCCREERY, 2022; GUPTA *et al.*, 2023). Furthermore, the electric properties of the MJs can be modulated by the electrode material, the electronic coupling between the electrodes and the molecules (MCCREERY, 2022; GUPTA *et al.*, 2023).

Regarding the electronic characterization of MJs, the typical studies are based on the analysis of the j/V behavior aiming to elucidate the electron transport mechanism,

which has been explored in terms of molecular thickness L, potential V, temperature T and molecular structure (BERGREN *et al.*, 2010; YAN; BERGREN; MCCREERY, 2011; SAYED *et al.*, 2012). For instance, the quantum mechanical tunneling is known to be a temperature independent process (DAVIES, 1998), which can be evaluated using either Arrhenius or attenuation plots on a semilog scale, which depict a linear behavior for an activationless transport (VAN NGUYEN *et al.*, 2020). In the first one, it is plotted $\ln j$ *versus* $1/T$ (BERGREN *et al.*, 2010), wherein the activation energy E_a is obtained from the slope. Whereas in the latter case, $\ln j$ (or R) is plotted against L, its slope supplies the value of β (SAYED *et al.*, 2012).

Aromatic molecular layers chemisorbed onto carbon-based contact have exhibited high reproducibility and temperature stability for electron transport (MCCREERY, 2022). The wide range of possible energy levels conferred by the sp^2 carbon-conjugated system of this electronic structure mediates the electron transport through molecular orbitals rather than through space (BERGREN *et al.*, 2010), implying a non resonant tunneling mechanism. In addition, the use of carbon surfaces favors a strong electronic coupling as a result of not only the covalent C-C bond formation between the substrate and aromatic molecular layer but also the energy level alignment (BERGREN *et al.*, 2010; YAN; BERGREN; MCCREERY, 2011; SAYED *et al.*, 2012). As mentioned in section 1.4, there is a barrier height associated with this alignment, which is related to the difference between the electrode's E_F and the HOMO or LUMO of the molecule. Therefore, the smaller the barrier height, the better alignment, leading to higher conductance.

The study of j-V curve of these aromatic MJs as a function of T or L has allowed us to determine E_a and β, showing that $j \propto \exp(-\beta L)$ similar to that obtained for aliphatic, oligopeptides and proteins, where conductance measurements were performed (ARTES *et al.*, 2011; WIERZBINSKI *et al.*, 2013). It is worthwhile to note that similar to the electrochemical counterpart k in the case of redox SAMs, the electron transport associated with the molecular conductance follows a quantum mechanical tunneling and is exponentially dependent on the molecular thickness L, such as $G \propto \exp(-\beta L)$. Therefore, the obtained results are in agreement with the theoretical relationship between G and k established in section 1.4.

The first approach of the quantum rate theory to study molecular conductance was realized in electrochemical settings using DNA nanowires aiming to measure the G employing ECS (RIBEIRO *et al.*, 2016). For this electrochemical system, the rate-conductance relationship was demonstrated. Later, the interpretation of the IS characterization of MJs through mesoscopic elements was reported (SANTOS *et al.*, 2020). In this work a set of MJs comprising azobenzene layers and carbon-based contacts with different L was studied by IS (see Fig. 6.1). For those MJs, the corresponding k was determined through an equivalent circuit analysis (see Fig. 6.2*a*), demonstrating that the quantum rate constant operates not only in nanoscale electrochemical systems but also in MJs. This allowed us to demonstrate quantitatively a relationship between electrochemical (k) and molecular electronic (G) concepts through C_μ within the framework of the quantum rate theory.

In terms of an equivalent circuit that models the impedance response of the electrochemical and molecular electronics settings, differences are spotted whether the elements C_μ and R_q operate in parallel or in series, as shown in Fig. 6.2. The electric current modelled by the RC circuit in Fig. 6.2*b*, characterizes the Faradaic current

of electrochemical interfaces, as explained in chapters $2-5$, recalling that the quantum contribution dominates the capacitive response as $C_\mu \sim C_q$. Conversely, the circuit shown in Fig. 6.2*a* depicts C_μ and R_q in parallel, which model the response of MJs (BUENO; DAVIS, 2020). Although C_μ is governed by the geometric contribution C_e, it is implied that the electronic structure of the molecular bridge associated with C_q participates in the transmission process as DOS $\propto C_q$. Hence, the electron transport mediated by the DOS has to overcome the resistance R_q for the current passage (BUENO; DAVIS, 2020).

In this final chapter, aromatic MJs comprising different molecular structures with different molecular thicknesses were studied by IS over a range of T and V. Equivalent circuit analyses were realized to determine the mesoscopic properties such as R_q, C_μ, and k. In addition, Arrhenius plots for G and k were analyzed aiming to demonstrate that these mesoscopic properties are temperature-independent. Finally, the IS characterization allowed us to confirm that G and k are correlated by C_μ, providing substantial experimental evidence, showing the capability of the quantum rate theory to address mesoscopic systems.

6.2 Materials and methods

In this chapter large-area MJs featuring different thicknesses were analysed, which were supplied by Prof. Dr. Richard L. McCreery from Department of Chemistry, University of Alberta, Canada.

6.2.1 Large-area molecular junctions

Fig 6.3 shows a schematic illustration of the large-area MJs (0.00125 cm^2) studied in this chapter. The multilayers of each MJs are comprised of three different molecules: fluorene (FL), azobenzene (AB), and nitroazobenzene (NAB). The aromatic molecules

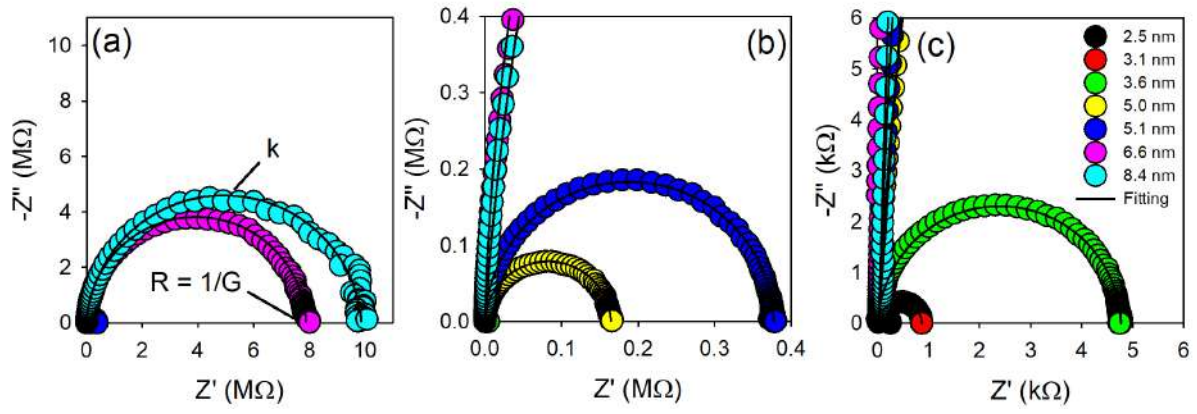

Figure 6.1: Impedance characterization measured at 0 V bias of azobenzene MJs with different thicknesses. (a) Nyquist diagrams of thickest MJs exhibiting higher impedance response. (b) and (c) Corresponds to the magnification of (a). The fitting curves were obtained using the equivalent circuit shown in Fig. 6.2*a*

Source: (SANTOS et al.*, 2020). Copyright 2020 Royal Society of Chemistry.*

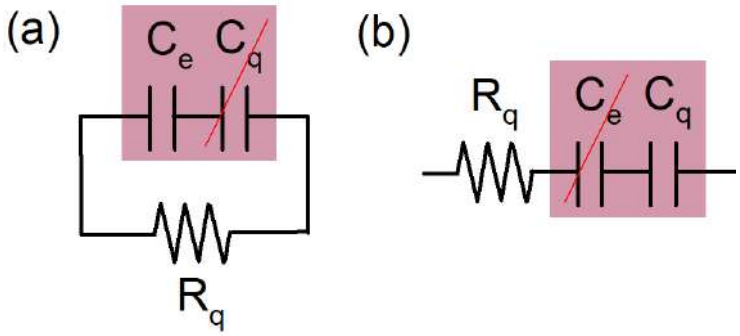

Figure 6.2: Difference between the equivalent circuit that models the response of the (a) MJ settings for studying molecular conductance and (b) electrochemical configuration for studying the ET constant rate. The purple boxes show the electrostatic and the quantum contributions of C_μ for both configurations. While C_e dominates the C_μ of MJs in (a), C_q rules the C_μ of SAMs in (b).

Source: Author (2023).

were chemisorbed on carbon substrates by electrochemical reduction of the corresponding diazonium ions (BERGREN *et al.*, 2010; YAN; BERGREN; MCCREERY, 2011), obtaining the following MJs with L values of 8.4 nm (NAB1), 10.2 nm (NAB2), 9.2 nm (AB), 4.3 nm (FL1) and 4.8 nm (FL2). The bottom and top contact are electron-beam deposited carbon films (eC), to which Au was deposited as the conducting lead.

6.2.2 Spectroscopy impedance measurements

The electrical characterization of the MJs was performed using an AUTOLAB potentiostat from METROHM, controlled by NOVA software, and equipped with a frequency response analysis (FRA) module. J–V curves were measured at $s = 100$ mV s^{-1} from - 1 V to 1 V for FL and NAB, and from - 1.5 V to 1.5 V for AB, in a two-electrode configuration at room temperature. IS measurements were recorded at different bias potentials, such as at 0, $\pm$ 0.05, $\pm$ 0.1, $\pm$ 0.15, and $\pm$ 2 V at room temperature, using 10 mV (peak to peak) perturbation, over a frequency range from 1 MHz to 0.1 Hz. Temperature experiments were performed in a Janis CCS-400H/204 cryogenic closed cycle system configuration (see Fig. 6.4), equipped with a 331 temperature controller and an HC-4E Cryopump compressor. The MJ contacts were welded to Cu wires (as shown in the inset of Fig. 6.4) and connected to alligator clips to plug into the potentiostat. The potentiostat was further connected to a no-break system to suppress the noise contributions from the supply power. IS measurements were carried out at 0, $\pm$ 0.1, and $\pm$ 0.15 V for each studied temperature, over a range from 243 to 313 K at vacuum, with an increment of 10 K between measurements. A time lag of 20 min was considered before measurement once the chamber reached the desired temperature.

6.2.3 Equivalent circuit analysis

The values of the circuital elements were obtained by fitting the raw impedance data of the MJs, using an equivalent circuit shown in Fig. 6.6*a*. The obtained values were reported for each chip for a total of five MJs (i.e., FL1, FL2, NAB1, NAB2, and AB).

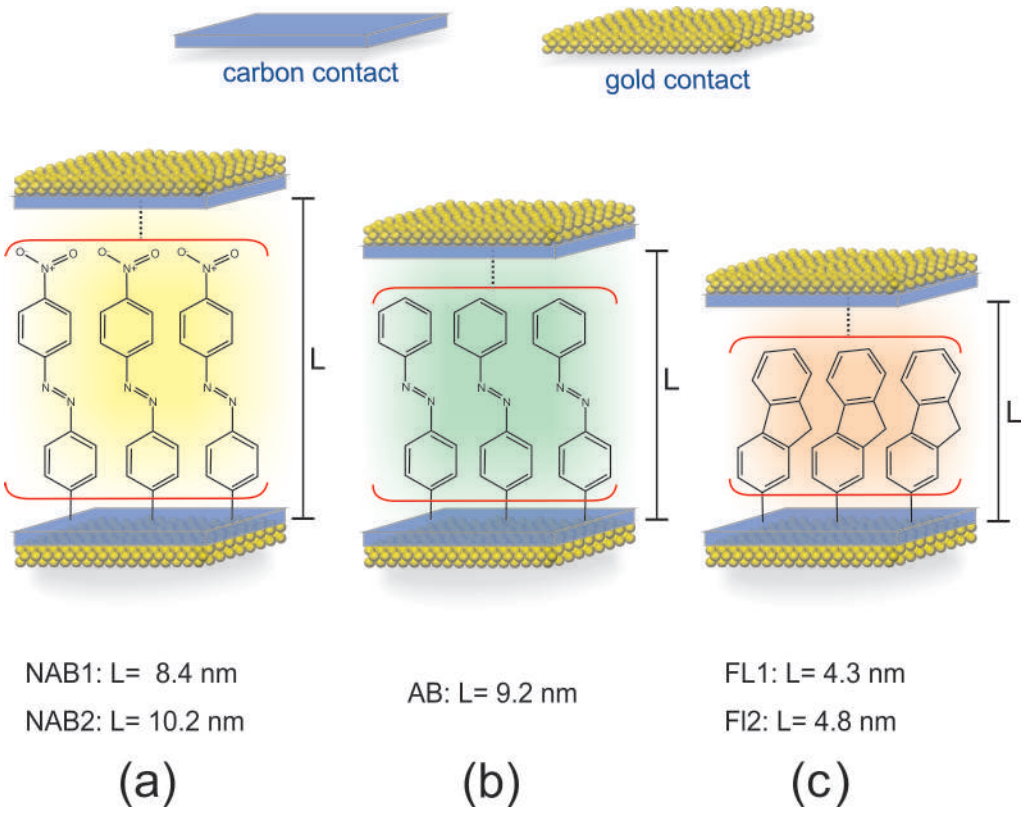

Figure 6.3: Schematic illustration of the studied MJs comprised of organic multilayers sandwiched between carbon and gold contacts. The molecular units that conform to the aromatic layer are (a) nitroazobenzene, (b) azobenzene, and (c) fluorene. The molecular thicknesses are 8.4 nm (NAB1), 10.2 nm (NAB2), 9.2 nm (AB), 4.3 nm (FL1), and 4.8 nm (FL2).

Source: Author (2023).

6.3 Results and discussion

The electrical characterization of the MJs is shown in Fig 6.5*a*, which overlays five $j - V$ curves on linear scales. All MJs feature a reversible junction conductance at the explored bias, that is, $\pm$ 1.5 V for AB and $\pm$ 1.0 V for both FL and NAB MJs. This reversible behaviour is attributed to the stability of the covalent bond between the aromatic molecule and the conducting carbon surface, as the $C - C$ bonding avoids electromigration (MCCREERY, 2022), a common problem of metal contacts where metallic atoms tend to migrate within the molecular layer at high bias, leading to irreversible increment of j (YAN; BERGREN; MCCREERY, 2011). Additionally, it is noteworthy that there is a decrease in j at high bias, showing strong dependence on both molecular structure and thickness, as reported in the literature for these carbon-based MJs (MCCREERY, 2022). For instance, for less thick MJs, j is the highest with a value of $\sim$ 0.25 A cm^2 at $\pm$ 1.0 V bias (see black and red curves). Whereas the lowest $j \sim 0.004$ A cm^2 at $\pm$ 1.5 V bias corresponds to AB (see blue curve), which lacks withdrawing groups such as the nitro group (CAREY; SUNDBERG, 2007). This nitro substituent improves the junction conductance, as seen in the case of NAB MJs with $j \sim 0.05$ A cm^2 at $\pm$ 1.0 V bias (see green and yellow curves).

Additional information is obtained from $j - V$ curves on the semilogarithmic scale shown in Fig 6.5*b*. Regardless of molecular thickness and structure, all $j - V$ curves show a similar behavior. At low bias ($< \pm$ 0.1 V), $|j|$ increases linearly with V, while

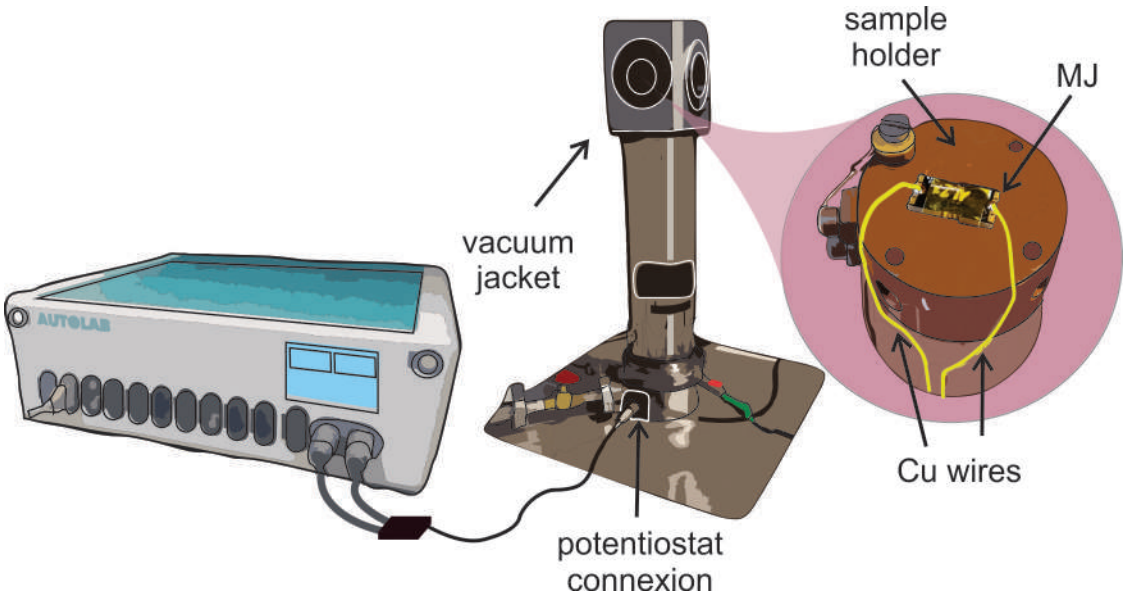

Figure 6.4: Schematic illustration of the cryogenic system used for temperature-controlled impedance measurements. The MJ was placed inside the vacuum jacket and was welded to Cu wires, as shown in the inset. The cu wires were then connected to the potentiostat using an adapter (potentiostat connection).

Source: Author (2023).

at higher bias $|j|$ follows an exponential function of V. Note that this behavior is also observed for electrochemical settings, such as redox SAM (HOSSAIN; BEVAN, 2016; VALIANTI; CUEVAS; SKOURTIS, 2019), where the same graphic is known as a Tafel plot, as described in section 1.6. Through the quantum rate model, the analysis of the

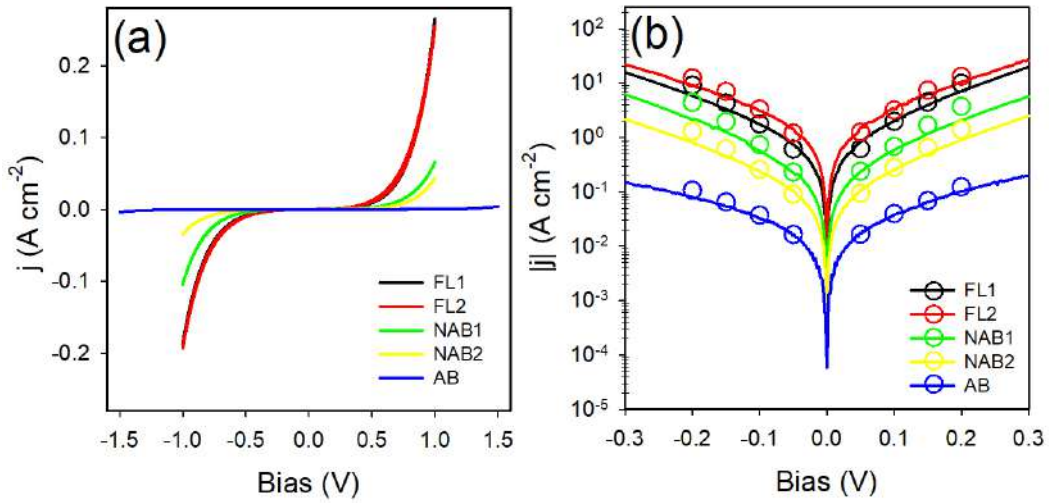

Figure 6.5: $j - V$ curves obtained for NAB, AB, and FL MJs from (a) DC scans at 100 mV s^{-1}. (b) Equivalence between the logarithm of the modulus of j *versus* bias V curves from DC (lines) and AC (circles) measurements. IS-obtained circles were calculated through the definition of G discussed in the text, using the values obtained in the equivalent circuit fitting (see Table O.1).

Source: Author (2023).

IS data using equivalent circuit fitting leads to a reasonable correspondence between j obtained from the DC and AC measurements as depicted in Fig 6.5*b*, where the IS-calculated circles (AC data) are consistent with the shapes of $j - V$ (DC data). The j was calculated from the mesoscopic element G using the equation $j = {}^{GV}/_{A}$ (see Appendix O), where $G = {}^{1}/_{R_q}$ and A is the molecular junction area. R_q was obtained employing the equivalent circuit analysis (see Fig 6.6*a*).

The impedance of MJs measured at different biases, at room temperature, is depicted by the Nyquist impedance spectra shown in Fig. 6.6, which evidences the dependence of the impedance on the bias potential in agreement with that observed in the $j - V$ curves. Additionally, the differences in the impedance patterns of the MJs are expected since j is inversely proportional to the resistance, more specifically R_q, which can be determined whether by graphical analysis (diameter semicircle) or by the equivalent circuit fitting (see Table O.1). Hence, the less resistance, the more conducting an MJ is, such as the case of FL (see Fig. 6.6*c–d*), in comparison with AB, which features higher resistance (see Fig. 6.6*b*). As mentioned above, the molecular structure and thickness affect how the MJ responds to voltage perturbation. In particular, these factors impact the dielectric constant of the molecular layer and, in turn, the polarizability or the capability of charge density distribution along the molecular layer. For instance, for aromatic MJs, the distribution of the electronic structure (i.e., HOMO-LUMO) along the molecular length, favored by the conjugate system, leads to better charge distribution (BERGREN *et al.*, 2010). Therefore, FL MJs may feature a better electronic distribution due to their smaller thickness. Finally, note that for all MJs there is symmetry in the electron transport when positively or negatively biased (see Fig 6.6*b–f*). For instance, the values of R_q are equivalent for a given potential regardless of the sign (see Table O.1). This can be attributed to the symmetric coupling between the molecule and the carbon contacts as well as the fact that both the bottom and top contacts are comprised of the same material (GUPTA *et al.*, 2023).

Fig. 6.7 shows the mesoscopic elements *versus* bias for all aromatic MJs as obtained by IS fitting (R_q and C_μ) and as calculated from the values of R_q and C_μ ($G = {}^{1}/_{R_q}$ and $k = {}^{1}/_{R_q C_\mu}$). Fig. 6.7*a* shows the logarithm of R_q as a function of bias, depicting the same trends for all MJs, supporting the above discussion about the influence of the electronic structure, molecular thickness and bias symmetry. It is important to highlight that SI allows us to measure this resistance directly in comparison with the DC measurements, which determine the resistance value indirectly from the slope of the $j - V$ curve (YAN; BERGREN; MCCREERY, 2011). Furthermore, Fig. 6.7*a* shows that R_q is highly sensitive to small variations of L, such as the case of FL1 and FL2, which despite their molecular thicknesses differing only by 0.5 nm, have different R_q values (see Table O.1). Also, the resistance of the observed electronic responses is dominated by the molecular component R_q owing to the contact resistance R_c corresponds to only 0.03 - 0.0003 % of the value of the total resistance for all MJs (see Table O.1).

On the other hand, C_μ does not vary with changes in bias potential as shown in Fig. 6.7*b*, its low value remains constant regardless of the chemical structure and thickness (ca. $C_\mu \sim 0.8$ – 1.5 nF)[1]. Recalling that C_μ considers both electrostatic and quantum capacitive contributions as ${}^{1}/_{C_\mu} = {}^{1}/_{C_e} + {}^{1}/_{C_q}$, we can say that the contribution attributed to C_q cannot be accessed since the DOS (i.e., ${}^{dn}/_{d\mu}$) associated with the left and right "plates" of this quantum capacitance (${}^{e^2}/_{C_q} = {}^{1}/_{(dn/d\mu)_l} + {}^{1}/_{(dn/d\mu)_r}$) are

[1]Normalized by the area $C_\mu \sim 0.6$ – 1.2 μF cm^{-2}.

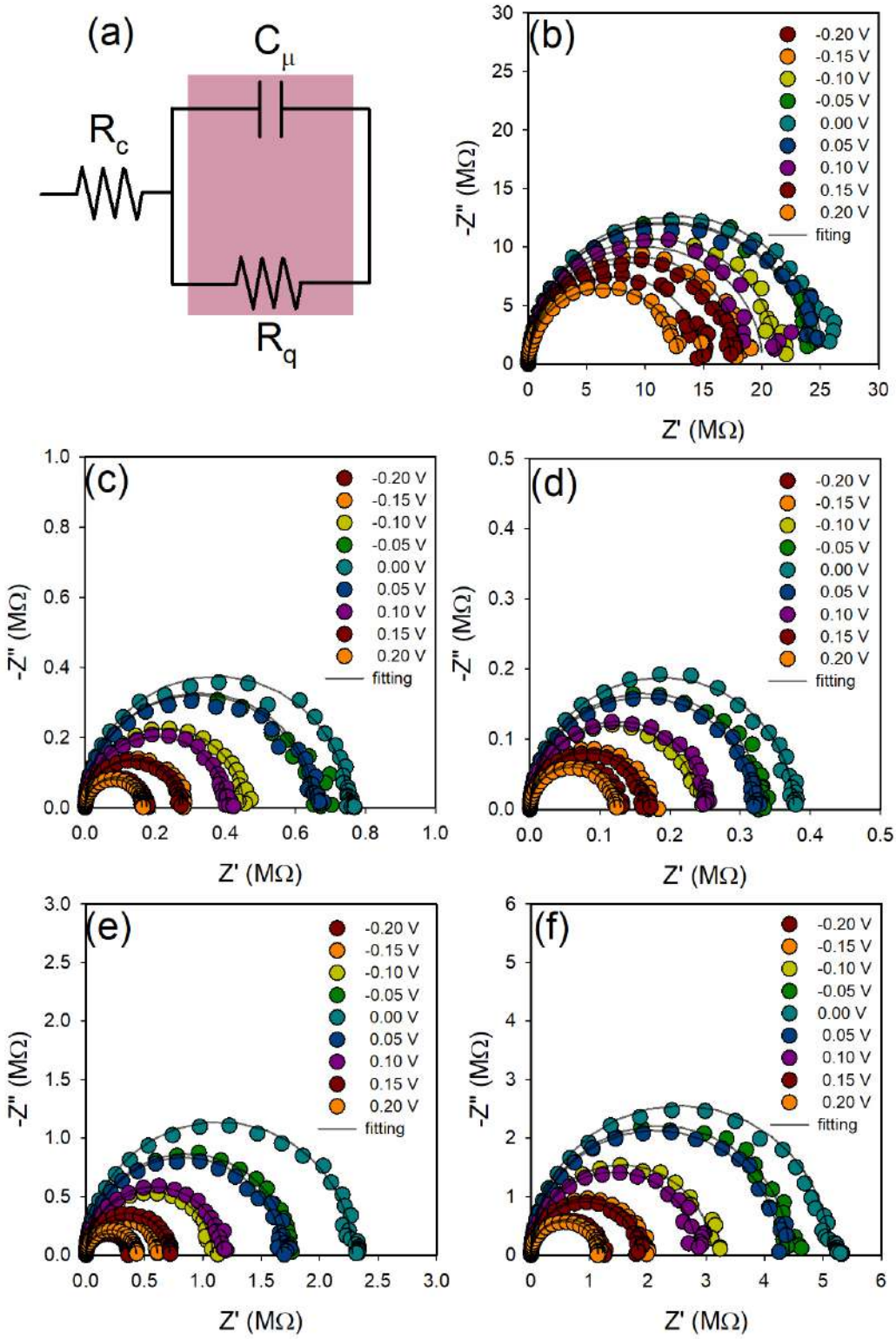

Figure 6.6: (a) Equivalent circuit constituted by C_μ and R_q in parallel, which are in series with R_c. Impedance Nyquist diagrams for (b) AB, (c) FL1, (d) FL2, (e) NAB1, and (f) NAB2, showing the variation of the impedance pattern as a function of bias at room temperature. Note the influence of the molecular structure on the impedance response.

Source: Author (2023).

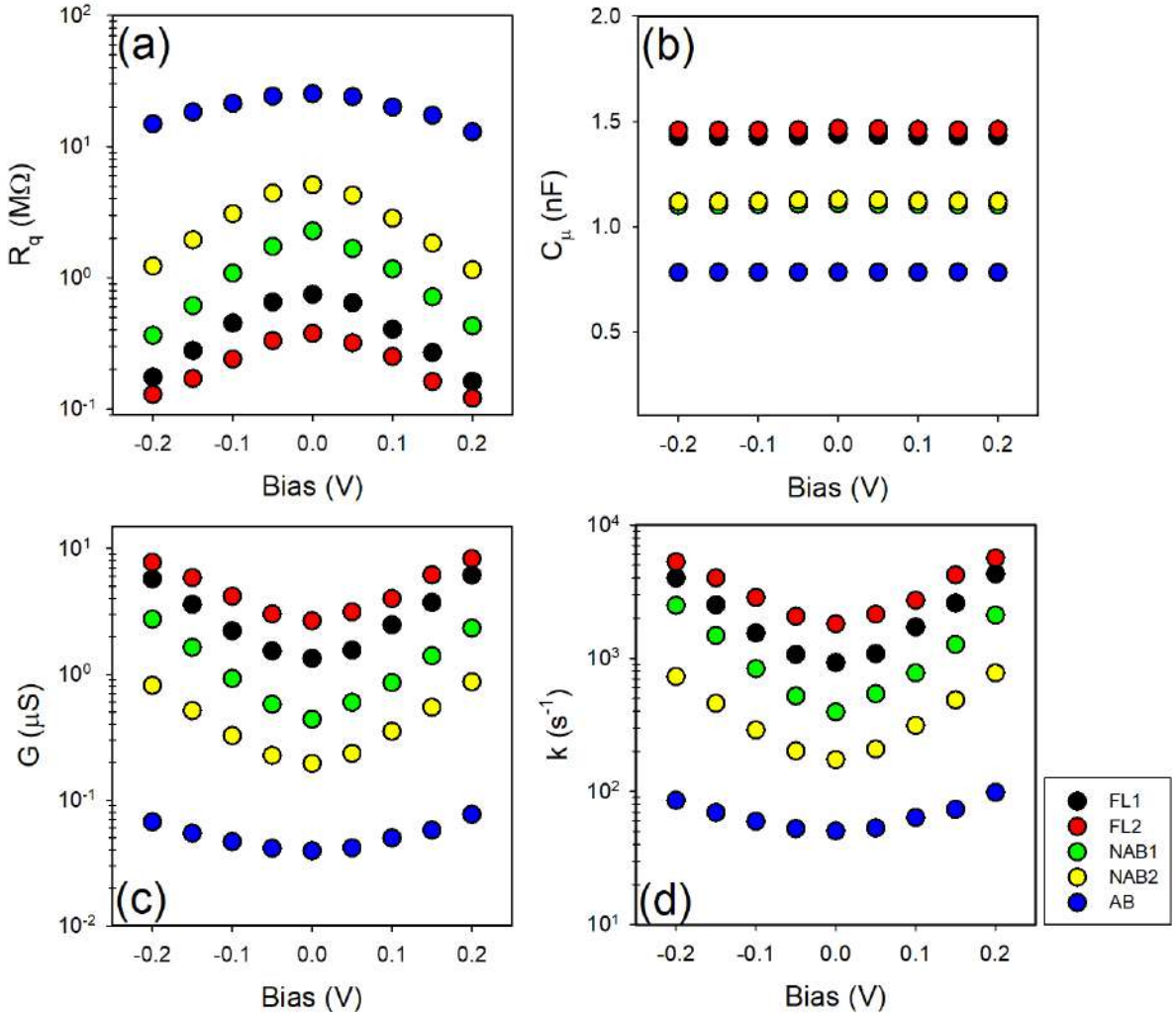

Figure 6.7: Electric properties for FL, NAB, and AB MJs as a function of bias. (a) R_q and (b) C_μ correspond to the electrical features obtained from circuit fitting. Whereas (c) G and (d) k correspond to the values calculated as $G = {}^1/_{R_q}$ and $k = {}^1/_{R_q C_\mu}$, respectively.

Source: Author (2023).

large enough due to these DOS being referred to the electronic structure of the conducting contacts (bottom and top carbon films). Meaning that the contribution of C_q is neglected, which leads to $C_\mu \propto C_e$. Accordingly, the obtained capacitance reports only on the electrostatic capacitive phenomenon, which is constant due to its dependence on the dielectric medium (molecular layer) and the distance separation of the "plates" (i.e., L). Note that C_e is not as sensitive as R_q due to the physics related to this resistance being quantum mechanical.

Regarding the involvement of the electronic structure of the molecular layer as conducting channels, the N values of the MJs were determined by using the expression $G = G_0 \exp(-\beta L)N$, where G was calculated from IS data measured at 0 V bias. For aromatic MJs with $L < 6$ nm the β value of 2.7 nm $^{-1}$ was obtained (SAYED *et al.*, 2012), and was used for an approximate determination of N. The low values of N for the smallest MJs, such as FL1 and FL2 with the lowest resistance, suggest that when the passage of current confronts high resistance associated with long distance, additional quantum channels are available to permit the transport of electrons.

Consequently, NAB2 has the largest amount of N, although its G is the lowest (see Table 6.1). Although the β value corresponds to less thick MJs, its use for N determination is consistent since sequential tunneling through the HOMO-LUMO orbitals of the molecular bridge (short distances) is the quantum mechanical mechanism proposed for aromatic structures (MCCREERY, 2022). Therefore, the values obtained for N inform the DOS that mediates the electron transport via sequential tunneling. For that reason, N for the thickest MJs has the highest amount of N, that is, 2.30×10^9 for NAB2.

Table 6.1: N calculation at 0 V bias at room temperature for β = 2.7 nm $^{-1}$.

MJ	G (μS)	L (nm)	N
AB	0.04	9.2	3.13×10^7
FL1	1.33	4.3	1.90×10^3
FL2	2.66	4.8	1.46×10^4
NAB1	0.44	8.4	4.01×10^7
NAB2	0.20	10.2	2.30×10^9

Source: Author (2023).

Note that G patterns shown in Fig. 6.7*c* are similar to that of k depicted in Fig. 6.7*d*, as $k = {}^{G}/_{C_\mu} \propto G$, suggesting that the quantum conductance (or resistance) property governs the electron transfer/transport phenomena of these junctions as well as the associated kinetics as depicted in Fig. 6.7. This demonstrates that the correlation between k and G by C_μ previously demonstrated in the latter chapters for electrochemical settings is also valid for MJs, for which several attempts were made for understanding the relationship between the conductance and the constant rate, as described in section 1.4.

To corroborate the quantumness of the electronic properties that govern the electrodynamics of the MJs, the temperature and bias potential were varied, and the E_a was determined. Fig. 6.8 shows the impedance Nyquist pattern for FL and NAB MJs at several temperatures between 243 and 313 K, measured at 0 V bias. The IS recorded at $\pm$ 0.10 and $\pm$ 0.15 V is presented in the Appendix P. Note that the IS data are suitably fitted by the circuit shown in Fig. 6.6*a*. Despite the impedance patterns recorded at different biases seem to respond to temperature changes, the variation of G, C_μ, and k with temperature was the main matter of study. Fig 6.9 and Fig 6.10 depict the electric response at the temperature range for FL and NAB, respectively.

Firstly, the $C_\mu - T$ curves on the linear scale shown by the panels *d* and *e* of Fig 6.9 and Fig 6.10, corroborate that the capacitive component does not contribute significantly to the electric response as discussed earlier. On the contrary, R_q exhibits a temperature dependence as shown earlier in the Nyquist plots, which is reflected in the conductance behavior. G plotted as a function of T on the semilogarithm scale (see the panels *a* and *d* of Fig 6.9 and Fig 6.10), reveals that the passage of current caused by the AC perturbation not only increases with bias voltage but also with an increment of temperature. Note that similarly with G, k responds in the same way to the variation of bias and T as observed in the panels *c* and *f* of Fig 6.9 and Fig 6.10, complying with $k \propto G$.

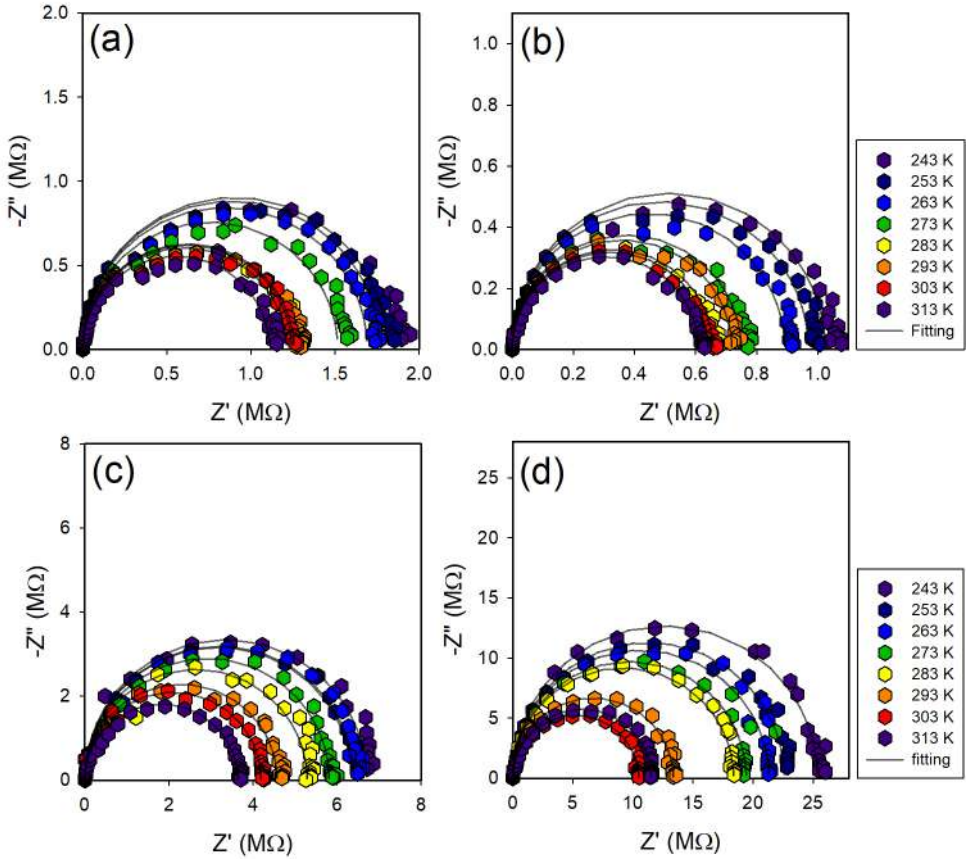

Figure 6.8: Impedance Nyquist diagrams for (a) FL1, (b) FL2, (c) NAB1, and (d) NAB2, showing the variation of the impedance pattern as a function of temperature at 0 V bias, which was fitted using the equivalent circuit shown in Fig. 6.6*a*.

Source: Author (2023).

The corresponding Arrhenius plots of $\ln G$ *versus* 1000/T and $\ln k$ *versus* 1000/T for FL and NAB MJs are shown in Fig 6.11 and Fig 6.12, respectively. All curves exhibit a linear response, from which E_a was determined from the expressions $G = A \exp^{-E_a/RT}$ and $k = A \exp^{-E_a/RT}$, which can be rewritten as $\ln G = \ln A - \frac{E_a}{R}\frac{1}{T}$ and $\ln k = \ln A - \frac{E_a}{R}\frac{1}{T}$, respectively, where $^{E_a}/_R$ is the slope of the trend line. The obtained parameters from this linear regression are summarized in Table 6.2 and Table 6.3 for FL and NAB MJs, respectively. The obtained values of E_a for FL ($\sim$ 40 meV) and for NAB ($\sim$ 60 meV) imply that the charge transport obeys a quantum mechanical tunneling, which is temperature-independent in agreement with the literature (BERGREN *et al.*, 2010; YAN; BERGREN; MCCREERY, 2011). It is worthwhile to observe that for each MJs the E_a obtained by either the conductance and constant rate Arrhenius plot at the same bias, are almost equal in compliance with the rate-conductance proportionality. Furthermore, the amount of N for the temperature range compiled by Table 6.4 suggests that the accessibility of these channels does not depend on the temperature. Note that the coefficient of variation for all MJs is < 0.3, thus, one can say that N does not significantly change with temperature, as expected for a tunneling mechanism (see Table 6.4).

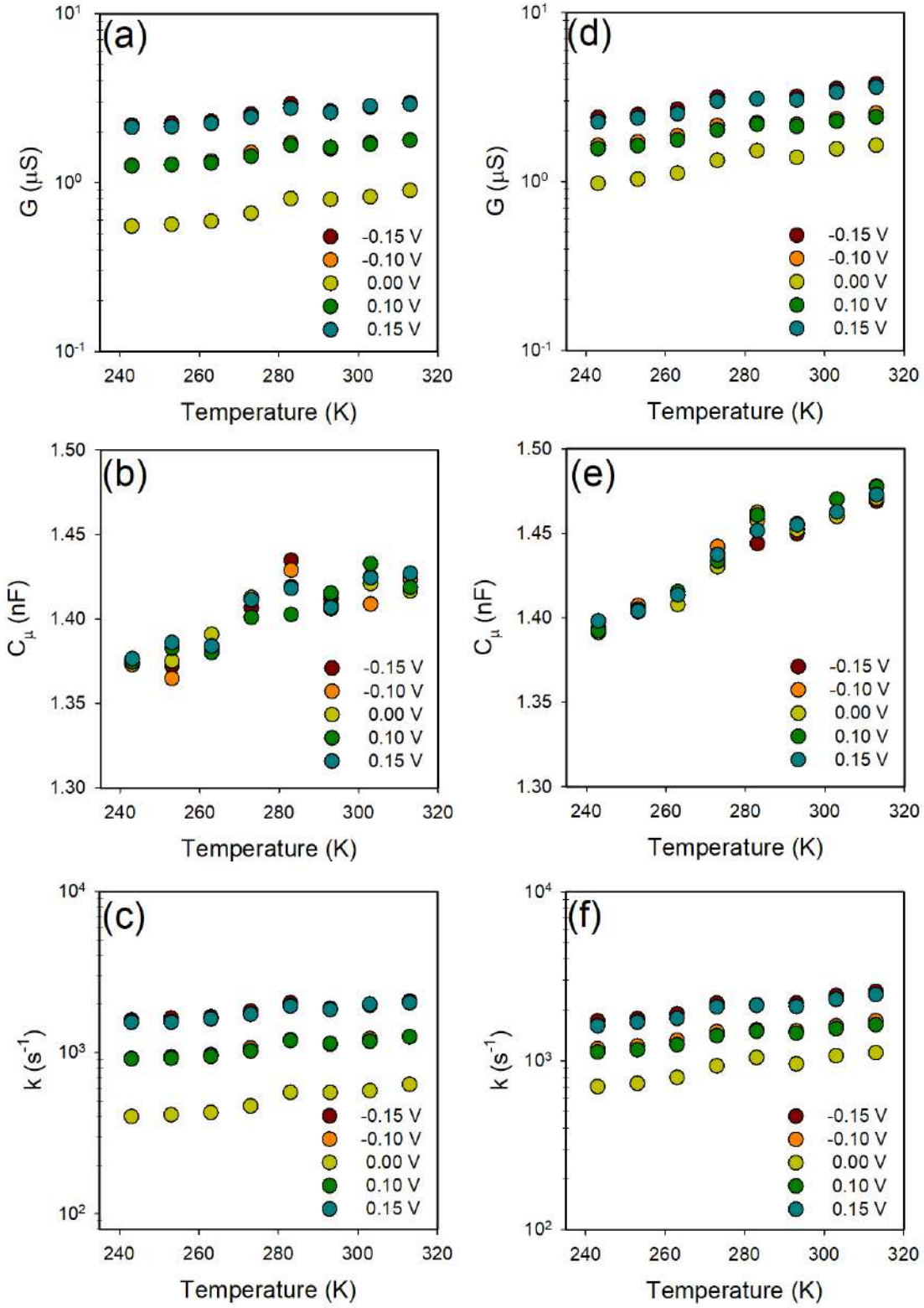

Figure 6.9: G, C_μ and k as a function of temperature measured at different bias for FL1 (a, b and c) and FL2 (d, e and f). Note that the value of C_μ for both FL MJs is in the order of nano Farads and is constant as the temperature changes, regardless of the bias.

Source: Author (2023).

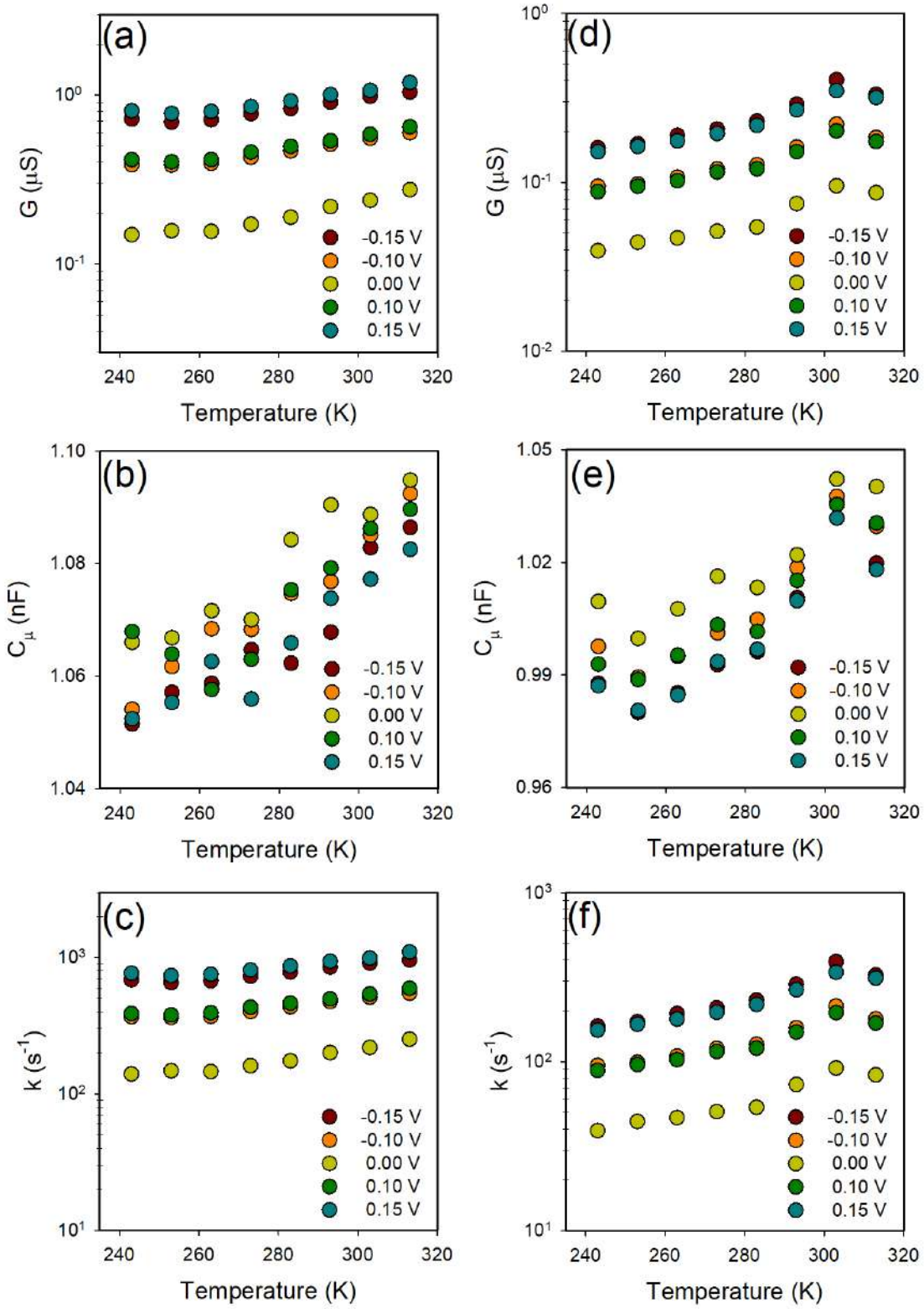

Figure 6.10: G, C_μ and k as a function of temperature measured at different bias for NAB1 (a, b and c) and NAB2 (d, e and f). Note that the value of C_μ for both FL MJs is in the order of nano Farads and is constant as the temperature changes, regardless of the bias.

Source: Author (2023).

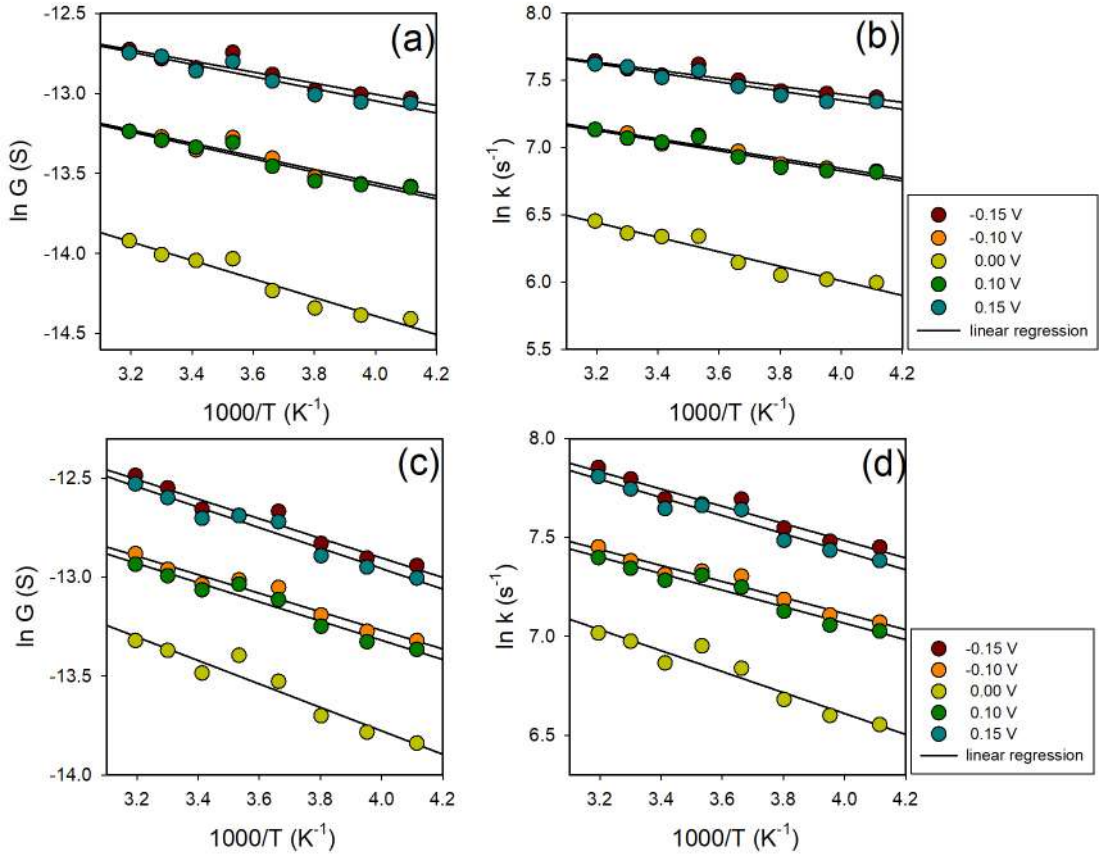

Figure 6.11: Arrhenius plots of G and k at different biases for FL1 (a and b) and FL2 (c and d). The E_a values are determined from the slope of the linear regression and are summarized in Table 6.2.

Source: Author (2023).

Table 6.2: Linear regression data from the Arrhenius plot for FL MJs and the values of E_a.

Plot	Bias	FL1				FL2			
	(V)	slope	SD	r^2	E_a (eV)	slope	SD	r^2	E_a (eV)
ln *G versus* T^{-1}	-0.15	-347	58	0.8345	0.030	-496	45	0.9445	0.043
	-0.10	-412	55	0.8873	0.035	-470	43	0.9439	0.040
	0.00	-579	62	0.9251	0.050	-593	68	0.9140	0.051
	0.10	-419	49	0.9099	0.036	-486	42	0.9488	0.042
	0.15	-380	46	0.9067	0.035	-518	45	0.9483	0.045
ln *k versus* T^{-1}	-0.15	-299	48	0.8438	0.026	-436	43	0.9358	0.038
	-0.10	-367	45	0.9018	0.032	-405	38	0.9423	0.035
	0.00	-542	60	0.9193	0.047	-530	63	0.9078	0.046
	0.10	-376	49	0.8906	0.032	-417	38	0.9434	0.036
	0.15	-340	41	0.9046	0.029	-457	43	0.9421	0.039

Source: Author (2023).

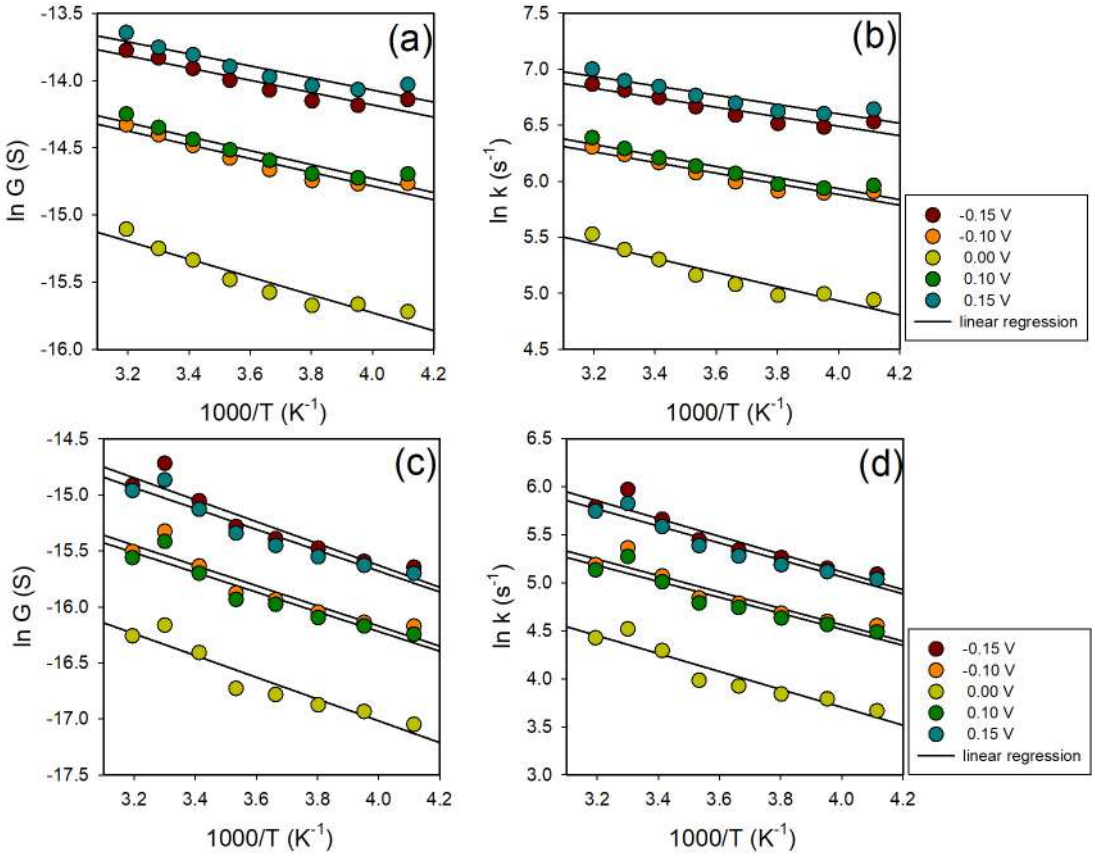

Figure 6.12: Arrhenius plots of G and k at different biases for NAB1 (a and b) and NAB2 (c and d). The E_a values are determined from the slope of the linear regression and are summarized in Table 6.3.

Source: Author (2023).

Table 6.3: Linear regression data from the Arrhenius plot for NAB MJs and the values of E_a.

Plot	Bias	NAB1				NAB2			
	(V)	slope	SD	r^2	E_a (eV)	slope	SD	r^2	E_a (eV)
ln *G versus* T^{-1}	-0.15	-456	64	0.8758	0.039	-977	142	0.8680	0.084
	-0.10	-511	61	0.9094	0.044	-900	140	0.8522	0.078
	0.00	-665	84	0.8972	0.057	-972	134	0.8809	0.084
	0.10	-520	68	0.8904	0.045	-879	122	0.8791	0.076
	0.15	-447	68	0.8562	0.039	-930	112	0.9073	0.080
ln *k versus* T^{-1}	-0.15	-423	62	0.8675	0.036	-925	131	0.8754	0.080
	-0.10	-476	60	0.8983	0.041	-852	130	0.8563	0.073
	0.00	-633	82	0.8928	0.055	-932	127	0.8823	0.080
	0.10	-493	62	0.9000	0.042	-831	114	0.8816	0.072
	0.15	-417	66	0.8474	0.036	-881	101	0.9143	0.076

Source: Author (2023).

Table 6.4: N calculation for 243 - 313 K temperature range at 0 V bias, for β = 2.7 nm $^{-1}$. $\overline{x}$ refers to the mean average value and SD refers to the standard error.

T (K)	FL1	FL2	NAB1	NAB2
243	7.86×10^2	5.36×10^3	1.36×10^7	4.65×10^8
253	8.05×10^2	5.66×10^3	1.44×10^7	5.21×10^8
263	8.41×10^2	6.15×10^3	1.43×10^7	5.53×10^8
273	9.38×10^2	7.32×10^3	1.57×10^7	6.06×10^8
283	1.14×10^3	8.36×10^3	1.73×10^7	6.41×10^8
293	1.13×10^3	7.64×10^3	2.00×10^7	8.82×10^8
303	1.17×10^3	8.57×10^3	2.18×10^7	1.13×10^8
313	1.28×10^3	9.00×10^3	2.52×10^7	1.02×10^8
$\overline{x} \pm$ SD	$1.0 \pm 0.2 \times 10^3$	$7 \pm 1 \times 10^3$	$1.8 \pm 0.4 \times 10^7$	$7 \pm 2 \times 10^8$

Source: Author (2023).

6.4 Conclusion

The impedance spectroscopy study of the MJs performed at different biases and temperatures has demonstrated that the associated electron transfer/transport phenomena obey the quantum mechanical tunneling and are controlled by the mesoscopic properties C_μ and R_q, thus proving that the rate–conductance relationship is described by the quantum rate expression $k = {}^{G}/_{C_\mu}$. Additionally, the determination of the amount of N enabled us to describe the participation of the electronic structure of the molecular layer within the framework of the quantum rate model. Finally, these results once again demonstrate that the quantum rate theory allows us to understand the electron transfer/transport phenomena of molecular electronic devices, which can be experimentally studied by IS.

References

ARTES, J. M. *et al.* Direct measurement of electron transfer distance decay constants of single redox proteins by electrochemical tunneling spectroscopy. **Acs Nano**, ACS Publications, v. 5, n. 3, p. 2060–2066, 2011.

BERGREN, A. J. *et al.* Electronic characteristics and charge transport mechanisms for large area aromatic molecular junctions. **The Journal of Physical Chemistry C**, ACS Publications, v. 114, n. 37, p. 15806–15815, 2010.

BUENO, P. R.; DAVIS, J. J. Charge transport and energy storage at the molecular scale: from nanoelectronics to electrochemical sensing. **Chemical Society Reviews**, Royal Society of Chemistry, v. 49, n. 21, p. 7505–7515, 2020.

CAREY, F. A.; SUNDBERG, R. J. **Advanced organic chemistry: part A: structure and mechanisms**. Springer Science & Business Media, 2007.

DAVIES, J. H. **The physics of low-dimensional semiconductors: an introduction**. Cambridge university press, 1998.

GUPTA, R. *et al.* Nanoscale molecular rectifiers. **Nature Reviews Chemistry**, Nature Publishing Group UK London, p. 1–17, 2023.

HOSSAIN, M. S.; BEVAN, K. H. Exploring bridges between quantum transport and electrochemistry. ii. a theoretical study of redox-active monolayers. **The Journal of Physical Chemistry C**, ACS Publications, v. 120, n. 1, p. 188–194, 2016.

MCCREERY, R. L. Carbon-based molecular junctions for practical molecular electronics. **Accounts of Chemical Research**, ACS Publications, v. 55, n. 19, p. 2766–2779, 2022.

RIBEIRO, W. C. *et al.* Molecular conductance of double-stranded DNA evaluated by electrochemical capacitance spectroscopy. **Nanoscale**, Royal Society of Chemistry, v. 8, n. 16, p. 8931–8938, 2016.

SANTOS, A. *et al.* Introducing mesoscopic charge transfer rates into molecular electronics. **Physical Chemistry Chemical Physics**, v. 22, n. 19, p. 10828–10832, 2020. ISSN 1463-9076. DOI: 10.1039/d0cp01621g.

SAYED, S. Y. *et al.* Charge transport in molecular electronic junctions: Compression of the molecular tunnel barrier in the strong coupling regime. **Proceedings of the National Academy of Sciences**, National Acad Sciences, v. 109, n. 29, p. 11498–11503, 2012.

VALIANTI, S.; CUEVAS, J. C.; SKOURTIS, S. S. Charge-Transport Mechanisms in Azurin-Based Monolayer Junctions. **The Journal of Physical Chemistry C**, ACS Publications, v. 123, n. 10, p. 5907–5922, 2019.

VAN NGUYEN, Q. *et al.* Molecular Signature and Activationless Transport in Cobalt-Terpyridine-Based Molecular Junctions. **Advanced Electronic Materials**, Wiley Online Library, v. 6, n. 7, p. 1901416, 2020.

VENKATRAMANI, R. *et al.* Breaking the simple proportionality between molecular conductances and charge transfer rates. **Faraday discussions**, Royal Society of Chemistry, v. 174, p. 57–78, 2014.

WIERZBINSKI, E. *et al.* The single-molecule conductance and electrochemical electron-transfer rate are related by a power law. **Acs Nano**, ACS Publications, v. 7, n. 6, p. 5391–5401, 2013.

YAN, H.; BERGREN, A. J.; MCCREERY, R. L. All-carbon molecular tunnel junctions. **Journal of the American Chemical Society**, ACS Publications, v. 133, n. 47, p. 19168–19177, 2011.

Conclusions

The findings presented in this study demonstrated that the quantum rate model provides an accurate interpretation of electron transfer and transport processes occurring at mesoscopic interfaces. The relationship between conductance G and quantum capacitance C_q proposed by the theory allowed us to understand and quantify the electron transfer kinetics k of electroactive interfaces whenever the degeneracy of the spin g_s and of the electrochemical current g_s are considered.

The quantum rate theory permitted the interpretation of the quantum resistance R_q obtained by equivalent circuit analysis as the contribution in series of two resistive terms, R_{qt} and R_s, which cannot be separated. The interpretation of R_q challenges the traditional understanding of R_{ct} in equivalent circuit analyses. Furthermore, it has been demonstrated that R_q establishes a quantized limit of the minimal resistance (or maximum conductance) in agreement with the theoretical value of 12.9 kΩ. Hence, it has been demonstrated that C_q and R_q govern the electrodynamics of the studying electrochemical interfaces.

From experimental point of view, it has been introduced a straightforward method to calculate k for heterogeneous electrochemical reactions, with C_q as the only variable, obtained from impedance-derived capacitive spectroscopy (ECS) that is in agreement with the C_q obtained from cyclic voltammetry (CV).

It has been demonstrated that the DOS of redox molecules assembled over conductive electrodes acts as accessible conductive quantum channels for ET reactions between electrodes and redox states in solution. The efficiency remains unaffected whether the ET process occurs in a single or two-step mechanism. Moreover, aligning the energy levels of capacitive states with that of the species in the bulk solution increases the number of quantum channels N available for ET reactions, potentially benefiting the development of advanced electrochemical nanoscale devices.

The study successfully demonstrated the amplification of the electrochemical capacitive current signal of the interface for the quantification of the NS1 DENV biomarker in undiluted serum samples with enhanced sensitivity and specificity. This novel strategy enabled the detection of small biological molecules and avoided false positive errors associated with matrix effects. Besides, the use of miniaturized gold electrodes showed promise for point-of-care (PoC) devices.

It has been demonstrated that the acidity of electroactive interfaces affects the mediation of diffusionless electron transfer process, specially when the redox probe undergoes to proton-coupled electron transfer reaction. It was observed an electrostatic repulsion between the negatively charged surface and redox species, which is triggered by high concentration of the redox probe. It was shown that whenever the electron transfer process is ruled by the C_q and R_q elements, the associated quantum capacitive states are enable to mediate the electron transfer due to the energy level alignment is sustained, leading to a diffusionless electron transfer process.

Impedance spectroscopy studies of aromatic MJs at different biases and temperatures showed the applicability of the quantum rate model to study the electron transfer/transport properties of molecular electronic settings. These phenomena are controlled by C_μ and R_q. The quantum rate expression $k = {}^{G}/_{C_\mu}$ successfully described the rate-conductance relationship. Also, the estimate value of N allowed to address the role played by electronic structure of the molecular layer within the framework of the quantum rate model.

In conclusion, the quantum rate theory, supported by experimental studies, allows us to gain insights into the electron transfer/transport phenomena of molecular electronic and electrochemical devices. The results obtained through various techniques, such as SI, validate the feasibility and potential applications of the quantum rate model in understanding and controlling electron transfer processes at the nanoscale interface, allowing us to develop novel and advanced electrochemical quantum devices.

Appendix A

Peptide Characterization: SS–Pep–Fc

The peptide Fc–Glu–Ala–Ala–Cys–Cys–NH_2 of MW = 733.16 g mol^{-1} (Fig. A.1*a*) was synthetized by solid phase approach and purified by HPLC. The successful of the synthesis was confirmed by mass spectrometry using electrospray positive ionization (ESI) in the m/z 300–2000 range (Fig. A.1*c*). The peptide purity ($>$ 93%) was assessed by analytical mode HPLC (Fig. A.1*b*). The retention time of 14.45 min, using the method of 5 to 95% of solvent B in 30 min with 1 mL min^{-1} (solvent A = 0.045% TFA/H_2O and B 0.036% (TFA/ACN v/v), corresponds to the purified peptide.

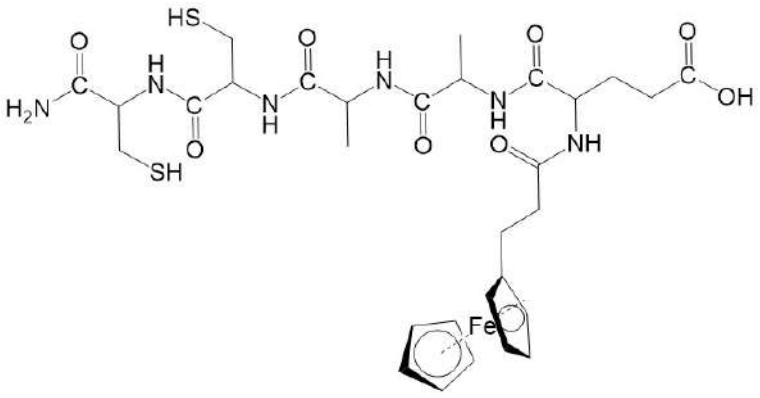

(a)

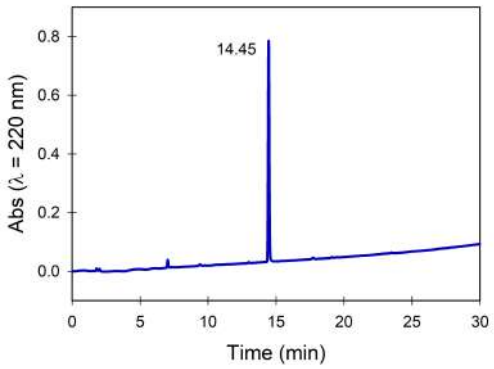

(b)

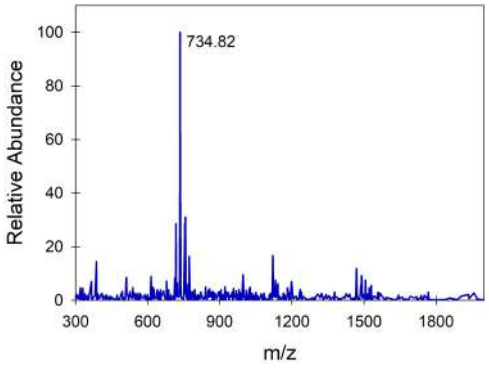

(c)

Figure A.1: (a) SS-Pep-Fc chemical structure. (b) Chromatogram of the purified peptide with retention time of 14.45 min. (c) Mass spectrum of the redox peptide was obtained using a Brucker system in positive mode: 734.82 g mol^{-1}, corresponding to the peak of 14.45 min in (b).

Source: Author (2023).

Appendix B

Determination of Electroactive Area of Au Electrode

The voltammogram of the last cycle of the sulphuric acid cleaning step reveals information about the quality of the surface of the gold electrode. Fig. B.1 depicts three main regions: (i) the oxygen reduction at lower potentials; (ii) non-Faradaic capacitive region that indicates contaminants adsorbed on the gold surfaces whether the current difference is out of the range around 0.3 and 0.9 μA; (iii) gold oxide formation at the surface of the polycrystalline electrode between $\sim$1.2 and 1.6 V, which reports on the orientation of the crystalline gold lattice. The area of the cathodic peak (reduction peak area A_r)is used to calculate the A_e, which is obtained by mathematical integration. The valued obtained is used in the following expression,

$$A_e = \frac{A_r[\mu A.V^{-1}]}{s[V.s^{-1}] \times 410[\mu C.cm^{-2}]} \tag{B.1}$$

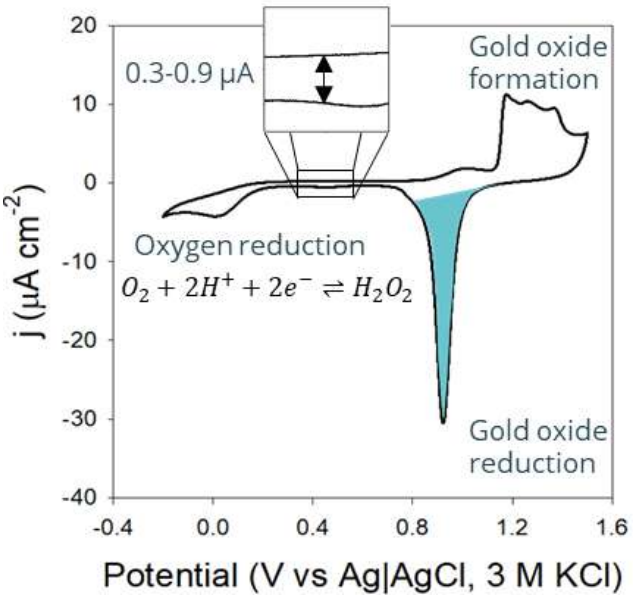

Figure B.1: Voltammogram of gold surface in 0.5 M H_2SO_4. Shaded region depicts A_r area of the cathodic peak

Source: Author (2022).

Appendix C

Peptide Characterization: Pep–Fc

The peptide Fc–Glu–Ala–Ala–Cys–NH_2 of 630.14 g mol^{-1} (Fig. C.1*a*), synthetized by solid-phase method and was purified by semi-preparative reverse-phase HPLC. Afterwards, the peptide was identified by electrospray mass spectrometry, using a Thermo LCQ-fleet spectrometer. Fig. C.1*c* shows the mass spectrum obtained in electrospray positive ionization mode at mass/charge ratio (m/z) of 200–1200. Eventually, the HPLC in analytical mode provided the peptide purity ($>$ 96%)(Fig. C.1*b*).

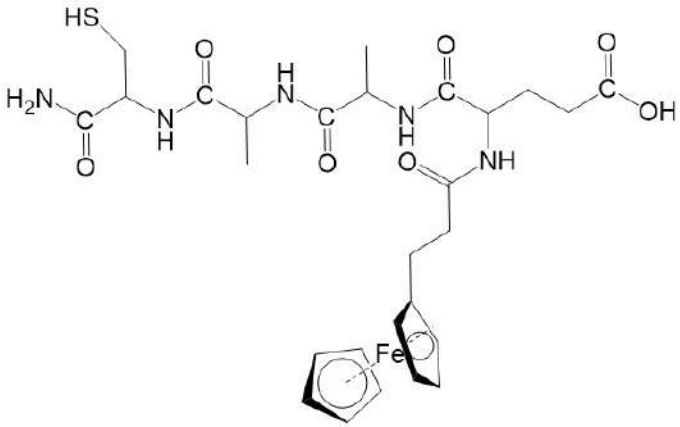

(a)

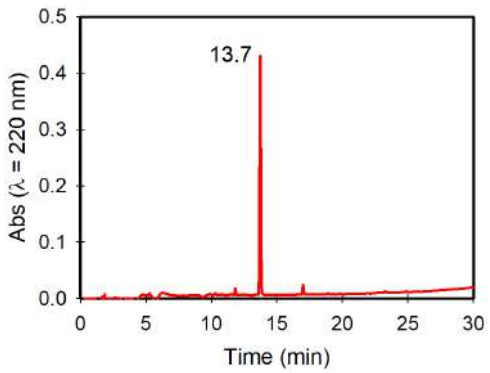

(b)

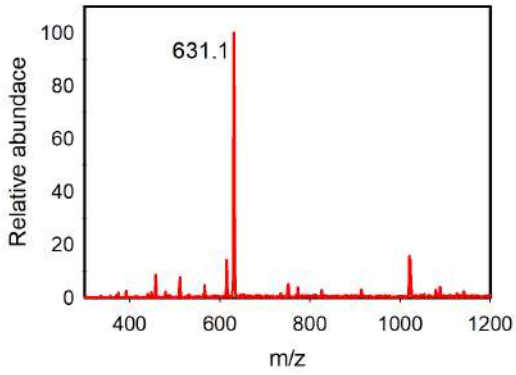

(c)

Figure C.1: (a) Pep–Fc chemical structure. (b) Chromatogram of the purified peptide with retention time of 13.7 min. (c) Mass spectrum of the redox peptide was obtaine using a Brucker system in positive mode: 630.14 g mol^{-1}, corresponding to the peak of 13.7 min in (b).

Source: Author (2023).

Appendix D

Non-Faradaic Circuit Elements

Table D.1 summarizes the values of circuit elements that comprises the non-Faradaic contribution measured at potential outside redox window (i.e., V_{out}= 0.1 V), using a supporting electrolyte of 20 mM $TBAClO_4$ in ACN/H_2O (1:4, v/v), for Pep-Fc and C11-FC monolayers.

Table D.1: Circuit parameters values.

SAM	Pep-Fc		C11-Fc	
	$\overline{x}$	$\sigma_{\overline{x}}$	$\overline{x}$	$\sigma_{\overline{x}}$
$C_m/\mu F\ cm^{-2}$	2.0	0.1	0.74	0.04
$C_t/\mu F\ cm^{-2}$	5.1	0.6	1.4	0.4
R_t/Ω	0.7	0.1	0.5	0.1

Appendix E

Diffusion *versus* Diffusionless Processes

The diffusion and diffusionless dependence of the ET kinetics of the studied heterogeneous settings was evaluated from the CVs measured at different scan rate s, for bare gold and Fc-COOH and for modified gold electrode with redox SAM. Plots of the anodic/cathodic current peaks i_p *versus* $s^{1/2}$ or s are shown in Fig. E.1. The linear dependence between i_p *versus* $s^{1/2}$ follows the relations described in Randles–Sevcik's for the redox Fc-COOH, indicating a diffusion-limited kinetics (Fig. E.1*a*), whereas for Pep-Fc the linear dependence between i_p *versus* s follows the Laviron's equation, for a diffusionless-limited kinetics (Fig. E.1*b*).

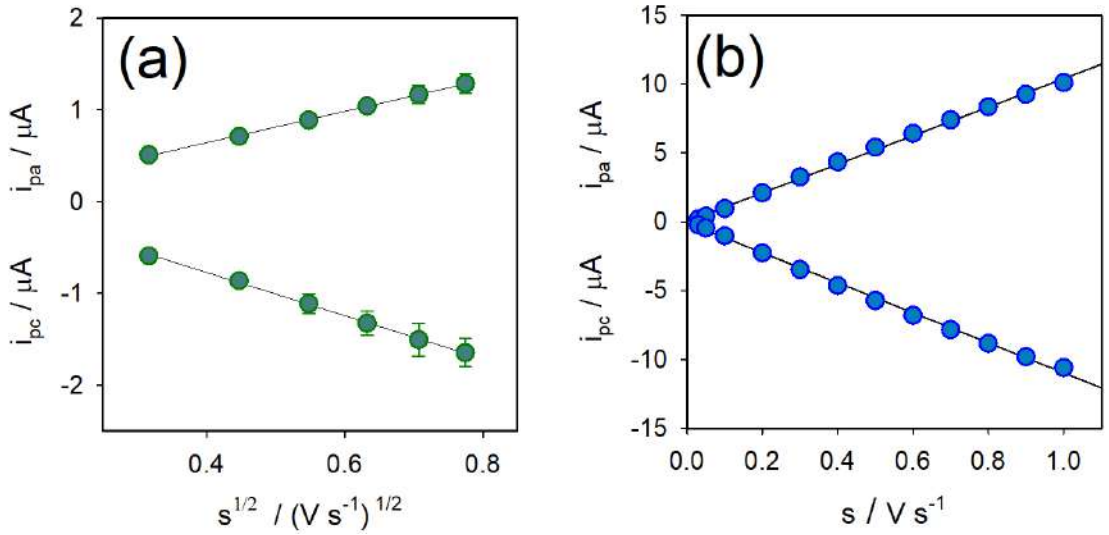

Figure E.1: The relationship between current peaks and scan rate. (a) i_p *versus* $s^{1/2}$ plot for both cathodic and anodic peak currents of 100 μM Fc-COOH, which was conducted in triplicate. Linear regression parameters (r^2=0.9992 and r^2=0.9988 for anodic and cathodic plots, respectively) indicate the $s^{1/2}$ linear dependence of i_p in the electrochemical reaction between the metal electrode and the redox probe free in solution, Fc-COOH that according to Randles–Sevcik equation, indicates a diffusion-controlled kinetics. (b) i_p *versus* s plot for both cathodic and anodic peak currents of Pep-Fc. Linear regression parameter (r^2=0.9997 and r^2=0.9974 for anodic and cathodic plots, respectively) indicate the s linear dependence of i_p in the electrochemical reaction between the metal electrode and a redox probe chemically attached to the electrode, which follows the Laviron equation, indicating a diffusionless kinetic situation. *Source: Author (2023).*

Appendix F

Electrochemical Impedance of Fc–COOH

Electrochemical characterization of Fc-COOH in direct contact with the electrode, measured at the formal potential E_F/e, in 20 mM $TBAClO_4$ supporting electrolyte, without intermediation of redox capacitive states. Fig. F.1*a* shows the impedimetric response, at low frequency, typical for a diffusion-controlled system. No relevant impedimetric information can be extracted, whereas Fig. F.1*b* depicts a capacitive feature attributed to the double layer capacitive disruption of the ions of the electrolyte by the presence of the Fc-COOH.

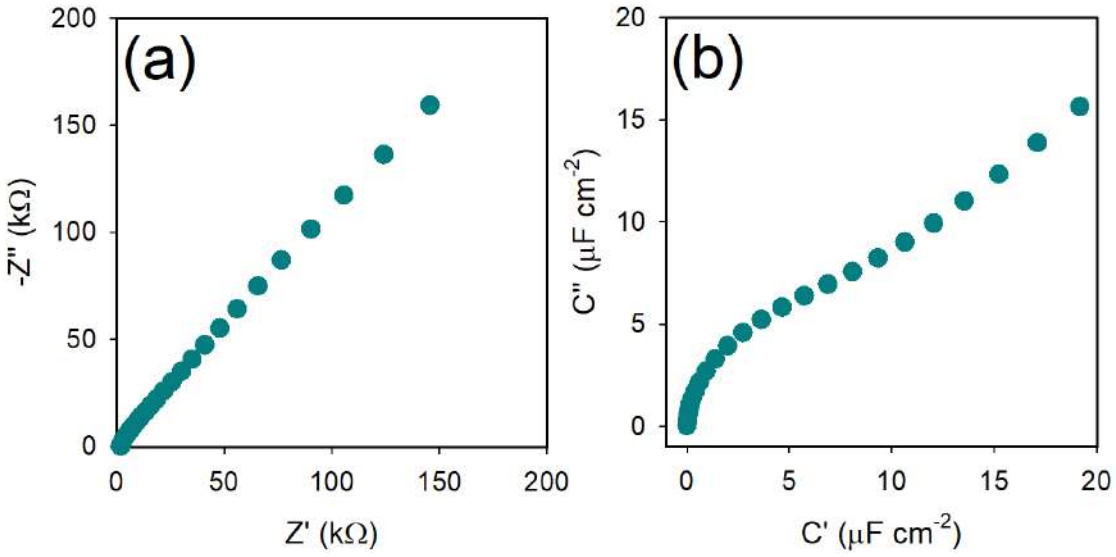

Figure F.1: (a) Impedimetric and (b) capacitive Nyquist plots of redox Fc-COOH.
Source: Author (2023).

Appendix G

Anodic Peak Deconvolution

CV of C11–Fc interface measured in the presence of Fc–COOH shows an oxidative peak with an additional contribution at lower potentials. A deconvolution of this anodic peak, as depicted in Fig. G.1, was conducted to revealing separate the two peaks with: one at 0.39 V and another at 0.45 V, corresponding to the individual peak potential contributions of the C11–Fc (see Fig. 3.5*a*) and Fc–COOH (see Fig. 3.1*a*). This evidence the two contributions and confirm the weaker alignment of the energy levels of states in solution and that of the electrode through two different paths: one through capacitive states in the interface and the other directly without intermediation of the capacitive states. Only the electron path associated with the capacitive states has a quantum efficient of transport, as discussed in the main text.

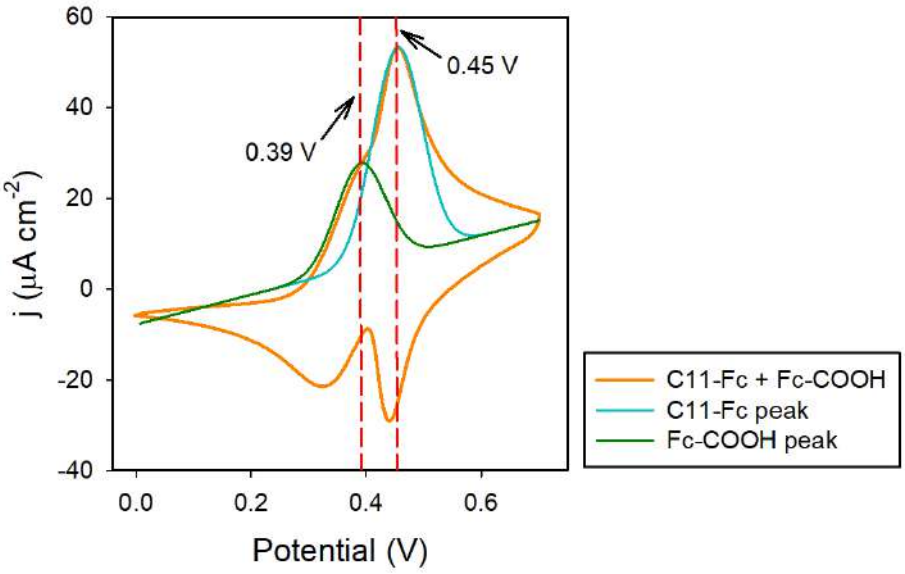

Figure G.1: (a) Anodic peak deconvolution of the cyclic voltammetry C11–Fc in 20 mM $TBAClO_4$ supporting electrolyte with 100 μM Fc-COOH.

Source: Author (2023).

Appendix H

Surface characterization of Miniaturized Gold Electrodes

Topological and roughness characterization of the bare miniaturized gold was performed by Dr. C. A. R. Costa and the staff of the Brazilian Nanotechnology National Laboratory (LNNano), part of the Brazilian Centre for Research in Energy and Materials (CNPEM), Brazil using an atomic force microscope. The micrograph shown by Fig. H.1, reveals that the electrode surface is composed of Au grains with a diameter ranging from 20 to 50 nm, with a roughness mean squared value, of 1.4 nm. Low surface roughness is required to achieve well organized self-assembled monolayer ensuring reproducible electrochemical response.

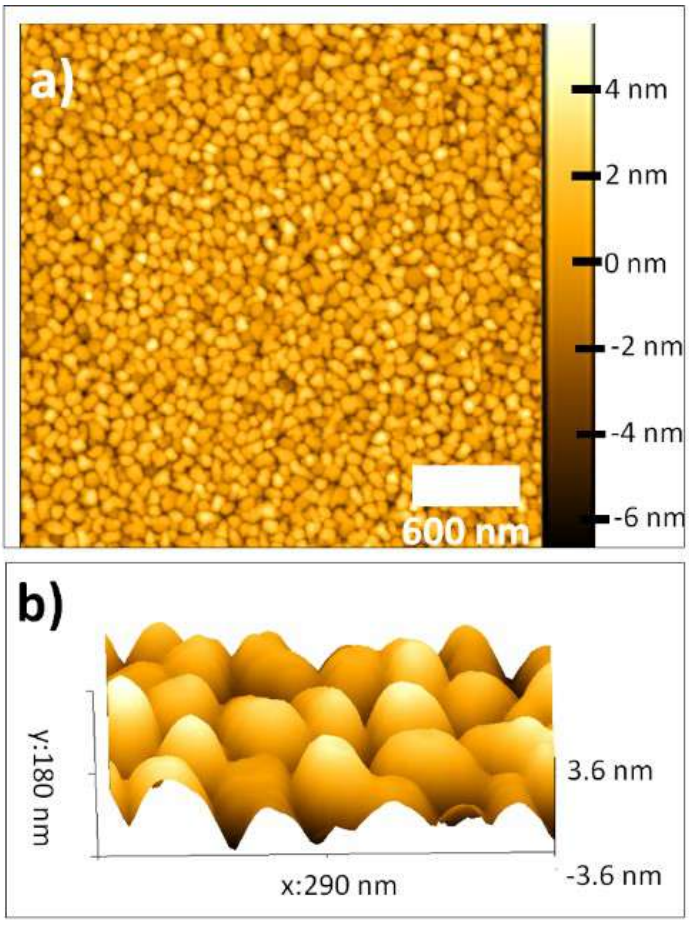

Figure H.1: (a) Atomic force microscopic topographical imaging of SiO_2/Au patterned electrodes. (b) Three-dimensional rendering of a selected region.

Appendix I

Equivalent Circuit Fitting of Modified Miniaturized Electrodes

Equivalent circuit fitting of the EIS raw data related to non-Faradaic and Faradaic response obtained at V_{out} = 0.1 V and $E_F/e \sim 0.36$ V, respectively, terface fabrication process measured in 20 mM $TBAClO_4$ in ACN/H_2O (1:4, $^{v}/_{v}$) as supporting electrolyte. Fig. I.1 shows the complex capacitive diagram of the non-Faradaic, Faradaic of Pep–Fc and Fc–COOH suitable fitted followed the equivalent circuit analysis performed in chapter 3. The inset shows the non-faradaic contribution measured at V_{out} = 0.1 V, which is minimal in comparison with the faradaic response measured at $E_F/e \sim 0.36$ V. Consequently, Table I.1 summarizes the values of circuit elements obtained for the non-Faradaic response.

Table I.1: Circuit parameters values.

Parameters	
$C_m/\mu F$	0.054
$C_t/\mu F$	1.468
R_t/Ω	430
R_s/Ω	1860

Source: Author (2023).

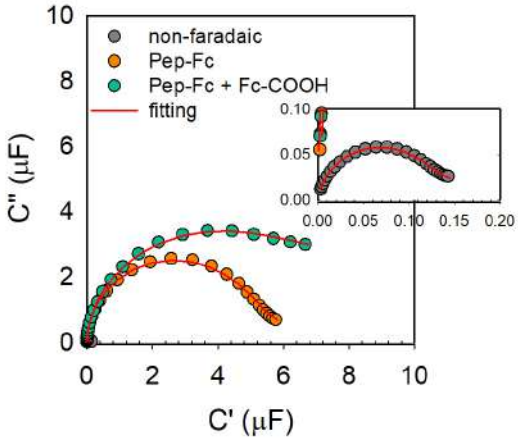

Figure I.1: Capacitive Nyquist plot of the redox interface before biosensing interface fabrication. *Source: Author (2023).*

Appendix J

Peptide Characterization: non-redox peptide

The peptide Glu–Ala–Ala–Cys–NH_2 of MW = 392.2 g mol^{-1} (Fig. J.1*a*) was synthetized by solid phase approach and was purified by semi-preparative reverse-phase HPLC. Afterwards, the peptide was identified by electrospray mass spectrometry, using a Thermo LCQ-fleet spectrometer. Fig. J.1*c* shows the mass spectrum obtained in electrospray positive ionization mode at mass/charge ratio (m/z) of 200–1200. Eventually, the HPLC in analytical mode provided the peptide purity (> 94%)(Fig. J.1*b*).

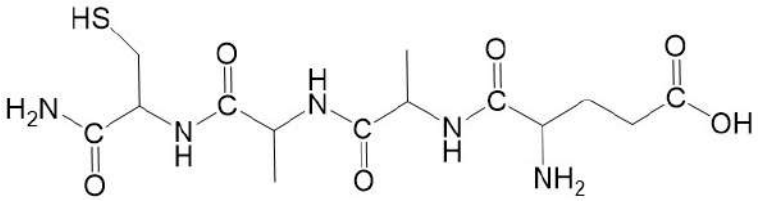

(a)

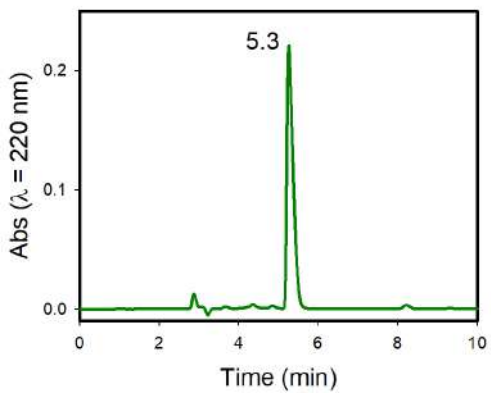

(b)

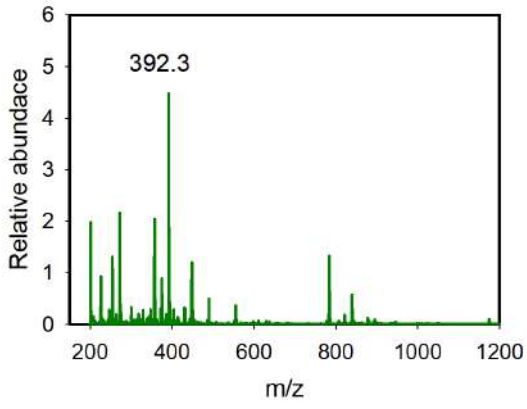

(c)

Figure J.1: (a) non-redox peptide chemical structure. (b) Chromatogram of the purified peptide with retention time of 5.3 min. (c) Mass spectrum of the peptide was obtained using a Brucker system in positive mode: 392.2 g mol^{-1}, corresponding to the peak of 5.3 min in (b).

Source: Author (2023).

Appendix K

Additional Electrochemical Characterization of Fc–COOH

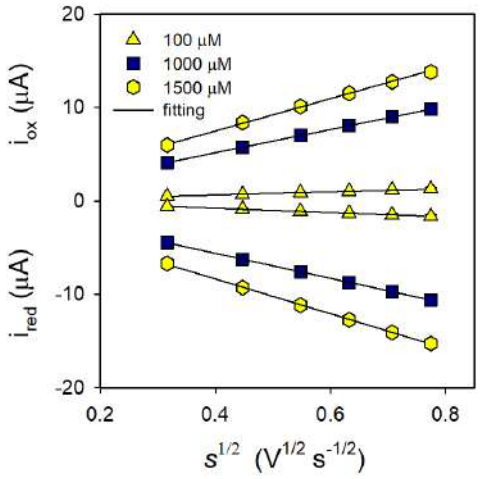

Figure K.1: The diffusion dependence of the ET kinetics between bare gold and Fc–COOH was evaluated from the CVs measured at different scan rate s for some plot for both cathodic and anodic peak currents of 100, 1000 and 1500 μM Fc-COOH, which was conducted in triplicate. The linear dependence between i_p *versus* $s^{1/2}$ follows the relations described in Randles–Sevcik's for the redox Fc–COOH, indicating a diffusion-limited kinetics for these studied concentrations. All linear regression have $r^2 \sim 0.998$ - 1.

Source: Author (2023).

The diffusion coefficients for $Fc–COO^-$ and $Fc^+–COO^-$ were calculated by replacing the obtained slope of the linear regression in Randles-Sevcik equation (see Eq. K.1). The obtained values are reported in Table K.1.

$$D_0 = \left(\frac{slope}{0.446\mathbf{n}FA_g[Fc-COOH]} \right)^2 \times \frac{\mathbf{R}T}{\mathbf{n}F} \tag{K.1}$$

where **n** is the number of electron involved in the redox reaction, F is the Faraday constant, A_g is the geometric area of the electrode and **R** is the ideal gas constant.

Table K.1: Diffusion constant values for representative [Fc–COOH]. Error bars represent one standard deviation of measurements on three separate electrodes.

[Fc–COOH] (μM)	$D_0^{Fc-COO^-}$ (10^{-18} cm^{-2} s^{-1})	$D_0^{Fc^+-COO^-}$ (10^{-18} cm^{-2} s^{-1})
100	3.84 ± 0.02	7.30 ± 0.06
1000	218.8 ± 0.3	252.3 ± 0.5
1500	424.0 ± 0.3	489.91 ± 0.05

Source: Author (2023).

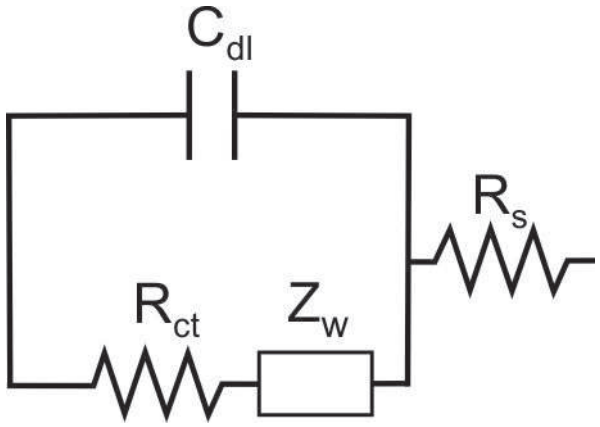

Figure K.2: Equivalent circuit that models the electroactive response of Fc–COOH at high concentrations. Z_w is the Warburg diffusion element, which models the diffusion process typical at low frequencies. The obtained values are reported in Table K.2

Source: Author (2023).

Table K.2: The electroactive response of [Fc–COOH] at high concentrations was fitted using the Randless-circuit shown by Fig. K.2.

Fc–COOH	R_{ct}
1000	108 ± 4
1100	120 ± 10
1250	110 ± 10
1500	140 ± 8

Source: Author (2023).

Appendix L

Pep–SAM: Diffusion-controlled kinetics of Fc–COOH

The diffusion dependence of the ET kinetics was evaluated from the CVs measured at different [Fc–COOH], for modified gold electrode with non-redox SAM. Plot of the anodic/cathodic current peaks i_p *versus* [Fc–COOH] is shown in Fig. L.1. The linear dependence between i_p *versus* [Fc–COOH] follows the relations described in Randles–Sevcik's for the redox Fc-COOH, indicating a diffusion-limited kinetics (Fig. L.1*a*)

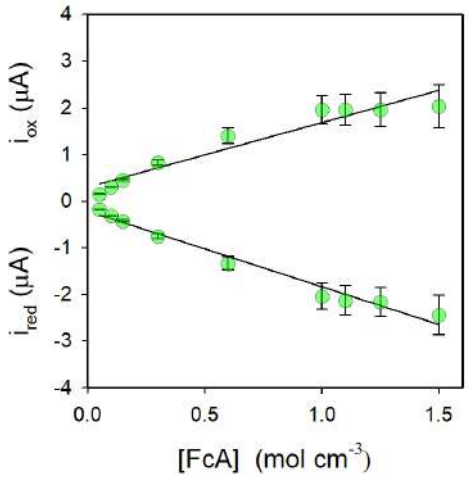

Figure L.1: i_p *versus* [Fc–COOH] plot for both cathodic and anodic peak currents, which was conducted in duplicate. Linear regression parameter (r^2 = 0.9261 and r^2 = 0.9765 for anodic and cathodic plots, respectively) indicate the [Fc–COOH] linear dependence of i_p in the electrochemical reaction between the metal electrode and the redox probe free in solution, which is in agreement with the Randles–Sevcik equation.

Source: Author (2023).

Appendix M

Equivalent Circuit Fitting of Pep–SAM in Function of [Fc–COOH]

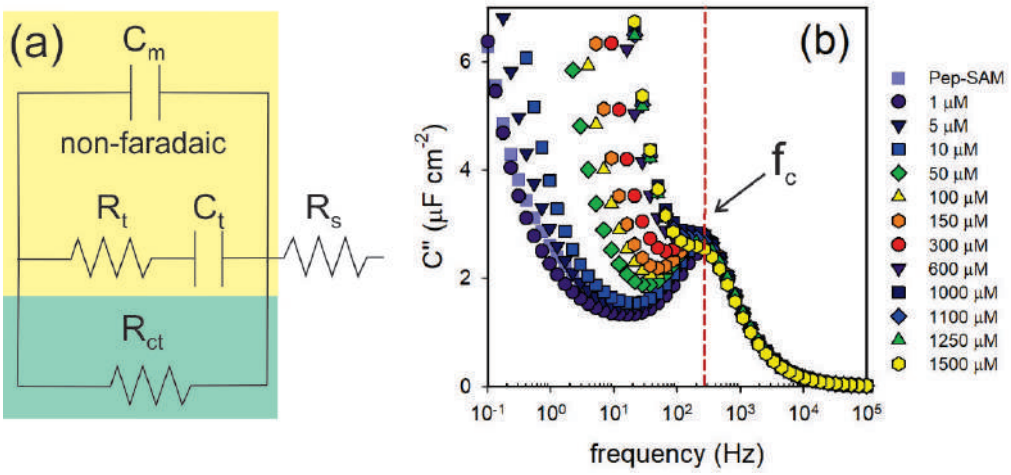

Figure M.1: (a) Bode capacitive diagram showing the peak value that informs on the relaxation process time-scale $\tau_t = R_t C_t$, which remains constant ~ 260 s^{-1}. (b) The equivalent circuit that models response of the Pep–SAM, which is comprised by the non-Faradaic branch and a parallel branch related with the resistive process such as R_{ct}. At Fc–COOH] > 50 μM, diffusive process are observed, thus the Warburg element is added in series with R_{ct}. The main elements are reported in Table 5.2, whereas additional values of R_s and C_m are 1980 ± 70 Ω and 0.449 ± 0.006 μF cm^{-2}, respectively.

Source: Author (2023).

Appendix N

Equivalent Circuit Fitting of Pep–rSAM in Function of [Fc–COOH]

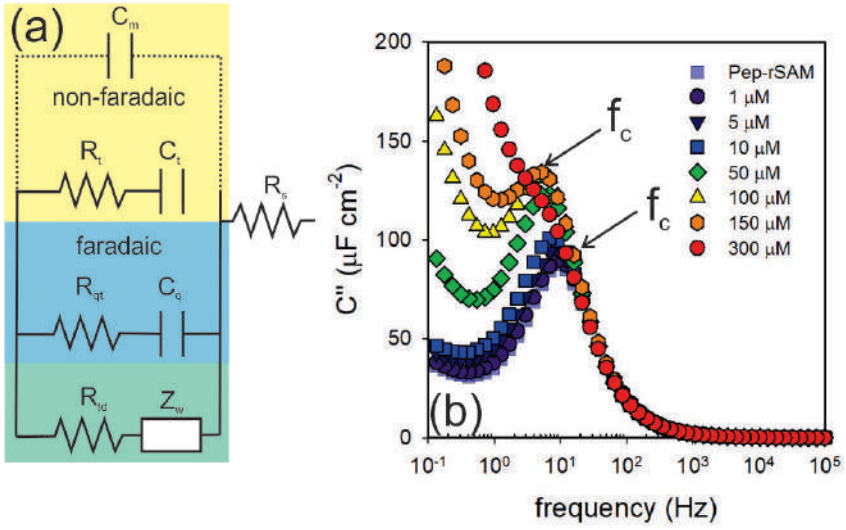

Figure N.1: (a) Bode capacitive diagram showing the peak value that informs on the relaxation process time-scale $\tau_q = R_q C_q = f_c^{-1}$ and consequently on the kinetics, recalling $f_c = {}^{k}/_{2}$. f_c decreases from 9.1 to 3.9 s^{-1} as [Fc–COOH] increases, until is not spotted. (b) The equivalent circuit that models response of Pep–rSAM, which is basically that studied in chapter 3.1. At Fc–COOH] > 1000 μM, diffusive process are observed, thus the Warburg element is added in series with R_{td}. The elements associated with the non-Faradaic response are summarized in Table D.1.

Source: Author (2023).

Appendix O

Density Current Calculation from IS Data for MJs

Table O.1: Data fitting using the equivalent circuit shown in Fig. 6.6 for the all the large-area MJ (0.00125 cm^2) performed at different bias potentials at room temperature. Additional mesoscopic properties are calculated from the obtained values of C_μ and R_q.

MJ	Bias (V)	C_μ (nF)	R_c (Ω)	R_q (MΩ)	$k = {}^1/_{R_q C_\mu}$ (s^{-1})	$G = {}^1/_{R_q}$ (μS)	$\lvert j\rvert = {}^{GV}/_{A}$ (μA cm^{-2})
AB	-0.2	7.82	69	14.93	86	0.07	11
	-0.15	7.83	70	18.37	70	0.05	7
	-0.10	7.83	69	21.40	60	0.05	4
	-0.05	7.83	70	24.23	53	0.04	2
	0.00	7.83	69	25.31	50	0.04	0
	0.05	7.83	69	24.02	53	0.04	2
	0.10	7.83	68	24.04	64	0.05	4
	0.15	7.83	69	17.36	74	0.06	7
	0.20	7.82	69	13.00	98	0.08	12
FL1	-0.20	14.27	41	0.18	3996	5.70	913
	-0.15	14.27	39	0.28	2513	3.59	430
	-0.10	14.29	39	0.45	1549	2.21	177
	-0.05	14.31	40	0.65	1068	1.53	61
	0.00	14.39	40	0.75	928	1.33	0
	0.05	14.34	39	0.41	1083	1.55	62
	0.10	14.31	40	0.27	1722	2.46	197
	0.15	14.30	40	0.16	2594	3.71	445
	0.20	14.31	40	0.18	4295	6.14	983
FL2	-0.2	14.59	44	0.13	5303	7.73	1238
	-0.15	14.58	44	0.17	4015	5.85	702

Continued on next page

Table O.1 – continued from previous page

MJ	Bias (V)	C_μ (nF)	R_c (Ω)	R_q (MΩ)	$k = {}^1/_{R_q C_\mu}$ (s^{-1})	$G = {}^1/_{R_q}$ (μS)	$\lvert j\rvert = {}^{GV}/_A$ (μA cm^{-2})
FL2	-0.10	14.58	44	0.24	2857	4.16	333
	-0.05	14.61	44	0.33	2063	3.01	121
	0.00	14.66	43	0.38	1812	2.66	0
	0.05	14.64	44	0.32	2138	3.13	125
	0.10	14.61	44	0.25	2725	3.98	318
	0.15	14.59	44	0.16	4226	6.17	740
	0.20	14.61	44	0.12	5661	8.27	1324
NAB1	-0.20	11.00	35	0.36	2492	2.74	439
	-0.15	11.01	36	0.61	1483	1.63	196
	-0.10	11.04	36	1.08	836	0.92	74
	-0.05	11.07	36	1.73	521	0.58	23
	0.00	11.09	36	2.28	396	0.44	0
	0.05	11.06	36	1.67	541	0.60	24
	0.10	11.04	35	1.17	776	0.86	68
	0.15	11.02	36	0.72	1268	1.40	168
	0.20	11.01	36	0.43	2110	2.32	372
NAB2	-0.2	11.18	43	1.23	727	0.81	130
	-0.15	11.19	42	1.95	459	0.54	62
	-0.10	11.20	42	3.09	289	0.32	26
	-0.05	11.26	42	4.42	201	0.23	9
	0.00	11.28	41	5.11	173	0.20	0
	0.05	11.26	42	4.27	208	0.23	9
	0.10	11.22	42	2.84	313	0.35	28
	0.15	11.21	39	1.83	486	0.55	65
	0.20	11.20	42	1.25	776	0.87	139

Source: Author (2023).

Appendix P

IS Data in Function of Temperature for MJs

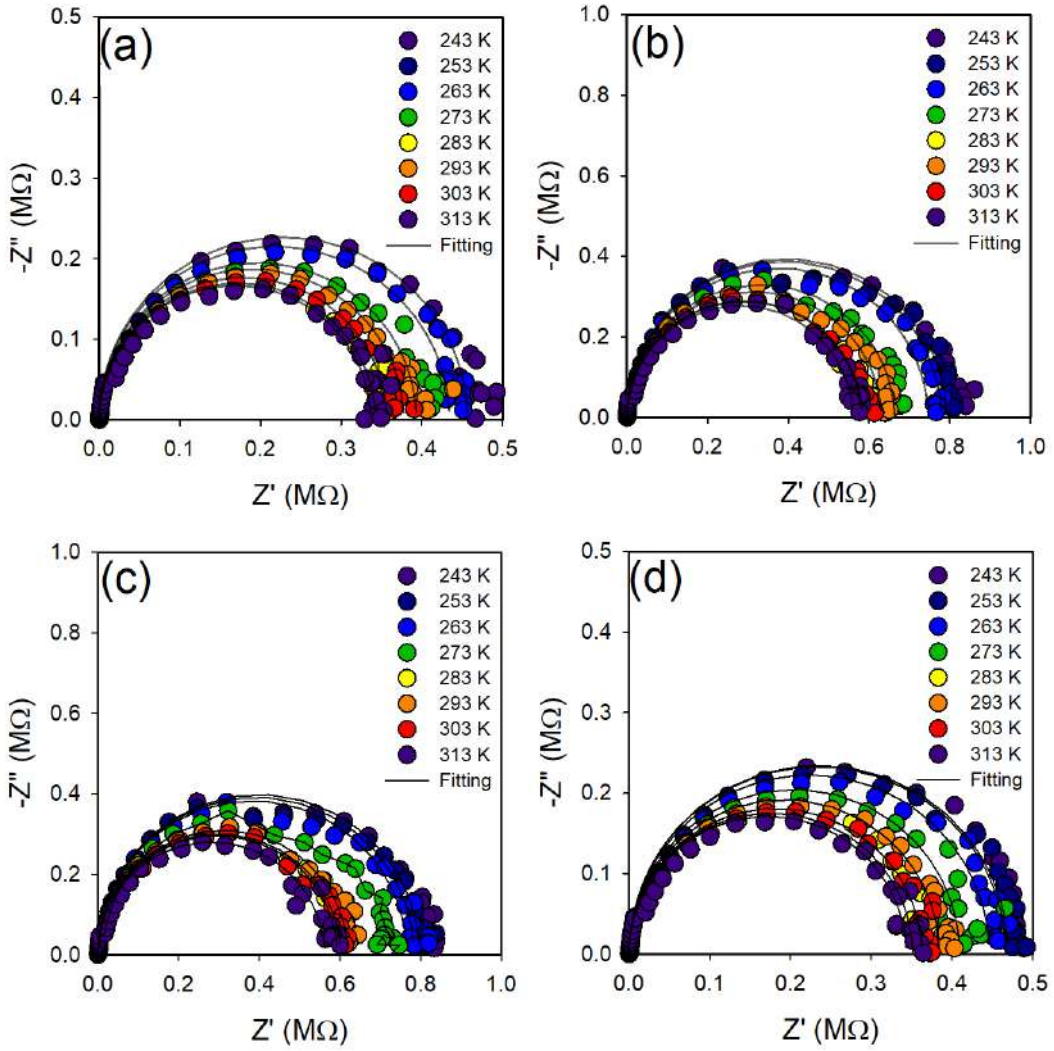

Figure P.1: Impedance Nyquist diagrams for FL1, showing the variation of the impedance pattern in functionof T measured at (a) -0.15 V, (b) -0.10 V, (c) 0.10 V and (d) 0.15 V, which were fitted using the equivalent circuit shown in Fig. 6.6*a*.

Source: Author (2023).

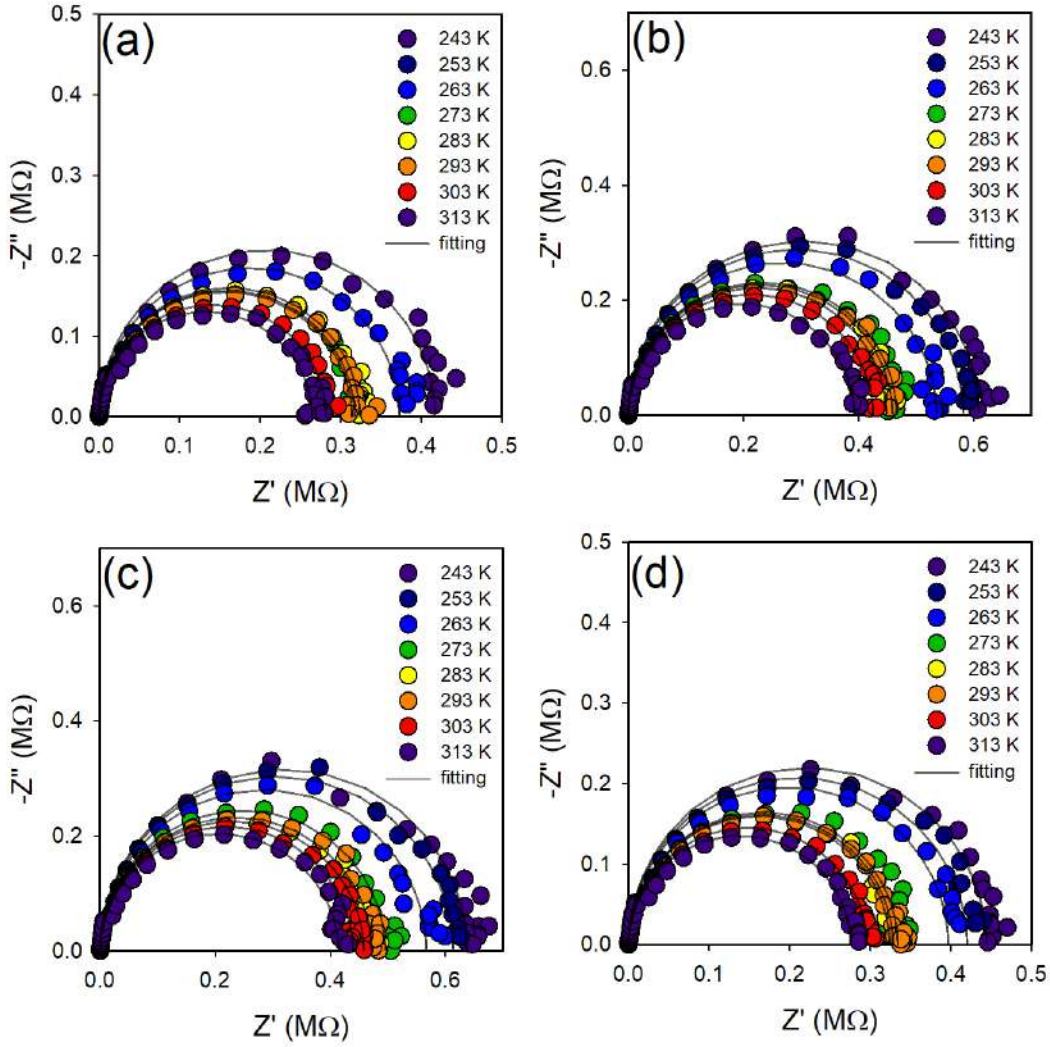

Figure P.2: Impedance Nyquist diagrams for FL2, showing the variation of the impedance pattern in functionof T measured at (a) -0.15 V, (b) -0.10 V, (c) 0.10 V and (d) 0.15 V, which were fitted using the equivalent circuit shown in Fig. 6.6*a*.

Source: Author (2023).

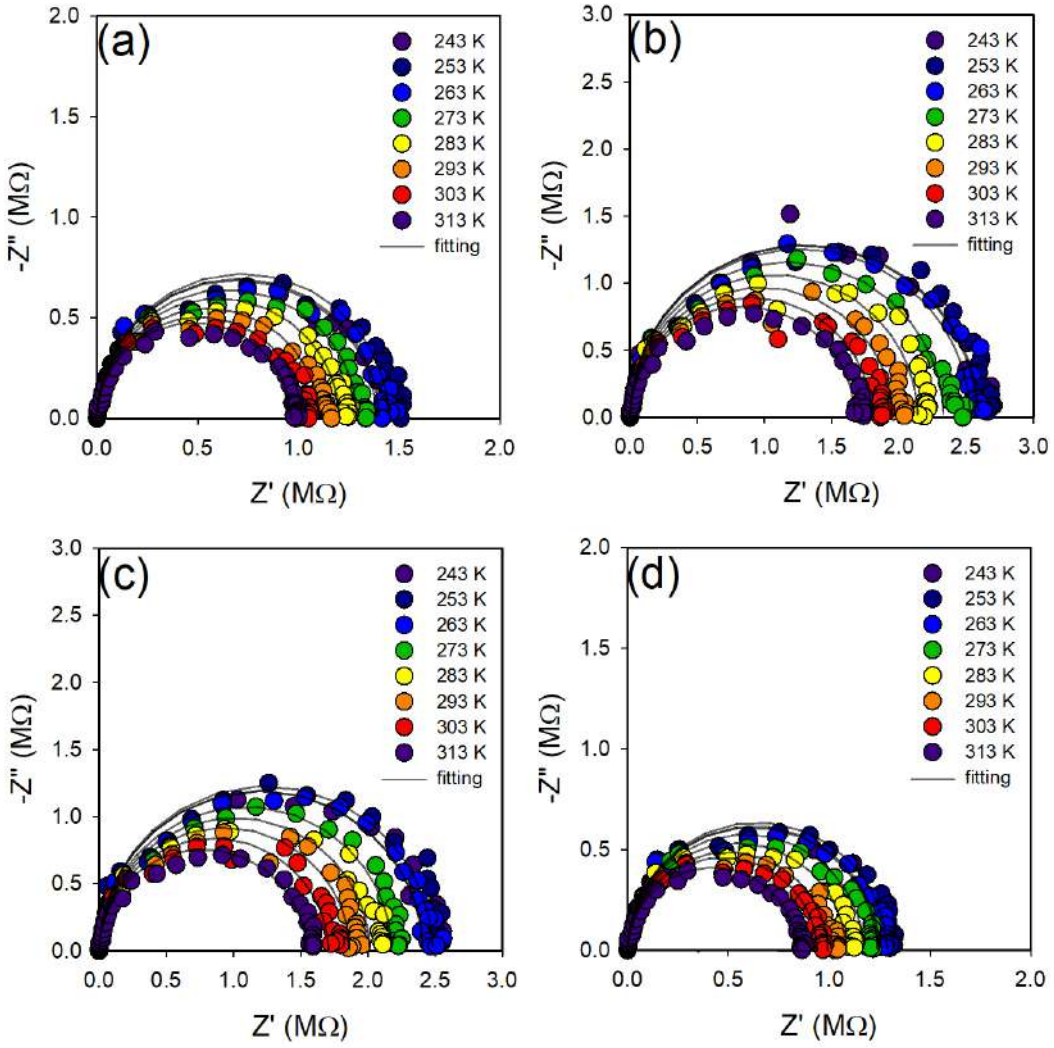

Figure P.3: Impedance Nyquist diagrams for NAB1, showing the variation of the impedance pattern in functionof T measured at (a) -0.15 V, (b) -0.10 V, (c) 0.10 V and (d) 0.15 V, which were fitted using the equivalent circuit shown in Fig. 6.6*a*.

Source: Author (2023).

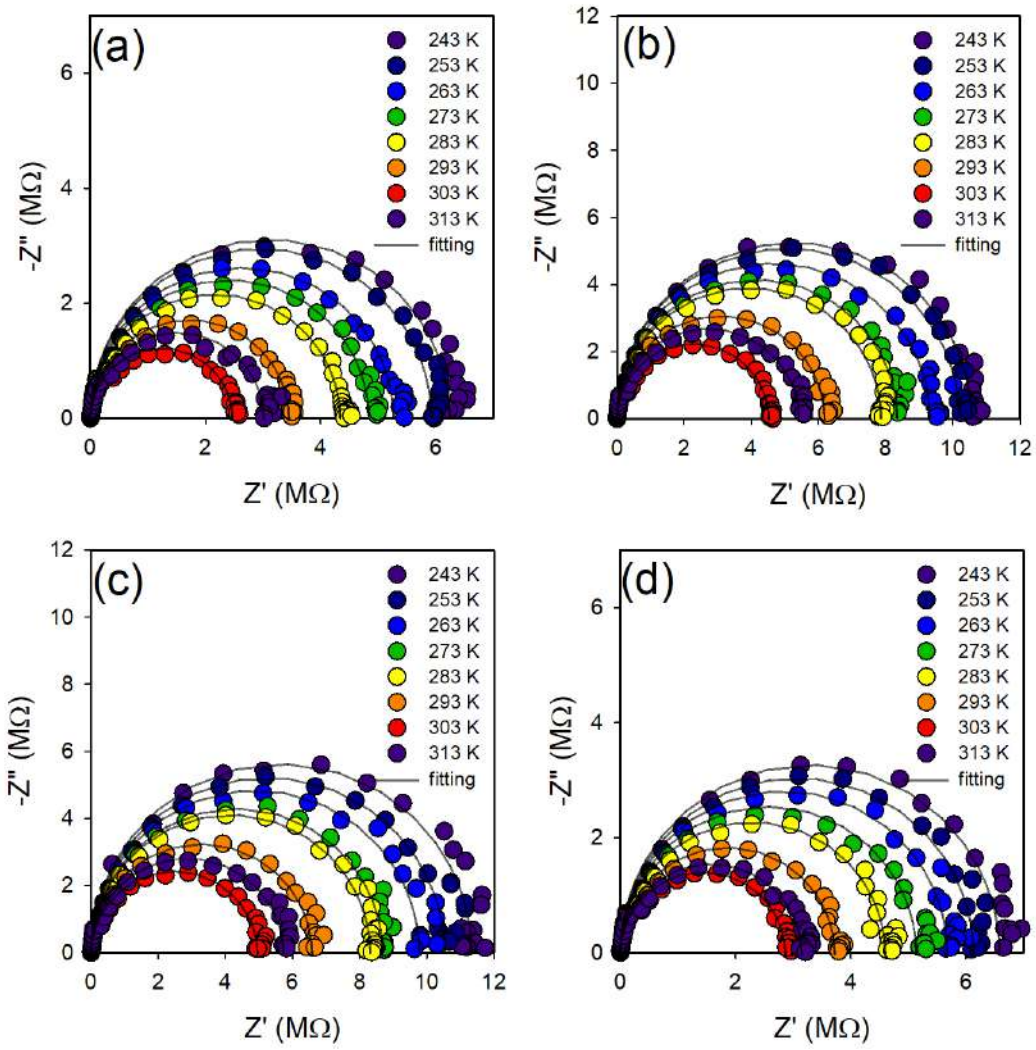

Figure P.4: Impedance Nyquist diagrams for NAB2, showing the variation of the impedance pattern in functionof T measured at (a) -0.15 V, (b) -0.10 V, (c) 0.10 V and (d) 0.15 V, which were fitted using the equivalent circuit shown in Fig. 6.6*a*.

Source: Author (2023).